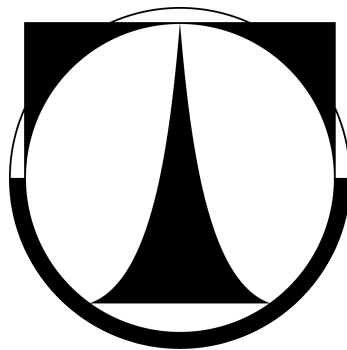


TECHNICAL UNIVERSITY OF LIBEREC

Faculty of Mechatronics, Informatics
and Interdisciplinary Studies



**Numerical modeling and experimental investigation
of flow in domains with moving boundaries**

Habilitation Thesis

Ing. Petr Šidlof, Ph.D.

September 2014

Acknowledgements

The papers reprinted within this thesis are a result of a fruitful cooperation with a number of colleagues from both Czech Republic and abroad. Having been part of the research teams of the Department of Dynamics and Vibrations of the Institute of Thermomechanics of the Czech Academy of Sciences (IT CAS), Groupe Dynamique des Fluides et Acoustique de l'École Nationale Supérieure de Techniques Avancées in France (ENSTA ParisTECH), NTI department of the Faculty of Mechatronics, Informatics and Interdisciplinary Studies at the Technical University of Liberec (FM TUL), CFD research group of the Department of Energy and Process Engineering at the Norwegian University of Science and Technology in Trondheim (NTNU) and Institut für Mechanik und Mechatronik of the Vienna University of Technology (TU Wien), in some cases for almost fifteen years and in others for at least a few months, proved as the cardinal impetus for realizing the research and publishing the results summarized in this thesis.

In the first place, I have to thank to Jaromír Horáček (IT CAS) for his long-term guidance, help, support and experience, for introducing me to the international community and also for his extremely kind personal approach. During the years at the Institute of Thermomechanics I have had pleasure to work with a number of other people, namely Jan G. Švec (affiliated also, during different times, to the University of Groningen, National Center for Voice and Speech in Denver, Medical Healthcom Ltd., Prague and later the Palacký University at Olomouc), Jan Veselý[†], Václav Vlček and others.

The results reprinted from the ExpFluids journal in sec. 4.4.2 were mostly achieved during my measurements at ENSTA in 2007. My grateful thanks belong to Olivier Doaré, Olivier Cadot, Antoine Chaigne and many other members of the department. It was highly inspiring to work at the DFA lab – a small group of efficient people with both theoretical skills and experimental background, long-term devoted to a specific scientific subject.

Although the paper published with my colleagues at NTNU Trondheim is not reprinted within this thesis, I would like to highly acknowledge the help, support and expertise of Bernd Müller, from whom I learned a lot. I still cannot get rid of a feeling that wherever I stayed in Europe, I had the opportunity to collaborate with extremely kind people.

The manuscript, which was accepted for publication in the BMMB journal and which is reprinted in sec. 4.3.2, was written in cooperation with Stefan Zörner, Andreas Hüppe and Manfred Kaltenbacher from TU Wien. In this case I could not have afforded to stay abroad a long time, but it turned out that a combination of multiple short-terms stays with intensive electronic contact is also a viable way of cooperation.

I also wish to thank to my colleagues and superiors at FM TUL, especially to Jiří Maryška for all his support, understanding and leadership. Technical University of Liberec has been my home

since seven years. I do realize that not everyone has an opportunity to get a good job within an inspiring team of people, and in the city where one feels at home.

Most of the parallel CFD computations were run on the facilities of the Supercomputing center of the Czech Technical University in Prague. I am grateful to Petr Pospíšil, who made this possible in a very friendly way and with zero bureaucracy. I wish such approach were possible in other aspects of our academic life, too.

Last, but most importantly, I would like to thank to my wife Katka and all my family. Many of my research stays and conference trips were dear-bought by my wife taking care of all our three beloved, wild kids.

Abstract

The habilitation thesis is based on author's contributions to the research of incompressible flow on moving geometries with two applications – flow past the vibrating vocal folds in human phonation, and flow-induced vibrations of elastically supported airfoils with two degrees of freedom. The thesis covers both experimental investigation and numerical simulation approaches. A short overview of numerical methods for the solution of incompressible flow is given, with a detailed explanation of two methods used by the author in his work – the Finite element and Finite volume methods. For both methods, the thesis explains how the domain deformation is treated in the cases, where remeshing or grid topology changes are not necessary.

The next part of the thesis deals with experimental methods in fluid mechanics. Emphasis is given on the methods used in the works of the author – pressure measurements, Pitot tube measurements, Particle image velocimetry and Reference-beam interferometry. For the sake of completeness, basic information and references to literature are given also for the other common measurement methods - Hot wire anemometry, Laser Doppler anemometry, Ultrasonic anemometry and others.

The next chapter devoted to human voice biomechanics contains an introductory part giving the basic information and context, and a short description of the human vocal tract physiology. The most important papers of the author are reprinted. The numerical studies start from a simple lumped-parameter structural model coupled to quasi-1D inviscid airflow, go over a finite element discretization of 2D Navier-Stokes equations towards a 3D parallelized finite volume model of airflow one-way coupled to an aeroacoustic solver. Further, two reprints on PIV measurements of airflow on two completely different physical models of vocal folds are given.

The last part of the thesis contains introduction to the classical theory of aeroelastic instability of airfoils, followed by two reprints of author's publications on the flutter instability. Again, both numerical and experimental approaches to the investigation of airflow past the self-oscillating airfoil are covered.

Contents

Acknowledgements	i
Abstract	iii
Contents	v
List of Abbreviations	ix
1 Introduction	1
2 Numerical modeling of incompressible viscous flow on moving geometries	3
2.1 Overview of the numerical methods in computational fluid dynamics	3
2.2 Finite element method for the incompressible Navier-Stokes equations in 2D	5
2.2.1 Arbitrary Lagrangian-Eulerian method	5
2.2.2 Semidiscretization of the Navier-Stokes equations in time	7
2.2.3 Linearization of the convective term	8
2.2.4 Weak formulation of the Navier-Stokes equations	9
2.2.5 Finite element discretization of the Navier-Stokes equations	12
2.2.6 Mesh motion	15
2.3 Finite volume method for the incompressible Navier-Stokes equations on unstructured polyhedral 3D meshes	16
2.3.1 Finite volume discretization of a general transport equation	17
2.3.2 Finite volume discretization of the Navier-Stokes equations	23
2.3.3 Finite volume discretization on a moving mesh	23
2.3.4 Mesh motion strategies	25

3	Experimental methods in fluid dynamics	29
3.1	Pressure measurements	29
3.1.1	Pressure taps	31
3.1.2	Static probes	31
3.1.3	Pressure-sensitive paints	31
3.2	Velocity measurements	32
3.2.1	Pitot tube measurements	32
3.2.2	Hot wire anemometry	33
3.2.3	Laser Doppler anemometry	33
3.2.4	Ultrasonic anemometry	34
3.2.5	Particle image velocimetry	35
3.2.6	Other velocity measurement methods	37
3.3	Density measurements	37
3.3.1	Reference-beam interferometry	37
4	Application: Flow-structure interaction and flow-induced sound in human voice biomechanics	41
4.1	Introduction	41
4.2	Physiology of human voice production	42
	Reprints	45
	P. Šidlof, J. G. Švec, J. Horáček, J. Veselý, I. Klepáček, R. Havlik: Geometry of human vocal folds and glottal channel for mathematical and biomechanical modeling of voice production, <i>Journal of Biomechanics</i> 41(5), Elsevier (2008)	46
4.3	Mathematical modeling of flow-structure-acoustic interaction in human larynx	57
4.3.1	Overview of concepts and methods	57
4.3.2	Author's contributions to computational modeling of phonation	58
	Reprints	60
	J. Horáček, P. Šidlof, J. G. Švec: Numerical simulation of self-oscillations of human vocal folds with Hertz model of impact forces, <i>Journal of Fluids and Structures</i> 20, Elsevier (2005)	61
	P. Šidlof, E. Lunéville, C. Chambeyron, O. Doaré, O. Cadot: Finite Element Modeling of Airflow During Phonation, <i>Applied and Computational Mechanics</i> 4, University of West Bohemia (2010)	78
	P. Šidlof, J. Horáček, V. Řidký: Parallel CFD simulation of flow in a 3D model of vibrating human vocal folds. <i>Computers & Fluids</i> 80, Elsevier (2013)	90
	P. Šidlof, S. Zörner, A. Hüppe: A hybrid approach to computational aeroacoustics of human voice production, <i>Biomechanics and Modeling in Mechanobiology</i> , Springer (2014, accepted for publication)	101

4.4	PIV measurements of flow in physical vocal fold models	118
4.4.1	Overview and context	118
4.4.2	Author's contributions to flow field measurements in vocal fold synthetic models	118
	Reprints	120
	J. Horáček, P. Šidlof, V. Uruba, J. Veselý, V. Radolf, V. Bula: Coherent structures in the flow inside a model of the human vocal tract with self-oscillating vocal folds, <i>Acta Technica, Institute of Thermomechanics (2010)</i>	121
	P. Šidlof, O. Doaré, O. Cadot, A. Chaigne: Measurement of flow separation in a human vocal folds model, <i>Experiments in Fluids 51, Springer (2011)</i>	138
5	Application: Flutter instability of airfoils with two degrees of freedom	153
5.1	Introduction	153
5.2	Classical theory of airfoil aeroelastic instability	154
5.3	Author's contributions to computational and experimental investigation of airfoil flutter	159
	Reprints	160
	P. Šidlof, M. Štěpán, V. Vlček, V. Řídký, D. Šimurda, J. Horáček: Flow past a self-oscillating airfoil with two degrees of freedom: measurements and simulations, <i>EPJ Web of Conferences 67, EDP Sciences (2014)</i>	161
	P. Šidlof, V. Vlček, M. Štěpán, J. Horáček, M. Luxa, D. Šimurda, J. Kozánek: Wind tunnel measurements of flow-induced vibration of a NACA0015 airfoil model, <i>Proceedings of the ASME PVP 2014 conference - symposium Fluid-structure interaction, ASME (2014, in press)</i>	169
6	Conclusion	179
	Bibliography	181

List of Abbreviations

ALE	Arbitrary Lagrangian-Eulerian
CCA	Constant current anemometer
CCD	Charge-coupled device
CDS	Central differencing scheme
CFD	Computational fluid dynamics
CFL	Courant-Friedrichs-Lewy
CMOS	Complementary metal-oxide-semiconductor
CV	Control volume
CVA	Constant voltage anemometer
CTA	Constant temperature anemometer
CPU	Central processor unit
DNS	Direct numerical simulation
DOF	Degree(s) of freedom
EA	Elastic axis
FE(M)	Finite element (method)
FV(M)	Finite volume (method)
HWA	Hot-wire anemometry
IPA	International phonetic alphabet
LED	Light-emitting diode
LES	Large eddy simulation
MRI	Magnetic resonance imaging
NSE	Navier-Stokes equations
NVD	Normalized variable diagram
PDA	Phase Doppler anemometry
PISO	Pressure implicit with splitting of operators
POD	Proper orthogonal decomposition
PSP	Pressure-sensitive paint
QUICK	Quadratic upstream interpolation for convective kinematics
SIMPLE	Semi-implicit method for pressure linked equations
TA	Thyroarytenoid
TVD	Total variation diminishing
UA	Ultrasonic anemometer
UV	Ultraviolet

Chapter 1

Introduction

Although the flow of fluids is described by seemingly simple Navier-Stokes equations, its nature can be extremely complex. Unlike the partial differential equations for the linear elasticity, acoustics, heat transfer, or electromagnetics, the Navier-Stokes equations contain a strong inherent nonlinearity in the convective term, which cannot be neglected (except for the case of low Reynolds number, creeping flows). The nonlinear convective term is the main cause of the fluid flow complexities, notable examples being the behavior of boundary layers, principal differences between subsonic and supersonic flow (although both described by identical equations) or the turbulence, where the energy of the large flow structures is transferred in a cascade of scales towards the smallest vortices dissipating the turbulent kinetic energy into heat. In 1932, British physicist Horace Lamb commented: *“I am an old man now, and when I die and go to heaven there are two matters on which I hope for enlightenment. One is quantum electrodynamics, and the other is the turbulent motion of fluids. About the former I am rather optimistic.”*

Fifty years later, Richard Feynman still calls turbulence *“the most important unsolved problem of classical physics”*. Until present, even the very proof of existence and smoothness of the solution of the Navier-Stokes equations in \mathbb{R}^3 for general smooth initial data remains unresolved and among the US\$1,000,000 Millennium Prize Problems awarded by the Clay Mathematics Institute. Analytic solutions of the Navier-Stokes equations are not available for most flow problems of engineering interest and the equations have to be solved numerically. However, the complexities of the fluid flow physics translate into the computational fluid dynamic (CFD) simulations, which should always be interpreted with caution, checked for mesh dependence, and verified on benchmark problems or, ideally, validated against experimental data. This is the reason why in investigation of various fluid flow problems the mathematical modeling and numerical simulation efforts have always been complemented by measurements.

In problems, where the geometry of the flow domain changes in time (due to an object moving in the fluid or due to deformations of the domain boundary), especially in the cases where the flow is coupled to an elastic structure, additional complications are encountered. This thesis summarizes the author’s contributions in the field of numerical modeling and experimental investigation of fluid flow on moving geometries with two specific applications – flow-induced vibrations of the human vocal folds and the flutter instability of airfoils. In chapter 2, two numerical concepts used by the author are described: finite element discretization of the 2D Navier-Stokes equations in the Arbitrary Lagrangian-Eulerian (ALE) approach, and collocated cell-centered finite volume

discretization of the 3D Navier-Stokes equations on unstructured meshes with explicit treatment of the mesh motion. Chapter 3 gives an overview of the experimental methods in fluid dynamics, with special emphasis on the methods used by the author himself and with ample references to relevant literature. The core of chapter 4 consists of reprints of the author's papers on the aerodynamics and biomechanics of human voice. Chapter 5 contains the context and introduction into the aeroelastic instability of airfoils, and reprints of author's papers on the investigation of the subsonic flow past a self-oscillating NACA0015 airfoil.

Chapter 2

Numerical modeling of incompressible viscous flow on moving geometries

2.1 Overview of the numerical methods in computational fluid dynamics

Historically, the first attempts to compute fluid flow numerically using computers were based on linearized potential equations in 2D. In order to resolve the flow past airfoils, a number of numerical codes have been developed, notably the Panel methods, which are still used up to present. Most of the modern commercial CFD codes resolving the 3D nonlinear viscous flow rely either on the Finite volume method (Fluent, Star CCM+) or Finite element method (Comsol Multiphysics, Ansys CFX, ADINA). In academia, a much wider class of methods is used. Below, the most common methods are listed and commented.

Finite difference method (FDM)

The Finite difference method works by approximating the derivatives in the partial differential equations by finite differences, evaluated from a computational molecule around a given point in the grid. High-order variants of the FDM exist, but require special treatment of the boundary condition to retain the order of accuracy. FDM is easy to understand and implement, but is applicable only for the solution on structured meshes and simple geometries.

Finite volume method (FVM)

FVM is probably the most widely used method in CFD. The computational domain is divided into control volumes (CV), with variables located in CV centroids. The approximate solution is assumed to be piecewise constant and the FVM is generally considered as first-order accurate. However, higher-order finite volume methods exist, e. g. with a linear distribution of the unknown over each CV. The key element of the FVM is the interpolation and evaluation of the fluxes through the control volume boundaries.

The major advantage of the FVM is that the method is inherently conservative – the conservation of mass, momentum and energy is exactly satisfied for any CV. Even a coarse-grid solution exhibits exact integral balances. The method is applicable on complex 3D geometries and unstructured meshes, with a more versatile choice of mesh element types than the Finite element method.

Finite element method (FEM)

In the Finite element method, the solution is approximated by continuous, piecewise polynomial functions. The governing equations are multiplied by suitable test functions and integrated over the computational domain. By a suitable choice of basis (shape) functions, a system of algebraic equations for the unknown coefficients in the approximate solution is assembled from the original partial differential equations. The basis functions are usually chosen with a small support, which leads to a sparse matrix of the system.

In FEM, accuracy can be increased either by mesh refinement (h-refinement) as in the FVM, by increasing the polynomial order (p-refinement), or by both (hp-refinement). Similarly as the FVM, FEM is routinely used on real-world 3D geometries.

Spectral element method

The Spectral element method is actually a variant of the FEM. The basis and test functions are high-order Legendre, Chebyshev or Lagrange polynomials (typically 10th order in CFD). Efficient high-order Gauss integration quadratures need to be implemented to compute the volume integrals.

Discontinuous Galerkin method

The Discontinuous Galerkin method is a hybrid method combining the FEM and FVM concepts. As in the FEM, the solution is approximated by piecewise polynomial functions, however these need not be continuous on the element boundaries. The interelement convection terms are resolved by numerical flux formulas, similarly as in the FVM. The method is very flexible, allows resolving discontinuities and steadily gains in popularity, especially in the research codes.

Spectral method

In contrast to the FEM, spectral methods approximate the solution by globally smooth functions. The method has very high accuracy (so-called exponential convergence), but can handle only simple geometries and limited boundary condition types.

Lattice Boltzmann method (LBM)

A completely different approach to the numerical solution of fluid flow is employed in the Lattice Boltzmann method. Unlike all of the methods mentioned so far, LBM does not solve the conservation laws. The fluid is treated as a set of fictitious mesoscopic particles, which propagate and collide among each other. Instead of the Navier-Stokes equations, LBM solves the discrete lattice Boltzmann equation.

A major advantage of the LBM is that it is mesh-free. Geometric complexity, mesh generation issues and domain deformation are not a challenge. Moreover, the implementation of LBM exhibits intrinsic linear scalability in parallel computing, since all the particle collisions are calculated locally. However, LBM encounters problems in turbulence modeling, and is still hardly applicable to transonic and supersonic flows.

The potential of the LBM is underlined by the fact that during recent years, two commercial codes based on the LBM – Powerflow and XFlow – emerged, the latter being marketed by a major computer-aided engineering company MSC Software. However, in the CFD community the LBM codes are still considered rather immature, needing much further development, testing and validation.

2.2 Finite element method for the incompressible Navier-Stokes equations in 2D

In this section, the numerical solution of the incompressible Navier-Stokes equations (NSE)

$$\begin{aligned} \frac{\partial \mathbf{u}}{\partial t} + (\mathbf{u} \cdot \nabla) \mathbf{u} + \frac{1}{\rho} \nabla p - \nu \Delta \mathbf{u} &= 0 & \text{in } (0, T) \times \Omega \\ \nabla \cdot \mathbf{u} &= 0 & \text{in } (0, T) \times \Omega \end{aligned} \quad (2.1)$$

for the fluid velocity \mathbf{u} and fluid dynamic pressure p and kinematic viscosity ν using the Finite element (FE) method will be shown. The standard Eulerian form of the governing equations (2.1) assumes a fixed computational domain Ω . However, the Eulerian time derivative $\partial/\partial t$ is not well defined in a time-dependent computational domain and thus (2.1) is not suitable for description of the flow on a computational mesh that deforms in time. Therefore it will be first reformulated using the Arbitrary Lagrangian-Eulerian (ALE) approach.

2.2.1 Arbitrary Lagrangian-Eulerian method

The fundamental concept of the ALE method, used in CFD problems with time-variable geometry (such as flow past flapping airfoils, floating objects, flow-induced vibration of structures or channel walls or flow in rotating machinery), is to relate the equations defined in the actual, “deformed” configuration – the domain Ω_t at time t – to a reference configuration Ω_0 , which is usually the domain at $t = 0$ (see Fig. 2.1). This is realized using the ALE mapping $A_t : \Omega_0 \mapsto \Omega_t$, which is for each $t \in [0, T]$ a smooth bijection (one-to-one mapping of Ω_0 onto Ω_t with continuous first partial derivatives).

The coordinates in the actual configuration – space coordinates – will be denoted by small letters; the coordinates in the reference configuration – reference coordinates – will be in uppercase. Hence we may write $\mathbf{x} = \mathbf{x}(t, X) = A_t(\mathbf{X})$, $\mathbf{X} = A_t^{-1}(\mathbf{x})$. In what follows, by

$$\Phi = \{(t, \mathbf{x}) : t \in (0, T), \mathbf{x} \in \Omega_t\} \quad (2.2)$$

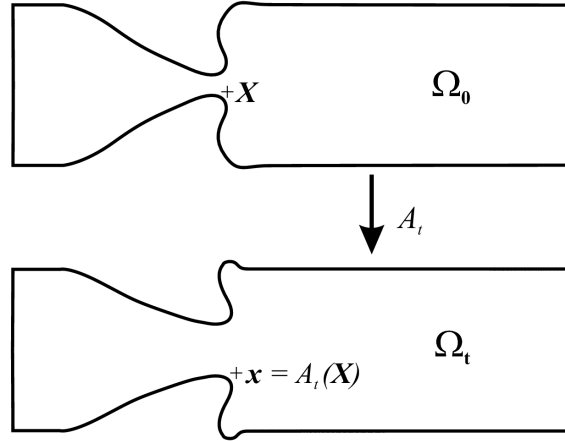


Figure 2.1: ALE mapping A_t - a smooth mapping of the reference configuration Ω_0 onto the actual configuration Ω_t . Reference coordinates \mathbf{X} and space coordinates \mathbf{x} .

we will denote the domain, where the velocity and pressure fields $\mathbf{u}(t, \mathbf{x})$ and $p(t, \mathbf{x})$ are defined. A function $f : \Phi \mapsto \mathbb{R}$, defined in the actual configuration, can be transformed into the reference configuration, where it will be referred to as \tilde{f} :

$$\tilde{f}(t, \mathbf{X}) = f(t, \mathbf{x}), \quad \mathbf{x} = A_t(\mathbf{X}). \quad (2.3)$$

The domain velocity, which might be also understood as the velocity of the nodes of the deformed mesh, is defined in the reference and space coordinates as

$$\begin{aligned} \tilde{\mathbf{w}}(t, \mathbf{X}) &= \frac{\partial}{\partial t} A_t(\mathbf{X}) = \frac{\partial}{\partial t} \mathbf{x}(t, \mathbf{X}), \\ \mathbf{w}(t, \mathbf{x}) &= \tilde{\mathbf{w}}(t, \mathbf{X}), \quad \mathbf{X} = A_t^{-1}(\mathbf{x}). \end{aligned} \quad (2.4)$$

In addition to the Eulerian and material time derivatives, used commonly in fluid mechanics, the ALE method defines yet another, ALE-derivative $\frac{D^A}{Dt} : \Phi \mapsto \mathbb{R}$:

$$\frac{D^A}{Dt} f(t, \mathbf{x}) = \frac{\partial}{\partial t} \tilde{f}(t, \mathbf{X}), \quad \mathbf{X} = A_t^{-1}(\mathbf{x}). \quad (2.5)$$

Using the definitions (2.5), (2.4), (2.3) and applying the chain rule, it can be shown (Šidlof, 2007) that for a function $f \in C^1(\Phi)$ with continuous first partial derivatives

$$\frac{D^A}{Dt} f = \frac{\partial f}{\partial t} + (\mathbf{w} \cdot \nabla) f. \quad (2.6)$$

The ALE derivative $D^A/Dt = \partial/\partial t + (\mathbf{w} \cdot \nabla)$ is analogous to the material derivative $D/Dt = \partial/\partial t + (\mathbf{u} \cdot \nabla)$ in Lagrangian approach. The difference is that in Lagrangian description we track the particles with velocity \mathbf{u} ; the ALE approach, on the other hand, follows the “deformation” of the particles of the reference configuration (the vertices of the computational mesh), whose velocity is the domain velocity \mathbf{w} .

The Navier-Stokes equations, defined in the time-dependent space-time domain Φ , can be obtained by substituting (2.6) for $f = \mathbf{u}$ into (2.1):

$$\begin{aligned} \frac{D^A}{Dt} \mathbf{u} + [(\mathbf{u} - \mathbf{w}) \cdot \nabla] \mathbf{u} + \frac{1}{\rho} \nabla p - \nu \Delta \mathbf{u} &= 0 \\ \nabla \cdot \mathbf{u} &= 0 \quad . \end{aligned} \quad (2.7)$$

2.2.2 Semidiscretization of the Navier-Stokes equations in time

The Navier-Stokes equations (2.7) are first discretized in time using a constant timestep τ . Let us define the discrete time level $t_i = i \tau$ and the approximate flow velocity, pressure and domain velocity on this time level

$$\mathbf{u}^i(\mathbf{x}) \approx \mathbf{u}(t_i, \mathbf{x}), \quad p^i(x) \approx p(t_i, \mathbf{x}), \quad \mathbf{w}^i(x) \approx \mathbf{w}(t_i, \mathbf{x}), \quad \mathbf{x} \in \Omega_{t_i} . \quad (2.8)$$

The Eulerian time derivative $\partial \mathbf{u} / \partial t$ can be approximated by second-order backward difference

$$\frac{\partial \mathbf{u}}{\partial t}(t_{n+1}, \mathbf{x}) \approx \frac{3 \mathbf{u}(t_{n+1}, \mathbf{x}) - 4 \mathbf{u}(t_n, \mathbf{x}) + \mathbf{u}(t_{n-1}, \mathbf{x})}{2 \tau} . \quad (2.9)$$

In the ALE formulation of the NSE (2.7), however, we use the ALE-derivative

$$\frac{D^A}{Dt} \mathbf{u}(t_{n+1}, \mathbf{x}) = \frac{\partial}{\partial t} \tilde{\mathbf{u}}(t_{n+1}, \mathbf{X}), \quad \mathbf{X} = A_{t_{n+1}}^{-1}(\mathbf{x}), \quad \mathbf{x} \in \Omega_{t_{n+1}} . \quad (2.10)$$

If we denote the ALE mappings of the reference point \mathbf{X} on the three time levels involved

$$\mathbf{x}^{n+1} = A_{t_{n+1}}(\mathbf{X}), \quad \mathbf{x}^n = A_{t_n}(\mathbf{X}), \quad \mathbf{x}^{n-1} = A_{t_{n-1}}(\mathbf{X}), \quad (2.11)$$

the ALE-derivative can be approximated by the formula

$$\begin{aligned} \frac{D^A \mathbf{u}}{Dt}(t_{n+1}, \mathbf{x}^{n+1}) &\approx \frac{3 \mathbf{u}^{n+1}(\mathbf{x}^{n+1}) - 4 \mathbf{u}^n(\mathbf{x}^n) + \mathbf{u}^{n-1}(\mathbf{x}^{n-1})}{2 \tau} = \\ &= \frac{3 \mathbf{u}^{n+1}(\mathbf{x}^{n+1}) - 4 \mathbf{u}^n(A_{t_n}(A_{t_{n+1}}^{-1}(\mathbf{x}^{n+1}))) + \mathbf{u}^{n-1}(A_{t_{n-1}}(A_{t_{n+1}}^{-1}(\mathbf{x}^{n+1})))}{2 \tau} , \end{aligned} \quad (2.12)$$

similarly as the Eulerian derivative (2.9). Provided that the ALE-mappings on time levels t_{n+1} , t_n and t_{n-1} are known, the finite difference (2.12) is now well-defined on $\Omega_{t_{n+1}}$. Introducing notation

$$\widehat{\mathbf{u}}^i(\mathbf{x}^{n+1}) = \mathbf{u}^i(A_{t_i}(A_{t_{n+1}}^{-1}(\mathbf{x}_{n+1}))) \quad (2.13)$$

and substituting (2.12) into (2.7) yields the semidiscrete Navier-Stokes equations for the functions $\mathbf{u}^{n+1} : \Omega_{t_{n+1}} \mapsto \mathbb{R}^2$ and $p^{n+1} : \Omega_{t_{n+1}} \mapsto \mathbb{R}$:

$$\begin{aligned} \frac{3\mathbf{u}^{n+1}}{2\tau} + [(\mathbf{u}^{n+1} - \mathbf{w}^{n+1}) \cdot \nabla] \mathbf{u}^{n+1} + \frac{1}{\rho} \nabla p^{n+1} - \nu \Delta \mathbf{u}^{n+1} &= \frac{4\widehat{\mathbf{u}}^n - \widehat{\mathbf{u}}^{n-1}}{2\tau} \\ \nabla \cdot \mathbf{u}^{n+1} &= 0. \end{aligned} \quad (2.14)$$

2.2.3 Linearization of the convective term

Due to the presence of the quadratic convective term $[(\mathbf{u}^{n+1} - \mathbf{w}^{n+1}) \cdot \nabla] \mathbf{u}^{n+1}$ in the Navier-Stokes equations (2.14), the system cannot be solved in a straightforward way. Instead, it is first necessary to linearize the equations, i. e. to replace the first occurrence of the unknown velocity vector \mathbf{u}^{n+1} by some vector \mathbf{u}^* , which is already available:

$$[(\mathbf{u}^{n+1} - \mathbf{w}^{n+1}) \cdot \nabla] \mathbf{u}^{n+1} \approx [(\mathbf{u}^* - \mathbf{w}^{n+1}) \cdot \nabla] \mathbf{u}^{n+1}. \quad (2.15)$$

One possible approach is to use the solution from the previous timestep \mathbf{u}^n , transformed to the actual configuration with the aid of the ALE-mapping (2.13):

$$\mathbf{u}^* = \widehat{\mathbf{u}}^n. \quad (2.16)$$

Time-lagging of the convective velocity might be sufficient for quasi-steady flows; to increase precision for the non-stationary flow it is better to employ an iteration process, using (2.16) as the first iteration.

Using the notation

$$\mathbf{u} \equiv \mathbf{u}^{n+1}, \mathbf{w} \equiv \mathbf{w}^{n+1}, p \equiv p^{n+1}, \Omega \equiv \Omega_{t_{n+1}}, \quad (2.17)$$

the resulting system can be formally rewritten as

$$\begin{aligned} \frac{3\mathbf{u}}{2\tau} + [(\mathbf{u}^* - \mathbf{w}) \cdot \nabla] \mathbf{u} + \frac{1}{\rho} \nabla p - \nu \Delta \mathbf{u} &= \frac{4\widehat{\mathbf{u}}^n - \widehat{\mathbf{u}}^{n-1}}{2\tau} \\ \nabla \cdot \mathbf{u} &= 0. \end{aligned} \quad (2.18)$$

2.2.4 Weak formulation of the Navier-Stokes equations

The starting point for the finite element discretization of any system of partial differential equations is its weak formulation. The weak solution of a partial differential equation may be understood as a generalization of the concept of classical solutions, whose derivatives concerned must exist everywhere in the computational domain $\Omega \equiv \Omega_{t_{n+1}}$. The weak solution, on the other hand, is defined in an “integral” sense. The concept of weak solutions remains consistent with the classical theory: it can be proven that a weak solution, which is sufficiently regular, is also a solution in the classical sense.

The pressure component of the solution will be sought in the Lebesgue space of square-integrable functions

$$L^2(\Omega) = \left\{ f : \Omega \mapsto \mathbb{R} : \sqrt[2]{\int_{\Omega} |f|^2 d\mu} < \infty \right\}. \quad (2.19)$$

As regards the velocity, the solution will be sought in the Sobolev space $\mathbf{Y} = (H^1(\Omega))^2$, where

$$H^1(\Omega) = \left\{ f \in L^2(\Omega) : \frac{\partial f}{\partial x_i} \in L^2(\Omega), i = 1, 2 \right\} \quad (2.20)$$

(Feistauer et al., 2003). For the weak formulation, the velocity and pressure test function spaces \mathbf{W} and Q are needed. The velocity test functions are zero on the boundaries, where the Dirichlet boundary condition is prescribed:

$$\mathbf{W} = \{ \mathbf{v} \in \mathbf{Y} : \mathbf{v}|_{\Gamma_{Dir}} = 0 \} \quad (2.21)$$

$$Q = L^2(\Omega). \quad (2.22)$$

The weak formulation of the NSE is obtained by multiplying the classical formulation (2.18) by an arbitrary test function from the relevant space and integrating over Ω :

$$\begin{aligned} \frac{3}{2\tau} \int_{\Omega} \mathbf{u} \cdot \mathbf{v} d\mathbf{x} + \int_{\Omega} ([(\mathbf{u}^* - \mathbf{w}) \cdot \nabla] \mathbf{u}) \cdot \mathbf{v} d\mathbf{x} + \int_{\Omega} \frac{1}{\rho} \nabla p \cdot \mathbf{v} d\mathbf{x} - \\ \int_{\Omega} \nu \Delta \mathbf{u} \cdot \mathbf{v} d\mathbf{x} = \frac{1}{2\tau} \int_{\Omega} (4\hat{\mathbf{u}}^n - \hat{\mathbf{u}}^{n-1}) \cdot \mathbf{v} d\mathbf{x} \quad \forall \mathbf{v} \in \mathbf{W}, \end{aligned} \quad (2.23)$$

$$\int_{\Omega} q \nabla \cdot \mathbf{u} d\mathbf{x} = 0 \quad \forall q \in Q. \quad (2.24)$$

Using Gauss’s theorem and the fact, that the test functions \mathbf{v} are zero on $\Gamma_{Dir} = \partial\Omega \setminus \Gamma_{nonDir}$, we can rewrite the third and fourth term from (2.23) as

$$\begin{aligned}
& \frac{1}{\rho} \int_{\Omega} \nabla p \cdot \mathbf{v} \, d\mathbf{x} - \int_{\Omega} \mathbf{v} \Delta \mathbf{u} \cdot \mathbf{v} \, d\mathbf{x} = \\
& = \frac{1}{\rho} \int_{\partial\Omega} p \mathbf{v} \cdot \mathbf{n} \, d\sigma - \frac{1}{\rho} \int_{\Omega} p \nabla \cdot \mathbf{v} \, d\mathbf{x} + \mathbf{v} \sum_{j=1}^2 \int_{\Omega} \nabla u_j \cdot \nabla v_j \, d\mathbf{x} - \mathbf{v} \sum_{j=1}^2 \int_{\partial\Omega} \nabla u_j \cdot \mathbf{n} v_j \, d\sigma = \\
& = \mathbf{v} \int_{\Omega} \nabla \mathbf{u} \cdot \nabla \mathbf{v} \, d\mathbf{x} - \frac{1}{\rho} \int_{\Omega} p \nabla \cdot \mathbf{v} \, d\mathbf{x} + \int_{\Gamma_{nonDir}} \left(-\mathbf{v} \frac{\partial \mathbf{u}}{\partial \mathbf{n}} + \frac{1}{\rho} p \mathbf{n} \right) \cdot \mathbf{v} \, d\sigma . \tag{2.25}
\end{aligned}$$

The last surface integral in (2.25) is usually set to zero (or a reference pressure p_{ref} by prescribing

$$\left(-\mathbf{v} \frac{\partial \mathbf{u}}{\partial \mathbf{n}} + \frac{1}{\rho} p \mathbf{n} \right) = \frac{1}{\rho} p_{ref} \mathbf{n} \tag{2.26}$$

on the boundaries, where a non-Dirichlet condition for the velocity is prescribed. Typically, this is the outflow Γ_{out} of the domain. In certain cases, however, this (so-called "do-nothing condition") becomes too vague. It does not even prevent the flow returning to the domain Ω through Γ_{out} . Thus, the total influx into the domain Ω can grow infinite and the numerical scheme tends to diverge, especially for higher Reynolds numbers.

To suppress this inconvenience, the boundary condition on Γ_{out} can be slightly modified. Applying Gauss's theorem on the \mathbf{u}^* -convected part of the second term in (2.23) and using (2.21) yields

$$\begin{aligned}
& \int_{\Omega} ([\mathbf{u}^* \cdot \nabla] \mathbf{u}) \cdot \mathbf{v} \, d\mathbf{x} = \sum_{i,j=1}^2 \int_{\Omega} u_i^* \frac{\partial u_j}{\partial x_i} v_j \, d\mathbf{x} = \sum_{i,j=1}^2 \left[\frac{1}{2} \int_{\Omega} u_i^* \frac{\partial u_j}{\partial x_i} v_j \, d\mathbf{x} + \frac{1}{2} \int_{\Omega} u_i^* \frac{\partial u_j}{\partial x_i} v_j \, d\mathbf{x} \right] = \\
& = \sum_{i,j=1}^2 \left[\frac{1}{2} \int_{\Omega} u_i^* \frac{\partial u_j}{\partial x_i} v_j \, d\mathbf{x} + \frac{1}{2} \int_{\partial\Omega} v_j u_i^* u_j n_i \, d\sigma - \frac{1}{2} \int_{\Omega} u_j \frac{\partial}{\partial x_i} [u_i^* v_j] \, d\mathbf{x} \right] = \\
& = \sum_{i,j=1}^2 \left[\frac{1}{2} \int_{\Omega} u_i^* \frac{\partial u_j}{\partial x_i} v_j \, d\mathbf{x} + \frac{1}{2} \int_{\Gamma_{out}} v_j u_i^* u_j n_i \, d\sigma - \right. \\
& \quad \left. \frac{1}{2} \int_{\Omega} u_j v_j \frac{\partial}{\partial x_i} u_i^* \, d\mathbf{x} - \frac{1}{2} \int_{\Omega} u_j u_i^* \frac{\partial v_j}{\partial x_i} \, d\mathbf{x} \right] = \frac{1}{2} \int_{\Omega} ([\mathbf{u}^* \cdot \nabla] \mathbf{u}) \cdot \mathbf{v} \, d\mathbf{x} + \\
& \quad \frac{1}{2} \int_{\Gamma_{out}} (\mathbf{u}^* \cdot \mathbf{n}) \mathbf{u} \cdot \mathbf{v} \, d\sigma - \frac{1}{2} \int_{\Omega} \mathbf{u} \cdot \mathbf{v} \nabla \cdot \mathbf{u}^* \, d\mathbf{x} - \frac{1}{2} \int_{\Omega} ([\mathbf{u}^* \cdot \nabla] \mathbf{v}) \cdot \mathbf{u} \, d\mathbf{x} = \\
& = \frac{1}{2} \int_{\Omega} ([\mathbf{u}^* \cdot \nabla] \mathbf{u}) \cdot \mathbf{v} \, d\mathbf{x} + \frac{1}{2} \int_{\Gamma_{out}} (\mathbf{u}^* \cdot \mathbf{n}) \mathbf{u} \cdot \mathbf{v} \, d\sigma - \frac{1}{2} \int_{\Omega} ([\mathbf{u}^* \cdot \nabla] \mathbf{v}) \cdot \mathbf{u} \, d\mathbf{x} , \tag{2.27}
\end{aligned}$$

since the continuity equation $\nabla \cdot \mathbf{u} = 0$ holds also for \mathbf{u}^* .

The new boundary integral which arose in (2.27) can be separated into the positive and negative parts:

$$\frac{1}{2} \int_{\Gamma_{out}} (\mathbf{u}^* \cdot \mathbf{n}) \mathbf{u} \cdot \mathbf{v} \, d\sigma = \frac{1}{2} \int_{\Gamma_{out}} (\mathbf{u}^* \cdot \mathbf{n})^+ \mathbf{u} \cdot \mathbf{v} \, d\sigma + \frac{1}{2} \int_{\Gamma_{out}} (\mathbf{u}^* \cdot \mathbf{n})^- \mathbf{u} \cdot \mathbf{v} \, d\sigma . \quad (2.28)$$

Since we wish to stabilize the solution by suppressing the return flow, that is

$$(\mathbf{u}^* \cdot \mathbf{n})^- \Big|_{\Gamma_{out}} = 0 , \quad (2.29)$$

we add the negative part to the boundary condition and leave the positive term in the weak formulation. More details can be found in Heywood et al. (1996). The new, more stable "modified do-nothing" boundary condition on Γ_{out} now reads

$$-v \frac{\partial \mathbf{u}}{\partial \mathbf{n}}(t, \mathbf{x}) + \frac{1}{\rho} p(t, \mathbf{x}) \mathbf{n}(\mathbf{x}) + \frac{1}{2} (\mathbf{u}^*(\mathbf{x}) \cdot \mathbf{n}(\mathbf{x}))^- \mathbf{u}(t, \mathbf{x}) = \frac{1}{\rho} p_{ref} \mathbf{n}(\mathbf{x})$$

for $\mathbf{x} \in \Gamma_{out}$, $t \in [0, T]$. (2.30)

If we substitute back all the results (2.25), (2.27) and (2.28) into the equations (2.23), (2.24) and make use of the downstream boundary condition (2.30), we can express the ultimate form of the weak semidiscretized ALE Navier-Stokes equations:

$$\begin{aligned} & \frac{3}{2\tau} \int_{\Omega} \mathbf{u} \cdot \mathbf{v} \, d\mathbf{x} + v \int_{\Omega} \nabla \mathbf{u} \cdot \nabla \mathbf{v} \, d\mathbf{x} - \frac{1}{\rho} \int_{\Omega} p \nabla \cdot \mathbf{v} \, d\mathbf{x} + \frac{1}{2} \int_{\Omega} ([(\mathbf{u}^* - 2\mathbf{w}) \cdot \nabla] \mathbf{u}) \cdot \mathbf{v} \, d\mathbf{x} \\ & \quad - \frac{1}{2} \int_{\Omega} ([\mathbf{u}^* \cdot \nabla] \mathbf{v}) \cdot \mathbf{u} \, d\mathbf{x} + \frac{1}{2} \int_{\Gamma_{out}} (\mathbf{u}^* \cdot \mathbf{n})^+ \mathbf{u} \cdot \mathbf{v} \, d\sigma = \\ & = \frac{1}{2\tau} \int_{\Omega} (4\hat{\mathbf{u}}^n - \hat{\mathbf{u}}^{n-1}) \cdot \mathbf{v} \, d\mathbf{x} - \frac{1}{\rho} \int_{\Gamma_{out}} p_{ref} \mathbf{v} \cdot \mathbf{n} \, d\sigma \quad \forall \mathbf{v} \in \mathbf{W}, \end{aligned} \quad (2.31)$$

$$- \int_{\Omega} q \nabla \cdot \mathbf{u} \, d\mathbf{x} = 0 \quad \forall q \in Q . \quad (2.32)$$

The weak solution of the problem is defined as a couple $(\mathbf{u}, p) \in \mathbf{Y} \times Q$ such that the weak Navier-Stokes equations (2.31), (2.32) hold and that the boundary conditions are satisfied in the sense of traces.

To simplify notation, we may introduce the forms

$$\begin{aligned}
a(U^*, U, V) &= \frac{3}{2\tau} (\mathbf{u}, \mathbf{v}) + \nu ((\mathbf{u}, \mathbf{v})) - \frac{1}{\rho} (p, \nabla \cdot \mathbf{v}) + (\nabla \cdot \mathbf{u}, q) + \frac{1}{2} ((\mathbf{u}^* - 2\mathbf{w}) \cdot \nabla) \mathbf{u}, \mathbf{v}) \\
&\quad - \frac{1}{2} ((\mathbf{u}^* \cdot \nabla) \mathbf{v}, \mathbf{u}) + \frac{1}{2} \int_{\Gamma_{out}} (\mathbf{u}^* \cdot \mathbf{n})^+ \mathbf{u} \cdot \mathbf{v} \, d\mathbf{x}, \tag{2.33}
\end{aligned}$$

$$f(V) = \frac{1}{2\tau} (4\hat{\mathbf{u}}^n - \hat{\mathbf{u}}^{n-1}, \mathbf{v}) - \frac{1}{\rho} \int_{\Gamma_{out}} p_{ref} \mathbf{v} \cdot \mathbf{n} \, d\sigma, \tag{2.34}$$

where $U = \{\mathbf{u}, p\}$, $U^* = \{\mathbf{u}^*, p\}$, $V = \{\mathbf{v}, q\}$, where $(\mathbf{u}, \mathbf{v}) = \int_{\Omega} \mathbf{u} \cdot \mathbf{v} \, d\mathbf{x}$ denotes the scalar product in $(L^2(\Omega))^2$ and $((\mathbf{u}, \mathbf{v})) = \int_{\Omega} \nabla \mathbf{u} \cdot \nabla \mathbf{v} \, d\mathbf{x}$ is the scalar product in $(H_0^1(\Omega))^2$. Using this notation, the problem can be formulated as follows:

Find $U = \{\mathbf{u}, p\} \in \mathbf{Y} \times Q$ such that the boundary conditions are satisfied in the sense of traces and that

$$a(U^*, U, V) = f(V) \quad \forall V = \{\mathbf{v}, q\} \in \mathbf{W} \times Q. \tag{2.35}$$

2.2.5 Finite element discretization of the Navier-Stokes equations

The finite element discretization of the incompressible Navier-Stokes equations will be shown in the 2D case. However, the procedure in 3D is almost identical, the major difference being the computational cost of the simulation. During author's FE simulations of the flow past vibrating vocal folds, a sparse direct linear solver UMFPack (Davis, 2006) was used. Since no parallelization was available, the memory requirements of the direct solver limited the CFD simulations to 2D cases.

The FE discretization is assembled on a polygonal approximation Ω_h of the computational domain Ω . Let us assume that the boundary $\partial\Omega_h$ is Lipschitz-continuous. Let $\mathcal{T}_h = \{K_i\}_{i \in \{1..n_h\}}$ be a regular finite element mesh over Ω_h , with elements K_i being closed polygons with mutually disjoint interiors such that

$$\bar{\Omega}_h = \bigcup_{i \in \{1..n_h\}} K_i \tag{2.36}$$

and the intersection of arbitrary two elements being either empty or their common vertex or edge (Feistauer et al., 2003). The subscript h usually represents the maximum diameter of all the elements,

$$h = \max_{i \in \{1..n_h\}} (\text{diam } K_i). \tag{2.37}$$

The velocity constituent of the approximate solution will be sought in the finite-dimensional space

$$\mathbf{Y}_h = \left\{ \mathbf{v}_h \in \left(C(\overline{\Omega}_h) \right)^2 : \mathbf{v}_h|_K \in P^{k+1}(K) \quad \forall K \in \mathcal{T}_h \right\}, \quad (2.38)$$

where $P^m(K)$ is the set of all polynomials defined on K of degree less than or equal to m . Similarly, the pressure constituent of the solution comes from the finite-dimensional space

$$Q_h = \left\{ q_h \in C(\overline{\Omega}_h) : q_h|_K \in P^k(K) \quad \forall K \in \mathcal{T}_h \right\}. \quad (2.39)$$

The solution is approximated by continuous piecewise-polynomial functions, and the spaces \mathbf{Y}_h , Q_h represent finite-dimensional approximations of the functional spaces \mathbf{Y} , Q . It can be anticipated that when decreasing the size of elements, i. e. for $h \rightarrow 0$, the approximation error diminishes and the approximate solution may converge to the exact solution. It can be proven that $\mathbf{Y}_h \subset \mathbf{Y}$, $Q_h \subset Q$. The spaces \mathbf{Y}_h , Q_h are called the finite element spaces, the functions $v_h \in \mathbf{Y}_h$, $p_h \in Q_h$ are sometimes referred to as finite elements. In the engineering community, v_h and p_h are called shape functions and the term finite element usually comprises both the type of the element K_i (triangle, quadrangle in 2D; tetrahedral, hexahedral elements in 3D) and the order of the polynomial v_h and p_h . In order to guarantee the numerical stability of the resulting scheme, the spaces \mathbf{Y}_h , Q_h cannot be chosen arbitrarily; they must fulfill the Babuška-Brezzi condition (Feistauer, 1993). For the P^{k+1}/P^k elements (called Taylor-Hood elements), this condition holds.

The test functions in the discretized equations come from spaces $\mathbf{W}_h \subset \mathbf{W}$ and Q_h , where

$$\mathbf{W}_h = \left\{ v_h \in \mathbf{Y}_h : \mathbf{v}_h|_{\Gamma_{Dir}} = 0 \right\}. \quad (2.40)$$

Now we are able to formulate the discrete problem: find a couple $U_h = \{\mathbf{u}_h, p_h\} \in \mathbf{Y}_h \times Q_h$ satisfying (in the sense of traces) a suitable approximation of the boundary conditions such, that

$$a(U_h^*, U_h, V_h) = f(V_h) \quad \forall V_h = \{\mathbf{v}_h, q_h\} \in \mathbf{W}_h \times Q_h. \quad (2.41)$$

First, it is necessary to construct the bases of the spaces \mathbf{Y}_h , Q_h . The basis of a n_h -dimensional space \mathbf{Y}_h will be denoted by $\{\mathbf{w}_i\}_{i=1}^{n_h}$, $\{q_i\}_{i=1}^{m_h}$ is the basis of the space Q_h of dimension m_h . In order to produce sparse matrices, it is suitable to choose basis functions with small support, for instance equal to one in one vertex of the mesh and zero elsewhere (in the case of linear P^1 -elements).

Once the basis functions are chosen, the approximate solution can be expressed as their linear combination

$$\mathbf{u}_h = \sum_{j=1}^{n_h} U_j \mathbf{w}_j, \quad p_h = \sum_{j=1}^{m_h} P_j q_j. \quad (2.42)$$

If a relation holds for an arbitrary element of a space, it must hold for all the elements of the basis and vice versa. Thus, using (2.42), we can equivalently rewrite the condition (2.41) as

$$a\left(U_h^*, \left\{ \sum_{j=1}^{n_h} U_j \mathbf{w}_j, \sum_{r=1}^{m_h} P_r q_r \right\}, \{\mathbf{w}_k, q_l\}\right) = f\left(\{\mathbf{w}_k, q_l\}\right) \quad \forall k \in \{1..n_h\} \quad \forall l \in \{1..m_h\}. \quad (2.43)$$

Let us assume that the vector U^* is known from the previous iteration. Looking back on the definitions (2.33), (2.34) of the (tri)linear forms $a(U^*, U, V)$ and $f(V)$, it is obvious that the equations (2.43) represent a system of linear algebraic equations for $(n_h + m_h)$ unknown real coefficients, which can be organized into vectors $\mathbf{U} = (U_1 \dots U_{n_h})^T$ and $\mathbf{P} = (P_1 \dots P_{m_h})^T$.

The linear system, which arises from the finite element discretization described above, has the block structure

$$\begin{pmatrix} \mathbb{A} + \mathbb{T} + \mathbb{C} + \mathbb{D} + \mathbb{E} & \mathbb{B} \\ \mathbb{B}^T & \mathbf{0} \end{pmatrix} \begin{pmatrix} \mathbf{U} \\ \mathbf{P} \end{pmatrix} = \begin{pmatrix} \mathbf{F} \\ \mathbf{0} \end{pmatrix}, \quad (2.44)$$

where

$$\begin{aligned} \mathbb{A} &= (a_{ij})_{i,j=1}^{n_h} & a_{ij} &= \nu \int_{\Omega} \nabla \mathbf{w}_j \cdot \nabla \mathbf{w}_i \, d\mathbf{x}, \\ \mathbb{T} &= (t_{ij})_{i,j=1}^{n_h} & t_{ij} &= \frac{3}{2\tau} \int_{\Omega} \mathbf{w}_j \cdot \mathbf{w}_i \, d\mathbf{x}, \\ \mathbb{C} &= (c_{ij})_{i,j=1}^{n_h} & c_{ij} &= \frac{1}{2} \int_{\Omega} \left(\left[(\mathbf{u}^* - 2\mathbf{w}) \cdot \nabla \right] \mathbf{w}_j \right) \cdot \mathbf{w}_i \, d\mathbf{x}, \\ \mathbb{D} &= (d_{ij})_{i,j=1}^{n_h} & d_{ij} &= -\frac{1}{2} \int_{\Omega} \left(\left[\mathbf{u}^* \cdot \nabla \right] \mathbf{w}_i \right) \cdot \mathbf{w}_j \, d\mathbf{x}, \\ \mathbb{E} &= (e_{ij})_{i,j=1}^{n_h} & e_{ij} &= \frac{1}{2} \int_{\Gamma_{out}} (\mathbf{u}^* \cdot \mathbf{n})^+ \mathbf{w}_j \cdot \mathbf{w}_i \, d\sigma, \\ \mathbb{B} &= (b_{ij})_{i=1, j=1}^{n_h, m_h} & b_{ij} &= -\int_{\Omega} q_j \nabla \cdot \mathbf{w}_i \, d\mathbf{x}, \\ \mathbf{F} &= (f_1 \dots f_{n_h})^T & f_i &= \frac{1}{2\tau} \int_{\Omega} (4\hat{\mathbf{u}}^n - \hat{\mathbf{u}}^{n-1}) \cdot \mathbf{w}_i \, d\mathbf{x} - \frac{1}{\rho} \int_{\Gamma_{out}} p_{ref} \mathbf{w}_i \cdot \mathbf{n} \, d\sigma. \end{aligned} \quad (2.45)$$

The matrices \mathbb{A} and \mathbb{T} , coming from the discretization of the viscous term and of the temporal derivative, are symmetric, while \mathbb{C} , \mathbb{D} (from the convective terms), \mathbb{E} and \mathbb{B} are generally nonsymmetric. By the symbol $\mathbf{0}$ we denote the zero matrix or vector.

Before solving the linear system (2.44) it is necessary to take into account the Dirichlet boundary conditions. The principle of the algorithm can be illustrated on a generic linear system

$$\mathbb{M}\boldsymbol{\varphi} = \mathbf{b} \quad (2.46)$$

with a matrix $\mathbb{M} = (m_{ij})_{i,j=1}^n$ and a right-hand side $\mathbf{b} = (b_1 \dots b_n)^T$. Imposing the Dirichlet condition is equivalent to blocking some of the degrees of freedom, i. e. to setting

$$\varphi_j = g_j \quad \forall j \in \mathcal{D}, \quad (2.47)$$

where g_j are prescribed values and \mathcal{D} is an index set of the blocked (Dirichlet) nodes. We will assume that the linear system has already been organized in such a way that the diagonal elements corresponding to non-Dirichlet nodes are non-zero, $m_{ii} \neq 0 \quad \forall i \notin \mathcal{D}$. In order to satisfy the Dirichlet conditions, the original system (2.46) is modified as follows: first the components of the right-hand side vector \mathbf{b} corresponding to the non-Dirichlet nodes are replaced by the values

$$b_i := b_i - \sum_{j \in \mathcal{D}} m_{ij} g_j \quad \forall i \notin \mathcal{D}. \quad (2.48)$$

Then, the matrix elements in the relevant columns are set to zero,

$$m_{ij} := 0 \quad \forall i \quad \forall j \in \mathcal{D}. \quad (2.49)$$

Finally, the matrix rows corresponding to the Dirichlet nodes are modified as follows:

$$\begin{aligned} m_{ij} &:= 0 && \forall i \in \mathcal{D} \quad \forall j \neq i, \\ m_{ii} &:= 1 && \forall i \in \mathcal{D}, \\ b_i &:= g_i && \forall i \in \mathcal{D}. \end{aligned} \quad (2.50)$$

2.2.6 Mesh motion

The solution of the discretized system (2.44), (2.45) depends on the knowledge of the domain velocity \mathbf{w} , which has not yet been discussed properly. According to the definition (2.4), the domain velocity is the time derivative of the ALE-mapping A_t . The task is to determine the explicit form of the ALE-mapping $A_t(\mathbf{X})$, which maps the reference, non-deformed domain Ω_0 onto the actual, deformed domain Ω_t , at time level t , provided that the shape of the domain boundary $\partial\Omega_t$ is prescribed. The mapping A_t must be smooth on Ω_t . Otherwise, however, the choice of A_t in the ALE approach is indeed arbitrary.

In simple cases, the form of the ALE-mapping may be guessed or derived on the basis of geometric considerations. Another possibility, which can be applied universally, is to seek the mapping A_t as a solution of an auxiliary boundary problem with a suitable operator. In the finite element CFD simulations of the author, the ALE-mapping was defined as a solution of the Laplace equation

$$\Delta A_t = 0 \quad \text{in } \Omega_0, \quad (2.51)$$

with the boundary conditions

$$A_t \Big|_{\Gamma_{fixed}} = Id, \quad A_t \Big|_{\Gamma_{moving}} = F_t(\mathbf{X}), \quad (2.52)$$

where Id is the identity mapping and F_t is a prescribed explicit function.

The system (2.51) has to be numerically solved in each timestep of the computation. Although the specific number depends on many factors, the practical computations showed that the solution of the auxiliary problem takes at most 5-10% of the total computational time.

The Laplace equation is not the only option for the solution of the mesh motion. As will be explained later in section 2.3.4, for various scenarios a number of different mesh motion solvers can be used.

2.3 Finite volume method for the incompressible Navier-Stokes equations on unstructured polyhedral 3D meshes

In the following section, the variant of the finite volume discretization of incompressible Navier-Stokes equations on unstructured polyhedral meshes, used in OpenFOAM, will be described. OpenFOAM ([The OpenFOAM Foundation, 2014](#)) is an open-source set of libraries for CFD, which is very powerful, but rather poorly documented. The pieces of information about the settings of the solvers and about the underlying physical models and numerical implementation are scattered over the official website of the project, scientific papers and workshop presentations of the main developers, and community forums. The ultimate source of information are the source codes of the libraries, however, these may be difficult to understand for those who are not experts in highly object-oriented C++ programming with a vast use of templates, overloading and polymorphism. In certain places, slightly non-standard terminology is used in OpenFOAM. For this sake, OpenFOAM variant of the nomenclature is given in footnotes where appropriate. Where possible, the notation introduced in this section is kept consistent with the class names used in OpenFOAM source codes.

The governing equations for the incompressible fluid flow read

$$\begin{aligned} \frac{\partial \mathbf{u}}{\partial t} + \nabla \cdot (\mathbf{u} \otimes \mathbf{u}) + \frac{1}{\rho} \nabla p - \nu \Delta \mathbf{u} &= 0 \\ \nabla \cdot \mathbf{u} &= 0, \end{aligned} \quad (2.53)$$

where \mathbf{u} is the flow velocity, p the fluid dynamic pressure, ρ density and ν the kinematic viscosity. The first equation expresses the conservation of momentum, the second one the conservation of mass. The convective term is written as a divergence of a tensor product, which is equivalent with the formulation (2.1).

The basic concept of the Finite volume method (FVM) is to divide the computational domain into a set of mutually disjoint control volumes (CVs), integrate the governing equations over an arbitrary CV, use the Gauss theorem where applicable and then discretize the volume and surface

integrals by some differencing scheme using the values and fluxes at the control volume and face centroids. In OpenFOAM, the CVs can have an arbitrary polyhedral shape, and the pressure and velocity are solved in a collocated way – they are both defined in the centroid \mathbf{P} with coordinate \mathbf{x}_P of the CV of volume V_P such, that

$$\int_{V_P} (\mathbf{x} - \mathbf{x}_P) dV = \mathbf{0} . \quad (2.54)$$

2.3.1 Finite volume discretization of a general transport equation

Before dealing with the nonlinear NSE, the finite volume discretization will be first explained for a general transport equation of a scalar property ϕ (such as temperature or concentration of a dissolved matter)

$$\underbrace{\frac{\partial \rho \phi}{\partial t}}_{\text{time derivative}} + \underbrace{\nabla \cdot (\rho \mathbf{u} \phi)}_{\text{convective term}} - \underbrace{\nabla \cdot (\rho \Gamma_\phi \nabla \phi)}_{\text{diffusive term}} = \underbrace{S_\phi(\phi)}_{\text{source term}} , \quad (2.55)$$

where Γ_ϕ is the diffusivity. To yield a second-order scheme, it is assumed that in each CV the quantity ϕ varies linearly both in space and time:

$$\begin{aligned} \phi(\mathbf{x}) &= \phi_P + (\mathbf{x} - \mathbf{x}_P) \cdot (\nabla \phi)_P \\ \phi(t + \Delta t) &= \phi^t + \Delta t \left(\frac{\partial \phi}{\partial t} \right)^t \end{aligned} \quad (2.56)$$

In the following, the subscript denotes evaluation in a particular point or face centroid, i. e. $\phi_P = \phi(\mathbf{x}_P)$, $\phi_f = \phi(\mathbf{x}_f)$ where $\int_f (\mathbf{x} - \mathbf{x}_f) dS = \mathbf{0}$, and the superscripts express the time level. The finite volume method starts from integration of (2.55) over the control volume V_P :

$$\frac{\partial}{\partial t} \int_{V_P} \rho \phi dV + \int_{V_P} \nabla \cdot (\rho \mathbf{u} \phi) dV - \int_{V_P} \nabla \cdot (\rho \Gamma_\phi \nabla \phi) dV = \int_{V_P} S_\phi(\phi) dV \quad (2.57)$$

The discretization of the volume integrals will be now shown one by one, following the PhD thesis of one of the founders of the OpenFOAM project Hrvoje Jasak (1996).

2.3.1.1 Discretization of the volume integral

Using the assumption of linear variation (2.56), in an incompressible model with $\rho = const$ the volume integral in (2.57) may be expressed as

$$\begin{aligned} \int_{V_P} \rho \phi(\mathbf{x}) dV &= \rho \int_{V_P} \phi_P + (\mathbf{x} - \mathbf{x}_P) \cdot (\nabla \phi)_P dV = \rho \phi_P V_P + \rho (\nabla \phi)_P \cdot \int_{V_P} (\mathbf{x} - \mathbf{x}_P) dV = \\ &= \rho \phi_P V_P, \end{aligned} \quad (2.58)$$

since $(\nabla \phi)_P = \text{const}$ and \mathbf{x}_P is the centroid of the CV. The term may be evaluated with the knowledge of the CV volume and value of the quantity ϕ in the CV centroid only, which is stored during the numerical solution. No interpolation is needed here.

2.3.1.2 Discretization of the convective term

Any vector-valued function \mathbf{g} under the divergence operator is first rewritten using the Gauss theorem. The control volume being polygonal, bounded with a set of flat faces f , the discretization of such term proceeds as follows:

$$\int_{V_P} \nabla \cdot \mathbf{g} dV = \oint_{\partial V_P} \mathbf{g} \cdot \mathbf{n} dS = \sum_f \left(\int_f \mathbf{g} \cdot \mathbf{n}_f dS \right) \quad (2.59)$$

Here \mathbf{n}_f denotes the unit outer normal to face f and S_f is the faces's area (see also Fig. 2.2). The function \mathbf{g} is again assumed linear and thus the surface integral may be evaluated as

$$\int_f \mathbf{g} \cdot \mathbf{n}_f dS = \mathbf{g}_f \cdot \mathbf{n}_f \int_f dS + \left(\int_f (\mathbf{x} - \mathbf{x}_f) \otimes \mathbf{n}_f dS \right) : (\nabla \mathbf{g})_f = \mathbf{g}_f \cdot \mathbf{n}_f S_f, \quad (2.60)$$

since x_f is the face centroid and thus the last surface integral is zero. Hence, for the second-order discretization of the divergence term we finally obtain a sum over the CV faces of a scalar product of the value of the function \mathbf{g} in the face centroid and the face area vector:

$$\int_{V_P} \nabla \cdot \mathbf{g} dV = \sum_f \mathbf{g}_f \cdot \mathbf{n}_f S_f. \quad (2.61)$$

In the second, convective term of (2.57), $\mathbf{g} = \rho \mathbf{u} \phi$. Using (2.61) we get

$$\int_{V_P} \nabla \cdot (\rho \mathbf{u} \phi) dV = \sum_f (\rho \mathbf{u} \phi)_f \cdot \mathbf{n}_f S_f = \sum_f \phi_f (\rho \mathbf{u}_f)_f \cdot \mathbf{n}_f S_f. \quad (2.62)$$

Eqn. (2.62) shows that for the calculation of the convective term, the value of the quantity ϕ_f in the face centroid is needed, together with the value of the mass flux through the face $(\rho \mathbf{u}_f)_f \cdot \mathbf{n}_f S_f$. The mass flux is obtained using interpolated values of ρ and \mathbf{u} . The face value ϕ_f may be computed from the value ϕ_P in the CV centroid and ϕ_N in the centroid of the neighboring element (see Fig. 2.2) using a variety of convection differencing schemes. The choice of the convective term differencing

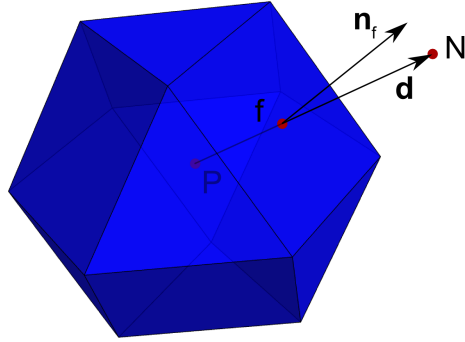


Figure 2.2: Polyhedral control volume with its centroid P , face f , unit outer normal vector to the face \mathbf{n}_f , centroid N of the neighboring control volume adjacent to face f and vector d connecting the centroids P and N .

scheme highly influences the behavior of the resulting numerical scheme. The classical options are the Central differencing scheme (CDS)¹

$$\phi_f = f_x \phi_P + (1 - f_x) \phi_N \quad (2.63)$$

with $f_x = \overline{fN}/\overline{PN}$. CDS is 2nd order, unbounded and unstable for convection-dominated flows. Another common choice is the Upwind differencing scheme²

$$\phi_f = \begin{cases} \phi_P & \text{for } (\rho \mathbf{u} \phi)_f \cdot \mathbf{n}_f S_f \geq 0 \\ \phi_N & \text{for } (\rho \mathbf{u} \phi)_f \cdot \mathbf{n}_f S_f < 0 \end{cases} \quad (2.64)$$

(1st order, bounded, introducing more numerical diffusion than CDS) and Quadratic upstream interpolation for convective kinematics (QUICK), which has greater formal accuracy, but requires the values in other neighboring elements, is difficult to implement on unstructured meshes and can create overshoots or undershoots. The choice of the scheme being a compromise between accuracy and stability, new classes of differencing schemes have been developed: Total variation diminishing (TVD) and, more recently, Normalized variable diagram (NVD) schemes. The motivation was to introduce a scheme with higher order of accuracy, while retaining the stability and suppressing the unwanted oscillations (wiggles) in the solution, which are created especially near high gradients in the solution. The basic idea behind TVD is to use a high-order scheme in conjunction with a flux limiter function, which ensures monotonicity preserving (the scheme does not create new local extrema, and the values of local extrema are decreasing in time). Similarly, NVD schemes also include local adjustments to the discretization of the convective term to ensure boundedness, using an indicator function based on the currently available solution. The details on these methods can be found in (Ferziger and Peric, 2002) or (Versteeg and Malalasekera, 2007), specific approaches to deal with unstructured meshes are described in (Jasak et al., 1999).

¹OpenFOAM terminology: Gauss linear

²OpenFOAM terminology: Gauss upwind

2.3.1.3 Discretization of the diffusive term

Similarly as in the case of the convective term, the third, diffusive term in (2.57) is first rewritten using the Gauss theorem and then the surface integral is evaluated over the faces of the CV:

$$\int_{V_P} \nabla \cdot (\rho \Gamma_\phi \nabla \phi) dV = \oint_{\partial V_P} \rho \Gamma_\phi \nabla \phi \cdot \mathbf{n} dS = \sum_f (\rho \Gamma_\phi \nabla \phi)_f \cdot \mathbf{n}_f S_f = \sum_f (\rho \Gamma_\phi)_f (\nabla \phi)_f \cdot \mathbf{n}_f S_f \quad (2.65)$$

In the case of orthogonal meshes, i. e. if the face normal vector \mathbf{n}_f is parallel to the vector \mathbf{d} (see Fig. 2.2), the face gradient can be calculated from the values in the adjacent cell centroids and

$$(\nabla \phi)_f \cdot \mathbf{n}_f S_f = S_f \frac{\phi_N - \phi_P}{|\mathbf{d}|} . \quad (2.66)$$

However, typical unstructured meshes generated on real-world, complex geometries are never perfectly orthogonal. In this case, approximation (2.66) would compromise the second-order accuracy of the numerical scheme. To circumvent this problem, OpenFOAM uses a concept of nonorthogonal correctors, which can be set up in a number of different ways. Details can be found in (Jasak, 1996), here it is important to state that the usage of nonorthogonal correctors has two important consequences: First, the nonorthogonal correction potentially creates unboundedness, although the diffusion term in its differential form exhibits bounded behavior. Similarly as in the case of the convective term, for a specific problem an appropriate compromise between accuracy and stability has to be balanced. Second, the time discretization of the nonorthogonal correctors is explicit. Even if an implicit time discretization scheme is selected globally, once the nonorthogonal correctors are employed, the solution may become unstable for large timesteps due to the explicit character of the correctors. From practical point of view, the Courant-Friedrichs-Lewy (CFL) condition does form a limitation even for implicit schemes, especially if mesh nonorthogonality is high.

2.3.1.4 Discretization of the source terms

By source term we understand any term in the governing equations, that cannot be written as a temporal, convective or diffusive. Due to the fact, that implicit discretization of the source terms is preferable, a linearization of the source term is needed:

$$S_\phi(\phi) = S_1 + S_2 \phi \quad (2.67)$$

Using (2.56), the volume integral in (2.57) is then evaluated as

$$\int_{V_P} S_\phi(\phi) dV = S_1 V_P + S_2 V_P \phi_P . \quad (2.68)$$

2.3.1.5 Temporal discretization

When the unsteady general transport equation (2.55) is solved numerically, the solution is stored in discrete timesteps. After spatial discretization, which was described in the previous section, the equation needs to be discretized in time. Integrating (2.57) over a timestep Δt and substituting (2.58), (2.62), (2.65) and (2.68) yields

$$\begin{aligned} \int_t^{t+\Delta t} \left[\frac{\partial}{\partial t} (\rho \phi_P V_P) + \sum_f \phi_f (\rho \mathbf{u})_f \cdot \mathbf{n}_f S_f - \sum_f (\rho \Gamma_\phi)_f (\nabla \phi)_f \cdot \mathbf{n}_f S_f \right] dt = \\ = \int_t^{t+\Delta t} (S_1 V_P + S_2 V_P \phi_P) dt . \end{aligned} \quad (2.69)$$

Taking into account the assumed linear variation of ϕ in time (2.56) and assuming that the control volumes V_P , density ρ and diffusivity Γ_ϕ do not change in time, the term containing the temporal derivative may be evaluated as

$$\int_t^{t+\Delta t} \frac{\partial}{\partial t} (\rho \phi_P V_P) = (\phi_P^n - \phi_P^0) \rho_P V_P , \quad (2.70)$$

where

$$\begin{aligned} \phi^0 &= \phi(t) , \\ \phi^n &= \phi(t + \Delta t) . \end{aligned} \quad (2.71)$$

The time discretization may be realized using various methods. When an explicit method is employed, the value in the new time level may be calculated directly from the cell and face values in the old timestep ϕ_P^0, ϕ_f^0 . The drawback of explicit time integration is that for the stability of the scheme it is imperative that the CFL condition is satisfied, which is a serious limitation especially for high-Reynolds-number unsteady flow simulations. The Courant number is defined for a quasi-1D case as $Co = u \Delta t / \Delta x$. For the unstructured 3D meshes, the CFL condition reads

$$Co = \frac{1}{2} \frac{\sum_f |\phi_f|}{V_P} \Delta t < 1 . \quad (2.72)$$

In the case of implicit methods, the discretization leads to solution of a linear system, which is much more computationally expensive than the direct evaluation of the explicit schemes. However, the coupling in the system is much stronger and, provided that all the terms are treated implicitly, the CFL condition does not form a limit and the fully implicit schemes are stable for large

timesteps. Here, the finite volume discretization will be demonstrated on the case of the implicit Crank-Nicholson method, which is based on the trapezoidal rule

$$\int_t^{t+\Delta t} \phi(t) dt = \frac{1}{2} (\phi^0 + \phi^n) \Delta t . \quad (2.73)$$

Combining (2.69), (2.70) and (2.73) yields

$$\begin{aligned} \frac{\phi_P^n - \phi_P^0}{\Delta t} \rho_P V_P &+ \frac{1}{2} \sum_f \phi_f^n (\rho \mathbf{u})_f^n \cdot \mathbf{n}_f S_f - \frac{1}{2} \sum_f (\rho \Gamma_\phi)_f (\nabla \phi)_f^n \cdot \mathbf{n}_f S_f + \\ &+ \frac{1}{2} \sum_f \phi_f^0 (\rho \mathbf{u})_f^0 \cdot \mathbf{n}_f S_f - \frac{1}{2} \sum_f (\rho \Gamma_\phi)_f (\nabla \phi)_f^0 \cdot \mathbf{n}_f S_f = \\ &= S_1 V_P + \frac{1}{2} S_2 V_P \phi_P^n + \frac{1}{2} S_2 V_P \phi_P^0 . \end{aligned} \quad (2.74)$$

Equation (2.74) represents an algebraic equation for the new value ϕ_P^n in the element P. The face value ϕ_f^n and the face gradient $(\nabla \phi)_f^n$ depend on the unknown values ϕ_N^n in the neighboring cells. Thus, (2.74) may be rewritten as

$$a_P \phi_P^n + \sum_N a_N \phi_N^n = R_P , \quad (2.75)$$

where the sum runs over all cells which have a common face with element P. The coefficient a_P includes contributions from the temporal derivative, convective and diffusive terms, and linear part of the source term. Coefficients a_N contain corresponding terms from the neighboring elements. The right-hand-side term R_P is formed from all the contributions that can be evaluated without knowledge of the new time-level value ϕ^n – the constant part of the source term and portions of the temporal derivative, convective and diffusive terms corresponding to the old time level. Equations (2.75) for all the control volumes form a system of linear algebraic equations

$$\mathbb{A} \phi = \mathbf{R} \quad (2.76)$$

with a sparse matrix \mathbb{A} whose bandwidth depends on how the elements are numbered.

The Crank-Nicholson temporal discretization requires storage of cell values for both old and new time levels. It is implicit, 2nd order accurate and unconditionally stable, but does not guarantee boundedness of the solution. Similarly as in the case of spatial discretization of the convective term, boundedness can be ensured by first-order temporal discretization such as backward Euler³ method. More details on the discretization practice when using forward Euler⁴ or backward differencing schemes can be found in (Jasak, 1996).

³OpenFOAM keyword: Euler implicit

⁴OpenFOAM keyword: Euler explicit

2.3.2 Finite volume discretization of the Navier-Stokes equations

The momentum conservation equation in (2.53) represents a special case of the general transport equation (2.55), where the transported property ϕ is the velocity itself. In the incompressible case, the pressure gradient term $\frac{1}{\rho}\nabla p$ acts as a momentum source. It is necessary to note that there is no transport equation for the pressure itself. The coupling between pressure and velocity can be understood as a constraint in the solution of the flow field: if a correct pressure field is applied in the momentum equations, the resulting velocity field satisfies the continuity equation. In the compressible NSE, the situation is different – the continuity equation may be used as a transport equation for density, and the pressure field is then calculated from the equation of state.

The major problem with the numerical solution of the NSE is the nonlinearity of the convective term $\nabla \cdot (\mathbf{u} \otimes \mathbf{u})$. The discretization of the convective term (2.62) turns in the case of the NSE into

$$\int_{V_P} \nabla \cdot (\rho \mathbf{u} \otimes \mathbf{u}) dV = \sum_f \mathbf{u}_f \otimes (\rho \mathbf{u})_f \cdot \mathbf{n}_f S_f. \quad (2.77)$$

From (2.77) it follows that direct discretization would lead to a system of nonlinear algebraic equations. Due to the high computational cost of the nonlinear solvers, linearization of the convective term is usually preferred, similarly as in the case of finite element CFD solvers. An existing face velocity flux $(\rho \mathbf{u}^*)_f \cdot \mathbf{n}_f S_f$, taken from the previous timestep, is used to evaluate the discretized convective term. This linearization does not influence negatively the results of steady-state simulations once convergence is reached. For unsteady simulations, the error introduced by the time-lag of the velocity flux depends on the timestep and may be either neglected, or minimized by an internal loop of iterations.

The second important issue in the discretization of the NSE is the pressure-velocity coupling. In monolithic methods, the coupled equations are discretized together, resulting in a single matrix for both the discretized pressure and velocity fields. However, most practical CFD codes based on the finite volume method solve the coupling between the pressure and velocity iteratively, using pressure predictor and corrector steps with optional under-relaxation. Two iterative algorithms are commonly used: Semi-Implicit Method for Pressure Linked Equations (SIMPLE), developed at Imperial College London in the early 1970's (Patankar and Spalding, 1972) for the steady-state flows, and Pressure Implicit with Splitting of Operators (PISO) by Issa (1986) for unsteady simulations.

For the FVM simulations realized in OpenFOAM and included in this thesis, the author used a modified version of the PISO algorithm⁵. In contrast to the standard PISO algorithm, it has a substep iteration loop: multiple cycles over the same timestep with the last iteration results (optionally relaxed) used as an initial guess for the next substep iteration. Additionally, the algorithm allows for automatic adaptive timestepping to keep the maximum local Courant number (2.72) close to a predefined limit.

2.3.3 Finite volume discretization on a moving mesh

Similarly as in the case of the Finite element method, a standard approach to the solution of problems on time-dependent geometries (moving meshes) is the Arbitrary Lagrangian Eulerian (ALE)

⁵OpenFOAM terminology: merged PISO-SIMPLE solver – pimpleFOAM

formulation of the governing equations. Details on the ALE approach can be found in the book chapter by [Donea et al. \(2004\)](#). Applying the general transport theorem to an arbitrary volume V_{Pt} , whose boundary ∂V_{Pt} moves with a mesh velocity \mathbf{w} , a new term containing the mesh velocity occurs in the integral form of the transport equation (2.57) ([Bos, 2010](#)). After application of the Gauss theorem, we get

$$\frac{\partial}{\partial t} \int_{V_{Pt}} \rho \phi \, dV + \oint_{\partial V_{Pt}} \rho (\mathbf{u} - \mathbf{w}) \cdot \mathbf{n} \phi \, dS - \oint_{\partial V_{Pt}} \rho \Gamma_\phi (\nabla \phi) \cdot \mathbf{n} \, dS = \int_{V_{Pt}} S_\phi (\phi) \, dV. \quad (2.78)$$

The finite volume discretization of equation (2.78) is performed almost identically as in sec. 2.3.1 and when the Crank-Nicholson scheme is used again, it yields

$$\begin{aligned} \frac{\rho_P \phi_P^n V_{Pt}^n - \rho_P \phi_P^0 V_{Pt}^0}{\Delta t} &+ \frac{1}{2} \sum_f \phi_f^n (\rho (\mathbf{u} - \mathbf{w}))_f^n \cdot \mathbf{n}_f S_f - \frac{1}{2} \sum_f (\rho \Gamma_\phi)_f (\nabla \phi)_f^n \cdot \mathbf{n}_f S_f + \\ &+ \frac{1}{2} \sum_f \phi_f^0 (\rho (\mathbf{u} - \mathbf{w}))_f^0 \cdot \mathbf{n}_f S_f - \frac{1}{2} \sum_f (\rho \Gamma_\phi)_f (\nabla \phi)_f^0 \cdot \mathbf{n}_f S_f = \\ &= S_1 V_P + \frac{1}{2} S_2 V_P^n \phi_P^n + \frac{1}{2} S_2 V_P^0 \phi_P^0. \end{aligned} \quad (2.79)$$

Compared to the FV discretization on a static mesh, there are only two differences: the temporal derivative includes the rate of change of the volume V_{Pt} , and the face flux includes grid convection. The relation between the latter two is defined by the Space Conservation Law ([Ferziger and Peric, 2002](#))

$$\frac{\partial}{\partial t} \int_{V_{Pt}} dV - \oint_{\partial V_{Pt}} \mathbf{w} \cdot \mathbf{n} \, dS = 0. \quad (2.80)$$

The law is always satisfied in the integral form (2.80), but it also needs to be preserved in the discrete form ([Jasak and Tuković, 2004](#)):

$$\frac{V_{Pt}^n - V_{Pt}^0}{\Delta t} - \sum_f \mathbf{w}_f \cdot \mathbf{n}_f S_f = 0. \quad (2.81)$$

This is why the grid motion flux ($\mathbf{w}_f \cdot \mathbf{n}_f S_f$) is calculated as a volume swept by face f of the polyhedral control volume within the current timestep, rather than by interpolating the mesh velocity \mathbf{w} .

2.3.4 Mesh motion strategies

In a typical CFD simulation on a moving geometry, the motion is prescribed (or induced) only on the boundary of the flow domain $\partial\Omega_t$, not in the whole interior Ω_t . For a given timestep, the algorithm knows the position (and velocity) of the gridpoints on the boundary, but not of the internal mesh points. The discussion here will be limited to the cases when the mesh topology (cell number, connectivity, orientation and numbering) does not change, i. e. when no remeshing or layer insertion, only pure mesh deformation is involved.

The internal nodes can move in an arbitrary way, but there is an obvious requirement that the mesh quality (orthogonality, aspect ratio and skewness of the elements) is not impaired by the deformation and that, in the extreme, the cells do not degenerate or flip with catastrophic consequences on the solution. For the unstructured 3D meshes on real-world geometries, finding a robust yet computationally cheap method for calculation of the internal gridpoint position proves to be an unexpectedly hard problem. In the following, several methods which can be used in various versions of OpenFOAM are listed and explained.

2.3.4.1 Spring analogy

An intuitive point-based method for the solution of the mesh deformation is the spring analogy, where the gridpoints are connected by linear springs along the grid edges (Blom, 2000). After imposing the position of the boundary nodes, the position of the internal nodes is solved by assembling a linear system from the force balance in all nodes. While this method may seem clear, simple and efficient, unfortunately it does not guarantee that the elements do not collapse. Indeed, in practical tests, two failure modes have been observed already for small boundary motions (Jasak and Tuković, 2004).

First, two gridpoints can easily collapse into a single one, since the force on a linear spring does not tend to infinity when the spring length approaches zero. This could be remedied by introducing a nonlinear force, however, at a very high price of turning the algorithm into solution of a system of nonlinear equations. Second, the linear spring analogy does not guarantee that a triangular face cannot flip edges. For this, torsional springs (again, with a nonlinearity to prevent edge flipping) would be needed. As a result, construction of a stable and robust spring-based system is possible, but the resulting numerical algorithm is so complex and computationally expensive that this method is very rarely used.

2.3.4.2 Solution of the Laplace equation

The internal gridpoint position may be also calculated by solving an auxiliary partial differential equation with a suitable operator. A common choice and the standard method implemented in the official version of OpenFOAM (current version 2.3.0) is the Laplace equation⁶

$$\nabla \cdot (\gamma \nabla \mathbf{w}) = 0 \quad \text{in } \Omega_t \tag{2.82}$$

⁶OpenFOAM terminology: motion solver velocityLaplacian

with a mesh diffusivity γ , which can be either constant or variable (e. g., linear, inverse quadratic or exponential function of the distance from the boundary). The new node position is then calculated as

$$\mathbf{x}^n = \mathbf{x}^0 + \mathbf{w} \Delta t . \quad (2.83)$$

A big advantage, at least seemingly, is that the existing finite volume machinery can be directly employed for the discretization of the Laplace equation (2.82) without any further programming effort. For small and simple boundary motions, this solver works well. In the CFD simulations of the author, a computational overhead of approximately 10–20 % for the discretization and numerical solution of the auxiliary Laplace equation was measured against the flow field solution (Šidlof et al., 2014c). However, this method does not guarantee that the mesh elements do not degenerate, either. Both author's own experience and detailed analyses of the code developers (Jasak and Tuković, 2004) proved that the method is, in some cases, frustratingly unstable even for moderate boundary motions, with simulation crashes caused by cell edge flipping. The official version of OpenFOAM contains several other mesh motion solvers⁷, but these are suited only for a limited class of applications.

2.3.4.3 Solution of the linear solid equation

A method for the grid motion solution, which is considered as very robust especially in the FEM community, is the solution of a linear solid equations

$$\begin{aligned} \nabla \cdot \boldsymbol{\sigma} &= 0 , \\ \boldsymbol{\varepsilon} &= \frac{1}{2} \left[\nabla \mathbf{y}_w + (\nabla \mathbf{y}_w)^T \right] , \\ \boldsymbol{\sigma} &= \mathbf{C} : \boldsymbol{\varepsilon} , \end{aligned} \quad (2.84)$$

where $\boldsymbol{\sigma}$ and $\boldsymbol{\varepsilon}$ are the stress and strain tensors, respectively, \mathbf{C} the fourth-order tensor of elastic coefficients and \mathbf{y}_w the grid node displacement. The idea behind this method is that the mesh can be regarded as a pseudo-solid material with a spatially variable stiffness. As far as the small-strain assumption is not excessively violated, in the FEM codes this method performs very well with a computational cost that is higher than in the case of the simple Laplace equation, but still acceptable. However, when the finite volume method is used for the solution of the mesh deformation by (2.84), a serious problem is encountered: because FV discretization is cell-centered and the solution for the gridpoint motion is needed in the cell vertices, interpolation is inevitable. It has been shown that it is highly problematic to construct an interpolation practice, which would prevent the cells from flipping and degenerating and that would work reliably even in the corner points, belonging to only one cell (Jasak and Tuković, 2004).

The pseudosolid mesh motion solver has disappeared from the official OpenFOAM branch in the early versions. However, it is still available within the community-developed OpenFOAM Extend Project (2014). In order to avoid the problems with the FV interpolation, the mesh-motion solution procedure is as follows:

⁷e. g. sixDoFRigidBodyMotion solver

- The polyhedral mesh is decomposed into tetrahedra by splitting the faces into triangles and adding a new gridpoint in the cell centroid
- Equation (2.84) is discretized using standard second-order FEM on the tetrahedral mesh
- Boundary conditions for the mesh motion equation are imposed
- The resulting FE matrix is solved using an iterative method, such as a preconditioned conjugate gradient solver

One might regard as an overkill to implement a fully-fledged FE solver into an existing FV code just to solve for the mesh motion. However, as indicated before, none of the previous methods is robust enough that it could be engaged generally and without strenuous case-specific tuning. A rough figure about the effort devoted to the implementation of the FEM-based pseudosolid solver may be guessed from the statements of the OpenFOAM developers, who claim that the implementation of the tetrahedral decomposition and FEM-specific classes and methods totals "just under 21 000 lines" against the approximately 100 000 lines of the entire OpenFOAM code ([Jasak and Tuković, 2004](#)).

Chapter 3

Experimental methods in fluid dynamics

It is far beyond the scope of this thesis to give a full overview of the methods used in experimental fluid dynamics. An exhaustive list and explanation is given e. g. in the 1500-page handbook by [Tropea et al. \(2007\)](#). Here, only a short survey of the methods for the measurement of velocity, pressure and density is summarized, with special emphasis on methods used by the author in his research, and with references to relevant literature. Among the numerous methods, it is important to distinguish between three classes: measurement in a single point, spatially integrated measurements and spatial distribution measurements. Although many of the measurement techniques can be adapted for supersonic flows, within this overview only subsonic flows will be considered.

In experimental investigation of flow in problems, where an object in the flow field or where the wall of a channel conveying fluid moves either due to fluid-structure interaction or by external excitation, additional complications may be encountered when using various measurement methods. First, the optical access to the field of interest may be limited due to object motion. For the PIV method, for instance, this influences both the optical access for the laser sheet and for the high-speed camera. Second, the moving object induces additional unsteadiness and disturbs the fluid field, so that the assumptions which hold for the fluid field around a static object (i. e., laminar or turbulent character of the flow, thickness of the boundary layer, turbulence intensity level etc.) may not hold any more.

3.1 Pressure measurements

In the experimental fluid dynamics community, the pressure at a certain point of fluid, as a scalar nondirectional measure of the molecular activity, is usually referred to as *static pressure* and denoted by p . In contrast, the *total pressure* p_0 , which quantifies the total energy of a fluid in a point, is a physical value which depends on the direction of the measuring device with respect to the flow. If gravity head can be neglected, which is the case in most air flow problems, total pressure p_0 is equal to stagnation pressure p_s , which is the pressure at a stagnation point (point, where the fluid velocity is zero and where all kinetic energy has been isentropically converted to pressure energy). The stagnation pressure can be measured by the Pitot probe (see Fig. 3.1). For the rest, we will assume that $p_s = p_0$.

For incompressible inviscid flows, i. e. for low Mach-number flows $M < 0.3$, the difference between the total and static pressure is called the *dynamic pressure*. From incompressible Bernoulli equation

$$p_0 - p = \frac{1}{2} \rho U^2, \quad (3.1)$$

where $U = |\mathbf{u}|$ is the flow velocity magnitude and ρ the fluid density. In the case of compressible steady inviscid subsonic flow, the term *dynamic pressure* is usually not used. For the relation between the total and static pressure it can be derived from the compressible Bernoulli equation that (Shapiro, 1954)

$$\frac{p_0}{p} = \left(1 + \frac{\kappa - 1}{2} M^2\right)^{\frac{\kappa}{\kappa - 1}}, \quad \frac{p}{p_0} = \left(1 + \frac{\kappa - 1}{2} M^2\right)^{-\frac{\kappa}{\kappa - 1}}, \quad (3.2)$$

where $\kappa = c_p/c_v$ is the specific heat ratio (for air, $\kappa = 7/5$) and $M = U/a$ is the Mach number with the speed of sound

$$a = \sqrt{\kappa \frac{p}{\rho}} = \sqrt{\kappa R T}. \quad (3.3)$$

Here ρ is the fluid density, $R = 287 \text{ J kg}^{-1} \text{ K}^{-1}$ is the specific gas constant for dry air and T the thermodynamic local static temperature.

If a differential pressure sensor is used for measurement of $(p_0 - p)$, equation (3.2) may be rewritten in a different form. For $M < 1$, the right-hand side of (3.2) can be expanded using the general binomial theorem

$$(x + y)^r = \sum_{k=0}^{\infty} \binom{r}{k} x^{r-k} y^k = x^r + r x^{r-1} y + \frac{r(r-1)}{2!} x^{r-2} y^2 + \frac{r(r-1)(r-2)}{3!} x^{r-3} y^3 + \dots \quad (3.4)$$

into

$$\begin{aligned} \left(1 + \frac{\kappa - 1}{2} M^2\right)^{\frac{\kappa}{\kappa - 1}} &= 1 + \frac{\kappa}{\kappa - 1} \frac{\kappa - 1}{2} M^2 + \frac{\kappa}{\kappa - 1} \frac{1}{\kappa - 1} \frac{1}{2!} \frac{(\kappa - 1)^2}{4} M^4 + \\ &+ \frac{\kappa}{\kappa - 1} \frac{1}{\kappa - 1} \frac{2 - \kappa}{\kappa - 1} \frac{1}{3!} \frac{(\kappa - 1)^3}{8} M^6 + \dots = \\ &= 1 + \frac{\kappa}{2} M^2 + \frac{\kappa}{8} M^4 + \frac{\kappa(2 - \kappa)}{48} M^6 + \dots \end{aligned} \quad (3.5)$$

Using the pressure-density relation

$$\frac{1}{2} \rho U^2 = \frac{1}{2} \kappa M^2 p \quad (3.6)$$

(see (3.3)) and substituting (3.5) into (3.2) we finally get

$$p_0 - p = \frac{1}{2} \rho U^2 \left(1 + \frac{M^2}{4} + \frac{(2 - \kappa) M^4}{24} + \dots \right) \quad (3.7)$$

Truncation of all but the first term of the expansion yields the well known incompressible form (3.1) with an error in the evaluation of the dynamic pressure $1/2 \rho U^2$ below 0.2% for $M < 0.09$. If the two first terms of (3.7) are retained, the formula is accurate up to $M = 0.55$. Employing the first three terms of the expansion allows to use the formula in the all subsonic range $M < 1$ (Tropea et al., 2007).

3.1.1 Pressure taps

A simple and convenient way how to measure the static pressure at certain point of a channel wall in wall-bounded flows is the usage of pressure taps. Usually, a small circular orifice flush with the channel wall is drilled, and connected by a tube with a pressure transducer of suitable sensitivity, range and frequency response. Miniature, on-chip transducers which can be mounted directly to the measurement place are also available. These sensors, which minimize the cavity length, have fast response and can be used for dynamic measurements. Six such sensors were mounted in the wall of the self-oscillating airfoil during wind-tunnel measurements of the author (see sec. 5.3).

For precise pressure tap measurements, care must be taken to compensate for the diameter of the tapping, cavity shape and alignment, compressibility effects, cavity and tube length. More information can be found i. e. in (Chue, 1975) or (Tropea et al., 2007).

3.1.2 Static probes

In cases where the static pressure in a single point in freestream is needed, it is possible to use the static pressure probes. A static probe is a slender tube with a port aligned parallel with the streamlines (see the static port of the Pitot-static tube in Fig. 3.1). In practice, more static ports are manufactured in one radial plane. Except for the physical arrangement of the probe, most considerations are similar as in the case of pressure taps.

3.1.3 Pressure-sensitive paints

In wind tunnel testing, spatial distribution of the pressure over the whole surface of an object subjected to airflow is often needed. One option is an array of pressure taps, connected to a pressure scanner. On large surfaces or when high spatial resolution is needed, this approach can be impractical. In these cases, the usage of pressure-sensitive paints can be considered.

A pressure-sensitive paint (PSP) is a luminescent material containing dye molecules, whose intensity of luminescence depends on the partial pressure of oxygen and thus the pressure of air. The dye molecules get excited by visible or UV light. After a characteristic lifetime, the dye molecule excites a photon at a different wavelength than that of the excitation light. If an oxygen molecule collides with the dye molecule, however, the energy is lost and no photon emitted. This mechanism is called oxygen quenching.

In practice, a dye layer of about $20 - 60 \mu\text{m}$ is applied to the surface of the object, often together with discrete pressure taps serving for reference and calibration. The surface is illuminated by a continuous light source and the paint's luminescence detected by a CCD digital camera or a photographic film. The intensity of the luminescence is inverse proportional to the partial pressure of oxygen. Moreover, in practical realization it is impossible to deliver the same intensity of the excitation light in to all places of the object, and the method thus needs calibration, which might be particularly difficult if the object is moving during measurement. The excitation light should have enough intensity at the excitation frequency, and preferably no frequency content within the luminescence frequency band. The usual choice is xenon-arc or halogen lamps, argon lasers or LEDs.

A large number of scientific papers have been published on the PSPs since its invention in 1935. The theoretical and practical analysis of the method can be found e. g. in a review paper of [Liu et al. \(1997\)](#) or in a monograph of the same authors ([Liu and Sullivan, 2005](#)).

3.2 Velocity measurements

3.2.1 Pitot tube measurements

A classical single-point velocity measurement method for medium and high Mach number flows is the Pitot tube measurement. The method is pressure-based, since the velocity is calculated from the difference of the total pressure p_0 and the static pressure p according to (3.1) for incompressible flow or (3.7) for higher flow velocities. An illustration of the Pitot-static tube configuration is given in Fig. 3.1. For cases with constant (or known) pressure profile, a Pitot impact probe with a static tap mounted flush with the channel wall may be used.

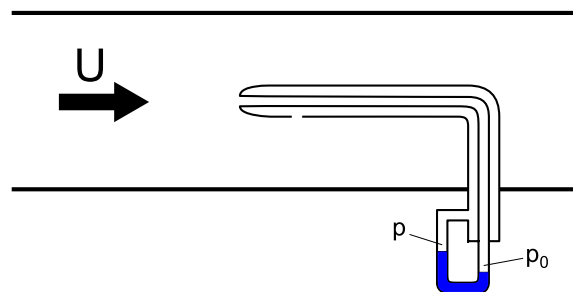


Figure 3.1: Schematic of the pitot-static tube measuring the difference between the total pressure p_0 and static pressure p .

Pitot tube measurement is a robust method for the measurement of steady flow velocity, widely used both in laboratory and in industry, particularly in aviation – a Pitot tube is currently a standard

for airspeed measurement and can be found on every military and civil airplane. In Pitot tube measurements, care must be taken not to influence the measured flow field by the presence of the probe, to align the probe with the flow direction, and to compensate for turbulent and viscosity effects if necessary. The method was used by the author in the measurements of inlet flow velocity in the suction-type wind tunnel with the self-oscillating airfoil model (see sec. 5.3). More details on the Pitot probe measurements can be found e. g. in (Bryer and Pankhurst, 1971), (Chue, 1975) or (Tropea et al., 2007).

3.2.2 Hot wire anemometry

Unlike Pitot tube measurements, hot-wire anemometry (HWA) can be used for measurement of turbulent velocity fluctuations with high temporal resolution. The method is based on measurement of change of heat transfer from a thin heated film or wire into the flowing fluid. The diameter of the heated wire ranges typically from 1 – 3 μm . The ability to capture rapid velocity fluctuations is due to the low thermal inertia of the sensor, which can be further compensated using suitable electrical connection and filtering of the signal. The HWA sensor is sensitive to the velocity component normal to the wire direction. Various HWA configurations (X-wires, V-probes, triple- and multiple-sensor probes) are commercially available to measure different velocity vector components, mean and fluctuating parts of the velocity and even the vorticity vector. From principle, HWA belongs to the class of single-point measurement methods.

The HWA sensors are built from a material, whose electrical resistance changes with temperature, and can be operated in three modes: constant-voltage anemometer (CVA), where the voltage across the wire is kept constant and the current measured, constant-temperature anemometer (CTA), where the resistance and consequently the temperature of the sensor is maintained constant and the voltage measured, and constant-current anemometer (CCA) with the electrical current kept constant and the resistance measured.

Detailed analysis and description of the thermal anemometry theory and applications can be found in monographs (Perry, 1982) or (Lomas, 1986).

3.2.3 Laser Doppler anemometry

Laser Doppler anemometry (LDA) exploits the Doppler effect, which occurs when an incident laser light with frequency f_i and wavelength λ_i scatters on a particle conveyed by the fluid with velocity \mathbf{u} . The frequency of the scattered light f_s , received on the detector, is modified by the Doppler shift as

$$f_s = f_i \frac{1 - \frac{\mathbf{u} \cdot \mathbf{e}_i}{c}}{1 - \frac{\mathbf{u} \cdot \mathbf{e}_s}{c}} \approx f_i + \frac{\mathbf{u} \cdot (\mathbf{e}_s - \mathbf{e}_i)}{\lambda_i}, \quad (3.8)$$

where \mathbf{e}_i and \mathbf{e}_s are the directional vectors of the incident light coming from the laser source and light scattered to the detector, respectively, and $c = \lambda_i f_i$ the speed of light. Since the Doppler shift is very low compared to the frequency of laser light (by the order of about 10^{11}) and thus virtually impossible to be measured directly, a dual-beam configuration is usually used. Here the source laser light is split into two beams, which intersect in the measurement volume under angle θ . The

scattered beams with frequencies f_{s1} and f_{s2} are then detected by a single detector, where a Doppler frequency f_D modulates the signal due to the interference between the two scattered beams:

$$f_D = f_{s1} - f_{s2} = \frac{\mathbf{u} \cdot (\mathbf{e}_{s1} - \mathbf{e}_{s2})}{\lambda_i} = \frac{2 \sin(\theta/2)}{\lambda_i} u_{\perp} \quad (3.9)$$

From (3.9) it can be seen that the Doppler frequency is proportional to the velocity component u_{\perp} perpendicular to the beam bisector, and independent of the detector position. Since the angle θ between the two incident beams is known accurately, there is no need to calibrate the LDA probe.

To determine the sign of the flow velocity u_{\perp} , which is not apparent from (3.9), in most of the LDA systems one of the incident beams is frequency-shifted by f_{Δ} using a Bragg cell, which produces a moving fringe pattern on the detector. A static particle with $u = 0$ will then appear as a frequency f_{Δ} on the detector, negative flow velocities will result in $f < f_{\Delta}$ and positive in $f > f_{\Delta}$.

LDA needs seeding particles introduced into the flow. The seeding particles must satisfy all the requirements as in the case of the PIV method, described in sec. 3.2.5. One of the major advantages of the LDA method against pressure-probe measurements and the HWA method is that it is non-intrusive, the probe does not disturb the flow field. However, optical access to the measurement volume must be ensured. The LDA is a single-point measurement method with spatial and temporal resolution, and as can be seen from (3.9), it is directionally sensitive. With a hardware and software extension, its variant called Phase Doppler Anemometry (PDA) is also capable of measuring the particle sizes. More details on the method can be found in a review paper of [Abbiss et al. \(1974\)](#), in the monograph ([Kopecký, 2008](#)) or in the handbook ([Tropea et al., 2007](#)).

3.2.4 Ultrasonic anemometry

The operating principle of the ultrasonic anemometers (UAs) is the measurement of different times needed by a high-frequency acoustic pulse to pass through the moving fluid in opposite directions. Usually, two probes, both containing a transmitter and a receiver, are set up around the measured volume. Multiple paths oriented at different angles may be used to acquire all components of the velocity vector. The signal from an UA is proportional to the velocity averaged over the path of the ultrasonic beam, and thus belongs to the class of spatially integrated velocity measurements.

Ultrasonic anemometers have no moving parts and are much more robust than classical laboratory equipment such as HWA or LDA. They require only initial calibration and can operate for a long time without any maintenance even in rough conditions. This is why they are often used in atmospheric measurements. Generally, the time resolution is lower than in HWA or LDA measurements. It is also necessary to keep in mind that ultrasonic anemometry provides integral (mean) value over the measurement path. With a compensation for the passage of the signal through the channel wall, UAs can be used to measure the mean flow velocity inside a channel, which has been used by the author in his measurements of mean subglottal airflow velocity in a synthetic vocal fold model measurements (see sec. 4.4.2). When used outside a channel, UAs are nonintrusive and do not disturb the measured flow field.

The theory of sonic anemometry is thoroughly explained in ([Cuerva and Sanz-Andrés, 2000](#)), practical details can be found e. g. in the monograph of [J.C. Kaimal \(1994\)](#).

3.2.5 Particle image velocimetry

Particle Image Velocimetry (PIV) is an optical non-intrusive method for measurement of the spatial distribution of the velocity field. It uses a laser sheet to illuminate the seeding particles moving with the fluid, one or multiple digital cameras to record the position of the particles and a software for the computation of the velocity field. A typical PIV setup is shown in Fig. 3.2.

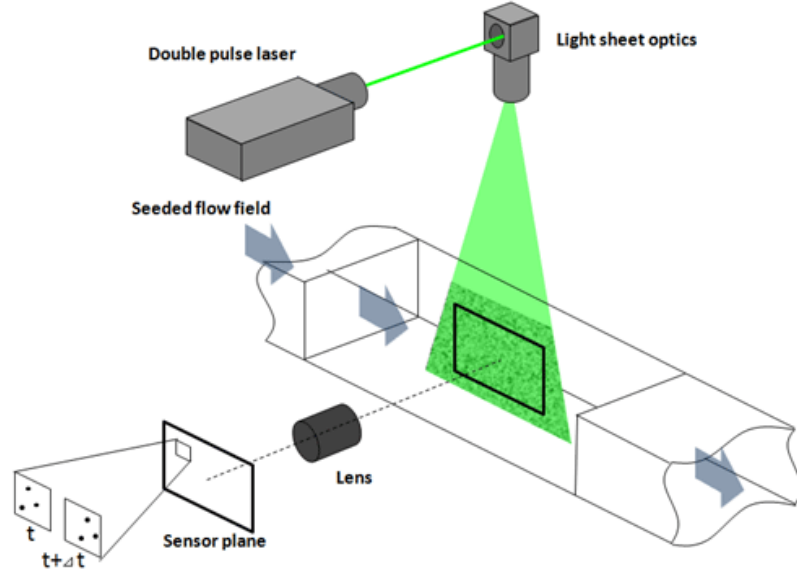


Figure 3.2: Principle of the PIV method in standard (single-camera) configuration. Adapted from [Seika Measurement Technology \(2014\)](#).

The PIV method relies on seeding particles introduced into the flow. The fundamental requirement is that the particles follow the fluid flow, i. e. that the particle velocity \mathbf{v}_p is equal to the local fluid velocity \mathbf{u} . For small particles (with the diameters in the orders of μm or tens of μm) and small to medium Reynolds numbers, the force exerted by the fluid on the particle is dominated by quasi-steady Stokes viscous drag force and so the equation of motion of a particle with velocity \mathbf{v}_p is approximately

$$\frac{4}{3} \pi r_p^3 (\rho_p - \rho_f) \frac{d\mathbf{v}_p}{dt} = -6 \pi \mu r_p (\mathbf{v}_p - \mathbf{u}) . \quad (3.10)$$

Hence, the difference between the particle and fluid velocity at a given particle acceleration may be estimated as

$$\mathbf{v}_p - \mathbf{u} = \frac{2}{9} r_p^2 \frac{\rho_f - \rho_p}{\mu} \frac{d\mathbf{v}_p}{dt} , \quad (3.11)$$

where μ is the fluid viscosity, r_p the seeding particle radius and ρ_p and ρ_f the density of the particle and fluid, respectively ([Tropea et al., 2007](#)). Equation (3.11) shows that if the particle density

is equal to the fluid velocity, the particles will follow the flow accurately. This can be relatively easily satisfied for liquids, e. g. with the usage of polyamide or hollow-glass particles, but virtually impossible to fulfill in air measurements. In these cases, the slip velocity $\mathbf{v}_p - \mathbf{u}$ can be minimized by using particles with a diameter r_p as small as possible.

The particles are illuminated in a selected plane by a laser sheet, generated by a double-pulsed laser system and formed by cylindrical optics (see Fig. 3.2). The images are recorded by a CCD or CMOS camera. The exposure time of the camera, length and energy of the laser pulse must be configured so that the particles appear as dots on the camera frames. This might be challenging in measurements in gases, since here small particles are required due to (3.11). However, the light scattering on particles with dimensions in the orders of micrometers lies in the Mie regime (van de Hulst, 1957), where the intensity of light scattered in the direction perpendicular to the incident laser sheet (i. e., in the direction where the camera is usually situated) is very low and highly dependent on the scattering angle θ . This is why high laser pulse energies are required, especially when larger areas need to be measured. Typically, the PIV systems are powered by two solid-state Nd:YAG lasers emitting at an infrared wavelength of 1064 nm, which can be frequency-doubled to generate laser pulses at a visible wavelength of 532 nm. About ten years ago, the Nd:YAG lasers were limited by the maximum repetition rate of the subsequent pulses of about 20 Hz. Recently, Nd:YAG lasers with repetition frequencies up to 15 kHz have been developed, making time-resolved PIV systems commercially available.

The position of the particles illuminated by the two laser pulses is recorded by a double-shuttered digital camera, hardware-synchronized with the laser switching system. For time-resolved PIV, a high-speed camera with a sufficient amount of internal memory is necessary. After the measurement, the camera frames are transferred to a computer and processed. The frames are divided into so-called interrogation areas (typically 16×16 to 64×64 pixels). Spatial correlation analysis of the two frames and knowledge of the time delay between the two laser pulses yields one velocity vector per interrogation area. Postprocessing methods such as outlier detection or median filtering are often used to improve the raw vector maps.

The PIV method requires optical access to the measurement section both for the laser and for the camera. Many of the flows of engineering interest are in air or water, which are transparent and thus well suited for the PIV measurement. For internal and channel flows, some parts of the channel walls have to be manufactured from a transparent material such as glass or perspex. Additional complications may occur if the channel walls are curved, depending on whether the curved channel parts intersect the optical path of the laser sheet (which was the case in author's PIV measurements of unsteady supraglottal flow field in a synthetic vocal fold model, see sec. 4.4.2), the field of view of the camera, or both.

In standard, single-camera configuration, the PIV method is capable of measuring two components of the velocity vector in a 2D plane. When two cameras are used, it is possible to acquire all three components of the velocity in a 2D plane (3D-PIV). With three or four cameras, telecentric lenses and corresponding software, volumetric PIV is possible, yielding the full distribution of all components of the velocity vector in a whole volume.

The standard 2D PIV described in this section was used by the author in his measurements of supraglottal velocity fields in a physical model of vocal folds (see sec. 4.4.2). Lately, numerous variants of the PIV method have been developed, e. g. particle tracking velocimetry (low-image-density PIV), stereoscopic and volumetric PIV, and others. More information on the particle-imaging techniques can be found in (Adrian, 1991, Raffel et al., 2007) or in (Kopecký, 2008).

3.2.6 Other velocity measurement methods

There are also other methods for measuring velocity of the fluid flow, namely turbine- and propeller-based anemometers. These are however rarely used in laboratory experiments and will not be covered here.

3.3 Density measurements

The optical methods for the measurement of density in gas flows rely on the fact that the index of refraction n of a gas is a linear function of the density ρ . The relation is given by the empirical Gladston-Dale equation

$$n - 1 = K \rho , \quad (3.12)$$

where K the Gladston-Dale constant, which is specific for a given gas and only weakly dependent on the wavelength of the light. When a light ray passes through a domain with variable index of refraction, two effects occur. First, the light ray is deflected by refraction, which might be visualized in the image plane. This effect is exploited in three methods – shadowgraphy, Schlieren and moiré deflectometry. It can be shown that the first of these techniques is sensitive to the second derivative of density and the latter two to the density gradient (Shapiro, 1954). All these methods are popular for compressible flow visualization, and can be also used in experimental investigation of heat transfer, mixing or stratified flow problems. A comprehensive overview of the optical density-based methods for the compressible flow is given e. g. in Shapiro (1954) or Verma et al. (2012).

When light passes through a test section containing gas with variable density and thus variable refractive index, the optical path length (optical phase) is also modified. By using a beam splitter and by interference of the test beam with a reference beam diverted outside the test section, interference fringes containing the information about density variations may be created, acquired by a classical or digital camera and evaluated. This is the operating principle of reference-beam interferometers.

3.3.1 Reference-beam interferometry

Compared to the shadowgraphy, Schlieren and moiré techniques, reference-beam interferometry requires precise and expensive equipment and is more complicated to operate. However, it provides more useful information, since the signal is directly proportional to the density, not its derivatives. A schematic of the Mach-Zehnder type interferometer used by the author and his colleagues in the measurements of unsteady flow field around a self-oscillating airfoil model in a wind tunnel (see sec. 5.3) is shown in Fig. 3.3. Fig. 3.4 demonstrates two sample interferograms acquired by a high-speed camera during an unsteady flow field measurement at a low and medium Mach number flow.

The interferometric fringes are usually indexed, with $i = 0$ for the fringe corresponding to the inflow velocity (density), positive increments where the airflow accelerates and negative where it decelerates. When the interferometer is set up in so-called *infinite fringe width* alignment (i. e., for zero flow velocity and thus no density perturbations the field appears uniformly illuminated with

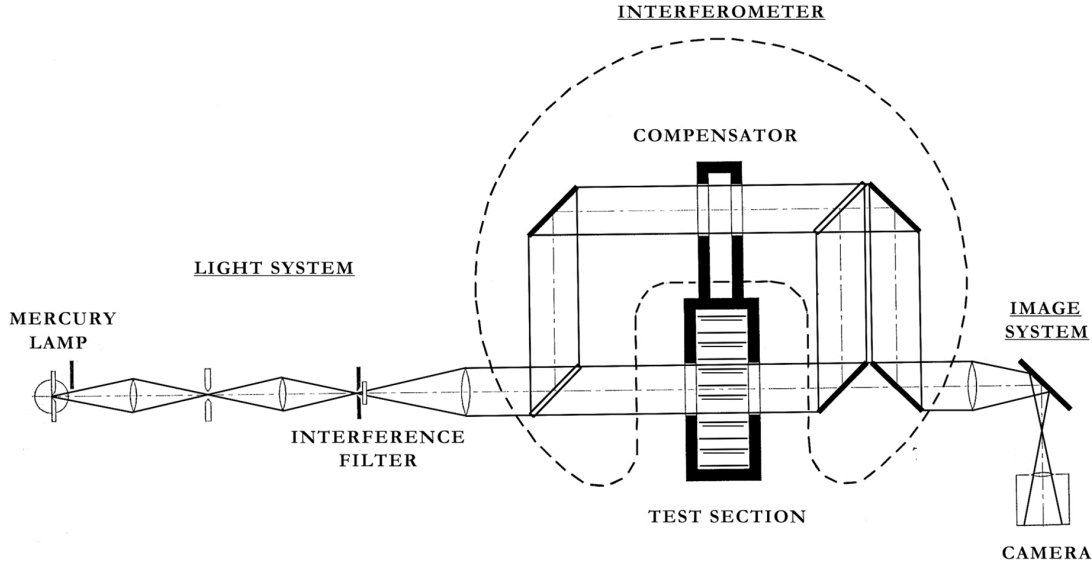


Figure 3.3: Schematic of the Mach-Zehnder interferometer in configuration used in author's measurements

no fringes), it can be derived from (3.12) that the difference between the densities $\rho^{(0)}$ and $\rho^{(i)}$ corresponding to the 0th and i th interferometric fringe is

$$\rho^{(0)} - \rho^{(i)} = i \frac{\lambda}{LK}, \quad (3.13)$$

where L is the test section width and λ the wavelength of the light source. For isentropic airflow,

$$\frac{p}{p_0} = \left(\frac{\rho}{\rho_0} \right)^\kappa \quad (3.14)$$

with $\rho_0 = p_0 / (RT_0)$, R the specific gas constant and T_0 the ambient thermodynamic temperature. In the case of a suction-type wind tunnel, the total pressure p_0 is approximately equal to the atmospheric pressure (neglecting the friction losses in the short inlet section of the channel). Combining (3.2) with (3.14) yields

$$\frac{\rho}{\rho_0} = \left(1 + \frac{\kappa - 1}{2} M^2 \right)^{\frac{\kappa - 1}{\kappa}}. \quad (3.15)$$

Setting $\rho = \rho^{(0)}$ and $M = M^{(0)}$, (3.15) is used for the calculation of the density $\rho^{(0)}$ at the zeroth fringe from the known inlet Mach number $M^{(0)}$ measured by a Pitot probe. Flow density $\rho^{(i)}$ in the subsequent fringes is then calculated from (3.13).

With the knowledge of the densities in the interferometric fringes, an approximation of the density distribution can be obtained by interpolation. Apparently, the spatial resolution of the method

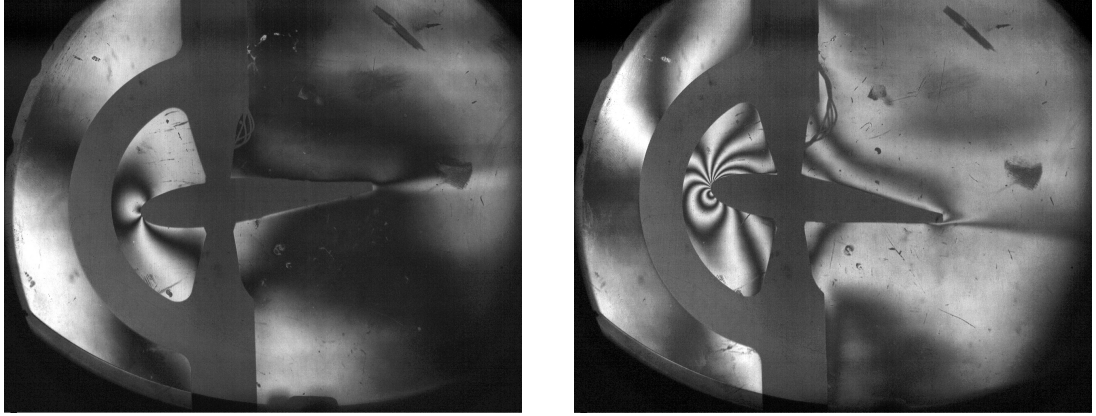


Figure 3.4: Interferograms obtained during wind-tunnel measurements an airfoil model during flutter instability. Inlet velocity $M = 0.23$ (left), $M = 0.4$ (right).

depends on the number of fringes present in the interferogram. The number of fringes increases with the Mach number, with the test section width L and with decreasing light wavelength λ . The difference in the number of the fringes for inlet flow velocity $M = 0.23$ and $M = 0.4$ can be seen in Fig. 3.4.

For the case of isentropic compressible flow of ideal gas, the pressure $p^{(i)}$ at a fringe with index i can be calculated from the total pressure p_0 , density ρ_0 and density at the 0th fringe $\rho^{(0)}$ as

$$p^{(i)} = p_0 \left(\frac{\rho^{(0)} - i \frac{\lambda}{LK}}{\rho_0} \right)^\kappa. \quad (3.16)$$

Using (3.2), the Mach number at fringe i is

$$M^{(i)} = \sqrt{\frac{2}{\kappa - 1} \left(\left(\frac{p^{(i)}}{p_0} \right)^{\frac{1-\kappa}{\kappa}} - 1 \right)}, \quad (3.17)$$

and the flow velocity

$$U^{(i)} = M^{(i)} \sqrt{\kappa R T^{(i)}} \quad (3.18)$$

with the local static temperature

$$T^{(i)} = T_0 \left(1 + \frac{\kappa - 1}{2} M^{(i)2} \right)^{-1}. \quad (3.19)$$

In reference-beam interferometric measurements, the mirrors, beam splitters and compensation glasses must be aligned perfectly in parallel to achieve the infinite fringe width configuration. Since

every mechanical movement of any part in the order comparable with the wavelength of the light, i. e. less than a micrometer, disturbs and influences the interferometric fringe pattern, high-precision and costly optical components are needed. Moreover, the setup is very sensitive and susceptible to misalignment e. g. due to thermal dilatation. Some of the challenging requirements are relieved in a modern variant called holographic interferometry, described in [Tropea et al. \(2007\)](#).

Compared to the PIV method, optical interferometry does not need any seeding particles. It can be well used in high subsonic, transonic and supersonic flows, where it might become difficult to satisfy requirement (3.11) on the tracer particles when employing PIV. On the contrary, for low Mach number flows, the spatial resolution of the reference-beam interferometry decreases rapidly. Unlike the PIV method, where the primary signal is the velocity vector map in a plane, interferometric methods measure the density, integrated along the path of the beam in the test section. For steady flows, 3D field can be obtained using tomographic techniques. Pressure and velocity magnitude fields may be calculated under the assumption of isentropic flow. However, the method has two specific drawbacks. First, it does not provide information on the direction of the flow. Second, a skilled operator with the knowledge of the flow physics is needed when using (3.13) to determine the regions of accelerating flow (increasing index) and decelerating flow (decreasing index). This seriously limits the possibility of fully automatic computer evaluation of the interferometric images.

Chapter 4

Application: Flow-structure interaction and flow-induced sound in human voice biomechanics

4.1 Introduction

A very complex case of internal flow on a moving geometry can be found in the biomechanics of human voice. From the technical point of view, human larynx in the phonatory configuration can be seen as a channel, whose cross-section varies in time due to interaction of the airflow with the elastic structures protruding from the channel wall. The sound, generated aerodynamically in the larynx, is then propagated and filtered in the vocal tract, radiated from mouth and perceived as voice.

There is no doubt that the possibility to produce voice is crucial for human communication, although many people do not realize this until they lose their voice temporarily (due to common respiratory inflammations) or permanently (after laryngeal cancers and various other vocal fold pathologies). Good knowledge and understanding of the processes and mechanisms which lead to healthy voice production is thus important and has extensive applications, e. g. for the development of voice prostheses for patients after total laryngectomy¹, training of voice professionals, pre-surgical predictions of voice quality, development of examination and therapeutic devices and others.

The fundamental physical processes of human voice production can be investigated either by measurements on physical models, excised larynges or living subjects, or by mathematical modeling. All of these approaches have their limitations, advantages and drawbacks, and to get a comprehensive understanding they have to be used concurrently. The current chapter summarizes the author's contributions in the field of human voice biomechanics. Section 4.2 explains the fundamental principles of voice production and laryngeal physiology, whose understanding is indispensable for any modeling efforts. In the next section, the author's own work in the field of mathematical modeling is summarized and given in context, starting with a simplified semi-analytic lumped-parameter

¹Surgical removal of larynx necessary after certain cancer types, approximately 30 000 patients per year worldwide. The contemporary substitute voice methods after total laryngectomy are the installation of the electrolarynx, tracheo-esophageal puncture or esophageal speech training, all of them producing unnatural and limited voice output.

model of vocal fold flow-induced vibrations, going over a 2D finite element model of laryngeal air-flow, a finite volume model solved on a large 3D grid on a parallel supercomputer, and ending with the results obtained using a hybrid aeroacoustic model solving both the incompressible fluid flow and the propagation of the flow-induced sound. The authors' publications on PIV measurements of airflow using two different physical models of vocal folds are reprinted and commented in section 4.4.

4.2 Physiology of human voice production

Human voice is created by passage of the airflow between vocal folds, which are located in the upper part of larynx (see Fig. 4.1, left). The vocal folds (also called vocal cords) are two symmetric soft tissue structures fixed between the thyroid cartilage and arytenoid cartilages; basically they are composed of the thyroarytenoid muscle (TA) and ligament covered by mucosa (see Fig. 4.1, right). The layers have very different material properties, with their elastic moduli varying by orders of magnitude. The three-layer model of vocal folds is only a simplified description, more detailed information can be found in the classical publication of Hirano et al. (1981) or in the monographs of Titze (1994, 2006).

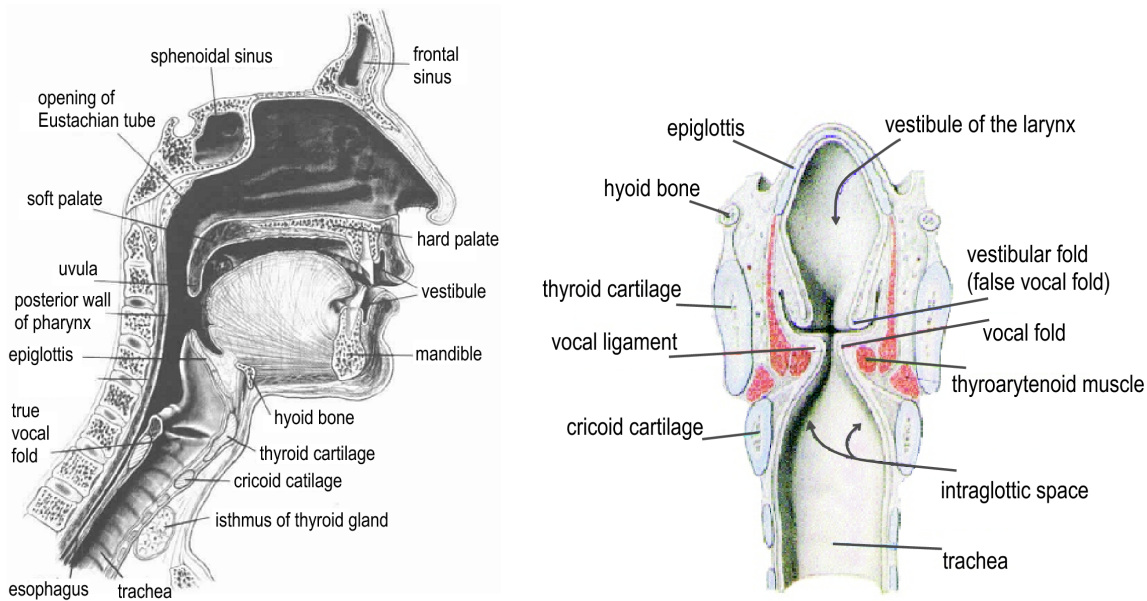


Figure 4.1: Scheme of the vocal tract in sagittal section (left) – the vocal folds are located in the region of the cricoid and thyroid cartilages. Detailed view of the larynx in coronal section (right) (Bunch, 1982).

When air is expired from the lungs, the constriction formed by the vocal folds (which is called the glottis) induces acceleration of the flow and creates underpressure. Under certain circumstances (subglottal pressure, glottal width, longitudinal tension in the TA and ligament), vocal fold oscillations may occur due to fluid-structure interaction. Creation of voice by vocal fold vibration is usually referred to as phonation. In regular loud phonation, the vocal folds collide and close the laryngeal channel completely, and the duration of the glottal closure may span a considerable part of

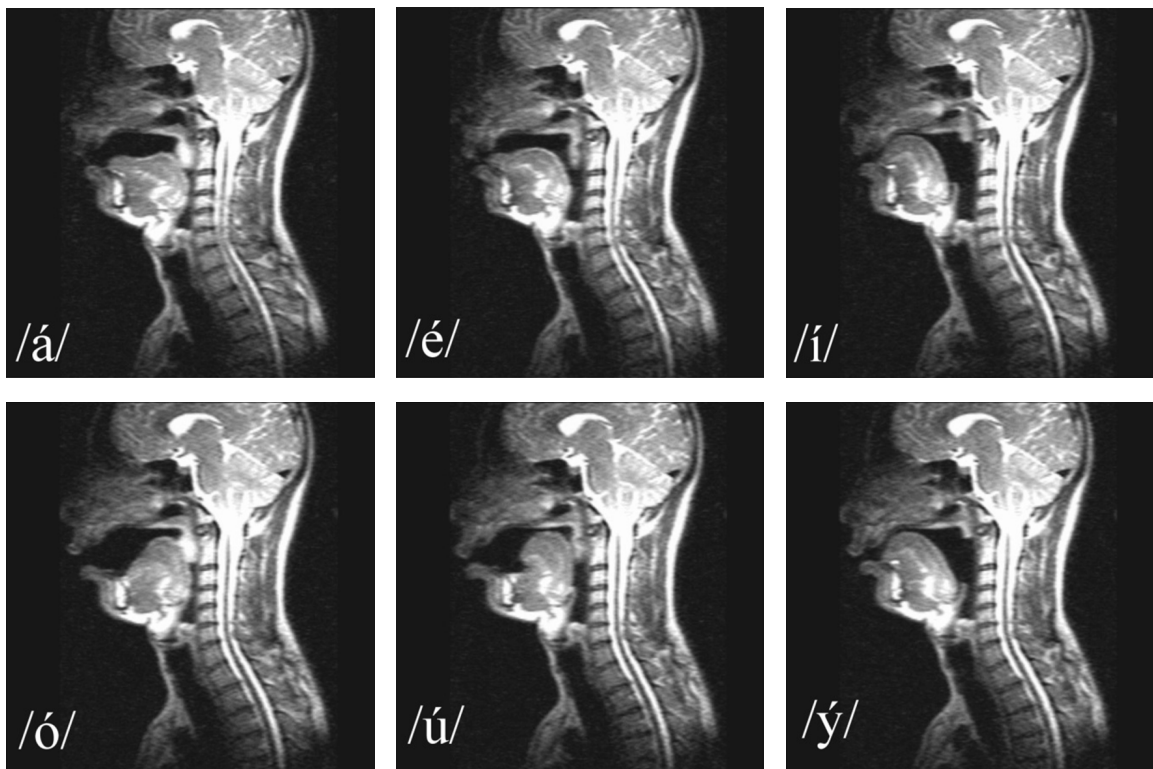


Figure 4.2: Magnetic resonance imaging (MRI) scans of the vocal tract during phonation of Czech vowels /a/, /ɛ/, /i/, /o/, /u/, /y/ (according to International Phonetic Alphabet, IPA)

the vibration period. When whispering or in breathy phonation, the vocal folds may vibrate without collisions. Even in the case of normal loud phonation, the vocal folds are capable of vibrating in different modes. The resulting voice is then classified into different registers, the two most important of them being the modal (chest) and falsetto registers. Independently of the voice pitch, the first two octaves (up to 350 Hz in men, approximately) are produced in the modal register, where the vocal folds vibrate as a whole, including the TA muscle and where the voice has ample, rich “color” (spectrum). When trying to reach higher frequencies, the vocal folds suddenly switch to falsetto register, where most of the vibration concentrates to the ligament and mucosa; the resulting voice color is rather “flat”. In training of the professional western-culture singers, a considerable effort is devoted to smooth the modal-falsetto transition – the subject tries to make the register switching as little audible as possible. In some other singing techniques like yodeling, on the contrary, the singer exploits the register transitions deliberately for artistic purposes.

In normal vocal fold vibration, there is a typical phase shift along the vertical axis: the inferior part of the vocal fold collides prior to the superior segment. In some rather irregular or pathological cases, longitudinal modes (2-0, 3-0 and higher) can be observed (Titze, 1994). For regular phonation, however, the vocal folds usually vibrate symmetrically and as a whole, i. e. in the 1-0 mode, with vibrational nodes at the anterior and posterior commissures and with the sole antinode in the middle.

The frequency of vibration is influenced by many factors, primarily by the longitudinal tension in the TA muscle and in the ligament. The periodical glottal closure modulates the airflow and

generates a sound with the fundamental frequency denoted usually F_0 . The spectrum of the acoustic signal also contains harmonic frequencies $f_k = k \cdot F_0$, $k = 2, 3, \dots$. Due to the turbulence, generated mainly in the shear layer of the jet, natural healthy voice always contains broadband noise of certain level.

The source sound produced by the vocal folds with vocal tract detached, which can be observed for example in experiments on excised larynges, does not resemble human voice; it can be compared to the sound produced when blowing a bird-call. Human voice results from the acoustic filtering of the source signal by the vocal tract. Based on the actual geometry of the vocal tract, which changes mainly by the posture of the tongue, certain frequencies in the spectrum are amplified and other suppressed: in this way, different vowels are generated from the same source signal. When pronouncing the vowels [a:] and [i:], for example, the source sound generated by the vocal folds is exactly the same; the difference is that for [a:] the tongue is retracted, forming a relatively large oral cavity (see Fig. 4.2). When producing the [i:] vowel, on the contrary, the tongue reduces the oral acoustic volume to minimum, which changes the resonance frequencies of the vocal tract completely. The vocal tract can be hence regarded as an acoustic filter, whose frequency response is determined by its dimensions and actual geometry.

It is necessary to note that the vocal fold vibration is a passive process. No sort of periodic muscle contraction is performed, the vibration is flow-induced. The onset of vocal fold vibration and the critical flow velocity to start the oscillations is highly sensitive to the material properties of the tissues involved, and also to the pre-phonatory geometry of the glottis, which is influenced by adduction of the arytenoids and activation of the TA muscle. For the development of physical vocal fold models and also for the purposes of mathematical modeling, it is important to know the shape of the vocal folds in phonatory position. Since the accurate data on the vocal fold geometry are still largely incomplete, our own measurement of the vocal fold shape from excised human larynges has been performed and published in a paper in *Journal of Biomechanics*, reprinted in the next section.

Reprints

- P. Šidlof, J. G. Švec, J. Horáček, J. Veselý, I. Klepáček, and R. Havlík. Geometry of human vocal folds and glottal channel for mathematical and biomechanical modeling of voice production. *Journal of Biomechanics*, 41(5):985–995, 2008



Journal of Biomechanics 41 (2008) 985–995

**JOURNAL
OF
BIOMECHANICS**

www.elsevier.com/locate/jbiomech
www.JBiomech.com

Geometry of human vocal folds and glottal channel for mathematical and biomechanical modeling of voice production

Petr Šidlof^{a,b,*}, Jan G. Švec^{c,d}, Jaromír Horáček^e, Jan Veselý^e, Ivo Klepáček^f, Radan Havlík^g

^a*Institute of Thermomechanics, Academy of Sciences of the Czech Republic, Dolejškova 5, 182 00 Prague 8, Czech Republic*

^b*Faculty of Mechatronics, Technical University of Liberec, Czech Republic*

^c*Faculty of Science, Department of Experimental Physics, Laboratory of Biophysics, Palacký University Olomouc, Olomouc, Czech Republic*

^d*Medical Healthcom, Ltd., Centre for Communication Disorders, Prague, Czech Republic*

^e*Institute of Thermomechanics, Academy of Sciences of the Czech Republic, Czech Republic*

^f*Anatomy Department, 3rd Faculty of Medicine, Charles University, Prague, Czech Republic*

^g*AUDIO-FON centr, Brno, Czech Republic*

Accepted 20 December 2007

Abstract

Current models of the vocal folds derive their shape from approximate information rather than from exactly measured data. The objective of this study was to obtain detailed measurements on the geometry of human vocal folds and the glottal channel in phonatory position. A non-destructive casting methodology was developed to capture the vocal fold shape from excised human larynges on both medial and superior surfaces. Two female larynges, each in two different phonatory configurations corresponding to low and high fundamental frequency of the vocal fold vibrations, were measured. A coordinate measuring machine was used to digitize the casts yielding 3D computer models of the vocal fold shape. The coronal sections were located in the models, extracted and fitted by piecewise-defined cubic functions allowing a mathematical expression of the 2D shape of the glottal channel. Left–right differences between the cross-sectional shapes of the vocal folds were found in both the larynges.

© 2008 Elsevier Ltd. All rights reserved.

Keywords: Vocal fold geometry; Glottal channel shape; Quantitative description

1. Introduction

Vocal fold geometry plays an important role in phonation as it influences the vibratory pattern of the vocal folds (Alipour and Scherer, 2000; Titze and Story, 2002). From the technical point of view, the vocal fold shape is directly related to the mass distribution in the vibrating elastic element, which influences strongly the vibration eigenmodes (Döllinger et al., 2005a; Horáček et al., 2005; Zhang and Jiang, 2005; Berry, 2001). Besides, vocal folds constitute the channel profile and thus their shape has a dramatic impact on glottal aerodynamics—a small variation of the vocal fold shape or position may change the flow regime and the resulting aerodynamic forces, which

excite the system (Li et al., 2006; Thomson et al., 2005; Vilain et al., 2004).

Quantitative information on the phonatory shape of human vocal folds has been scarce. Accurate data are lacking, especially on the coronal cross-sectional shape of the vocal folds and no comprehensive dataset specifying the geometry of the entire glottal channel has been published so far. Scientists developing mathematical and physical models of the vocal folds and glottal flow and studying vocal fold deformation or glottal fluid–structure interaction (Scherer et al., 2002; Rosa et al., 2003; Kob et al., 2005; Thomson et al., 2005; Erath and Plesniak, 2006a, b; Fulcher et al., 2006) are therefore forced to base their channel geometries on incomplete and somewhat arbitrary information.

First notable studies regarding vocal fold geometry were published in the 1960s by Hollien and Curtis (1960), Hollien et al. (1968), Hollien and Colton (1969) who measured the

*Corresponding author. Tel.: +420 266 053 442; fax: +420 286 584 695.
E-mail address: sidlof@it.cas.cz (P. Šidlof).

vocal fold cross-sectional area and thickness in vivo with the aid of X-ray laminagraphy. Despite the technological progress in medical imaging techniques in the last decades, the standard non-invasive 3D imaging methods such as CT or MRI have been problematic to use for the purposes of capturing and measuring the phonatory geometry of the vocal folds in living human subjects. When the vocal folds are vibrating, their shape cannot be accurately measured using these, and the shape of vocal folds in breathing position is largely changed (Hirano, 1975). Up to present, the only detailed data on vocal fold geometry have been obtained from excised larynges rather than living vocal folds.

Berry et al. (2001b) succeeded as the first in measuring the vocal fold geometry in excised canine larynges using lead molds. However, the molds only allowed measuring the medial surface of the vocal folds within the convergent part of the glottis. As an alternative method, Berry et al. (2001a) developed a technique for stereoscopic observation of the medial surface of the vocal fold in a hemilarynx using a plexiglass and a prism. This method, in combination with high-speed imaging technique, has proven to be able to bring highly useful data, especially on the vocal fold trajectories and variation of the coronal shape of the vocal fold during vibration (Döllinger et al., 2005; Döllinger and Berry, 2006a; Zhang et al., 2006). These studies, however, have not offered the complete mathematically defined shape of the prephonatory glottal channel.

The primary goal of this study was to obtain information on the static prephonatory shape of the vocal folds and the glottal channel from excised human larynges, which could be directly used, e.g. for construction of aerodynamic models of vocal folds and glottal airways. A plaster-casting methodology was used to capture the shape of the glottal airflow channel. The casts were digitized on a coordinate measuring machine (CMM) and reconstructed in 3D modeling software. Finally, the cross-sectional shapes of the glottal channel were fitted with a piecewise polynomial function resulting in 2D mathematical models of the glottal geometry.

2. Material and methods

After obtaining approvals of the Ethical committee of the Czech Medical Chamber from the Faculty Hospital in Brno (dated February 10, 1999) and the Ethical committee of the Faculty Hospital of the 1st Faculty of Medicine of Charles University in Prague (dated March 4, 2002), 17 excised human larynges were obtained from the hospital Bulovka in Prague and the Anatomy Department of the 1st Faculty of Medicine. The larynges were quick frozen in liquid nitrogen and kept in a freezer at about -20°C . For the purpose of the current study 10 of the larynges were used, eight of which were able to produce phonation. Before testing, the larynges were immersed in saline solution for several hours for slow defrosting at room temperature.

Two out of the eight larynges were analyzed successfully—larynx no. 8 (female, 72 years) and larynx no. 10 (female, 69 years). Both the larynges were found free of pathology. In both cases, the shape of the vocal folds at two different phonatory configurations (low and high longitudinal tension of the vocal folds, i.e., low and high fundamental frequency of phonation) was evaluated. The experimental setup was similar to the one used in previous studies of Vilkman (1987) and Horáček et al. (2001). The procedure for preparation of the laryngeal casts was the following: the soft tissues superior

to the vocal folds were removed, including the ventricular folds. The larynx was mounted on a base plate by means of steel pins that were pushed through the external tissue at the lower part of the larynx and pressed against the plate by a metal ring to attain an airtight junction (see Fig. 1). The arytenoid cartilages were fixed in a holder *H* and the adduction of the vocal folds was adjusted via screw *SC*. Then, the airflow was switched on and the passive tension of the vocal folds was adjusted by manipulating the position of the thyroid cartilage at point *T* until the vocal folds produced stable sustained vibrations. The configuration was fixed by the needles *N* (see Fig. 1). The airflow, humidified and warmed up to 37°C , was blown up through the larynx into open space.

The vocal fold vibrations were monitored using laser vibrometry (Polytec OFV 302), videostroboscopy (B&K 4913 stroboscope unit) and the generated sound was measured by a sound level meter (B&K 2239). Simultaneously, the subglottal pressure was recorded using dynamic pressure transducers. Fig. 2 shows the signals measured on larynx no. 8 just before casting. After recording the signals, the airflow was stopped and a thin mixture of dental plasters, especially suited for casting purposes (10% Dental Rapid alabaster plaster—Bergard, Germany, 20% Mramorit hard stone plaster—Dental Prague, Czech Republic, 70% Superstone hard IV class plaster—Bergard Germany) was slowly poured into the larynx from above. When the mixture hardened (typically 5–10 min), the fixed larynx was turned upside down and the plaster was poured into the subglottal space. A metal bridge was used to join the upper and lower parts of the casts in order to fix their exact position with respect to each other. Since a small gap was present between the vocal folds, the plaster could fill the space and tightly connect the upper and lower parts of the cast.

After hardening, the bridge was disassembled and the plaster cast was broken into supraglottal and subglottal parts and removed from the larynx. The special type of plaster yielded a clean break between the parts

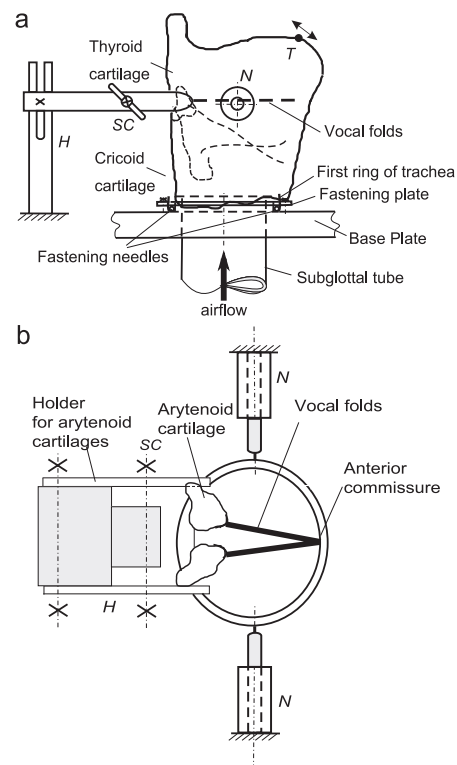


Fig. 1. Fixation of the larynx on the base plate.

with a minimal damage around the rupture. This allowed reassembling the two parts in their original position using the metal bridge. The whole procedure is shown in Fig. 3.

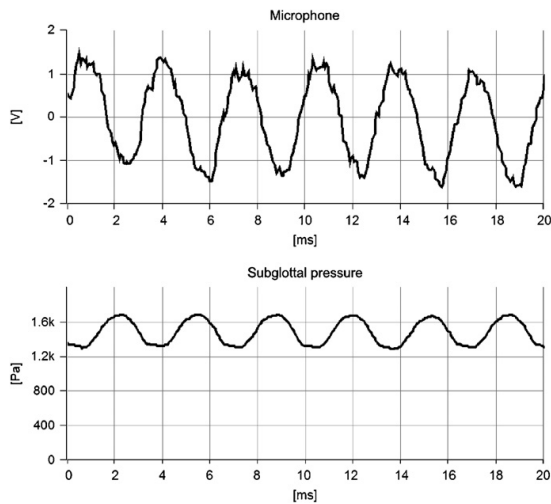


Fig. 2. Microphone and subglottal pressure signals recorded from the larynx no. 8 just before the casting procedure.

Since the larynx was not damaged during the casting procedure, after a bath and rehydration in saline solution the larynx was capable of phonating again. The vibration pattern appeared similar to the pattern before casting. When the fixation screws and needles were adjusted and phonation at a different frequency achieved, it was possible to create another cast of the same larynx.

2.1. Digitizing the casts for the 3D computer model

The vocal fold plaster casts were digitized using the Wenzel LH-87 mechanical bridge-type CMM. With the scanning probe head, CMM can measure complex surfaces with high density (approximately 30 samples/mm) and precision of up to 1 μm . Since the instrument required the surface to be accessible from one direction, the subglottal and supraglottal parts of the cast needed to be measured separately and then reassembled digitally. After digitization, the entire glottal space was reconstructed in the Rhino 3D NURBS modeling software. The whole procedure used for determination of the vocal fold geometry is demonstrated in Fig. 4.

2.2. Determination of the vocal fold shape in 2D sections

To obtain 2D models of the cross-sectional shapes of the vocal folds, the coronal sections, taken from the 3D computer vocal fold model (Fig. 4c), were used. The membranous glottal length L_m was determined from the videostroboscopic records. The coordinate system was defined in the following way (see Fig. 5): x denotes the inferior–superior axis (along the thickness T of the vocal folds), with positive values rising in the superior direction, y -axis is in the medial–lateral

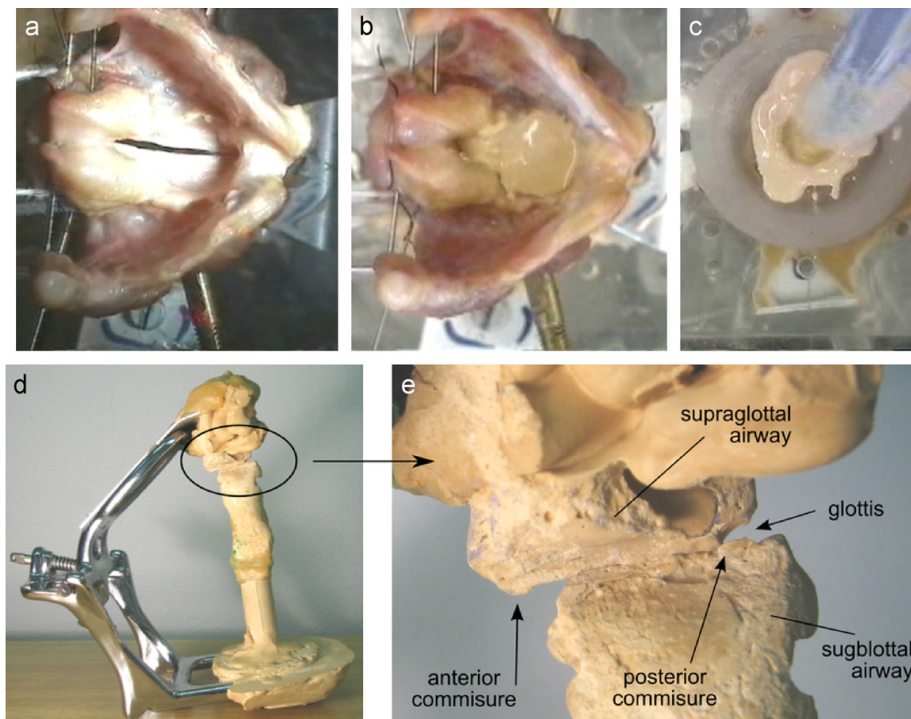


Fig. 3. Preparation of the vocal fold casts: (a) the larynx with the vocal folds in phonation position before casting, (b) plaster filling the supraglottal space of the larynx, (c) plaster filling the subglottal space of the larynx, (d) the final supraglottal and subglottal casts fixed together, (e) detailed lateral view of the glottal region of the cast (color online).

988

P. Šidlof et al. / Journal of Biomechanics 41 (2008) 985–995

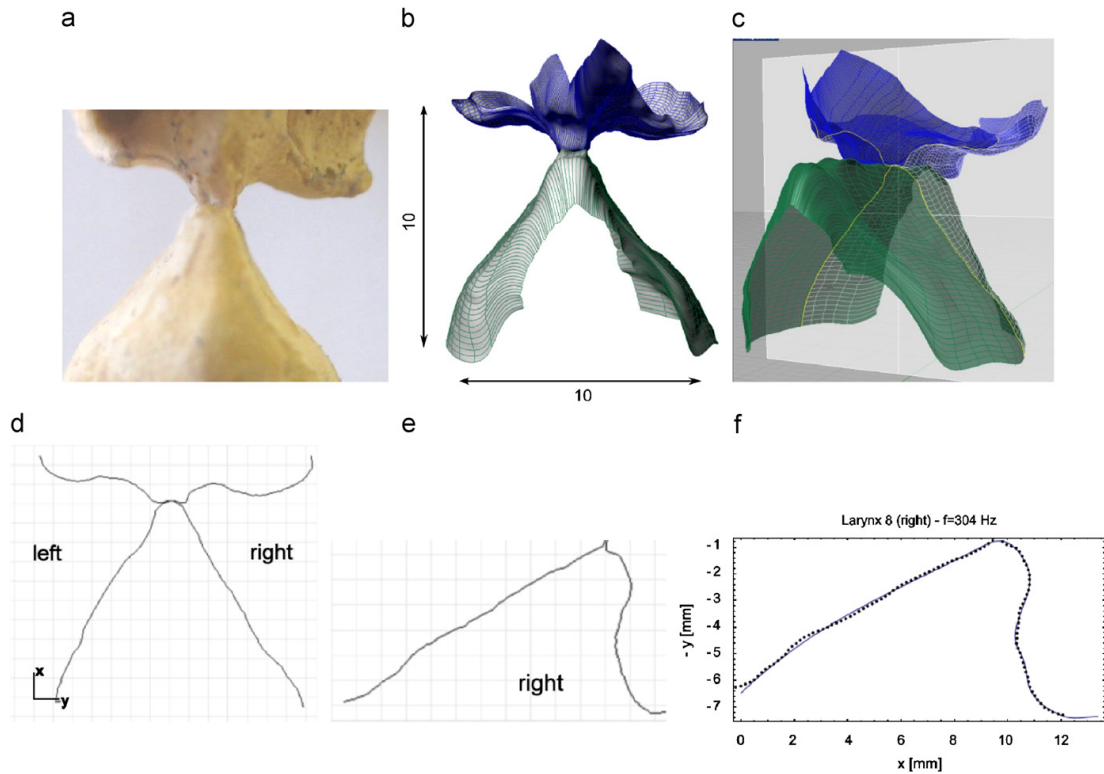


Fig. 4. Determination of the vocal fold geometry: (a) detailed frontal view of the plaster cast of the glottal channel, (b) the 3D computer model, (c) location of the mid-membranous coronal section, (d) the 2D geometry of that coronal section, (e) the right part of the coronal section corresponding to the shape of the right vocal fold, (f) the regression curve representing the best mathematical fit of the glottal channel shape (color online).

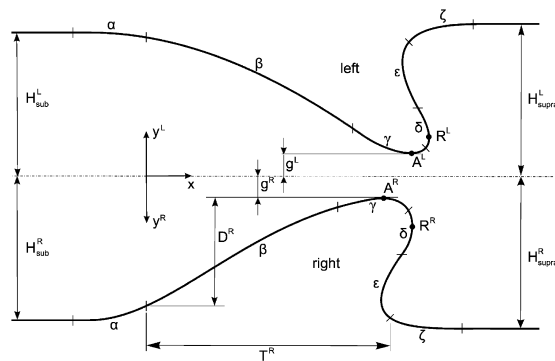


Fig. 5. Geometric definitions in the 2D mathematical description of the glottal channel: segments α – ζ , depth D , thickness T , apex A , “perpendicularity point” R , glottal half-aperture g , asymptotic channel depths H_{sub} and H_{supra} . Superscripts R and L indicate the right and left parts, respectively.

direction (along the depth D of the vocal folds), and z denotes the anterior–posterior axis (along the length L of the vocal folds, perpendicular to the figure plane).

Smooth piecewise-defined third-order polynomials (cubic splines) were used as the regression functions. The glottal channel geometry was described by two curves $\{x, y_R\}$, $\{x, y_L\}$ for the right and left vocal folds, respectively, each consisting of six consecutive segments α – ζ (Fig. 5). The shape in segments α , β , γ , and ζ was expressed as a function $y(x)$. Since the vocal fold contour reverses direction in segments δ and ϵ , it was defined here as a function $x(y)$, instead. The regression curves, lying within the segments β – ϵ , were completed by the downstream and upstream segments α and ζ , using the approximate data on the inferior and superior end of the glottal channel measured manually from the physical casts. Thus, the whole curve can be expressed in this form:

$$\begin{aligned}
 y(x) &= \text{const.} = H_{sub}, & x \leq X_{\alpha-}, \\
 y(x) &= \alpha_3 x^3 + \alpha_2 x^2 + \alpha_1 x + \alpha_0, & X_{\alpha-} < x \leq X_{\beta\gamma}, \\
 y(x) &= \beta_3 x^3 + \beta_2 x^2 + \beta_1 x + \beta_0, & X_{\beta\gamma} < x \leq X_{\gamma\delta}, \\
 y(x) &= \gamma_3 x^3 + \gamma_2 x^2 + \gamma_1 x + \gamma_0, & X_{\beta\gamma} < x \leq X_{\gamma\delta}, \\
 x(y) &= \delta_3 y^3 + \delta_2 y^2 + \delta_1 y + \delta_0, & Y_{\gamma\delta} < y \leq Y_{\delta\epsilon}, \\
 x(y) &= \epsilon_3 y^3 + \epsilon_2 y^2 + \epsilon_1 y + \epsilon_0, & Y_{\delta\epsilon} < y \leq Y_{\zeta+}, \\
 y(x) &= \zeta_3 x^3 + \zeta_2 x^2 + \zeta_1 x + \zeta_0, & X_{\zeta+} < x \leq X_{\zeta+}, \\
 y(x) &= \text{const.} = H_{supra}, & x > X_{\zeta+},
 \end{aligned}
 \tag{1}$$

where α_i, \dots, ζ_i , $i = 0, 1, 2, 3$ are the spline parameters, $X_{\lambda\mu}$, $Y_{\lambda\mu}$ represent the coordinates of the boundary between segments λ and μ , and $X_{\zeta-}$, $X_{\zeta+}$ stand for left and right boundaries of segments α , ζ , respectively. Defining the thickness T and the depth D of the vocal folds is challenging, since there are no sharp edges or distinct physiological margins of the vocal folds. In the mathematical model the thickness T was defined as the horizontal distance from the α/β segment boundary to the ϵ/ζ boundary (Fig. 5). The depth D was similarly defined as the vertical distance from the α/β segment boundary to the apex A . Furthermore, these definitions were used:

- The channel x -axis was set so that $g_L \approx g_R$ and that the 3D vocal fold contours were approximately symmetrical with respect to the sagittal plane. The inferior and superior margins of the glottal channel (i.e., $X_{\alpha-}$, $X_{\zeta+}$) were recognized as the approximate locations where the vocal fold surface begins to flat off to the straight subglottal or supraglottal tract wall.
- The inferior and superior vocal fold margins (i.e., the α/β and ϵ/ζ boundary in Fig. 5) were manually located on the casts as the points where the cast surface changes its curvature and starts to approach

the subglottal or supraglottal space. These points were not always clearly evident in the casts and some arbitrariness could not be avoided here.

- The boundaries between the segments β/γ and δ/ϵ were determined automatically by the nonlinear regression algorithm as the points which yielded the best fit.

For all the regression variables, statistical parameters such as confidence intervals and correlation matrices were calculated. However, the most convenient verification of the regression quality of the model was found to be the visual comparison of the regression curve to the measured data (see Fig. 6).

3. Results

For the larynxes no. 10 vibrating at the frequency of 308 Hz, no. 10 at 676 Hz, and no. 8 at 148 Hz, the vocal channel geometries were described as single 2D coronal

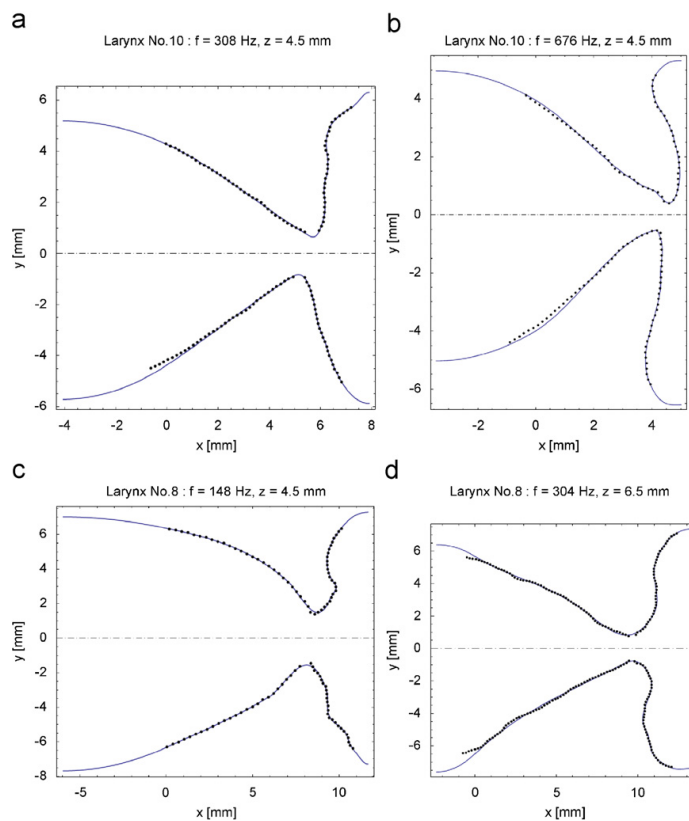


Fig. 6. (a) Geometry of the mid-membranous coronal section of the glottal channel for larynx no. 10 (female, 69 years) vibrating at lower frequency $F_0 = 308$ Hz. Mean subglottal pressure $p_{\text{sub}} = 1830$ Pa, membranous glottal length $L_m = 8.0$ mm. Points measured by the CMM are shown together with the regression curves. The left vocal fold is on the top and the right one on the bottom. The channel axis is dashed. The same configuration holds also for all the following figures. (b) Geometry of the mid-membranous coronal section of the glottal channel for larynx no. 10 (female, 69 years) vibrating at higher frequency $F_0 = 676$ Hz. Mean subglottal pressure $p_{\text{sub}} = 3150$ Pa, membranous glottal length $L_m = 8.4$ mm. (c) Geometry of the mid-membranous coronal section of the glottal channel for larynx no. 8 (female, 72 years) vibrating at lower frequency $F_0 = 148$ Hz. Mean subglottal pressure $p_{\text{sub}} = 578$ Pa, membranous glottal length $L_m = 9.0$ mm. (d) Geometry of the mid-membranous coronal section of the glottal channel for larynx no. 8 (female, 72 years) vibrating at higher frequency $F_0 = 304$ Hz. Mean subglottal pressure $p_{\text{sub}} = 1470$ Pa, membranous glottal length $L_m = 12.75$ mm.

sections only, taken in the middle of the membranous vocal fold length. For the purposes of 3D modeling, eight coronal sections along the anterior–posterior axis z were analyzed for the larynx no. 8 vibrating at 304 Hz, with a step of $\Delta z = 1$ mm. The origin of the z -axis was set to the anterior commissure ($z = 0$). The location of the mid-membranous section for larynx no. 8 at 304 Hz corresponds to $z = 6.5$ mm. As can be seen on the cast in Fig. 3e, the subglottal and supraglottal airways are shifted with respect to each other when observed laterally: the subglottal channel spans approximately from $z = -2$ to 4 mm while the supraglottal channel from $z = 2$ to 19 mm. Therefore, it was possible to extract the 2D sections in the interval $z = 4.5$ –11.5 mm only.

The measured points and the regression splines for the mid-membranous coronal sections of the larynx no. 10 at $F_0 = 308$ and 676 Hz are demonstrated in Fig. 6a and b, respectively. Fig. 6c and d provide the results for the larynx no. 8 at $F_0 = 148$ and 304 Hz. Multiple coronal sections obtained from the larynx no. 8 at $F_0 = 304$ Hz are shown together in Fig. 7. Tables 1 and 2 provide the regression parameters for all the analyzed glottal contours. Table 3 lists the coordinates of the segment boundaries and provides the values of selected geometrical parameters: the vocal fold thickness T and depth D , minimum glottal half-aperture g (distance from the vocal fold apex to the channel axis), x -coordinate of the vocal fold apex A and the coordinates of the “perpendicularity point” R (location where the upper vocal fold surface becomes perpendicular to the x -axis, see Fig. 5).

4. Discussion and conclusion

A new methodology for determining the vocal fold shape from excised larynges was developed. Excised human larynges, which were quick frozen and later gradually thawed in saline solution, were used. According to Tayama et al. (2002), the freezing and thawing procedures should not affect the geometry of excised larynges significantly. Plaster casts were used to capture the shape of the vocal folds in phonatory position. The surface roughness of the casts was lower than 0.05 mm, only on a few locations there were artifacts where the surface quality was locally deteriorated by presence of small (<0.5 mm) voids of unknown origin. The casting method made it possible to remove the plaster material from the larynx without destroying the larynx itself and therefore could be used to create two casts from the same larynx in different configurations. The main advantage of the method was that it allowed capturing the shape of the whole vocal folds, i.e., the inferior, medial as well as the superior surfaces, including the adjoining vocal tract. The accuracy of the vocal fold shape determination was dependent on the quality of the plaster casts, proper disassembling and reassembling of the cast, and on the accuracy of the cast analysis. Combination of various technical issues along this chain caused that only a small number of larynges measured (two out of eight) could have been accurately analyzed. Among the other six larynges, some of them were not capable of phonating regularly or at both frequencies, in some of them a non-demountable holder was used, which prevented measuring the contours by

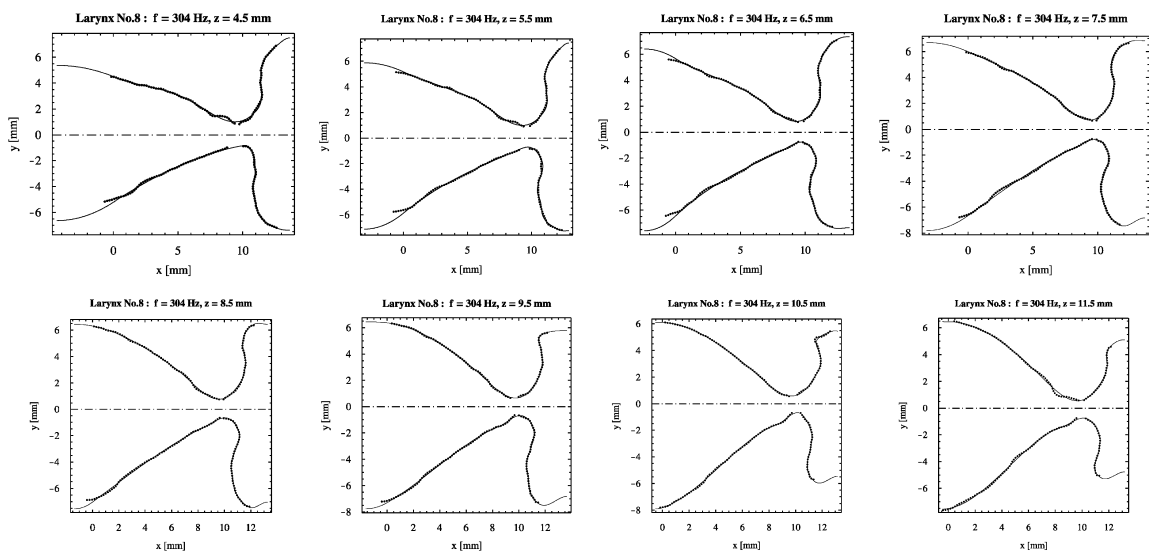


Fig. 7. Shapes of eight coronal sections through the glottal channel, larynx no. 8 vibrating at higher frequency $F_0 = 304$ Hz. Mean subglottal pressure $p_{\text{sub}} = 1470$ Pa.

Table 1
Spline parameters $\alpha_0, \dots, \gamma_0, \dots, \gamma_3$ describing the glottal channel geometry for all the sections analyzed (see Eq. (1))

	α_0	α_1	α_2	α_3	β_0	β_1	β_2	β_3	γ_0	γ_1	γ_2	γ_3
No. 10—308 Hz, $z = 4.5$ mm (mid-membranous)												
Left	4.275993	-0.4531229	-0.0557414	0.0000000	4.275993	-0.4531229	-0.0773585	0.00775016	-651.19605	358.01372	-65.423889	3.9785210
Right	4.358565	-0.6616203	-0.0813899	0.0000000	4.358565	-0.6616203	-0.0320538	0.00471844	-197.36708	125.33255	-26.263262	1.8251095
No. 10—676 Hz, $z = 4.5$ mm (mid-membranous)												
Left	3.956262	-0.5889571	-0.0858372	0.0000000	3.956262	-0.5889571	-0.1906315	0.03619953	-321.44355	227.62234	-53.353519	4.1480066
Right	3.996595	-0.6044812	-0.0880997	0.0000000	3.996595	-0.6044812	-0.2743482	0.05268842	1285.12215	-862.22941	191.797484	-14.1251673
No. 8—148 Hz, $z = 4.5$ mm (mid-membranous)												
Left	6.366587	-0.2182768	-0.0182805	0.0000000	6.366587	-0.2182768	0.0005478	-0.00451026	-153.28401	63.94616	-8.549997	0.3729682
Right	6.321931	-0.4555631	-0.0381530	0.0000000	6.321931	-0.4555631	0.0065934	-0.00214442	-59.88495	29.81463	-4.549309	0.2228234
No. 8—304 Hz, $z = 4.5$ mm												
Left	4.508483	-0.3960938	-0.0455807	0.0000000	4.508483	-0.3960938	0.0638564	-0.00838648	-5.47126	4.50055	-0.737004	0.0352745
Right	5.216338	-0.6511770	-0.0749346	0.0000000	5.216338	-0.6511770	0.0172239	0.00042127	-1445.05514	435.67192	-43.739606	1.4631448
No. 8—304 Hz, $z = 5.5$ mm												
Left	5.176557	-0.4638754	-0.0766924	0.0000000	5.176557	-0.4638754	0.0427497	-0.00518064	-6.29406	5.15428	-0.856918	0.0416036
Right	5.882271	-0.8198576	-0.1355468	0.0000000	5.882271	-0.8198576	0.0468596	-0.00187714	-187.80142	63.91442	-7.165113	0.2659487
No. 8—304 Hz, $z = 6.5$ mm (mid-membranous)												
Left	5.670004	-0.6193288	-0.1299379	0.0000000	5.670004	-0.6193288	0.0753278	-0.00854395	-13.18546	7.94874	-1.222472	0.0569816
Right	6.460492	-0.9495921	-0.1992286	0.0000000	6.460492	-0.9495921	0.0678481	-0.003332679	-153.25026	53.56176	-6.133961	0.2318685
No. 8—304 Hz, $z = 7.5$ mm												
Left	5.985282	-0.4413701	-0.0690161	0.0000000	5.985282	-0.4413701	0.0054135	-0.00259468	-13.56730	8.32036	-1.287163	0.0599742
Right	6.653765	-0.7226027	-0.1129918	0.0000000	6.653765	-0.7226027	-0.0026527	0.00165408	-141.19253	49.84461	-5.745641	0.2181198
No. 8—304 Hz, $z = 8.5$ mm												
Left	6.316027	-0.1992095	-0.0727758	0.0000000	6.316027	-0.1992095	-0.0616439	0.00196450	-16.58697	9.51536	-1.417926	0.0640784
Right	7.036246	-0.7473088	-0.2730092	0.0000000	7.036246	-0.7473088	-0.0031016	0.00143260	-163.30385	55.33964	-6.144305	0.2249870
No. 8—304 Hz, $z = 9.5$ mm												
Left	6.365809	-0.1003164	-0.0315522	0.0000000	6.365809	-0.1003164	-0.0853733	0.00310266	-14.47671	8.62039	-1.290868	0.0580494
Right	7.298733	-0.5733478	-0.1803334	0.0000000	7.298733	-0.5733478	-0.0576905	0.00529590	-163.91142	55.76264	-6.200423	0.2270198
No. 8—304 Hz, $z = 10.5$ mm												
Left	6.091072	-0.0112244	-0.0108938	0.0000000	6.091072	-0.0112244	-0.1108507	0.00507821	-11.62734	7.44421	-1.146510	0.0524690
Right	7.820425	-0.3323614	-0.3225719	0.0000000	7.820425	-0.3323614	-0.1343454	0.01028933	-266.84356	88.49469	-9.651662	0.3477628
No. 8—304 Hz, $z = 11.5$ mm												
Left	6.445661	0.0343574	0.2744010	0.3578040	6.445661	0.0343574	-0.1246640	0.00514541	-6.58054	5.80844	-0.972619	0.0463567
Right	7.513060	-0.1540328	-0.1757441	0.0000000	7.513060	-0.1540328	-0.1791963	0.01328831	-149.41784	50.47668	-5.578419	0.2032553

All the lengths are in millimeters.

992

P. Šidlof et al. / Journal of Biomechanics 41 (2008) 985–995

Table 2
Spline parameters $\delta_{0,3}$ – $\zeta_{0,3}$ describing the glottal channel geometry for all the sections analyzed (see Eq. (1))

	δ_0	δ_1	δ_2	δ_3	ϵ_0	ϵ_1	ϵ_2	ϵ_3	ζ_0	ζ_1	ζ_2	ζ_3
No. 10–308 Hz, $z = 4.5$ mm (mid-membranous)												
Left	3.92430	3.260647	-1.543763	0.2374805	-4.29246	8.36779	-2.182927	0.1873431	1081.7439	-432.1432	57.70806	-2.5617917
Right	3.93548	2.161231	-0.889548	0.1326607	2.38969	2.44339	-0.566927	0.0510165	-70.2824	23.8170	-2.36951	0.0727518
No. 10–676 Hz, $z = 4.5$ mm (mid-membranous)												
Left	4.35410	0.990559	-0.481293	0.0618155	-2.56049	7.19993	-2.251796	0.2170428	-77.5176	49.1639	-9.72546	0.6412352
Right	3.62260	1.487330	-0.970613	0.1985575	2.63021	1.74295	-0.557470	0.0509429	-88.5801	58.1349	-11.83745	0.8031357
No. 8–148 Hz, $z = 4.5$ mm (mid-membranous)												
Left	27.29210	-22.468381	9.212039	-1.2213611	16.19069	-3.54021	0.541789	-0.0213214	-106.8595	25.7014	-1.88964	0.0450271
Right	-4.23440	11.040711	-2.988854	0.2688979	-111.02762	61.58361	-10.458382	0.5953474	1482.2524	-404.6750	36.86596	-1.1156563
No. 8–304 Hz, $z = 4.5$ mm												
Left	5.80626	5.356488	-1.701710	0.1809945	9.07316	1.97650	-0.536123	0.0470190	845.1023	-198.1806	15.55545	-0.4052909
Right	9.12789	1.822854	-0.574223	0.0563049	-37.16235	25.63073	-4.573840	0.2741702	-140.2510	30.8202	-2.13822	0.0492797
No. 8–304 Hz, $z = 5.5$ mm												
Left	6.81665	3.779490	-1.044679	0.0919291	14.23137	-1.20679	0.073052	0.0084117	1441.3054	-353.3610	28.93729	-0.7877166
Right	7.76565	3.438234	-1.195542	0.1260979	-28.47353	21.46167	-3.927943	0.2405863	-1368.7689	324.5308	-25.50884	0.6682373
No. 8–304 Hz, $z = 6.5$ mm (mid-membranous)												
Left	7.10477	3.445437	-0.937147	0.0808829	-29.17020	20.26277	-3.455280	0.2008116	-254.3748	56.4325	-4.04933	0.0966861
Right	7.90034	3.212825	-1.100932	0.1123805	-41.51771	27.02679	-4.687434	0.2724632	-396.5633	93.6445	-7.22894	0.1858257
No. 8–304 Hz, $z = 7.5$ mm												
Left	8.73819	1.860063	-0.435532	0.0307918	3.14652	5.94356	-1.429565	0.1114500	-384.8130	88.1318	-6.60783	0.1650732
Right	8.58004	2.478601	-0.845587	0.0836012	-21.03413	16.15870	-2.800990	0.1643040	-609.3961	145.5034	-11.40045	0.2965695
No. 8–304 Hz, $z = 8.5$ mm												
Left	8.90206	1.699121	-0.301535	0.0104124	3.80570	5.83781	-1.421860	0.1115013	-1017.1006	237.9552	-18.42668	0.4753148
Right	8.87091	2.683218	-0.984842	0.1044630	-4.87986	8.62390	-1.614656	0.1018986	-1030.3988	246.8547	-19.53203	0.5140165
No. 8–304 Hz, $z = 9.5$ mm												
Left	9.48010	1.399324	-0.242269	0.0085498	-230.24825	149.30439	-30.659890	2.0937416	-126.7778	29.3821	-2.17093	0.0534641
Right	9.15055	2.301508	-0.815617	0.0831572	-13.36511	12.67074	-2.231539	0.1316286	-530.1418	127.3434	-10.01369	0.2612746
No. 8–304 Hz, $z = 10.5$ mm												
Left	10.22625	0.327278	0.265649	-0.0634394	-25.14644	28.47898	-7.202620	0.5969711	-3099.8896	714.2984	-54.76370	1.3994278
Right	10.31172	0.252636	0.214847	-0.0668813	7.85980	3.18578	-0.951825	0.0874508	-771.4565	187.9437	-15.10477	0.4034472
No. 8–304 Hz, $z = 11.5$ mm												
Left	10.15122	0.456414	0.224207	-0.0615776	-1.81770	11.80846	-3.364771	0.3166432	-266.6618	57.1931	-3.98583	0.0918767
Right	9.09843	2.179248	-0.662795	0.0603599	-0.35812	9.98342	-2.784166	0.2497025	-641.8529	156.8240	-12.62902	0.3378424

All the lengths are in millimeters.

Table 3

Segment boundaries X_{z-} to X_{z+} , subglottal and supraglottal channel heights $H_{\text{sub/supra}}$, vocal fold thicknesses and depths T , D , orifice half heights g and apex and reflection point coordinates A_x , R_x , R_y for all the sections analyzed (see Eq. (1), Fig. 5)

	X_{z-}	$X_{z\beta}$	$X_{z\beta'}$	$X_{z\delta}$	$Y_{z\delta}$	$Y_{z\delta c}$	$X_{z\zeta}$	$Y_{z\zeta}$	X_{z+}	H_{sub}	H_{supra}	T	D	g	A_x	R_x	R_y	
No. 10—308 Hz, $z = 4.5$ mm (mid-membranous)																		
Left	-3.43066	0.00	5.48496	6.14796	1.52095	2.96251	7.22466	5.72789	7.90	4.97	6.31	7.22	3.62	0.65	5.71	6.18	1.82	
Right	-3.43066	0.00	4.79990	5.71480	1.79025	3.01629	6.82270	5.02012	7.90	5.03	5.86	6.82	3.54	0.82	5.14	N/A	N/A	
No. 10—676 Hz, $z = 4.5$ mm (mid-membranous)																		
Left	-5.97021	0.00	4.03835	4.89370	0.87477	2.74320	4.12814	4.81203	5.01	7.02	5.32	4.13	3.55	0.41	4.59	4.97	1.41	
Right	-5.97021	0.00	4.14882	4.31087	0.86287	2.13609	3.94520	5.84534	5.01	7.68	6.55	3.95	3.47	0.53	4.15	4.35	1.23	
No. 8—148 Hz, $z = 4.5$ mm (mid-membranous)																		
Left	-5.97021	0.00	6.95838	9.46105	2.24753	3.14478	10.09626	6.34856	11.66	7.02	7.29	10.10	4.87	1.50	8.76	9.82	2.95	
Right	-5.97021	0.00	5.90344	9.25417	3.01639	5.06520	10.77900	6.37661	11.66	7.68	7.29	10.78	4.77	1.55	8.11	9.32	3.50	
No. 8—304 Hz, $z = 4.5$ mm																		
Left	-4.06451	0.00	6.11554	11.07029	1.88654	2.92322	12.60185	6.87622	13.62	5.20	7.49	12.60	3.50	1.01	9.41	11.45	3.14	
Right	-4.06451	0.00	9.97143	10.88943	1.84294	5.10890	12.57662	7.18833	13.62	5.70	7.38	12.58	4.39	0.83	10.17	10.98	2.52	
No. 8—304 Hz, $z = 5.5$ mm																		
Left	-4.34497	0.00	5.38054	10.87318	1.92045	4.46263	12.19135	6.94488	12.89	5.37	7.42	12.19	4.19	0.99	9.28	11.24	2.99	
Right	-4.34497	0.00	8.97030	10.77428	1.69836	4.66708	12.23248	7.20353	12.89	6.63	7.25	12.23	5.16	0.73	9.72	10.89	2.21	
No. 8—304 Hz, $z = 6.5$ mm (mid-membranous)																		
Left	-3.02426	0.00	6.60200	10.94120	2.07421	5.50130	12.34927	7.07527	13.38	5.88	7.36	12.35	4.83	0.84	9.31	11.19	3.02	
Right	-3.02426	0.00	8.78619	10.70021	1.63259	4.98115	11.96087	7.29231	13.38	7.12	7.36	11.96	5.69	0.77	9.69	10.84	2.20	
No. 8—304 Hz, $z = 7.5$ mm																		
Left	-2.38317	0.00	6.02514	10.65617	1.50514	4.10783	12.22228	6.64702	13.62	6.41	6.83	12.22	5.26	0.72	9.38	11.24	3.27	
Right	-2.38317	0.00	8.25981	10.59569	1.35760	5.12245	11.65247	7.34825	13.62	7.59	6.83	11.65	5.89	0.76	9.74	10.83	2.15	
No. 8—304 Hz, $z = 8.5$ mm																		
Left	-3.19759	0.00	6.36032	10.54912	1.22400	3.69419	12.11123	6.36463	13.26	6.69	6.45	12.11	5.54	0.78	9.59	11.60	3.43	
Right	-3.19759	0.00	8.68794	10.96891	1.37321	4.58768	11.76849	7.37120	13.26	7.81	7.04	11.77	6.39	0.65	10.04	11.13	2.00	
No. 8—304 Hz, $z = 9.5$ mm																		
Left	-1.36865	0.00	6.55310	11.05013	1.48269	4.86571	12.08509	5.60967	13.64	6.45	5.77	12.09	5.70	0.66	9.75	11.78	3.56	
Right	-1.36865	0.00	8.46815	10.92697	1.26791	4.88906	11.39849	7.28231	13.64	7.55	6.82	11.40	6.61	0.68	10.11	11.16	2.06	
No. 8—304 Hz, $z = 10.5$ mm																		
Left	-1.58969	0.00	6.49395	11.14835	1.56851	3.76947	12.74529	5.44372	13.16	6.45	5.46	12.75	5.50	0.59	9.68	11.92	3.31	
Right	-1.58969	0.00	8.60485	10.97147	1.55241	2.63991	11.28142	5.69089	13.16	7.75	5.46	11.28	7.13	0.69	10.12	11.25	2.62	
No. 8—304 Hz, $z = 11.5$ mm																		
Left	-0.51517	0.00	6.27783	11.14827	1.52217	3.16777	12.11298	4.58892	13.19	6.09	5.11	12.11	5.89	0.56	9.67	11.89	3.20	
Right	-0.51517	0.00	8.51752	11.10808	1.54894	3.27815	11.22127	5.05792	13.19	7.91	4.77	11.22	6.76	0.76	10.10	11.35	2.49	

the CMM. Some of the casts were damaged when preliminary tests using different digitization methods were performed.

Subjectively, the larynx no. 8 at 304 Hz passed the whole procedure (casting, CMM measurement, coronal section extraction and regression) most successfully, and is considered to reflect the shape of the vocal folds most realistically. This is why this larynx was chosen not only for the 2D analysis of the mid-membranous section, but also for the mathematical description of the vocal channel contours in multiple coronal sections along the anterior-posterior axis. Even though such description is still not sufficient to design an exact and complete 3D model, it may be helpful in cases when 3D data are needed.

The results show that in all the cases the shapes of the left and right vocal folds were slightly different. This complements the findings of previous anatomical studies, which showed that slight left–right asymmetry is common

in normal larynges (Hirano et al., 1989; Lindestad et al., 2004). The thicknesses and depths of the left and right vocal folds in mid-membranous sections differed by up to 0.7 and 0.8 mm, respectively, which corresponds to up to 6% and 15% difference of the total measured thickness and depth, respectively. An interesting result is the difference in the positions of the right and left vocal fold apices along the glottal channel, dividing the convergent and divergent parts of glottis. That difference was found to be up to 0.65 mm. Such a difference may play an important role in the separation of the airflow from the glottal channel wall and contribute to the Coanda effect (see, e.g., Erath and Plesniak, 2006a, b). The effect of increased F_0 in the same larynx was reflected in longer membranous length L_m of the vocal folds; no corresponding simple trends were found in the other shape parameters, however.

The most comprehensive quantitative description based on real measurements, which was published so far, is

probably that of Berry et al. (2001b). This work, however, was on canine larynges. The shape which has been most widely used in mathematical and physical modeling of human voice seems to be model “M5”, which was proposed by Scherer et al. (2002) and has been used, among others, in theoretical and experimental studies of himself, Thomson et al. (2005), Fulcher et al. (2006), or Erath and Plesniak (2006a, b). The geometry of the “M5” model is piecewise linear with rounded corners. Compared to the “M5” model, the vocal fold shapes measured within our work have rather curved contours in the medial part, and a more distinct apex. In contrast to the study of Berry et al. (2001a, b) the shape covered in our work is larger, and it includes also the superior vocal fold surface and the transition of the vocal fold to the subglottal channel. Similar to Berry et al. (2001a, b), our method did not allow to distinguish the vibrating and non-vibrating portions of the human glottal channel. To obtain such an information the alternative method of Berry et al. (2001a) or Döllinger and Berry (2006b) could be useful, although here the spatial resolution is limited by the number of sutures embedded in the vocal folds.

A disadvantage of using excised larynges is that the thyroarytenoid (TA) muscle is not active. The TA muscle is known to alter the geometry of the vocal folds and make the cross-sectional shape more bulged and vertically thicker (Hirano, 1975). This means that the geometry may not be exactly the same in the excised and in vivo larynges. However, the excised larynx is arguably still the most accurate source of data on the real vocal folds for the purposes of biomechanical modeling because it offers measurements in controllable conditions.

This study was primarily intended to present simple functional description of the 2D vocal channel contours for the purposes of 2D modeling, where such data are often needed. Coronal sections of the glottal channel were fitted by cubic splines. The regression model was designed as being smooth in the whole interval, describing independently the left and right vocal folds to account for vocal fold asymmetry. We found that a simple function such as the one offered by Titze (1989), Berry (2001b) or even a multipart spline as presented here would be insufficient to describe the complex, 3D geometry of the entire glottal channel (see the lateral view of the cast in Fig. 3e and frontal view in Fig. 4a).

The 3D computer models, which are shown in Fig. 4b,c, covered the complete glottal channel except of short regions (up to 2 mm) adjacent to anterior and posterior commissures. These correspond to the very extremities of the casts, which could not be reached by the CMM in current setup. Dropping the concept of simple functional description of the contours, the method could be in future used to get a complete 3D model: the CMM could be set up to scan the surface from different directions and the whole channel modeled directly in 3D in a CAD or 3D modeling software. Another challenging possibility may be to try to obtain the data directly from MRI or CT measurements.

According to our knowledge, the results reported here are the first to mathematically describe the complete 2D glottal channel, from the straight inflow part (trachea) up to the straight outflow passage (supraglottal space). The described geometry can be used for constructing realistic mathematical and physical models of human vocal folds. For technical reasons, the ventricular folds were removed from the larynges and their geometry was not analyzed here. In future, however, it will be useful to include also the shape of the ventricular folds as they can affect the supraglottal airflow and influence the vocal fold vibration (Alipour et al., 2007).

Conflict of interest statement

None of the authors is aware to be in a relationship with an organization or person, which might have inappropriately biased the work.

Acknowledgments

The authors acknowledge the financial support of the Grant Agency of the Czech Republic within the project No. 106/98/K019 Mathematical and Physical Modeling of Vibroacoustic Systems in Biomechanics of Voice and Hearing and the support of the Academy of Sciences of the Czech Republic within the project No. IAA2076401 Mathematical Modeling of Human Vocal Folds Oscillations, research plan no. AV0Z20760514. The authors also wish to express special thanks to the Research Institute of Textile Machines, Liberec, for their help with measurements on the coordinate measuring machine.

References

- Alipour, F., Scherer, R.C., 2000. Vocal fold bulging effects on phonation using a biophysical computer model. *Journal of Voice* 14, 470–483.
- Alipour, F., Jaiswal, S., Finnegan, E., 2007. Aerodynamic and acoustic effects of false vocal folds and epiglottis in excised larynx models. *Annals of Otology, Rhinology and Laryngology* 116 (2), 135–144.
- Berry, D.A., 2001. Mechanism of modal and non-modal phonation. *Journal of Phonetics* 29, 431–450.
- Berry, D.A., Montequin, D.W., Tayama, N., 2001a. High-speed digital imaging of the medial surface of the vocal folds. *Journal of the Acoustical Society of America* 110, 2539–2547.
- Berry, D.A., Clark, M.J.O., Montequin, D.W., Titze, I.R., 2001b. Characterization of the medial surface of the vocal folds. *Annals of Otology, Rhinology and Laryngology* 110, 470–477.
- Döllinger, M., Berry, D.A., 2006a. Computation of the three-dimensional medial surface dynamics of the vocal folds. *Journal of Biomechanics* 39, 369–374.
- Döllinger, M., Berry, D.A., 2006b. Visualization and quantification of the medial surface dynamics of an excised human vocal fold during phonation. *Journal of Voice* 20 (3), 401–413.
- Döllinger, M., Berry, D.A., Berke, G.S., 2005. Medial surface dynamics of an in vivo canine vocal fold during phonation. *Journal of the Acoustical Society of America* 117, 3174–3183.
- Erath, B.D., Plesniak, M.W., 2006a. An investigation of jet trajectory in flow through scaled vocal fold models with asymmetric glottal passages. *Experiments in Fluids* 41 (5), 735–748.

- Erath, B.D., Plesniak, M.W., 2006b. The occurrence of the Coanda effect in pulsatile flow through static models of the human vocal folds. *Journal of the Acoustical Society of America* 120 (2), 1000–1011.
- Fulcher, L.P., Scherer, R.C., Zhai, G., Zhu, Z., 2006. Analytic representation of volume flow as a function of geometry and pressure in a static physical model of the glottis. *Journal of Voice* 20, 489–512.
- Hirano, M., 1975. Phonosurgery: basic and clinical investigations. *Otologia (Fukuoka)* 21 (Suppl. 1), 239–442.
- Hirano, M., Yukizano, K., Kurita, S., Hibi, S., 1989. Asymmetry of the laryngeal framework: a morphologic study of the cadaver larynges. *Annals of Otology, Rhinology and Laryngology* 98, 135–140.
- Hollien, H., Colton, R.H., 1969. Four laminagraphic studies of vocal fold thickness. *Folia Phoniatrica* 21, 179–198.
- Hollien, H., Curtis, J., 1960. A laminagraphic study of vocal pitch. *Journal of Speech and Hearing Research* 3, 361–371.
- Hollien, H., Coleman, R., Moore, P., 1968. Stroboscopic laminagraphy of the larynx during phonation. *Acta oto-laryngologica* 65, 209–215.
- Horáček, J., Švec, J.G., Veselý, J., Vilkman, E., Klepáček, I., Vetešník, A., 2001. Measurement of the vocal-fold vibration behaviour in excised human larynges. In: *Proceedings of the Second International Workshop on Models and Analysis of Vocal Emissions for Biomedical Applications*, University of Firenze, Firenze, Italy.
- Horáček, J., Šidlof, P., Švec, J.G., 2005. Numerical simulation of self-oscillations of human vocal folds with Hertz model of impact forces. *Journal of Fluids and Structures* 20, 853–869.
- Kob, M., Krämer, S., Prévot, A., 2005. Acoustic measurement of periodic noise generation in a hydrodynamical vocal fold model. In: *Forum Acusticum 2005*, Budapest, Hungary.
- Li, S., Scherer, R.C., Wan, M.X., Wang, S.P., Wu, H.H., 2006. The effect of glottal angle on intraglottal pressure. *Journal of the Acoustical Society of America* 119, 539–548.
- Lindestad, P.-Å., Hertegård, S., Björck, G., 2004. Laryngeal adduction asymmetries in normal speaking subjects. *Logopedics Phoniatrics Vocology* 29, 128–134.
- Rosa, M.O., Pereira, J.C., Grellet, M., Alwan, A., 2003. A contribution to simulating a three-dimensional larynx model using the finite element method. *Journal of the Acoustical Society of America* 114, 2893–2905.
- Scherer, R.C., Shinwari, D., De Witt, K.J., Zhang, C., Kucinski, B.R., Afjeh, A.A., 2002. Intraglottal pressure distributions for a symmetric and oblique glottis with a uniform duct. *Journal of the Acoustical Society of America* 112, 1253–1256.
- Tayama, N., Chan, R.W., Kaga, K., Titze, I.R., 2002. Functional definitions of vocal fold geometry for laryngeal biomechanical modeling. *Annals of Otology, Rhinology and Laryngology* 111, 83–92.
- Thomson, S.L., Mongeau, L., Frankel, S.H., 2005. Aerodynamic transfer of energy to the vocal folds. *Journal of the Acoustical Society of America* 118, 1689–1700.
- Titze, I.R., 1989. A 4-parameter model of the glottis and vocal fold contact area. *Speech Communication* 8 (3), 191–201.
- Titze, I.R., Story, B.H., 2002. Rules for controlling low-dimensional vocal fold models with muscle activation. *Journal of the Acoustical Society of America* 112, 1064–1076.
- Vilain, C.E., Pelorson, X., Fraysse, C., Deverge, M., Hirschberg, A., Willems, J., 2004. Experimental validation of a quasi-steady theory for the flow through the glottis. *Journal of Sound and Vibration* 276, 475–490.
- Vilkman, E., 1987. An apparatus for studying the role of the cricothyroid articulation in the voice production of excised human larynges. *Folia Phoniatrica* 39, 169–177.
- Zhang, Y., Jiang, J.J., 2005. Spatiotemporal chaos in excised larynx vibrations. *Physical Review E* 72 (Art. No. 035201R).
- Zhang, Z., Neubauer, J., Berry, D.A., 2006. Aerodynamically and acoustically driven modes of vibration in a physical model of the vocal folds. *Journal of the Acoustical Society of America* 120, 2841–2849.

4.3 Mathematical modeling of flow-structure-acoustic interaction in human larynx

4.3.1 Overview of concepts and methods

In the available literature, numerous mathematical models of phonation can be found. An extensive overview is given in a recent review paper of [Alipour et al. \(2011\)](#). Basically, the models can be divided into two large families. First, the low-order models, where the complex interaction between the airflow and the nonlinear tissue structures is modeled by a small number of discrete masses supported by linear springs and dampers, coupled to simplified and often linearized flow models. Although this may seem a serious oversimplification of the real physiological situation, such models proved very useful especially for modeling of phonation onset mechanisms. The main advantage of these models is that the equations may be solved either analytically, or using simple and very fast numerical methods for ordinary differential equations, making it possible to perform nearly real-time simulations on current computers.

The cornerstone of the reduced-order mathematical models of phonation was set by [Ishizaka and Flanagan \(1972\)](#) more than 40 years ago. Their vocal fold model consists of two discrete masses interconnected by springs and dampers and coupled to potential quasi-1D airflow. Its variants, e. g., ([Lucero, 1993](#), [Pelorson et al., 1994](#), [Story and Titze, 1995](#), [Sciamarella and d'Alessandro, 2004](#), [Horáček et al., 2005](#), [Zhang, 2008](#), [Yang et al., 2010](#)), are widely used up to present. However, since the low-order models do not resolve accurately neither the glottal airflow nor the viscoelastic deformation of the vocal folds, increasing effort has been devoted to numerical solution of the 2D or 3D Navier-Stokes equations on computational domains approximating the glottal channel, and to proper modeling of the structural mechanics.

These high-order models are described by partial differential equations. The equations contain important nonlinearities, coming from three major sources: nonlinearity due to the convective term in the Navier-Stokes equations, geometric nonlinearity in the elastomechanics due to large deformations, and material nonlinearities of the living tissues. In the case of loud phonation, yet another nonlinearity appears due to vocal fold collisions. The nonlinear partial differential equations have to be solved numerically, leading to systems with large number of unknowns. The standard choice of the numerical method for the solution of the elasticity is the finite element method ([Bathe, 1996](#)). In some cases with simple geometry, high-order variants of the finite difference method are sometimes used, too ([Bae and Moon, 2008](#), [Larsson and Müller, 2009](#)). For the numerical modeling of fluid dynamics, the choice is much wider – finite volume methods ([Renotte et al., 2000](#), [Alipour and Scherer, 2004](#), [Puncochářová-Pořízková et al., 2011](#), [Matheus and Brücker, 2011](#)), stabilized finite element methods ([de Oliveira Rosa et al., 2003](#), [Thomson et al., 2005](#), [Tao et al., 2007](#), [Suh and Frankel, 2008](#), [Sváček, 2011](#)) and finite difference methods ([Zhao et al., 2002](#), [Sciamarella and Quéré, 2008](#), [Larsson and Müller, 2009](#)), discontinuous Galerkin finite element method ([Feistauer et al., 2013](#)) or Lattice-Boltzmann methods ([Kucinski et al., 2008](#)) have all been employed for the solution of the laryngeal airflow.

Even the high-order models usually do not try to model the phonation in all its complexity, and contain certain simplifications and reductions. With respect to the fluid-structure interaction, the problem is sometimes simplified to static vocal fold case ([Suh and Frankel, 2007, 2008](#), [Larsson and Müller, 2009](#), [Mihaescu et al., 2010](#), [Schwarze et al., 2011](#)), forced vocal fold oscillation ([Alipour et al., 1996a](#), [Renotte et al., 2000](#), [Zhao et al., 2002](#), [Alipour and Scherer, 2004](#), [Bae and Moon,](#)

2008, Sciamarella and Quéré, 2008, Puncochářová-Pořízková et al., 2011, Mattheus and Brücker, 2011, Zheng et al., 2011a). Some works use models with the airflow fully coupled to elastic tissue oscillations (de Oliveira Rosa et al., 2003, Thomson et al., 2005, Tao and Jiang, 2007, Luo et al., 2008, Link et al., 2009, Zheng et al., 2009, Sváček, 2011). The computational cost of the high-order methods can be drastically reduced by solving the problem only in 2D. Actually, only a few of the computational models published (de Oliveira Rosa et al., 2003, Suh and Frankel, 2007, 2008, Mihaescu et al., 2010, Schwarze et al., 2011, Mattheus and Brücker, 2011) solve the flow field in 3D, and most of them on a static geometry. One of the most complex approaches to phonation modeling was recently published in the works of Zheng et al. (2010, 2011b) and Seo and Mittal (2011), who used the immersed boundary method for incompressible low-Mach number flow coupled to a finite element solver for the viscoelastic tissue to calculate the 3D flow field and flow-induced vibrations of the vocal folds including glottal closure and contact forces. Using the aerodynamic-acoustic splitting technique, the acoustic field was then calculated by solving linearized perturbed compressible equations.

4.3.2 Author's contributions to computational modeling of phonation

The following section contains reprints of author's four selected publications in the field of computational modeling of phonation. The papers are listed chronologically and reflect the progress from a fast, reduced-order semi-analytic code over high-order models in 2D towards parallelized codes for the solution of the flow-acoustic interaction on large 3D computational grids.

The first paper reprinted from *Journal of Fluids and Structures* was published prior to author's PhD thesis, as a single exception among all the reprints. However, the contents of the paper were not used in the thesis and the author feels that it is important to put the following high-order models into context, and to show that a simplified lumped-parameter model may be highly useful e. g. for prediction of phonation onset parameters. The paper demonstrates how the linearized model can be employed to compute critical flow velocity and stability maps for the flutter-type instability of a rigid elastically supported body vibrating in the wall of a channel by solving an eigenvalue problem. The full, nonlinear system of ordinary differential equations is used for the numerical simulation of post-critical vocal fold oscillations, including vocal fold collision modeling.

The following two publications in *Applied and Computational Mechanics* (journal without impact factor) and *Computers & Fluids* report on a 2D finite element and a 3D finite volume model of airflow in a computational domain with forced vocal fold motion. The results of the numerical simulations (together with findings from experimental studies, see Sec. 4.4) demonstrate that the 2D models capture well the flow field in the subglottal channel and in the convergent part of the glottis, where the flow has dominantly planar character. In the divergent part of glottis, however, the flow separates and coherent vortex structures are generated in the shear layer of the jet. In this region, the real 3D vortex dynamics are fundamentally different from the simplified 2D model. The necessity to use large 3D computational grids to resolve the supraglottal flow field accurately has also technical consequences: on current computers, it is not practical to run such numerical simulations on a single CPU core. In order to get the result in a reasonable time, the code has to be run in parallel on an appropriate parallel hardware.

The relation between the flow field and the aerodynamically generated sound is complex, and still subject to ongoing research. The last reprint of the manuscript accepted for publication in *Biomechanics and Modeling in Mechanobiology* reports on a hybrid aeroacoustic model of human

voice production, developed in close cooperation between the author, S. Zörner and A. Hüppe from Vienna University of Technology. Using Lighthill's analogy and a perturbation-based approach, the aeroacoustic sound sources are identified and the propagation and radiation of the sound modeled.

Reprints

- J. Horáček, P. Šidlof, and J. G. Švec. Numerical simulation of self-oscillations of human vocal folds with Hertz model of impact forces. *Journal of Fluids and Structures*, 20(6):853–869, August 2005
- P. Šidlof, E. Lunéville, C. Chambeyron, O. Doaré, A. Chaigne, and J. Horáček. Finite element modeling of airflow during phonation. *Applied and Computational Mechanics*, 4(1):121–132, July 2010
- P. Šidlof, J. Horáček, and V. Řidký. Parallel CFD simulation of flow in a 3D model of vibrating human vocal folds. *Computers & Fluids*, 80:290–300, 2013
- P. Šidlof, S. Zörner, and A. Hüppe. A hybrid approach to computational aeroacoustics of human voice production. *Biomechanics and Modeling in Mechanobiology*, pages 1–17, 2014c



ELSEVIER

Journal of Fluids and Structures 20 (2005) 853–869

JOURNAL OF
FLUIDS AND
STRUCTURES

www.elsevier.com/locate/jfs

Numerical simulation of self-oscillations of human vocal folds with Hertz model of impact forces

J. Horáček^{a,*}, P. Šidlof^a, J.G. Švec^b^a*Institute of Thermomechanics, Academy of Sciences of the Czech Republic, Dolejškova 5, 182 00 Prague 8, The Czech Republic*^b*Medical Healthcom Ltd., Centre for Communication Disorders, Řešovská 10/491, 181 00 Prague 8, The Czech Republic*

Received 10 September 2004; accepted 6 May 2005

Available online 14 July 2005

Abstract

A mathematical model was developed previously (by Horáček and Švec in 2002a) for studying the influence of the geometrical, viscoelastic and vibrational characteristics of the human vocal folds on their self-sustained oscillations in phonatory air-flow. That model is advanced here by: (i) extending the equations for unsteady aerodynamic forces from small to realistic vibrational amplitudes of the vocal folds; (ii) implementing the Hertz model of impact forces for vocal-fold collisions; (iii) adjusting the elastic support of the vocal-fold-shaped vibrating element for more flexible tuning of the natural frequencies of vibrations; and (iv) moving from frequency domain calculations towards on-line simulations in the time domain. Using a parabolic vocal-fold shape and vocal-fold natural frequencies close to 100 Hz, the model exhibits vibrations for flow velocities, flow volumes and subglottal pressures above 0.5 m/s, 0.1 l/s, and 0.15 kPa, respectively. During collisions, the model reveals impact stress values up to 3 kPa. As these values are close to those measured in humans, the model is found suitable for studying phenomena and estimating values, which are difficult to observe and measure in the living vocal folds.

© 2005 Elsevier Ltd. All rights reserved.

Keywords: Flow induced vibrations; Human voice biomechanics; Post-critical behaviour

1. Introduction

Vibrations of vocal folds are of extraordinary importance for production of human voice. As the vocal folds are difficult to study in vivo, the mathematical and numerical models could be very helpful for understanding the mechanism of voice production. First lumped-parameters dynamic models of the vocal-fold self-oscillations were developed already at the beginning of seventies of the last century (Ishizaka and Flanagan, 1972) and their different variations remain to be widely used (Liljencrants, 1991; Pelorson et al., 1994; Herzel and Knudsen, 1995; Story and Titze, 1995; Lous et al., 1998; De Vries et al., 1999; Ikeda et al., 2001). New versions of the self-oscillating vocal-fold models have been described during the last 2 years (LaMar et al., 2003; Sciamarella and d'Alessandro, 2004; Adachi and Yu, 2005; Drioli, 2005).

A short overview of numerous existing models can be found, e.g., in the dissertation of Kob (2002). A frequent problem of the developed mathematical models is the relationship of their input parameters to the real material

*Corresponding author. Tel.: +420 2 66053125; fax: +420 2 8584695.

E-mail address: jaromirh@it.cas.cz (J. Horáček).

properties of the vocal folds and to the aerodynamic properties of the phonatory airstream. The aerodynamic forces have usually been approximated by quasi-steady forces given by the Bernoulli law. The latest finite-element models developed for vibration of the vocal folds in viscous fluid flow described by the Navier–Stokes equations (Thomson et al., 2003; Alipour et al., 2000) are still in a preliminary phase and their reliability and usability for an on-line numerical simulation of the vocal-fold self-oscillations with impacts is limited. A sufficiently accurate description of unsteady viscous fluid flow characteristics measured on oscillating rigid replicas of vocal folds during their collisions appears problematic (Deverge et al., 2003). Similar problems of flow-induced vibrations for flows in collapsible tubes were studied, e.g., by Cancelli and Pedley (1985), where the dominant mechanism for self-sustained vibrations relied on flow separation and a pressure recovery downstream of the narrowest section of the tube.

The authors have developed a linear aeroelastic model in order to study the influence of different geometrical and elastic properties of the vocal folds on phonation thresholds (Horáček and Švec, 2002a, b). An inviscid incompressible 1-D fluid flow theory was used in the model for expressing the unsteady aerodynamic forces and the parameters of the model, i.e., the mass, stiffness and damping matrices were approximately related to the geometry, size and material density of real vocal folds as well as to the known or prescribed fundamental natural frequencies and damping. In the current paper, the model is advanced by: (i) extending the equations for unsteady aerodynamic forces from small perturbations to realistic vibrational amplitudes; (ii) implementing the Hertz model of impact forces for vocal fold collisions; (iii) improving the tuning possibilities of the natural frequencies of the vocal folds by replacing the continuous elastic foundation by a two-spring elastic support; and (iv) moving from frequency domain calculations towards on-line simulations in the time domain. First the mathematical model is formulated and the solution procedures are presented, then the results of the on-line simulations are demonstrated, and finally the model behaviour is related to the real vocal folds by comparing its output data to values measured in living subjects.

2. Mathematical model

The model of the glottis with the vocal folds is shown in Fig. 1 as a channel with planar symmetry conveying air. The length of the channel, L , is measured parallel to both the plane of symmetry and the direction of air-flow.

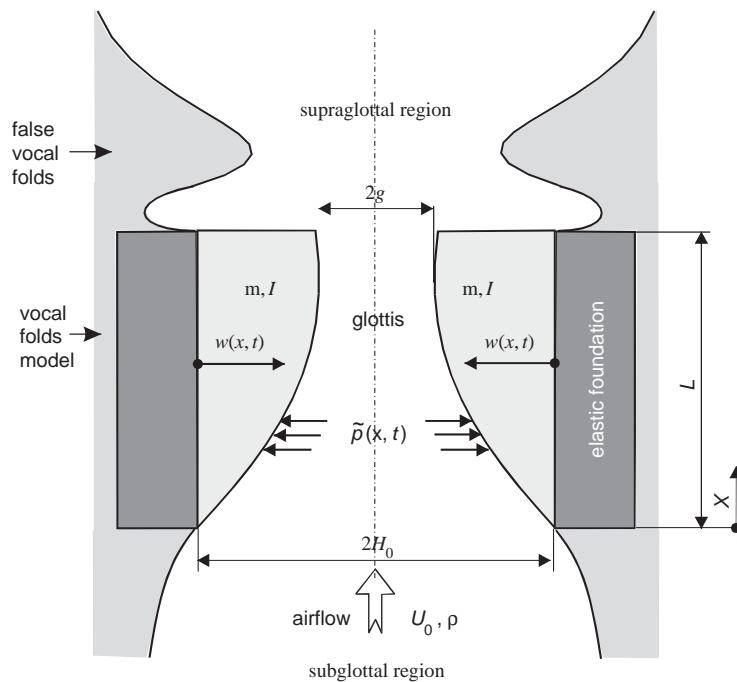


Fig. 1. Schematic of the glottal space.

The channel walls are created by two vocal-fold-shaped rigid bodies of mass m and moment of inertia I , which are vibrating symmetrically in the opposite phase with identical amplitudes on an elastic foundation. The rigid bodies oscillate in the fluid of density ρ flowing in the channel with the mean flow velocity U_0 at the inlet ($x = 0$), where the cross-section of the channel equals $2H_0$. The minimum cross-section of the channel for a steady state at zero air-flow, the so-called glottal width, is denoted by $2g$ (Fig. 1). The vibrating element has a smooth convergent glottal inlet and a short, not highly divergent, outlet, which is terminated with a sharp edge at which the flow separation occurs. Symmetric oscillations of the vocal folds are assumed, allowing modelling only a half of the glottal region (Fig. 2(a)).

2.1. Equations of motion for the vocal-fold-shaped vibrating element

The vocal fold can be approximated by a two-degree-of-freedom rigid body element with a defined shape $a(x)$, where x is the axial coordinate. The element is supported by two discrete springs with stiffnesses c_1 and c_2 (Fig. 2) and its vibration is described by its rotation and translation. An equivalent three-mass system can be used to formulate the equations of motion of the element, based on the three conditions of identical total mass, static moment and moment of inertia of the rigid body. The vibrating rigid body with mass m , moment of inertia I , and the centre of gravity T at the

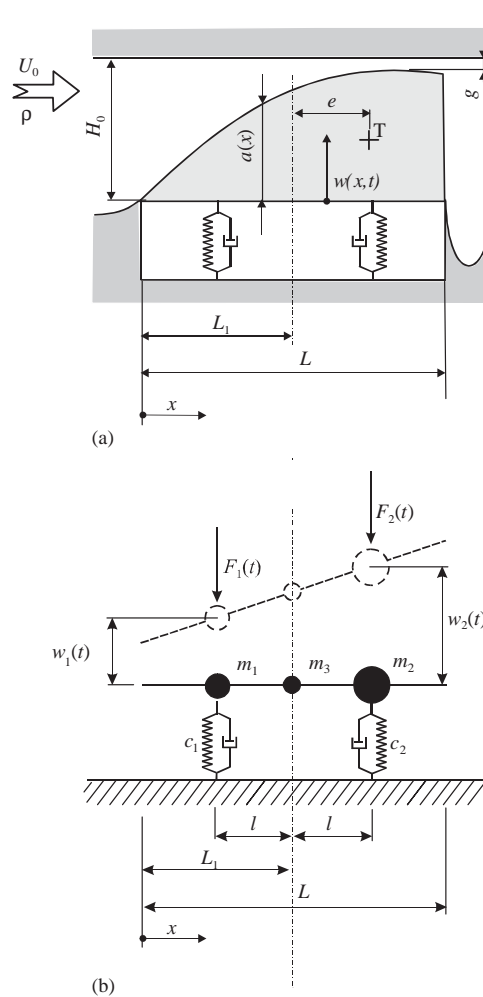


Fig. 2. Two-degree-of-freedom model.

location e (the eccentricity—see Fig. 2(a)) is replaced by the masses

$$m_{1,2} = \frac{1}{2l^2}(I + me^2 \mp mel), \quad m_3 = m \left[1 - \left(\frac{e}{l} \right)^2 \right] - \frac{I}{l^2} \quad (1)$$

joined together by a rigid massless rod of the total length L . The distance between the masses m_1 and m_2 is denoted as $2l$ and the distance L_1 from the upstream end of the rod defines their position (see Fig. 2(b)). The displacements of the masses m_1 and m_2 are denoted as $w_1(t)$ and $w_2(t)$, where t is time. The length L should approximately correspond to the anatomical data; the lengths l and L_1 can, however, be varied for the purpose of tuning of the model.

The displacement of the rigid massless rod can be written as

$$w(x, t) = (x - L_1)V_1(t) + V_2(t), \quad (2)$$

where the rotation and translation of the rigid body element was introduced as

$$V_1(t) = \frac{w_2(t) - w_1(t)}{2l}, \quad V_2(t) = \frac{w_2(t) + w_1(t)}{2}. \quad (3)$$

When the glottis is open, the force and moment equilibrium equations can be used to express the equivalent excitation aerodynamic forces $F_1(t)$ and $F_2(t)$ acting on the vocal folds (Fig. 2(b))

$$F_1(t) = \frac{h}{2} \int_0^L \left(1 - \frac{x}{l} + \frac{L_1}{l} \right) \tilde{p}(x, t) dx, \quad F_2(t) = \frac{h}{2} \int_0^L \left(1 + \frac{x}{l} - \frac{L_1}{l} \right) \tilde{p}(x, t) dx, \quad (4)$$

where h is the width of the channel (identical with the width of the rigid body) and $\tilde{p}(x, t)$ is the air pressure along the vibrating body surface. The width of the channel is measured perpendicular to the direction of air-flow and parallel to the plane of symmetry.

After expressing the potential and kinetic energies of the system in a similar way as in the previous article (Horáček and Švec, 2002a) and their substitution in the Lagrange equations, the equations of motion are obtained in the form

$$\mathbf{M}\ddot{\mathbf{V}} + \mathbf{B}\dot{\mathbf{V}} + \mathbf{K}\mathbf{V} + \mathbf{F} = 0, \quad (5)$$

where the following displacement and excitation force vectors were introduced

$$\mathbf{V} = \begin{bmatrix} V_1(t) \\ V_2(t) \end{bmatrix}, \quad \mathbf{F} = \begin{bmatrix} F_1(t) \\ F_2(t) \end{bmatrix} \quad (6)$$

and where \mathbf{M} , \mathbf{B} , \mathbf{K} are the structural mass, damping and stiffness matrices

$$\mathbf{M} = \begin{bmatrix} -lm_1 & m_1 + \frac{m_3}{2} \\ +lm_2 & m_2 + \frac{m_3}{2} \end{bmatrix}, \quad \mathbf{B} = \varepsilon_1 \mathbf{M} + \varepsilon_2 \mathbf{K}, \quad \mathbf{K} = \begin{bmatrix} -c_1 l & c_1 \\ +c_2 l & c_2 \end{bmatrix}. \quad (7)$$

The damping matrix \mathbf{B} represents a proportional model of structural damping; $\varepsilon_1, \varepsilon_2$ are constants adjusted hereafter according to the desired damping ratios for the two natural modes of vibration of the system. The structure of the matrices \mathbf{M} and \mathbf{K} reveals that a mass coupling caused by the mass m_3 is generally in the system even if $\mathbf{F} = 0$.

2.2. Aerodynamic unsteady forces for open glottis

The unsteady continuity and 1-D Euler equations for incompressible fluid can be used to express the aerodynamic forces acting on the vibrating element (Norton, 1989; Horáček and Švec, 2002a). The equation for unsteady pressure in the glottis was derived in a linear form by Horáček and Švec (2002a, p. 937, Eq. (16)) supposing only small flow velocity perturbations ($\tilde{u}\partial\tilde{u}/\partial x \rightarrow 0$). Here, we generalize the equation by incorporating also the nonlinear term $\tilde{u}\partial\tilde{u}/\partial x$. Using the velocity potential $\Phi(x, t)$ for the unsteady component of the flow velocity $\tilde{u}(x, t) = \partial\Phi(x, t)/\partial x$, the unsteady component of the pressure can be formulated in a nonlinear form as

$$\tilde{p}(x, t) = -\rho \left[\frac{\partial\Phi}{\partial t} + \bar{U}(x) \frac{\partial\Phi}{\partial x} + \frac{1}{2} \left(\frac{\partial\Phi}{\partial x} \right)^2 \right], \quad (8)$$

where the mean (steady) flow velocity in the glottis for $x \in (0, L)$ can be expressed from the continuity equation as

$$\bar{U}(x) = U_0/[1 - a(x)/H_0]. \quad (9)$$

Using the boundary conditions for the flow at the inlet ($x = 0$) and outlet ($x = L$)

$$\tilde{u} = \partial\Phi/\partial x = 0|_{x=0} \quad \text{and} \quad \tilde{p} = 0|_{x=L}, \quad (10)$$

considering the displacement $w(x, t) \ll H_0$ and using the same procedure as in the previous paper (Horáček and Švec, 2002a, pp. 937–938, Eqs. (9)–(10)) the unsteady component of the pressure can be written as

$$\begin{aligned} \tilde{p}(x, t) = & -\rho\{K_1(x)[V_1(t)]^2 + K_2(x)V_2(t) + K_3(x)[V_2(t)]^2 + K_4(x)[\dot{V}_1(t)]^2 + K_5(x)\dot{V}_2(t) + K_6(x)V_2(t)\dot{V}_2(t) \\ & + K_7(x)[\dot{V}_2(t)]^2 + K_8(x)\dot{V}_1(t) + K_9(x)\dot{V}_1(t)V_1(t) + K_{10}(x)\dot{V}_1(t)V_2(t) + K_{11}(x)\dot{V}_1(t)\dot{V}_2(t) + K_{12}(x)V_1(t) \\ & + K_{13}(x)V_1(t)V_2(t) + K_{14}(x)V_1(t)\dot{V}_2(t) + K_{15}(x)\ddot{V}_1(t) + K_{16}(x)\ddot{V}_2(t)\}, \end{aligned} \quad (11)$$

where the coefficients $K_i(x)$ ($i = 1, 2, \dots, 16$) are complicated functions, which are specified in Appendix A. The general forms of Eq. (11) for pressure as well as the coefficients $K_i(x)$ were calculated by using the symbolic manipulation capabilities of the software *Mathematica*.

Then, the aerodynamic forces $F_1(t)$ and $F_2(t)$ can be expressed as nonlinear functions of the displacements $V_1(t)$ and $V_2(t)$ by calculating the integrals (4). Using the *Mathematica* for numerical integration of the coefficients $K_i(x)$ the resulting aerodynamic forces exciting the vocal folds are obtained for open glottis:

$$\begin{aligned} F_1(t) = & -\rho\{K_1^{\text{int}1}[V_1(t)]^2 + K_2^{\text{int}1}V_2(t) + K_3^{\text{int}1}[V_2(t)]^2 + K_4^{\text{int}1}[\dot{V}_1(t)]^2 + K_5^{\text{int}1}\dot{V}_2(t) + K_6^{\text{int}1}V_2(t)\dot{V}_2(t) \\ & + K_7^{\text{int}1}[\dot{V}_2(t)]^2 + K_8^{\text{int}1}\dot{V}_1(t) + K_9^{\text{int}1}\dot{V}_1(t)V_1(t) + K_{10}^{\text{int}1}\dot{V}_1(t)V_2(t) + K_{11}^{\text{int}1}\dot{V}_1(t)\dot{V}_2(t) + K_{12}^{\text{int}1}V_1(t) \\ & + K_{13}^{\text{int}1}V_1(t)V_2(t) + K_{14}^{\text{int}1}V_1(t)\dot{V}_2(t) + K_{15}^{\text{int}1}\ddot{V}_1(t) + K_{16}^{\text{int}1}\ddot{V}_2(t)\}, \end{aligned} \quad (12)$$

$$\begin{aligned} F_2(t) = & -\rho\{K_1^{\text{int}2}[V_1(t)]^2 + K_2^{\text{int}2}V_2(t) + K_3^{\text{int}2}[V_2(t)]^2 + K_4^{\text{int}2}[\dot{V}_1(t)]^2 + K_5^{\text{int}2}\dot{V}_2(t) \\ & + K_6^{\text{int}2}V_2(t)\dot{V}_2(t) + K_7^{\text{int}2}[\dot{V}_2(t)]^2 + K_8^{\text{int}2}\dot{V}_1(t) + K_9^{\text{int}2}\dot{V}_1(t)V_1(t) + K_{10}^{\text{int}2}\dot{V}_1(t)V_2(t) \\ & + K_{11}^{\text{int}2}\dot{V}_1(t)\dot{V}_2(t) + K_{12}^{\text{int}2}V_1(t) + K_{13}^{\text{int}2}V_1(t)V_2(t) + K_{14}^{\text{int}2}V_1(t)\dot{V}_2(t) + K_{15}^{\text{int}2}\ddot{V}_1(t) + K_{16}^{\text{int}2}\ddot{V}_2(t)\}, \end{aligned} \quad (13)$$

where the following notation was introduced:

$$K_i^{\text{int}1} = h \int_0^L K_i(x) \frac{l + L_1 - x}{2l} dx \quad \text{and} \quad K_i^{\text{int}2} = h \int_0^L K_i(x) \frac{l - L_1 + x}{2l} dx, \quad i = 1, \dots, 16. \quad (14)$$

2.3. Model of the vocal-fold collisions

The Hertz model of impact (Brepta and Prokopec, 1972; Stronge, 2000; Püst and Peterka, 2003) is implemented here to account for vocal-fold collisions. The impact force F_H is considered as

$$F_H = k_H \delta^{3/2} (1 + b_H \dot{\delta}), \quad k_H \cong \frac{4}{3} \frac{E}{1 - \mu_H^2} \sqrt{r}, \quad (15)$$

where δ is the penetration of the vocal-fold element through the contact plane (see Fig. 3), E is Young's modulus, μ_H is the Poisson ratio, b_H is a damping factor and r is the radius of curvature of the impacting body surfaces approximated by the shape $a(x)$ of the vocal-fold model in the contact point according to the equation

$$\frac{1}{r} = \frac{|d^2a/dx^2|}{[1 + (da/dx)^2]^{3/2}}. \quad (16)$$

The geometry of the vocal fold is approximated by a general parabolic function:

$$a(x) = a_1x + (a_2/2)x^2. \quad (17)$$

The moving surface of the vibrating vocal-fold element (see Fig. 3) is described by the function

$$y(x, t) = a(x) + w(x, t) = a(x) + (x - L_1)V_1(t) + V_2(t), \quad x \in (0, L). \quad (18)$$

From here the coordinates of the contact point can be determined as

$$\begin{aligned} x_{\text{max}}(t) &= \min\{L, \max[0, -[V_1(t) + a_1]/a_2]\}, \\ y_{\text{max}}(t) &= y[x_{\text{max}}(t)] = a[x_{\text{max}}(t)] + [x_{\text{max}}(t) - L_1]V_1(t) + V_2(t). \end{aligned} \quad (19)$$

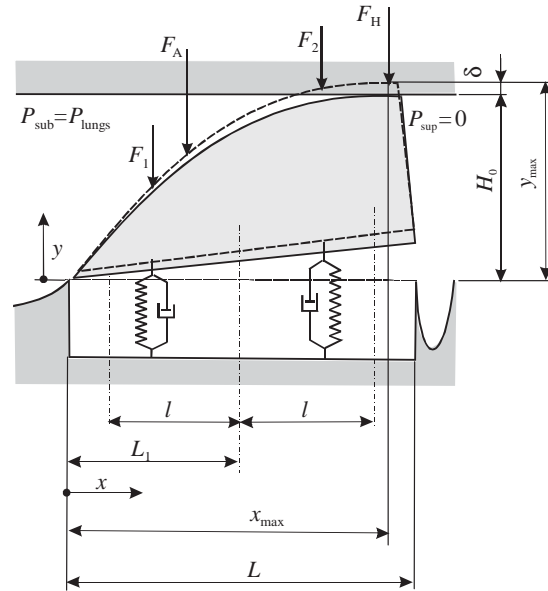


Fig. 3. Schema of the model for the closed glottis when the vocal-fold-shaped element is loaded by a resulting aerodynamic force F_A and the Hertz contact force F_H .

Using these equations, the Hertz impact force (15) can be rewritten (see Fig. 3) in the form

$$F_H(t) = k_H [y_{\max}(t) - H_0]^{3/2}, \quad (20)$$

where the damping factor b_H in the contact is neglected.

During the impact, when the glottis is closed, the aerodynamic forces (12) and (13) are switched off. There are three types of forces acting on the vocal-fold-shaped element during this time (Fig. 3): (i) the Hertz force, Eq. (20); (ii) the subglottal pressure P_{sub} , which is acting on the subglottal part of the element surface (this pressure equals the lungs pressure P_{lungs} and is kept steady as the lungs are considered a big air reservoir ($P_{\text{lungs}} = P_{\text{sub}} = \text{const.}$); and (iii) the supraglottal pressure, which is acting on the supraglottal part of the element surface. That pressure is set here to zero ($P_{\text{sup}} = 0$).

After integration of the pressure $P_{\text{sub}} = P_{\text{lungs}}$ in the interval $x \in (0, x_{\max}(t))$, the aerodynamic force can be expressed as $F_A(t) = P_{\text{sub}} x_{\max}(t) h$. Finally, the resulting forces in the equations of motion (5) during vocal-fold contact (see Figs. 2 and 3) can be approximated as

$$\begin{aligned} F_1(t) &= F_H(t) \frac{L_1 + l - x_{\max}(t)}{2l} + P_{\text{sub}} h x_{\max}(t) \frac{L_1 + l - x_{\max}(t)/2}{2l}, \\ F_2(t) &= F_H(t) \frac{x_{\max}(t) - L_1 + l}{2l} + P_{\text{sub}} h x_{\max}(t) \frac{x_{\max}(t)/2 - L_1 + l}{2l}. \end{aligned} \quad (21)$$

3. Numerical solution

3.1. Solution of the linearized problem—computation of stability boundaries

For calculating the stability boundaries, only small vibration amplitudes without collisions and small velocity perturbations ($\tilde{u} \partial \tilde{u} / \partial x \rightarrow 0$) can be considered. In this case, the perturbation pressure (8) is given by the simplified equation

$$\tilde{p} = -\rho \left(\frac{\partial \Phi}{\partial t} + \bar{U}(x) \frac{\partial \Phi}{\partial x} \right). \quad (22)$$

That results in a substantial simplification of Eq. (11) for the pressure

$$\tilde{p}(x, t) = -\rho \left[\ddot{V}_1(t)K_{15}(x) + \ddot{V}_2(t)K_{16}(x) + \dot{V}_1(t)K_8(x) + \dot{V}_2(t)K_5(x) \right] + V_1(t)K_{12}(x) + V_2(t)K_2(x). \quad (23)$$

Subsequently, the linear approximation of the forces $F_{1,2}(t)$ is given by Eqs. (12) and (13), where only the corresponding constants $K_i^{\text{int } 1}, K_i^{\text{int } 2}$ ($i = 2, 5, 8, 12, 15, 16$) are not equal to zero.

Substituting the linearized aerodynamic forces $F_{1,2}(t)$ in the equations of motion (5) and dividing this equation by $ml/2$ yields the following physically well-structured equations of motion of the coupled aeroelastic system in a linear approximation:

$$\bar{\mathbf{M}}\ddot{\mathbf{V}} + \bar{\mathbf{B}}\dot{\mathbf{V}} + \bar{\mathbf{K}}\mathbf{V} = \frac{\rho h L^3}{m H_0} \left[\hat{\mathbf{M}}\ddot{\mathbf{V}} + \frac{U_0}{L} \hat{\mathbf{B}}\dot{\mathbf{V}} + \frac{U_0^2}{L^2} \hat{\mathbf{K}}\mathbf{V} \right], \quad (24)$$

where

$$\bar{\mathbf{M}} = \begin{bmatrix} -\left(\frac{I}{m l^2} + \left(\frac{e}{l}\right)^2 - \frac{e}{l}\right) & \left(1 - \frac{e}{l}\right) \\ +\left(\frac{I}{m l^2} + \left(\frac{e}{l}\right)^2 + \frac{e}{l}\right) & \left(1 + \frac{e}{l}\right) \end{bmatrix}, \quad \bar{\mathbf{B}} = \bar{e}_1 \bar{\mathbf{M}} + \bar{e}_2 \bar{\mathbf{K}}, \quad \bar{\mathbf{K}} = \Omega_0^2 \begin{bmatrix} -1 & 1 \\ c_2 & c_2 \\ c_1 & c_1 \end{bmatrix} \quad (25)$$

are the dimensionless mass, damping and stiffness matrices for the rigid body vibrating in vacuo, $\Omega_0^2 = 2c_1/m$. The expression

$$\bar{\mathbf{V}} = \begin{bmatrix} 1 & 0 \\ 0 & 1/l \end{bmatrix} \mathbf{V} \quad (26)$$

gives the vector of dimensionless displacements. The elements in the matrices of the aerodynamic mass $\hat{\mathbf{M}}$, damping $\hat{\mathbf{B}}$ and stiffness $\hat{\mathbf{K}}$, which are complicated functions of the channel geometry, are specified in an analytical form for the special case $L_1 = L/2$ in Appendix B.

The unsteady aerodynamic forces on the right-hand side of Eq. (24) are obviously proportional to the dimensionless added mass of fluid ($\rho h L^3/m H_0$) and they have a lucid physical meaning. The first term corresponds to the aerodynamic inertia forces, the second term to the aerodynamic damping forces ($\sim U_0$) related to the Coriolis forces, and the third term to the aerodynamic stiffness forces ($\sim U_0^2$), which are related to the centrifugal forces. The Coriolis and centrifugal forces are increasing functions of the fluid flow velocity U_0 , causing aeroelastic instability and self-oscillations.

The numerical procedure for calculation of the stability boundaries from Eq. (24) was presented in the previous paper by Horáček and Švec (2002a) and will only be outlined here. Assuming $\bar{\mathbf{V}} = \bar{\mathbf{V}}_0 e^{st}$ for the dynamic response, the solution is given by the numerical computation of the eigenvalues $s = \mathcal{R}e(s) + i \mathcal{I}m(s)$ and eigenmodes ${}^T \bar{\mathbf{V}}_0 = (V_{01}, V_{02}/l)$ for the eigenvalue problem. In this way, it is possible to calculate the critical flow velocity $U_{0,\text{crit}}$ at which the real part of the eigenvalue changes the sign from a negative [$\mathcal{R}e(s) < 0$] to a positive value [$\mathcal{R}e(s) > 0$]. Here, the system either becomes unstable by divergence (when $\mathcal{I}m(s) = 0$), or it becomes unstable by flutter simulating the start of phonation (when $\mathcal{I}m(s) > 0$). The calculated stability boundaries for some of the relevant input parameters of the model are presented in Figs. 4 and 5 (see also Section 5.1).

3.2. Solution for the nonlinear model—simulation of self-oscillations

In order to simulate the postcritical behaviour and study the self-oscillations of the vocal folds, the nonlinear model was used and the numerical solution was implemented in the *Mathematica 5* (Wolfram, 2003). The equations of motion (5) were transformed into the system of four ordinary first-order differential equations:

$$\dot{Z}_1 = \psi_1(Z_1, Z_2, V_1, V_2), \quad \dot{Z}_2 = \psi_2(Z_1, Z_2, V_1, V_2), \quad \dot{V}_1 = Z_1, \quad \dot{V}_2 = Z_2 \quad (27)$$

and a fourth-order standard Runge–Kutta method with adaptive step size was used for the solution. The functions ψ_1, ψ_2 were determined differently for the contact regime (see Eqs. (21)) and the non-contact regime (see Eqs. (12) and (13)). The integrals (14) were pre-calculated for given input data before starting the on-line simulation.

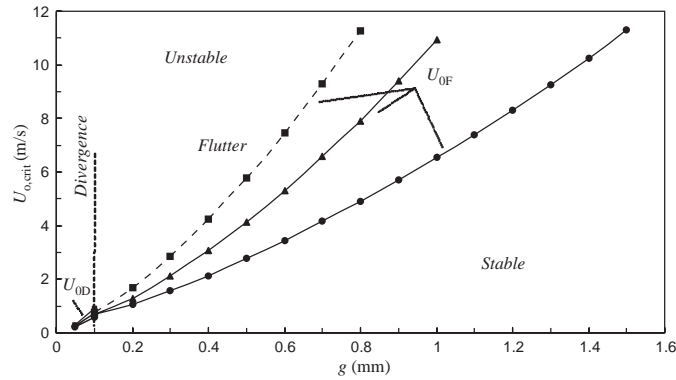


Fig. 4. Stability map for the model with the first natural frequency $f_1 = 100$ Hz and second natural frequency: ---■---, $f_2 = 160$ Hz; —▲—, $f_2 = 130$ Hz; —●—, $f_2 = 105$ Hz.

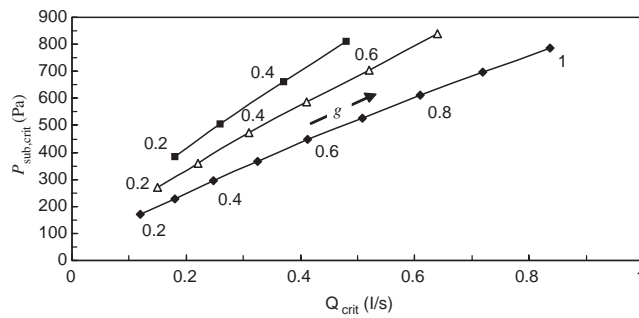


Fig. 5. Calculated critical values (flutter boundaries) for loosing the stability of the vocal fold model. The subglottal pressure $P_{\text{sub,crit}}$ and flow rate Q_{crit} for various glottal half-gaps $g = 0.2$ – 1 mm and for various values of natural frequencies: —●—, $f_1 = 100$ Hz, $f_2 = 105$ Hz; —△—, $f_1 = 150$ Hz, $f_2 = 155$ Hz; —■—, $f_1 = 200$ Hz, $f_2 = 205$ Hz.

4. Basic input data for numerical analysis

The *input parameters* for the numerical examples and analysis were determined from the published data on the vocal folds [e.g., Titze (1989)]. The density, thickness and length of the vocal folds were taken as follows: $\rho_h = 1020$ kg/m³, $L = 6.8$ mm, $h = 10$ mm. A convex shape $a(x)$ was considered according to Eq. (17), where the dimensionless coefficient $a_1 = 1.858$ and $a_2 = 319.722$ m⁻¹ were used. This shape corresponds to the geometry of the vocal fold with an intermediate bulging (Berry et al., 1994). From these data, the parameters needed for construction of the matrix \mathbf{M} were calculated, i.e., the eccentricity $e = 0.77106 \times 10^{-3}$ m, the total mass $m = 2.6731 \times 10^{-4}$ kg and the moment of inertia $I = 1.306 \times 10^{-9}$ kgm². The air density value of $\rho = 1.2$ kg/m³ was used.

The natural frequencies of the vibrating element and their bandwidths were selected to reflect the experimental data obtained from the true vocal folds (Kaneko et al., 1981, 1983, 1987; Švec et al., 2000). The natural frequencies f_1, f_2 were varied in order to account for different vocal-fold adjustments (examples of some of the values used are shown in Section 5). The 3 dB half-power bandwidths Δf_1 and Δf_2 were fixed to 23 and 29 Hz, respectively. A tuning procedure, based on solving an inverse problem, was used to find the stiffness coefficients c_1, c_2 of the elastic foundation and the damping coefficients $\bar{\varepsilon}_1, \bar{\varepsilon}_2$ in the structural matrices $\bar{\mathbf{B}}$ and $\bar{\mathbf{K}}$ in Eq. (25). For calculating the coefficients $\bar{\varepsilon}_1, \bar{\varepsilon}_2$ for given values Δf_1 and Δf_2 , the procedure was the same as described in the previous paper (Horáček and Švec, 2002a). To obtain the complex stiffness coefficients c_1 and c_2 for two prescribed natural frequencies f_1 and f_2 , the following two equations were used, which result from the equation of motion (5) for the undamped system ($\mathbf{B} = 0$) vibrating in vacuo ($\mathbf{F} = 0$):

$$[c_1 + (m_1 + m_3/4)(2\pi f_1)^2][c_2 + (m_2 + m_3/4)(2\pi f_1)^2] - (m_3^2/16)(2\pi f_1)^4 = 0 \quad (i = 1, 2). \quad (28)$$

The use of a two-spring elastic support rather than an elastic continuous foundation appeared highly advantageous here, as it enabled tuning of both the natural frequencies (in contrast to only one) and it avoided problems with complex stiffness coefficients experienced in the authors' original model. Symmetric positions of the springs at the distances $L_1 = L/2$ and $l = 0.344L$ (see Fig. 2) were used as these provided optimal tuning possibilities: here both the coefficients c_1, c_2 were real numbers for almost all the ratios $f_2/f_1 > 1.02$. This appears important, as the second natural frequency f_2 of the vocal folds is, in optimal situations, expected to be close to f_1 (Liljencrants, 1991; Berry, 2001). However, the vocal folds could vibrate also when f_2 is higher and further away from f_1 (Ishizaka and Flanagan, 1972; Liljencrants, 1991).

For the impact model, the values $E = 8$ kPa and $\mu_H = 0.4$ (Berry and Titze, 1996; De Vries et al., 1999) were used, which according to Eq. (15) yielded the contact stiffness coefficient $k_H \doteq 730 \text{ N m}^{-2/3}$. The damping in the contact was neglected ($b_H = 0$) in the numerical examples. Finally, the height H_0 of the channel, for a given vocal-fold-shaped element and a glottal half-width g , was expressed as $H_0 = \max_{x \in (0,L)} a(x) + g$ (see Fig. 2(a)).

5. Results of the numerical computations and simulations and their discussion

5.1. Stability map for the linearized model of the vocal-fold vibration

Fig. 4 shows the instability boundaries ($U_{0,\text{crit}}$) of the model as the functions of the glottal half-width g . The boundaries are shown for $f_1 = 100$ Hz and three higher natural frequencies $f_2 = 105$ Hz, $f_2 = 130$ Hz and $f_2 = 160$ Hz. Two types of instabilities are observed in the model: divergence and flutter. The divergence instability occurs at narrow glottal gaps ($g \gtrsim 0.1$ mm) above the critical flow velocity U_{0D} . According to the linear approach it results in a suction of the vocal folds together or their abduction without any vibration. The flutter instability takes place when the glottal gap g is wider than approximately 0.1 mm. Here, the vibrations start above the critical flow velocity U_{0F} .

The U_{0F} value is considerably different for the different ratios of the natural frequencies f_2/f_1 : when the higher natural frequency f_2 of the system approaches f_1 the instability boundaries for flutter become lower and the initialization of vibrations (and thus the phonation) is easier. As the glottal gap is widened, however, the critical flow velocities U_{0F} generally rise, requiring higher flow values to start the vibrations and making the phonation more difficult.

5.2. Phonation thresholds according to the linear model—comparison of the model to the known in vivo experimental data

The flutter stability boundaries of the model can be related to the phonation threshold values observed in humans. For that, however, it is useful to replace the flow velocity and glottal gap values by the more easily measurable values of the phonation threshold pressure (which corresponds to the critical subglottal pressure $P_{\text{sub,crit}} = P_{\text{lungs}}$) and the phonation threshold air-flow (which corresponds to the critical volume flow rate Q_{crit}). This can be done using the Bernoulli and continuity equations for the steady components of the pressure $\bar{P}(x)$ and the fluid velocity $\bar{U}(x)$

$$P_{\text{lungs}} = \bar{P}(L) + \frac{1}{2}\rho\bar{U}^2(L) \quad \text{and} \quad H_0 h U_0 = [H_0 - a(L)]h\bar{U}(L). \quad (29)$$

Assuming $\bar{P}(L) = P_{\text{sup}} = 0$, the following approximate formula can be derived to relate the pressure in lungs to the air-flow velocity:

$$P_{\text{lungs}} = \frac{1}{2}\rho U_0^2 \left\{ \frac{H_0}{H_0 - a(L)} \right\}^2. \quad (30)$$

The air-flow velocity U_0 (m/s) is simply related to the mean glottal flow volume rate Q (1/s) by the formula:

$$Q = U_0 2H_0 h. \quad (31)$$

Eqs. (30) and (31) relate these quantities to the critical flow velocity for flutter ($U_{0,\text{crit}} = U_{0F}$).

The flutter thresholds are presented in Fig. 5 showing the values of the calculated critical subglottal pressure $P_{\text{sub,crit}}$ (Pa) versus the critical flow rates Q_{crit} (1/s) for various prephonatory glottal half-gaps ($g = 0.2$ – 1 mm) and for three different ratios of the natural frequencies ($f_1/f_2 = \frac{100}{105}, \frac{150}{155}$ and $\frac{200}{205}$). The corresponding flutter (fundamental) frequencies F_0 were always found close to the frequencies f_1 and f_2 , i.e., $F_0 \simeq 100, 150$ and 200 Hz, respectively. Fig. 5 reveals the critical subglottal pressures and the critical air-flows of the model to be between 0.15 and 0.9 kPa and 0.1 and 0.9 1/s, respectively, which compares well with the range of the values found in humans (Schutte, 1980). The graph shows an increasing threshold pressure value with increasing F_0 , which is in agreement with measured data (e.g., Titze, 1992). Also, the increase of the computed subglottal pressure $P_{\text{sub,crit}}$ with the glottal half-width g (see Figs. 4 and 5)

Table 1

The comparison of the expected values P_{th} , Eq. (32) with the computed values $P_{sub,crit}$ from Eq. (24) for phonation thresholds at different fundamental frequencies F_0

F_0 (Hz)	$P_{sub,crit}$ (Pa) (computed—from Eq. (24))	P_{th} (Pa) (formula (32))	
		Males	Females
100	152	182	157
150	270	234	177
200	384	307	206

The glottal half-gap value of $g = 0.2$ mm was used for computation.

corresponds qualitatively to the findings of Chan et al. (1997) in the studies on phonation threshold pressure in a physical model of the vocal-fold mucosa.

A more detailed comparison is offered in Table 1, which relates the model thresholds to the expected phonation threshold values calculated from the formula derived by Titze (1992) and Titze et al. (2003)

$$P_{th} = 0.14 + 0.06(F_0/F_{0N})^2, \quad (32)$$

where F_0 is the fundamental (pitch) frequency and F_{0N} is a nominal (speaking) fundamental frequency ($F_{0N} = 120$ Hz for males and $F_{0N} = 190$ Hz for females). Again, the model values are not far from the expected values, suggesting the model behaviour is in reasonable agreement with reality.

5.3. Simulation of the nonlinear oscillations of the vocal folds in time domain

Whereas the threshold states can be studied with the linear model, studying the postcritical behaviour of the vocal folds including the impacts requires the nonlinear model. A typical starting phase of the on-line simulation is demonstrated in Fig. 6. The input parameters of the simulation example correspond to the unstable (flutter) region in the stability map in Fig. 4 for $f_1 = 100$ Hz and $f_2 = 105$ Hz. The motions $w_1(t)$ and $w_2(t)$ of the masses m_1 and m_2 are shown in the phase plane in Figs. 6(a) and (b), respectively, and in the time domain with a marked impact duration in each vibration period in Figs. 6(c) and (d). Initial conditions: $w_1(0) = w_2(0) = 0.1$ mm and $\dot{w}_1(0) = \dot{w}_2(0) = 0$ for the vocal-fold motion were assumed in this case. The glottal area $S(t)$, i.e., the minimal cross-sectional channel area:

$$S(t) = 2hH(x_{max}(t), t) = 2h[H_0 - y_{max}(t)] \quad \text{for noncontact phase } (y_{max} < H_0),$$

$$S(t) = 0 \quad \text{for contact phase } (y_{max} \geq H_0) \quad (33)$$

is shown in the time domain in Fig. 6(e) and the unsteady component of the glottal pressure $p(t) = \bar{p}(x, t)|_{x=L-0.5\text{ mm}}$ in Fig. 6(f). The spectrum of the glottal pressure, which contains many harmonics, is shown in Fig. 7. The motion of the vocal-fold model during one period of oscillations is animated in Fig. 8.

Fig. 9 shows the dependency of the fundamental vibration frequency $F_0 = 1/T$ (flutter frequency) on the air-flow velocity for three sets of the natural frequencies f_1 and f_2 and for three glottal half gaps g . The resulting F_0 is close to the f_1 and f_2 and slightly increases when increasing the air-flow velocity. Regular self-oscillations with stable F_0 were observed in a wide range of physiologically real input parameters (U_0, g) when the prescribed natural frequencies f_1 and f_2 were close. When the second natural frequency f_2 was increased (e.g. $f_2 = 150$ Hz) while keeping the f_1 at 100 Hz, however, the model revealed rather unstable behaviour with significant hysteresis and sudden jumps between prevailing subharmonic, regular and chaotic oscillations and impactless regimes.

Fig. 10 shows typical behaviour of the aeroelastic model for the natural frequencies $f_1 = 100$ Hz, $f_2 = 105$ Hz and the glottal half-gap $g = 0.3$ mm. The behaviour corresponds to an experiment, in which the flow rate Q was incrementally increased and decreased, and the open quotient OQ (defined as the open time of the glottis divided by the oscillatory period T) was observed. When increasing the flow rate, the self-oscillations occurred above the critical value $Q_{crit} \cong 0.18$ 1/s. At the critical value, the vibration pattern was without collisions and $OQ \cong 1$. Above this flow rate ($Q > 0.18$ 1/s) the regular self-oscillations with impacts occurred ($OQ < 1$). Further up, above the value of $Q \cong 0.43$ 1/s, the vibration regime changed from regular to quasiperiodic (subharmonic), which subsequently changed to chaotic (irregular) once the value of $Q \cong 0.46$ 1/s was crossed. For this value the corresponding subglottal pressure $P_{lungs} = 1.3$ kPa, i.e., the so-called phonation instability pressure (Jiang et al., 2003; Jiang and Titze, 1993), was obtained

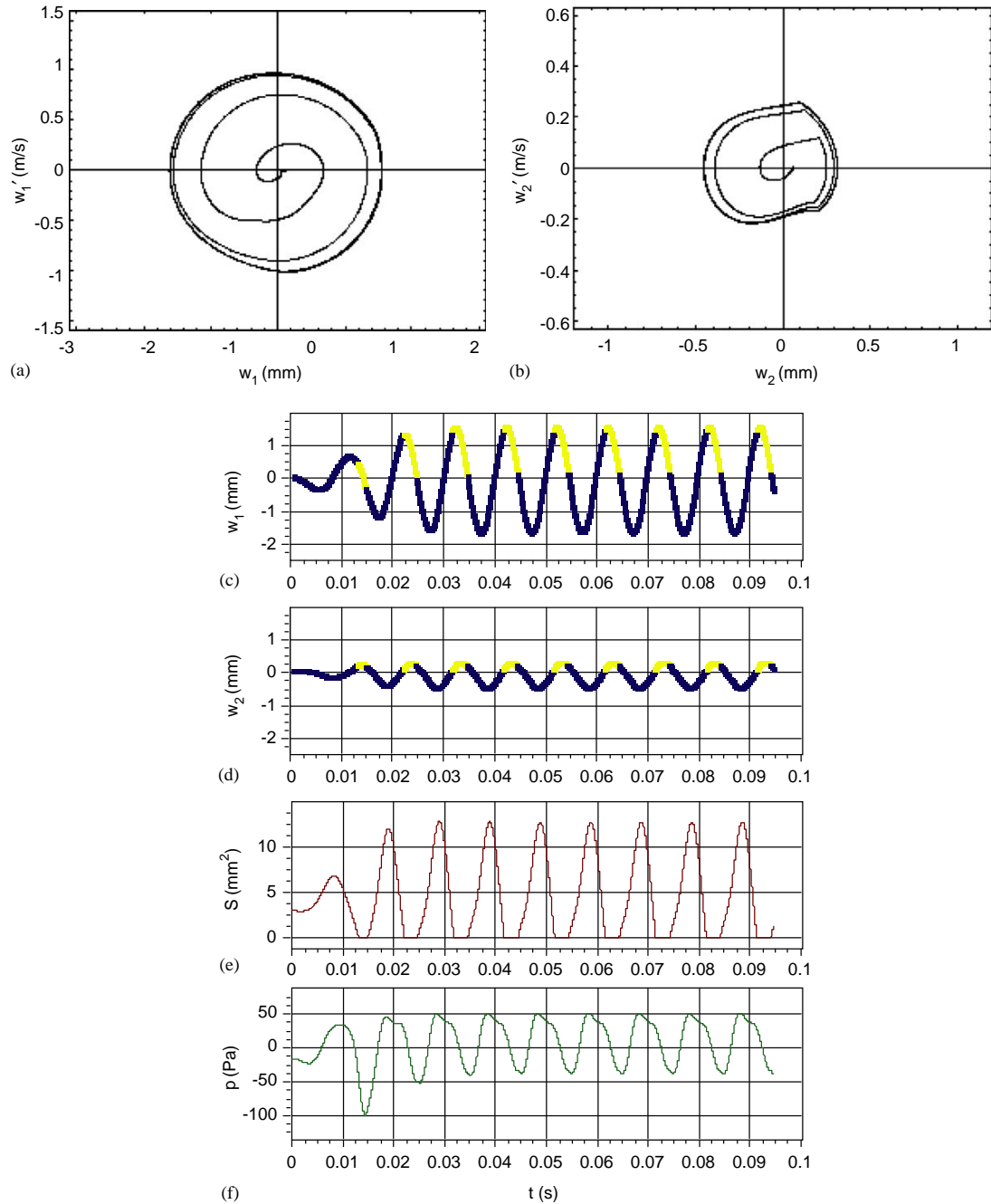


Fig. 6. Example of numerical simulation of the self-oscillations: (a) and (b) phase-plane diagrams for displacement $w_1(t)$ and $w_2(t)$, respectively; (c) and (d) displacements $w_1(t)$ and $w_2(t)$, respectively, with marked impact duration within each period of vibration; (e) glottal area $S(t)$; and (f) glottal pressure $p(t) = \tilde{p}(x, t)|_{x=L-0.5 \text{ mm}}$. The input parameters are the same as in Fig. 4, and the air-flow velocity is $U_0 = 1.6 \text{ m/s}$, glottal half-gap $g = 0.2 \text{ mm}$, prescribed natural frequencies $f_1 = 100 \text{ Hz}$, $f_2 = 105 \text{ Hz}$, time step of numerical integration $\tau = 0.02 \text{ ms}$, mean flow rate $Q = 0.181 \text{ l/s}$ and pressure in lungs $P_{\text{lungs}} = 380 \text{ Pa}$.

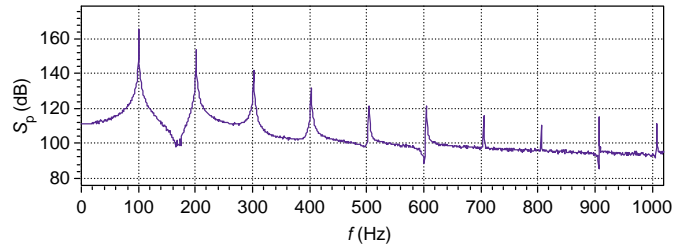


Fig. 7. Spectrum of glottal pressure $\tilde{p}(t) = \tilde{p}(x, t)|_{x=L-0.5\text{ mm}}$; all parameters as in Fig. 6.

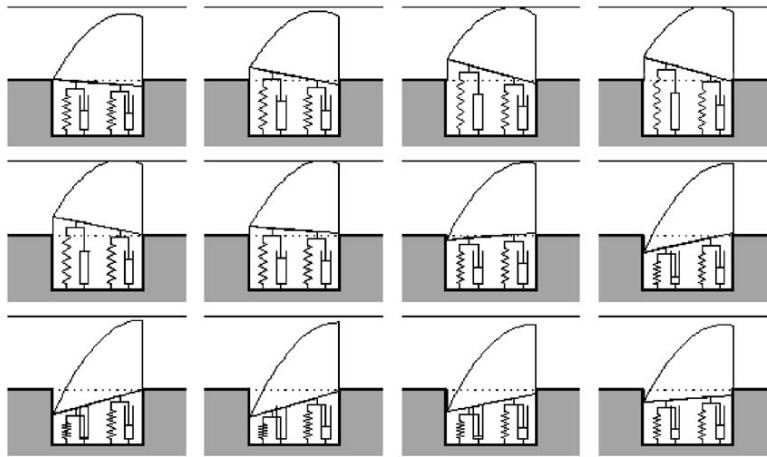


Fig. 8. Phases (animation) of the vocal-fold motion during one oscillation cycle; all parameters as in Fig. 6.

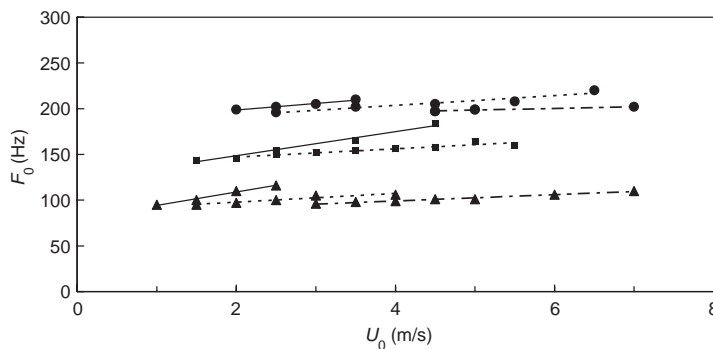


Fig. 9. Fundamental frequency F_0 for self-oscillations versus oncoming flow velocity U_0 for various natural frequencies f_1, f_2 of the vocal-fold model: \blacktriangle , $f_1 = 100\text{ Hz}, f_2 = 105\text{ Hz}$; \blacksquare , $f_1 = 150\text{ Hz}, f_2 = 155\text{ Hz}$; \bullet , $f_1 = 200\text{ Hz}, f_2 = 205\text{ Hz}$; and for several glottal half-gaps g : —, $g = 0.2\text{ mm}$; - - -, $g = 0.3\text{ mm}$; ····, $g = 0.5\text{ mm}$.

from Eq. (30). Decreasing subsequently the flow rate from the values $Q > 0.461/s$, the chaotic oscillations subsided down to $Q \cong 0.431/s$, revealing a hysteresis in the values of the phonation instability pressure. Similar, but much smaller hysteresis was observed also for the values of the critical flow rate Q_{crit} . In comparison to the normally expected values of the open quotient measured in human vocal folds, $0 < OQ < 0.5$ (Baken and Orlikoff, 2000), the OQ values from 0 to 0.7 obtained here are reasonable.

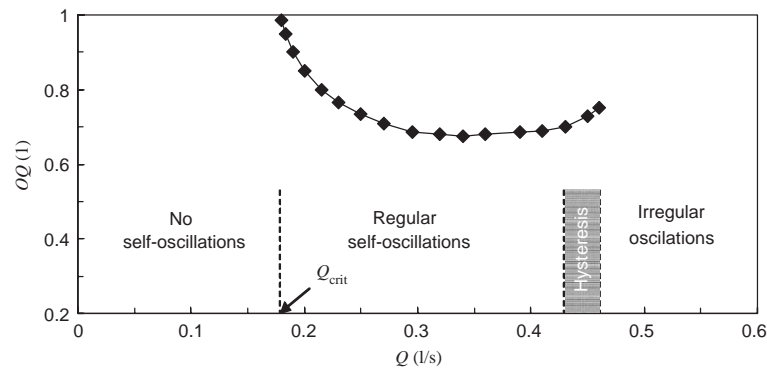


Fig. 10. Open quotient OQ for self-oscillations versus flow volume velocity Q for $f_1 = 100$ Hz, $f_2 = 105$ Hz and the glottal half-gap $g = 0.3$ mm.

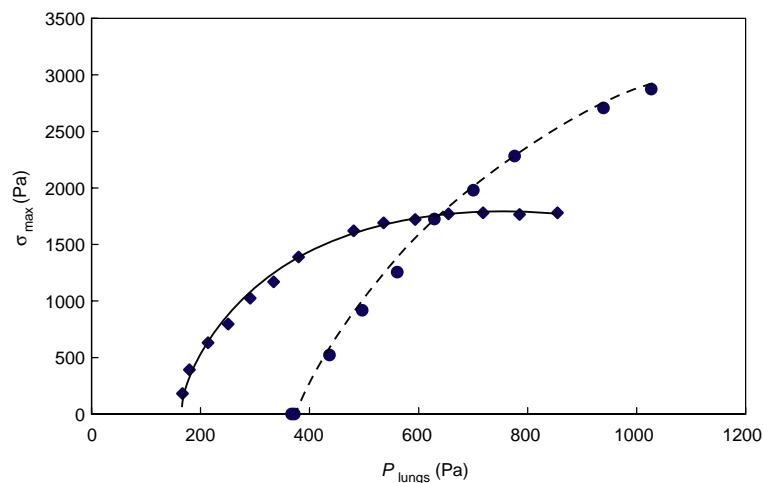


Fig. 11. Maximum impact stress during self-oscillations versus pressure in lungs for $f_1 = 100$ Hz, $f_2 = 105$ Hz and the glottal half-gaps: \blacklozenge $g = 0.2$ mm; \bullet , $g = 0.5$ mm.

Finally, to evaluate the impact forces of the vocal folds resulting from the Hertz model it is useful to relate these to the impact stress, which is easier to measure in the real vocal folds. Impact stress σ (Pa) is defined as the impact force divided by the contact area. The maximum impact stress σ_{\max} can be calculated as the maximum value in one oscillation period according to the formula (Brepta and Prokopec, 1972):

$$\sigma_{\max} = \frac{3 F_{H,\max}}{2 \pi R^2}, \quad R = \sqrt[3]{\frac{3}{4} r \frac{(1 - \nu^2)}{E} F_{H,\max}}, \quad (34)$$

where $F_{H,\max} = \max_{\tau \in (t, t+T)} F_H(\tau)$ is the maximum contact force (20) during the oscillatory period T and R is the maximum contact radius.

The calculated results are presented in Fig. 11, where the maximum impact stress σ_{\max} is shown for two glottal half-gaps of 0.2 and 0.5 mm as a function of the pressure in the lungs. Each curve begins at a corresponding value of the phonation threshold pressure (P_{th}), at which the impacts are none or very small and thus $\sigma_{\max} \cong 0$, and ends at the phonation instability pressure. The threshold pressure σ_{\max} increases with P_{lungs} and reaches its maximum at the phonation instability pressure, where for the smaller g it is possible to see a plateau. The calculated values ($0 < \sigma_{\max} < 3$ kPa) for the maximum impact stress in Fig. 11 compare well to the range of the impact stress values

measured on the real vocal folds (Jiang and Titze, 1994; Hess et al., 1998; Verdolini et al., 1999), and indicate that the impact forces implemented in the model are not far from reality.

6. General discussion and conclusion

Perhaps the most dominant feature of the current model advancement is the inclusion of the Hertz model, which expresses the impact force as a function of vocal-fold curvature and material parameters of the vocal-fold tissue. Such a feature is strategically advantageous for studying potential mechanisms of vocal-fold damage through self-exposure to vibration (Titze et al., 2003): thinner vocal folds are generally exposed to different collision forces than thicker vocal folds. In this respect, the Hertz model can be considered more realistic than the abruptly changing of spring stiffness (Ishizaka and Flanagan, 1972), which has been used in other low-order vocal-fold models. The Hertz model is noticeably easier to use than, for example, the finite-element models (Gunter, 2003), but further justification of the Hertz model is needed and the tissue parameters still need more experimental data to rely on. Nevertheless, the good correspondence of the impact stress values reported in human vocal folds with the values calculated here makes the model a promising tool for future investigations of the factors related to vocal-fold collisions.

While the curved surface of the vocal folds is suitable for implementation of the Hertz model of impacts, the mathematical expression of the aerodynamic forces is more complex than in the models with a straight profile between the lower and upper margins of the vocal folds. Consequently, features that are relatively easy to implement in straight-profile vocal-fold models, such as the dependency of the flow-separation point on the divergence of the glottal channel (Pelorson et al., 1994; Lous et al., 1998; Lucero, 1999; Drioli, 2005) require calculating the complex integral functions given in Eq. (14) for every successive time step in this model. The simulations are then highly time-consuming. Fortunately, the flow-separation point is not expected to travel very far from the upper vocal-fold edge in our model, because the particularly curved geometry reduces the divergence of the oscillating glottal channel to only an exit part, which is relatively short. To avoid excessive complexity, the flow-separation point was therefore fixed to the upper vocal-fold edge. Such a simplification appears acceptable here: the calculated stability boundaries approximately correspond to the measured thresholds of phonation in humans and reasonably relate to the conditions and mechanism for starting the vocal-fold vibration. When the instability boundaries for flutter of the aeroelastic system are crossed, the energy transfer from the air-flow to the vocal folds starts to maintain the self-oscillations.

The vibration and stability characteristics obtained for the system studied appear to be important in further research on modelling of the vocal-fold vibration, or in design of artificial aids and vocal-fold replacements for possible use in laryngology. Considering the good correspondence of the model behaviour and its output variables to behaviour and data observed in humans, the model is expected to be useful in studying phenomena and estimating values that are difficult to observe and measure in the living vocal folds.

Acknowledgements

This research has been financially supported by the Grant Agency of the Academy of Sciences of the Czech Republic, Project No. IAA20766401 *Mathematical modelling of human vocal fold oscillations*.

Appendix A

The coefficients $K_i(x)$ ($i = 1, 2, \dots, 16$) in Eq. (11) for the pressure $\tilde{p}(x, t)$ on the surface of the vibrating element were calculated using the symbolic manipulation capabilities of the *Mathematica* software and expressed in the following equations:

$$K_1(x) = -\frac{1}{2}L_1^2U_0^2[I_3'(L)]^2 + \frac{1}{2}L_1^2U_0^2[I_3'(x)]^2 - L_1U_0I_3'(L)I_4'(L) - \frac{1}{2}[I_4'(L)]^2 + L_1U_0I_3'(x)I_4'(x) + \frac{1}{2}[I_4'(x)]^2, \quad (\text{A.1})$$

$$K_2(x) = U_0\bar{U}(L)I_3'(L) - U_0\sqrt{b^2 - 4ac}\bar{U}(x)I_3'(x) - \bar{U}(L)I_5'(L) + \bar{U}(x)I_5'(x), \quad (\text{A.2})$$

$$K_3(x) = -\frac{1}{2}U_0^2[I_3'(L)]^2 + \frac{1}{2}U_0^2[I_3'(x)]^2 + U_0I_3'(L)I_5'(L) - \frac{1}{2}[I_5'(L)]^2 - U_0I_3'(x)I_5'(x) + \frac{1}{2}[I_5'(x)]^2, \quad (\text{A.3})$$

$$K_4(x) = -\frac{1}{2}[I_1'(L)]^2 + \frac{1}{2}[I_1'(x)]^2, \quad (\text{A.4})$$

$$K_5(x) = U_0 I_3(L) - U_0 I_3(x) - I_5(L) + I_5(x) - \bar{U}(L) I_2'(L) + \bar{U}(x) I_2'(x), \quad (\text{A.5})$$

$$K_6(x) = U_0 I_2'(L) I_3'(L) - U_0 I_2'(x) I_3'(x) - I_2'(L) I_5'(L) + I_2'(x) I_5'(x), \quad (\text{A.6})$$

$$K_7(x) = -\frac{1}{2} [I_2'(L)]^2 + \frac{1}{2} [I_2'(x)]^2, \quad (\text{A.7})$$

$$K_8(x) = -L_1 U_0 I_3(L) + L_1 U_0 I_3(x) - I_4(L) + I_4(x) - \bar{U}(L) I_1'(L) + \bar{U}(x) I_1'(x), \quad (\text{A.8})$$

$$K_9(x) = -L_1 U_0 I_1'(L) I_3'(L) + L_1 U_0 I_1'(x) I_3'(x) - I_1'(L) I_4'(L) + I_1'(x) I_4'(x), \quad (\text{A.9})$$

$$K_{10}(x) = U_0 I_1'(L) I_3'(L) - U_0 I_1'(x) I_3'(x) - I_1'(L) I_5'(L) + I_1'(x) I_5'(x), \quad (\text{A.10})$$

$$K_{11}(x) = -I_1'(L) I_2'(L) + I_1'(x) I_2'(x), \quad (\text{A.11})$$

$$K_{12}(x) = -L_1 U_0 \bar{U}(L) I_3'(L) + L_1 U_0 \bar{U}(x) I_3'(x) - \bar{U}(L) I_4'(L) + \bar{U}(x) I_4'(x), \quad (\text{A.12})$$

$$K_{13}(x) = L_1 U_0^2 [I_3'(L)]^2 - L_1 U_0^2 [I_3'(x)]^2 + U_0 I_3'(L) I_4'(L) - U_0 I_3'(x) I_4'(x) - L_1 U_0 I_3'(L) I_5'(L) - I_4'(L) I_5'(L) + L_1 U_0 I_3'(x) I_5'(x) + I_4'(x) I_5'(x), \quad (\text{A.13})$$

$$K_{14}(x) = -L_1 U_0 I_2'(L) I_3'(L) + L_1 U_0 I_2'(x) I_3'(x) - I_2'(L) I_4'(L) + I_2'(x) I_4'(x), \quad (\text{A.14})$$

$$K_{15}(x) = -I_1(L) + I_1(x), \quad K_{16}(x) = -I_2(L) + I_2(x), \quad (\text{A.15})$$

where

$$I_1(x) = \frac{1}{2} \int_0^x \xi(\xi - 2L_1) \bar{H}(\xi) d\xi, \quad I_2(x) = \int_0^x \xi / \bar{H}(\xi) d\xi, \quad I_3(x) = \int_0^x 1 / \bar{H}(\xi) d\xi, \\ I_4(x) = \int_0^x (\xi - L_1) \bar{U}(\xi) / \bar{H}(\xi) d\xi, \quad I_5(x) = \int_0^x \bar{U}(\xi) / \bar{H}(\xi) d\xi; \quad \bar{H}(\xi) = H_0 - a(\xi), \quad (\text{A.16})$$

$I_i'(x)$ ($i = 1, \dots, 5$) are the derivatives of the functions $I_i(x)$ and the mean flow velocity $\bar{U}(x)$ is given by the formula (9).

Appendix B

The elements of aerodynamic mass $\hat{\mathbf{M}}$, damping $\hat{\mathbf{B}}$ and stiffness $\hat{\mathbf{K}}$ matrices in the equations of motion (24) for the linear approximation are given by

$$\hat{\mathbf{M}} = \begin{bmatrix} \frac{L}{l} \left(j_1 - \frac{1}{2} i_1(1) \right) & 2j_2 - i_2(1) \\ \frac{L}{l} \left(j_{10} - \frac{1}{2} i_1(1) \right) & 2j_{11} - i_2(1) \end{bmatrix}, \quad \hat{\mathbf{B}} = \begin{bmatrix} \frac{L}{l} (2j_3 + j_7 - j_{20}) & 2(j_4 - j_7) + j_{21} \\ \frac{L}{l} (2j_{12} + j_{16} - j_{20}) & 2(j_{13} - j_{16}) + j_{21} \end{bmatrix}, \\ \hat{\mathbf{K}} = \begin{bmatrix} \frac{L}{l} (2j_5 + j_8 - j_{22}) & 2(j_6 - j_8) + j_{23} \\ \frac{L}{l} (2j_{14} + j_{17} - j_{22}) & 2(j_{15} - j_{17}) + j_{23} \end{bmatrix}, \quad (\text{B.1})$$

where

$$j_1 = \int_0^1 i_1(z)(1-z) dz, \quad j_2 = \int_0^1 i_2(z)(1-z) dz, \quad j_3 = \int_0^1 g_1(z)(1-z) dz, \quad (\text{B.2})$$

$$j_4 = \int_0^1 g_2(z)(1-z) dz, \quad j_5 = \int_0^1 g_4(z)(1-z) dz, \quad j_6 = \int_0^1 g_5(z)(1-z) dz, \quad (\text{B.3})$$

$$j_7 = \int_0^1 i_3(z)(1-z) dz, \quad j_8 = \int_0^1 g_3(z)(1-z) dz, \quad j_{10} = \int_0^1 i_1(z)z dz, \quad (\text{B.4})$$

$$j_{11} = \int_0^1 i_2(z)z \, dz, \quad j_{12} = \int_0^1 g_1(z)z \, dz, \quad j_{13} = \int_0^1 g_2(z)z \, dz, \quad (\text{B.5})$$

$$j_{14} = \int_0^1 g_4(z)z \, dz, \quad j_{15} = \int_0^1 g_5(z)z \, dz, \quad j_{16} = \int_0^1 i_3(z)z \, dz, \quad j_{17} = \int_0^1 g_3(z)z \, dz, \quad (\text{B.6})$$

$$i_1(z) = \int_0^z G^{-1}(\xi)\xi(\xi-1) \, d\xi, \quad i_2(z) = \int_0^z G^{-1}(\xi)\xi \, d\xi, \quad (\text{B.7})$$

$$i_3(z) = \int_0^z G^{-1}(\xi) \, d\xi, \quad i_4(z) = \int_0^z G^{-2}(\xi)\left(\xi - \frac{1}{2}\right) \, d\xi, \quad i_5(z) = \int_0^z G^{-2}(\xi) \, d\xi, \quad (\text{B.8})$$

$$g_1(z) = i_4(z) + \frac{1}{2}G^{-2}(z)z(z-1), \quad g_2(z) = i_5(z) + G^{-2}(z)z, \quad (\text{B.9})$$

$$g_3(z) = G^{-2}(z), \quad g_4(z) = \left(z - \frac{1}{2}\right)G^{-3}(z)z, \quad g_5(z) = G^{-3}(z), \quad (\text{B.11})$$

$$j_{20} = \frac{1}{2}i_3(1) + g_1(1), \quad j_{21} = i_3(1) - g_2(1), \quad (\text{B.12})$$

$$j_{22} = g_4(1) + \frac{1}{2}g_3(1), \quad j_{23} = g_3(1) - g_5(1), \quad (\text{B.13})$$

$$G(\xi) = 1 - \frac{a(\xi L)}{H_0}. \quad (\text{B.14})$$

References

- Adachi, S., Yu, J., 2005. Two-dimensional model of vocal fold vibration for sound synthesis of voice and soprano singing. *Journal of the Acoustical Society of America* 117, 3213–3224.
- Alipour, F., Berry, D.A., Titze, I.R., 2000. A finite-element model of vocal-fold vibration. *Journal of the Acoustical Society of America* 108, 3003–3012.
- Baken, R.J., Orlikoff, R., 2000. *Clinical Measurement of Speech and Voice*, second ed. Singular.
- Berry, D.A., 2001. Mechanism of modal and non-modal phonation. *Journal of Phonetics* 29, 431–450.
- Berry, D.A., Titze, R., 1996. Normal modes in continuum model of vocal fold tissues. *Journal of the Acoustical Society of America* 100, 3345–3354.
- Berry, D.A., Herzel, H., Titze, R., Krischer, K., 1994. Interpretation of biomechanical simulations of normal and chaotic vocal fold oscillations with empirical eigenfunctions. *Journal of the Acoustical Society of America* 95, 3595–3604.
- Brepta, R., Prokopec, M., 1972. *Wave Propagation and Impacts in Solids*. Academia, Praha (in Czech).
- Cancelli, C., Pedley, T.J., 1985. A separated-flow model for collapsible-tube oscillations. *Journal of Fluid Mechanics* 157, 375–404.
- Chan, R.W., Titze, I.R., Titze, M.R., 1997. Further studies of phonation threshold pressure in a physical model of the vocal fold mucosa. *Journal of the Acoustical Society of America* 101, 3722–3727.
- Deverge, M., Pelorson, X., Vilain, C., Lagree, P.Y., Chentouf, F., Willems, J., Hirschberg, A., 2003. Influence of collision on the flow through in-vitro rigid models of the vocal folds. *Journal of the Acoustical Society of America* 114, 3354–3362.
- De Vries, M.P., Schutte, H.K., Verkerke, G.J., 1999. Determination of parameters for lumped parameter models of the vocal folds using a finite-element method approach. *Journal of the Acoustical Society of America* 106, 3620–3628.
- Drioli, C., 2005. A flow waveform-matched low-dimensional glottal model based on physical knowledge. *Journal of the Acoustical Society of America* 117, 3184–3195.
- Gunter, H.E., 2003. A mechanical model of vocal-fold collision with high spatial and temporal resolution. *Journal of the Acoustical Society of America* 113, 994–1000.
- Herzel, H., Knudsen, C., 1995. Bifurcations in a vocal fold model. *Nonlinear Dynamics* 7, 53–64.
- Hess, M.M., Verdolini, K., Bierhals, W., Mansmann, U., Gross, M., 1998. Endolaryngeal contact pressures. *Journal of Voice* 12, 50–67.
- Horáček, J., Švec, J.G., 2002a. Aeroelastic model of vocal-fold-shaped vibrating element for studying the phonation threshold. *Journal of Fluids and Structures* 16, 927–951.
- Horáček, J., Švec, J.G., 2002b. Instability boundaries of a vocal fold modelled as a flexibly supported rigid body vibrating in a channel conveying fluid. In: *Proceedings of the Fifth International Symposium on FSI, AE and FIV + N, 2002 ASME International Mechanical Engineering Congress*, November 2002, New Orleans, Louisiana, USA, IMECE 2002-32285, pp. 17–22.
- Ikeda, T., Matsuzaki, Y., Aomatsu, T., 2001. A numerical analysis of phonation using a two-dimensional flexible channel model of the vocal folds. *ASME Journal of Biomechanical Engineering* 123, 571–579.

- Ishizaka, K., Flanagan, J.L., 1972. Synthesis of voiced sounds from a two-mass model of the vocal cords. *The Bell System Technical Journal* 51, 1233–1268.
- Jiang, J., Titze, I., 1993. A methodological study of hemilaryngeal phonation. *Laryngoscope* 103, 872–882.
- Jiang, J., Titze, I., 1994. Measurement of vocal fold intraglottal pressure and impact stress. *Journal of Voice* 8, 132–144.
- Jiang, J.J., Zhang, Yu., Ford, Ch.N., 2003. Nonlinear dynamics of phonations in excised larynx experiments. *Journal of the Acoustical Society of America* 114, 2198–2205.
- Kaneko, T., Uchida, K., Suzuki, H., Komatsu, K., Kanesaka, T., Kobayashi, N., Naito, J., 1981. Mechanical properties of the vocal fold: measurement in vivo. In: Stevens, K.N., Hirano, M. (Eds.), *Vocal Fold Physiology*. University of Tokyo Press, Tokyo, pp. 365–376.
- Kaneko, T., Komatsu, K., Suzuki, H., Kanesaka, T., Masuda, T., Numata, T., Naito, J., 1983. Mechanical properties of the human vocal fold resonance characteristics in living humans and in excised larynges. In: Titze, I.R., Scherer, R.C. (Eds.), *Vocal Fold Physiology: Biomechanics, Acoustics and Phonatory Control*. The Denver Center for the Performing Arts, Denver, CO, USA, pp. 304–317.
- Kaneko, T., Masuda, T., Shimada, A., Suzuki, H., Hayasaki, K., Komatsu, K., 1987. Resonance characteristics of the human vocal fold in vivo and in vitro by an impulse excitation. In: Baer, T., Sasaki, C., Harris, K.S. (Eds.), *Laryngeal Function in Phonation and Respiration*. A College-Hill Press, Little, Brown and Company, Boston, pp. 349–365.
- Kob, M., 2002. *Physical Modelling of the Singing Voice*. Logos-Verlag, Berlin.
- LaMar, M.D., Qi, Y., Xin, J., 2003. Modeling vocal fold motion with a hydrodynamic semicontinuum model. *Journal of the Acoustical Society of America* 114, 455–464.
- Liljencrants, J., 1991. A translating and rotating mass model of the vocal folds. In: *Speech Transmission Laboratory—Quarterly Progress and Status Report 1/1991*, Stockholm, Sweden, pp. 1–18.
- Lous, N.J.C., Hofmans, G.C.J., Veldhuis, R.N.J., Hirschberg, A., 1998. A symmetrical two-mass vocal-fold model coupled to vocal tract and trachea, with application to prosthesis design. *Acustica—Acta Acustica* 84, 1135–1150.
- Lucero, J.C., 1999. A theoretical study of the hysteresis phenomenon at vocal fold oscillation onset–offset. *Journal of the Acoustical Society of America* 105, 423–431.
- Norton, M.P., 1989. *Fundamentals of Noise and Vibration Analysis for Engineers*. Cambridge University Press, Cambridge.
- Pelorsson, X., Hirschberg, A., Van Hase, R.R., Wijnands, A.P.J., Auregan, Y., 1994. Theoretical and experimental study of quasisteady-flow separation within the glottis during phonation. Application to a modified two-mass model. *Journal of the Acoustical Society of America* 96, 3416–3431.
- Püst, L., Peterka, F., 2003. Impact oscillator with Hertz's model of contact. *Meccanica* 38, 99–114.
- Schutte, H.K., 1980. The efficiency of voice production. Doctoral dissertation, Groningen.
- Sciamarella, D., d'Alessandro, C., 2004. On the acoustic sensitivity of a symmetrical two-mass model of the vocal folds to the variation of control parameters. *Acta Acustica united with Acustica* 90, 746–761.
- Story, B.H., Titze, I.R., 1995. Voice simulation with a body cover model of the vocal folds. *Journal of the Acoustical Society of America* 97, 1249–1260.
- Stronge, W.J., 2000. *Impact Mechanics*. Cambridge University Press, Cambridge, UK.
- Švec, J.G., Horáček, J., Šram, F., Veselý, J., 2000. Resonance properties of the vocal folds: in vivo laryngoscopic investigation of the externally excited laryngeal vibrations. *Journal of the Acoustical Society of America* 108, 1397–1407.
- Thomson, S.L., Mongeau, L., Frankel, S.H., 2003. Physical and numerical flow-excited vocal fold models. In: *Third International Workshop MAVEBA 2003*, Firenze University Press, pp. 147–150.
- Titze, I.R., 1989. Physiologic and acoustic differences between male and female voices. *Journal of the Acoustical Society of America* 85, 1699–1707.
- Titze, I.R., 1992. Phonation threshold pressure: a missing link in glottal aerodynamics. *Journal of the Acoustical Society of America* 91, 2928–2934.
- Titze, I.R., Švec, J.G., Popolo, P.S., 2003. Vocal dose measures: quantifying accumulated vibration exposure in vocal fold tissues. *Journal of Speech, Language and Hearing Research* 46, 919–932.
- Verdolini, K., Hess, M.M., Titze, I.R., Bierhals, W., Gross, M., 1999. Investigation of vocal fold impact stress in human subjects. *Journal of Voice* 13, 184–202.
- Wolfram, S., 2003. *The Mathematica Book*, fifth ed. Wolfram Media.



Finite Element Modeling of Airflow During Phonation

P. Šidlof^{a,b,*}, E. Lunéville^c, C. Chambeyron^c, O. Doaré^d, A. Chaigne^d,
J. Horáček^b

^aTechnical University of Liberec, Faculty of Mechatronics, Informatics and Interdisciplinary Studies,
Studentská 2, 461 17 Liberec 1, Czech Republic

^bInstitute of Thermomechanics, Academy of Sciences of the Czech Republic, Dolejškova 5, 182 00 Praha 8, Czech Republic

^cÉcole Nationale Supérieure de Techniques Avancées, Unité de Mathématiques Appliquées, 32 Boulevard Victor, 75739 Paris, France

^dÉcole Nationale Supérieure de Techniques Avancées, Unité de Mécanique, Chemin de la Humière, 91761 Palaiseau cedex, France

Received 31 August 2009; received in revised form 7 July 2010

Abstract

In the paper a mathematical model of airflow in human vocal folds is presented. The geometry of the glottal channel is based on measurements of excised human larynges. The airflow is modeled by nonstationary incompressible Navier-Stokes equations in a 2D computational domain, which is deformed in time due to vocal fold vibration. The paper presents numerical results and focuses on flow separation in glottis. Quantitative data from numerical simulations are compared to results of measurements by Particle Image Velocimetry (PIV), performed on a scaled self-oscillating physical model of vocal folds.

© 2010 University of West Bohemia. All rights reserved.

Keywords: vocal folds, airflow, numerical modeling, ALE, flow separation

1. Introduction

Human voice is created by passage of airflow between vocal folds, which are located in the upper part of larynx. The physiology of the vocal folds is complex; a thorough anatomic and functional information comprehensible to an engineer can be found e.g. in the monograph of Titze [23]. Basically, the vocal folds (formerly called vocal cords) are two symmetric soft tissue structures fixed between the thyroid and arytenoid cartilages. They are composed of the thyroarytenoid muscle and ligament covered by mucosa.

When air is expired from lungs, the constriction formed by the vocal folds (which is called *glottis*) induces acceleration of the flow. Under certain circumstances (subglottal pressure, glottal width, longitudinal tension in the thyroarytenoid and ligament), fluid-structure interaction between the elastic structure and airflow may invoke vocal fold oscillations. It is important that the vibration is a passive process – when voicing, no sort of periodic muscle contraction is performed.

In mathematical modeling of vocal fold vibration, a classical approach is to reduce the mechanical part of the problem into a small system of rigid masses, springs and dampers, which is further coupled to a simplified flow model (see e.g. the fundamental work of Ishizaka & Flanagan from 1972 [10], or for example the models of Titze or Pelorson [22, 16]). The models often comprise semiempirical relations and constants. Although these lumped-parameter models are still widely used and can provide useful and computationally inexpensive data in specific cases,

*Corresponding author. Tel.: +420 485 353 015, e-mail: sidlof@it.cas.cz.

P. Šidlof et al. / Applied and Computational Mechanics 4 (2010) 121–132

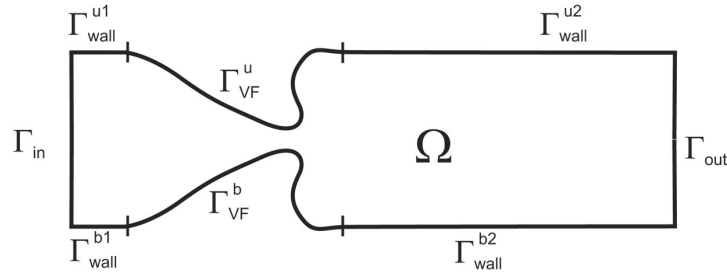


Fig. 1. Sketch of the computational domain and definition of its boundary parts

some more complex techniques have also been employed in recent years [21, 5, 28]. These are related mainly to the boom of finite element and finite volume codes, which allow realistic modeling both of the flow and of the elastic deformations.

Within this paper, a finite element model of airflow through vibrating vocal folds is described. The model enables to study the development of pressure and velocity fields along the vibrating vocal folds, observe the behavior of the pulsating glottal jet and vortex dynamics downstream glottis. In particular, the mathematical model is used to assess flow separation in glottis – a phenomenon, which is not yet fully understood, even though it is of high importance and interest for vocal fold researchers. The numerical results are compared with experimental data, obtained on a physical self-oscillating vocal fold model by means of Particle Image Velocimetry (PIV) measurements.

2. Methods

2.1. Mathematical model

In the first approximation, it can be assumed that the flow field in the glottal region does not change significantly along the anterior-posterior axis. Thus, it seems reasonable to investigate only 2D flow fields in the coronal plane. In the mathematical model, this approach facilitates substantially the numerical computation: the 3D and 2D models do not differ in principle, but the latter requires much less computational power. The Mach numbers encountered in phonation are rather low (in the order of magnitude, $Ma = 0.1$). This allows to model the flow as incompressible. In the works on phonatory airflow, there has been controversy whether the viscous effects play an important role or not. In the model presented here, viscosity was taken into account.

In the following, we are going to describe the flow of an incompressible viscous Newtonian fluid in a bounded 2D domain. Let $\Omega_t \subset \mathbb{R}^2$ be the domain occupied by the fluid (the subscript ‘ t ’ is used to denote the time-variable domains). The boundary $\Gamma_t = \partial\Omega_t$ is composed of four non-intersecting parts (see Fig. 1):

$$\Gamma_t = \Gamma_{in} \cup \Gamma_{out} \cup \Gamma_{wall} \cup \Gamma_{VF,t}, \quad (1)$$

where Γ_{in} and Γ_{out} are virtual boundaries representing the inlet and outlet, $\Gamma_{wall} = \Gamma_{wall}^{b1} \cup \Gamma_{wall}^{b2} \cup \Gamma_{wall}^{u1} \cup \Gamma_{wall}^{u2}$ is the fixed wall, which is not a function of time, and $\Gamma_{VF,t} = \Gamma_{VF,t}^b \cup \Gamma_{VF,t}^u$ stands for the surface of the moving vocal folds. The superscripts ‘ b ’ and ‘ u ’ denote the bottom and upper parts, respectively.

The flow is modeled by incompressible non-stationary Navier-Stokes equations in 2D, which are numerically solved by the finite element method (FEM). The main complication

P. Šidlof et al. / Applied and Computational Mechanics 4 (2010) 121–132

is that due to vocal fold vibration, the computational domain Ω_t changes in time (which implies that the mesh is deformed, too); this would make the straightforward FE discretization inconvenient. Therefore the equations are reformulated using arbitrary Lagrangian-Eulerian (ALE) approach [15]. The ALE-form of the Navier-Stokes equations reads

$$\begin{aligned} \frac{D^A}{Dt} \mathbf{u} + [(\mathbf{u} - \mathbf{w}) \cdot \nabla] \mathbf{u} + \nabla p - \nu \Delta \mathbf{u} &= 0 & \text{in } \Omega_t \\ \operatorname{div} \mathbf{u} &= 0 & \text{in } \Omega_t \end{aligned} \quad , \quad (2)$$

where \mathbf{u} is flow velocity, p stands for kinematic pressure, ν is kinematic viscosity. The vector \mathbf{w} denotes the *domain velocity* (velocity of the meshpoints) and $\frac{D^A}{Dt}$ is so-called *ALE-derivative*, which can be easily discretized even in time-dependent computational domains.

Setting the boundary conditions represents a rather delicate question. On the outlet Γ_{out} , a common choice is the “do-nothing condition” [24]

$$\begin{aligned} -\nu \frac{\partial \mathbf{u}}{\partial \mathbf{n}}(t, \mathbf{x}) + p(t, \mathbf{x}) \mathbf{n}(\mathbf{x}) &= p_{ref} \mathbf{n}(\mathbf{x}) \\ \text{for } \mathbf{x} \in \Gamma_{out}, t \in [0, T] \end{aligned} \quad , \quad (3)$$

where $\partial/\partial \mathbf{n}$ denotes the normal derivative, $\mathbf{n}(\mathbf{x})$ is the unit outer normal to Γ_{out} and p_{ref} is a reference pressure. In certain cases, however, this condition becomes too vague – it allows the flow returning to the domain Ω_t through Γ_{out} (e.g. when a large vortex arrives to Γ_{out}). Thus, the total influx into the domain Ω_t can grow infinite and the numerical scheme tends to diverge. To suppress this inconvenience, the boundary condition (3) can be modified during the derivation of the weak form of the equations.

On the inlet Γ_{in} , two conditions were tested: either a parabolic profile of the vertical velocity component, or the (modified) do-nothing condition as on Γ_{out} . The difference $p_{ref}^{in} - p_{ref}^{out}$ then represents the transglottal pressure (approximately equal to the lung pressure during phonation), which drives the flow.

Since we use a viscous model, the “no-slip condition”

$$\mathbf{u}(t, \mathbf{x}) = \mathbf{0} \quad \text{for } \mathbf{x} \in \Gamma_{wall}, t \in [0, T] \quad (4)$$

is prescribed on the fixed walls Γ_{wall} . On the moving vocal fold surfaces, the velocity of the fluid particles must be equal to the velocity of the moving surface, which is given by the domain velocity \mathbf{w} .

For the structural part of the problem, the real, continuously elastic vocal fold was modeled by a rigid body supported by two springs and dampers (similarly as in previous work [9]). The kinematic model reflects two basic modes of the vocal fold motion: vertical shift and rocking. It is not difficult to derive the equations of motion of the system in a standard form

$$\mathbb{M} \ddot{\mathbf{q}} + \mathbb{B} \dot{\mathbf{q}} + \mathbb{K} \mathbf{q} = \mathbf{F} \quad , \quad (5)$$

where \mathbb{M} , \mathbb{B} , \mathbb{K} are the mass, damping and stiffness matrices, \mathbf{q} denotes the vector of generalized coordinates (shift and rotation) and $\mathbf{F} = (F_f, M_f)^T$ stands for the vector of generalized forces (vertical force and momentum), induced on the boundary $\Gamma_{VF,t}$ by the flow.

The full coupled problem can be solved in the following procedure: Assuming that the solution of the Navier-Stokes equations (2) on a specific time level t and domain Ω_t is known,

P. Šidlof et al. / Applied and Computational Mechanics 4 (2010) 121–132

the total vertical force F_f and momentum M_f , by which the fluid acts on the vocal fold, is given by the integration of the stress vector $\boldsymbol{\tau}$ over the surface of the moving vocal fold:

$$F_f = \int_{\Gamma_{VF,t}^b} \tau_2 \, d\sigma = \int_{\Gamma_{VF,t}^b} \sum_{j=1}^2 \mathbb{T}_{2j} n_j \, d\sigma, \quad (6)$$

$$M_f = \int_{\Gamma_{VF,t}^b} \sum_{l=1}^2 \left(\mathbb{T}_{1l} n_l x_2 - \mathbb{T}_{2l} n_l x_1 \right) d\sigma. \quad (7)$$

Here \mathbb{T} is the stress tensor and \boldsymbol{n} the unit outer normal to the vocal fold surface. The stress tensor \mathbb{T} is calculated from the pressure and velocity fields $p(t, \boldsymbol{x})$ and $\boldsymbol{u}(t, \boldsymbol{x})$ on time level t according to the constitutive relation valid for Newtonian fluids.

Once the excitation forces are known, it is possible to proceed to the next time level $t + \tau$ by performing one step of the Runge-Kutta method in the time-discretized equations of motion. This yields new coordinates of the structure, which uniquely determine the shape of the domain $\Omega_{t+\tau}$. With the knowledge of the solution from the previous two time levels, the Navier-Stokes equations can be numerically solved on the new time level $t + \tau$ and new domain $\Omega_{t+\tau}$ using the finite element method.

2.2. Discretization and numerical solution

The finite element method, which is widely used for numerical solution of elliptic and parabolic partial differential equations for instance in structural mechanics, seems to be somewhat less popular in computational fluid dynamics (CFD); actually most of the commercial CFD codes employ some variant of the finite volume method. This is caused by the computational costs of the FEM (with the same number of mesh elements, lower-order methods – such as the finite volume method – offer less accurate, but less computationally expensive solutions), but also by the fact, that for high Reynolds numbers the standard finite element method does not give reliable results. To understand this unfavorable feature, it is necessary to realize that for high-velocity flows the viscous term in the Navier-Stokes equations becomes insignificant against the convective term. It is well known that for such systems with dominating convection (sometimes also called singularly perturbed problems), standard finite element method is not suitable as it produces nonphysical, “spurious” oscillations in the solution [8]. There exist several stabilization concepts, which can help overcome this numerical problem, namely streamline diffusion method (alias streamline upwind Petrov-Galerkin method, SUPG), Galerkin least-squares method or residual-based stabilizations [12]. These methods, however, require a very careful choice of the stabilization parameters. Since the Reynolds numbers of typical glottal flows do not usually exceed values of $\text{Re} = 1\,000 - 5\,000$, the standard, non-stabilized finite element numerical scheme was used in this study.

For the numerical solution of the Navier-Stokes equations using FEM, these need first to be semidiscretized in time. Let us define the discrete time level $t_i = i \tau$, where τ is a constant timestep, and the approximate flow velocity, pressure and domain velocity on this time level

$$\boldsymbol{u}^i(\boldsymbol{x}) \approx \boldsymbol{u}(t_i, \boldsymbol{x}), p^i(x) \approx p(t_i, \boldsymbol{x}), \boldsymbol{w}^i(x) \approx \boldsymbol{w}(t_i, \boldsymbol{x}), \boldsymbol{x} \in \Omega_{t_i}. \quad (8)$$

Using a second-order backward difference in time for the ALE-derivative, we get the semi-discrete Navier-Stokes equations for the functions $\boldsymbol{u}^{n+1} : \Omega_{t_{n+1}} \mapsto \mathbb{R}^2$ and $p^{n+1} : \Omega_{t_{n+1}} \mapsto \mathbb{R}$

P. Šidlof et al. / Applied and Computational Mechanics 4 (2010) 121–132

$$\frac{3 \mathbf{u}^{n+1}}{2 \tau} + [(\mathbf{u}^{n+1} - \mathbf{w}^{n+1}) \cdot \nabla] \mathbf{u}^{n+1} + \nabla p^{n+1} - \nu \Delta \mathbf{u}^{n+1} = \frac{4 \hat{\mathbf{u}}^n - \hat{\mathbf{u}}^{n-1}}{2 \tau}$$

$$\operatorname{div} \mathbf{u}^{n+1} = 0, \quad (9)$$

where $\hat{\mathbf{u}}^i(\mathbf{x}^{n+1}) = \mathbf{u}^i(A_{t_i}(A_{t_{n+1}}^{-1}(\mathbf{x}_{n+1})))$ and A_{t_i} is the ALE-mapping of the undeformed, “reference” domain Ω_0 onto the current, deformed domain Ω_{t_i} .

Due to the presence of the nonlinear, convective term $[(\mathbf{u}^{n+1} - \mathbf{w}^{n+1}) \cdot \nabla] \mathbf{u}^{n+1}$ in the Navier-Stokes equations (9), the system cannot be solved in a straightforward way. Instead, it is first necessary to linearize the equations, i.e. to replace the first occurrence of the sought velocity vector \mathbf{u}^{n+1} by some vector \mathbf{u}^* , which is already known:

$$[(\mathbf{u}^{n+1} - \mathbf{w}^{n+1}) \cdot \nabla] \mathbf{u}^{n+1} \approx [(\mathbf{u}^* - \mathbf{w}^{n+1}) \cdot \nabla] \mathbf{u}^{n+1}. \quad (10)$$

For quasisteady flows it is possible to use the solution from the previous timestep \mathbf{u}^n . To increase precision for the non-stationary flow it is better to employ an iteration process, using \mathbf{u}^n as the first iteration.

To simplify the equations, let us further denote $\mathbf{u} \equiv \mathbf{u}^{n+1}$, $\mathbf{w} \equiv \mathbf{w}^{n+1}$, $p \equiv p^{n+1}$, $\Omega \equiv \Omega_{t_{n+1}}$ and $\Gamma_{VF} \equiv \Gamma_{VF, t_{n+1}}$. The starting point for the finite element discretization of any system of partial differential equations is its weak (variational) form. It is obtained by multiplying the classical form (9) by an arbitrary test function from the relevant functional space (see [8] for details) and integrating over Ω :

$$\frac{3}{2\tau} \int_{\Omega} \mathbf{u} \cdot \mathbf{v} \, dx + \int_{\Omega} \left([(\mathbf{u}^* - \mathbf{w}) \cdot \nabla] \mathbf{u} \right) \cdot \mathbf{v} \, dx + \int_{\Omega} \nabla p \cdot \mathbf{v} \, dx -$$

$$\int_{\Omega} \nu \Delta \mathbf{u} \cdot \mathbf{v} \, dx = \frac{1}{2\tau} \int_{\Omega} (4\hat{\mathbf{u}}^n - \hat{\mathbf{u}}^{n-1}) \cdot \mathbf{v} \, dx \quad \forall \mathbf{v} \in \mathbf{W}, \quad (11)$$

$$\int_{\Omega} q \operatorname{div} \mathbf{u} \, dx = 0 \quad \forall q \in Q. \quad (12)$$

In our case, the pressure solution is from the space of square-integrable functions $p \in L^2(\Omega)$, the velocity solution will be sought in the Sobolev space $\mathbf{u} \in \mathbf{Y} = (H^1(\Omega))^2$, and the velocity and pressure test function spaces \mathbf{W} and Q are defined as follows:

$$\mathbf{W} = \{ \mathbf{v} \in \mathbf{Y} : \mathbf{v}|_{\Gamma_{in} \cup \Gamma_{wall} \cup \Gamma_{VF}} = 0 \} \quad (13)$$

$$Q = L^2(\Omega). \quad (14)$$

Using Green’s theorem, the boundary conditions and the properties of the test functions (see [18] for details), we get the ultimate form of the weak semidiscretized ALE Navier-Stokes equations:

$$\frac{3}{2\tau} \int_{\Omega} \mathbf{u} \cdot \mathbf{v} \, dx + \nu \int_{\Omega} \nabla \mathbf{u} \cdot \nabla \mathbf{v} \, dx - \int_{\Omega} p \operatorname{div} \mathbf{v} \, dx + \frac{1}{2} \int_{\Omega} \left([(\mathbf{u}^* - 2\mathbf{w}) \cdot \nabla] \mathbf{u} \right) \cdot \mathbf{v} \, dx$$

$$- \frac{1}{2} \int_{\Omega} \left([\mathbf{u}^* \cdot \nabla] \mathbf{v} \right) \cdot \mathbf{u} \, dx + \frac{1}{2} \int_{\Gamma_{out}} (\mathbf{u}^* \cdot \mathbf{n})^+ \mathbf{u} \cdot \mathbf{v} \, dx =$$

$$= \frac{1}{2\tau} \int_{\Omega} (4\hat{\mathbf{u}}^n - \hat{\mathbf{u}}^{n-1}) \cdot \mathbf{v} \, dx - \int_{\Gamma_{out}} p_{ref} \mathbf{v} \cdot \mathbf{n} \, d\sigma \quad \forall \mathbf{v} \in \mathbf{W}, \quad (15)$$

$$\int_{\Omega} q \operatorname{div} \mathbf{u} \, dx = 0 \quad \forall q \in Q, \quad (16)$$

P. Šidlof et al. / Applied and Computational Mechanics 4 (2010) 121–132

where $(\mathbf{u}^* \cdot \mathbf{n})^+$ denotes the positive part of the scalar product introduced to stabilize the outflow boundary condition.

The weak Navier-Stokes equations (15,16) were discretized in space using standard Galerkin finite element method on a triangular mesh with Taylor-Hood P^2/P^1 (quadratic for velocity, linear for pressure) or P^3/P^2 (cubic for velocity, quadratic for pressure) elements. The mesh was refined near glottis in order to resolve better for large gradients in the solution and for flow separation downstream glottis.

The numerical solution of the discretized problem was implemented using an open-source library Mélima [14]. For the solution of the resulting linear system (with typically 200 000 degrees of freedom), a direct linear solver UMFPack [4] was used. This package, which is used as a default sparse matrix solver in recent versions of Matlab, uses a direct multifrontal method, suitable for generally nonsymmetric sparse matrices. Its performance may be boosted by installation of a suitable BLAS (Basic Linear Algebra Subsystem). On Intel processors, the overall performance of the binary code can be further improved by compiling the libraries and the program source code with Intel Fortran Compiler (instead of GNU Fortran compiler, such as f77 or gfortran), and by setting appropriate optimization flags.

2.3. Geometry of the glottal channel

The vocal fold geometry plays a crucial role in phonation. The vocal fold shape is directly related to the mass distribution in the vibrating elastic element, which influences strongly the vibration eigenmodes [2]. Besides, vocal folds constitute the channel profile and thus their shape has a dramatic impact on glottal aerodynamics – a small variation of the vocal fold shape or position may change the flow regime and the resulting aerodynamic forces, which excite the system [21, 25]. However, quantitative information on the phonatory shape of human vocal folds has been scarce. Accurate data are lacking especially on the coronal cross-sectional shape of the vocal folds.

Many of the current vocal fold models (both mathematical and physical) use the geometry specified originally by Scherer [17]. The major advantage of this so-called M5 shape is that it is simple and easily parametrizable. However, it seems to be based on somewhat arbitrary information, not on precise anatomic data. The geometry of the mathematical model presented in this paper, i.e. the 2D shape of the vocal folds and adjoining vocal tract, was specified according to measurements on excised human larynges. Details can be found in [20].

2.4. Physical model of vocal folds

To validate the results from the mathematical model, a self-oscillating physical model of vocal folds was fabricated at ENSTA Paris. Detailed description of this model and results of the measurements can be found e.g. in [18, 19]. Let us just say here that it was designed as a vocal-fold-shaped element vibrating in the wall of a rectangular wind tunnel. The model is 4 : 1 scaled; to avoid difficulties with asymmetric vocal fold vibration, one of the vocal folds is static. Best possible effort was made to keep the important dimensionless parameters (Reynolds and Strouhal numbers) of the model close to the real situation. The shape of the vocal folds was specified in the same fashion as in the mathematical model.

The experimental setup was equipped with a PIV system (Dantec – New Wave Research Solo III) for measuring airflow velocity fields, an ultrasonic flowmeter (GE Panametric GC 868) measuring the flow rate, and two B&K 4507C accelerometers fixed under the vibrating vocal fold used to record mechanical vibration. The acoustic data were measured by dynamic pressure transducers (Validyne DP15TL) and measuring microphones (G.R.A.S. 1/8" type 2692).

P. Šidlof et al. / Applied and Computational Mechanics 4 (2010) 121–132

3. Results

The numerical model was used to perform a series of computations for a broad range of parameters, representing various types of phonation. Here we will demonstrate results of one specific numerical simulation, whose parameters were set to match the vibration pattern of one of the most stable modes of the physical model: forced 2DOF vibration with frequency $f = 10.9$ Hz (corresponding to about $f = 90$ Hz in lifesize), periodic oscillation with an amplitude of about 1.5 mm without vocal fold collisions (modeling breathy phonation or whispering) and transglottal pressure $\Delta p = 45$ Pa (180 Pa in lifesize). The computational mesh was triangular and consisted of 16537 P^3/P^2 (bicubic for velocity, parabolic for pressure) elements. The nonstabilized finite element scheme implemented on this mesh allows to reach Reynolds numbers of about 5 000, which is sufficient to model the values observed in human vocal folds. Timestep of the numerical simulation was set to $\tau = 0.5$ ms.

Fig. 2 demonstrates the calculated velocity fields for these parameters at four time instants of one vocal fold oscillation cycle. We see that the airflow separates from the vocal fold wall shortly downstream the narrowest cross-section and forms a jet. The vortices, which shed from the shear layer of the jet, propagate slowly downstream and interact with the jet and among themselves. Instead of remaining symmetric with regard to the channel axis, the jet tends to adhere to one of the vocal fold surfaces by Coanda effect. This effect occurs very distinctly when the glottis closes. The glottal jet skews from the straight direction when glottis is widely open, too, but in this case it does so rather due to interaction with vortex structures downstream glottis.

The flow velocity fields calculated by the numerical code can be directly compared to results of PIV measurements on the physical model. However, it is necessary to realize that we handle 2D vector data from an inherently nonstationary process. Thus, it is nearly always possible to find time instants where the results appear to match well, but also those where the velocity fields look different. Objectively, it can be stated that the result of the numerical simulation shown in Fig. 2 matches with the experimental results in terms of maximum jet velocity ($u_{max} = 12$ m/s in numerical results, $u_{max} = 11$ m/s in PIV measurements) and general flow structure.

Unlike the global, time-developing velocity fields, there are certain features of the glottal flow which may be extracted from the results and compared directly. One of them, which is of high interest for vocal fold researchers, is the position of the flow separation point, which was identified and processed from both numerical and experimental results.

In many simplified models of airflow in vocal folds, the position of the separation point is either fixed to the superior margin of the vocal folds [26, 27] or supposed to move along the divergent part of glottis. In the latter case, its position is usually specified using a semiempirical criterion, which states that the jet separates at the position where the channel cross-section A reaches

$$A/A_{min} = FSR, \quad (17)$$

where A_{min} is the minimum glottal cross-section and FSR so-called “flow separation ratio”. In numerous published papers, the ratio is assumed to remain constant during vocal fold oscillation cycle, and various values of FSR are proposed: Deverge et al. [6] sets $FSR = 1.2$ (based on the pioneer work of Pelorson [16] and private communication with Liljencrants), Lucero et al. [13] uses $FSR = 1.1$. In their comparative study, Decker [5] tested different values of the flow separation ratio: $FSR = 1.2$ and $FSR = 1.47$ (according to finite volume computations of Alipour [1]). Recently, Cisonni [3] published data on flow separation point ratio computed by inverse simplified flow models.

P. Šidlof et al. / Applied and Computational Mechanics 4 (2010) 121–132

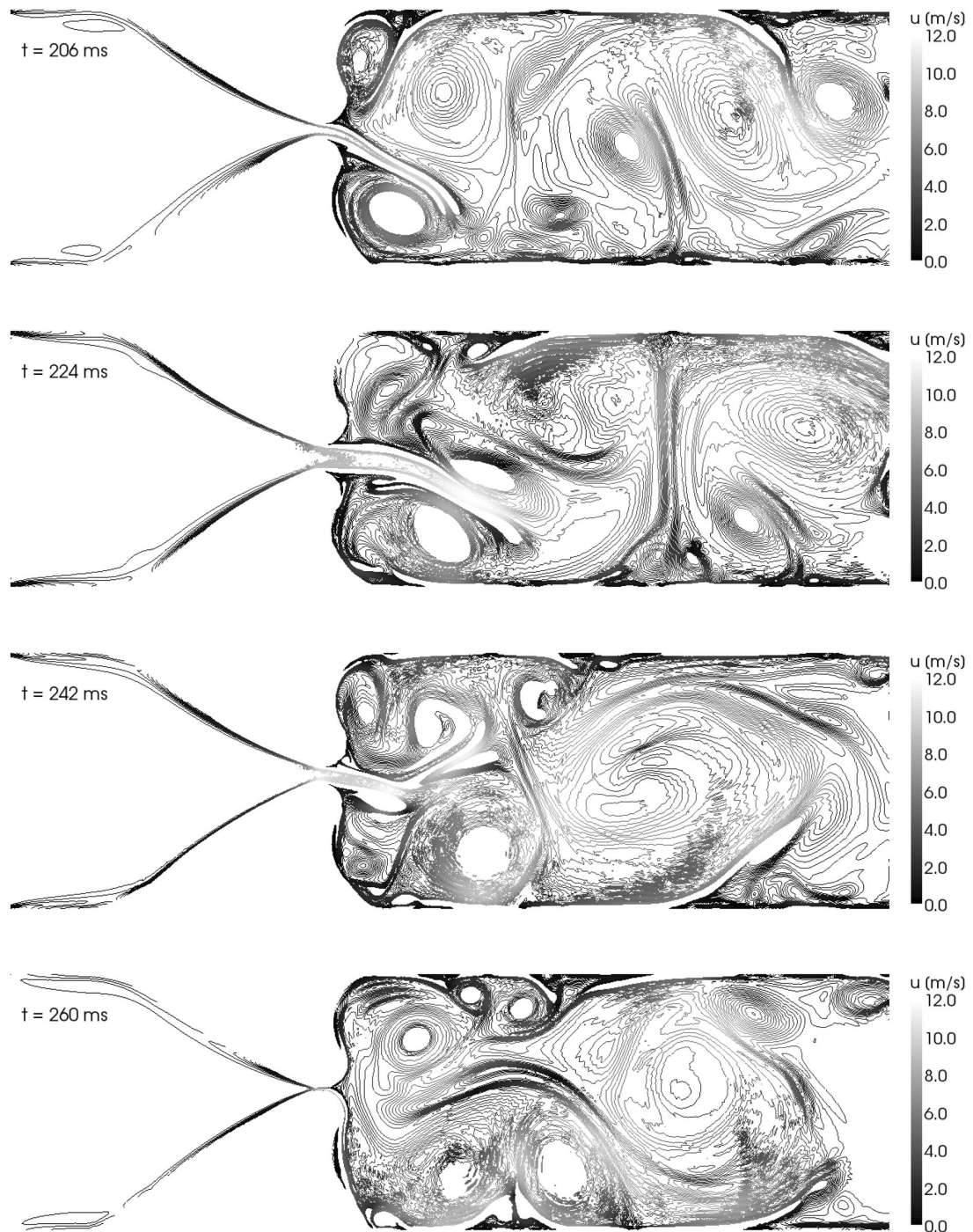


Fig. 2. Velocity fields in glottis in four phases of one vocal fold vibration cycle. Half of the opening phase ($t = 206$ ms), fully open glottis ($t = 224$ ms), middle of the closing phase ($t = 242$ ms), maximum vocal fold closure ($t = 260$ ms). Vorticity contours colored by velocity magnitude)

P. Šidlof et al. / Applied and Computational Mechanics 4 (2010) 121–132

All the works mentioned so far implicitly assume that the flow field is symmetric. Since this is rarely the case in real vocal folds, it seems adequate to measure the flow separation ratio from the channel axis and define it independently for upper and lower vocal fold. If we consider that in real physiology, the vocal channel is not horizontal but vertical, and call these “left” and “right” flow separation ratio, we may plot them in time and compare how do they behave in the computational and physical models.

Fig. 3 shows the computational and experimental results for the left separation ratio FSR-L. During most of the oscillation cycle, the ratio remains between 1.1–1.3, which is in good agreement with the values mentioned in previous paragraph. The experimental data are more scattered mostly due to lower resolution of the measured velocity fields. However, when vocal folds come close each other (i.e. near the dashed line denoting beginning of the opening phase, and at the right side of the plot near end of the closing phase), the ratio increases. The same, even much more prominent behavior, can be seen in Fig. 4 for FSR-R. In principle, this quantifies what has been stated before – near glottal closure the jet tends to adhere to one of the vocal folds (right one, in this case).

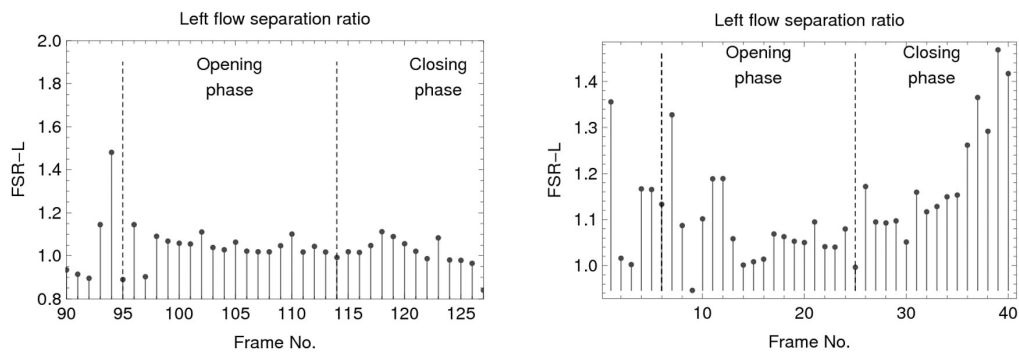


Fig. 3. Left flow separation ratio – computational (left) and experimental (right)

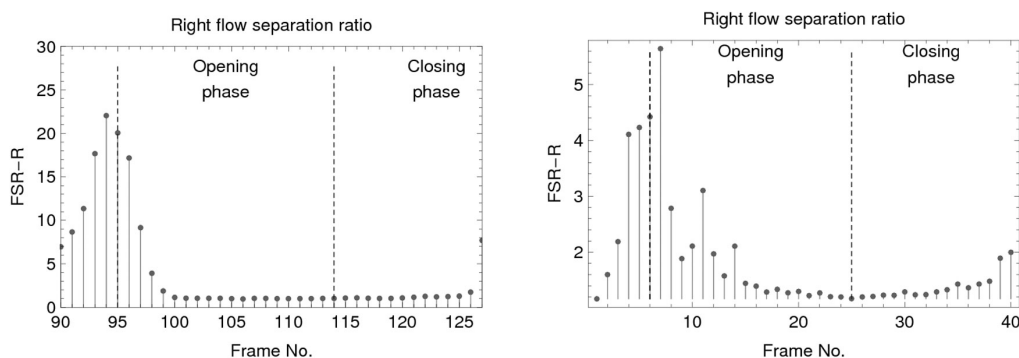


Fig. 4. Right flow separation ratio – computational (left) and experimental (right)

To demonstrate how the flow separation behaves in overall, it is possible to plot the glottal orifice width together with the position of the flow separation point for both sides together (see Fig. 5). The plot shows four periods of oscillation. Apparently the jet inclines rather to the right side. Even though the flow separation process is not perfectly periodic (also due to interaction of the jet with stochastic turbulent structures downstream glottis), it is obvious that from the perspective of flow separation, important matters occur when the vocal folds get close together.

P. Šidlof et al. / Applied and Computational Mechanics 4 (2010) 121–132

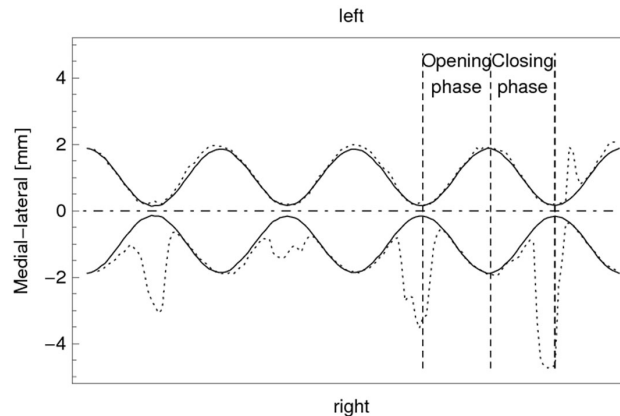


Fig. 5. Glottis opening (solid line) and position of the flow separation point (dotted line) in four vocal fold oscillation cycles. Computational results

4. Conclusion

A new, finite element model of phonatory airflow was developed. The computational results compare well with the experimental data obtained from a physical vocal fold model in terms of maximum glottal jet velocity, location of major vortex structures and overall flow dynamics, and seem to correspond when compared visually. However, it should be noted that the flow is neither stationary nor perfectly periodical, and thus such comparison of the flow patterns might be somewhat subjective.

There are some aspects, which restrict the class of vocal fold regimes possible to model computationally – the main limitation is currently the fact that within the mathematical model, the vocal folds are not allowed to collide. The processes accompanying glottal closure are complex and from the algorithmic point of view, the separation of the computational domain into two, necessity to introduce additional boundary conditions and to handle pressure discontinuity when reconnecting the domains represent a very complicated problem. Yet it will be necessary to deal with this task in future, if the mathematical model should be employed to model regular loud human phonation.

The next problem which arises is that the vortex dynamics in 2D and 3D are different. In 2D, the primary mechanism of vortex vanishing is viscous dissipation. In 3D reality, on the other hand, the original single vortex tube might disintegrate into several smaller vortices, which mutually interact and tend to align their axes with the flow direction. As a result, in a 2D section the vortices seem to dissipate and disappear faster. Consequently, results of a 2D simulation may be reliable near glottis, which has a strong effect of bi-dimensionalizing the airflow, but must be judged carefully further downstream.

The model was also used to assess and quantify flow separation in glottis. Both numerical and experimental results suggest that the usage of the classical flow separation criterion with values ranging from 1.1 to 1.3 seems to be quite plausible for the most of the vocal fold oscillation cycle, where the vocal folds are not too close together. Near glottal closure, however, the airflow separates much further downstream since it tends to adhere to one of the vocal folds.

Although more experimental data with higher resolution would be needed to draw more systematic and definitive conclusions, we believe that the results presented here give new insight into the problematic of flow separation during human phonation.

P. Šidlof et al. / Applied and Computational Mechanics 4 (2010) 121–132

Acknowledgements

The research has been financially supported by the Grant Agency of the Academy of Sciences of the Czech Republic, project No. KJB200760801 *Mathematical modeling and experimental investigation of fluid-structure interaction in human vocal folds*, research plan no. AV0Z20760514. Let us also acknowledge the support of UME ENSTA Paris, who provided the experimental background.

References

- [1] Alipour, F., Scherer, R., Flow separation in a computational oscillating vocal fold model, *Journal of the Acoustical society of America* 116 (3) (2004), 1 710–1 719.
- [2] Berry, D. A., Mechanism of modal and non-modal phonation, *Journal of Phonetics* 29 (2001), 431–450.
- [3] Cisonni, J., Van Hirtum, A., Pelorson, X., Willems, J., Theoretical simulation and experimental validation of inverse quasi-one-dimensional steady and unsteady glottal flow models, *Journal of the Acoustical society of America* 124 (1) (2008), 535–545.
- [4] Davis, T. A., UMFPack: unsymmetric multifrontal sparse LU factorization package, University of Florida, Gainesville, FL, USA. <http://www.cise.ufl.edu/research/sparse/umfpack/>.
- [5] Decker, G. Thomson, S., Computational simulations of vocal fold vibration: Bernoulli versus navier-stokes, *Journal of Voice* 21 (3) (2007), 273–284.
- [6] Deverge, M., Pelorson, X., Vilain, C., Lagree, P., Chentouf, F., Willems, J., Hirschberg, A., Influence of collision on the flow through in-vitro rigid models of the vocal folds. *Journal of the Acoustical Society of America* 114(2003), 3 354–3 362.
- [7] Erath, B., Plesniak, M., The occurrence of the coanda effect in pulsatile flow through static models of the human vocal folds. *Experiments in Fluids* (41) (2006), 735–748.
- [8] Feistauer, M., Felcman, J., Straškraba, I., *Mathematical and computational methods for compressible flow*, Clarendon Press, Oxford, 2003.
- [9] Horáček, J., Šidlof, P., Švec, J. G., Numerical simulation of self-oscillations of human vocal folds with Hertz model of impact forces, *Journal of Fluids and Structures* 20 (2005), 853–869.
- [10] Ishizaka, K., Flanagan, J., Synthesis of voiced sounds from a two-mass model of the vocal cords. *The Bell System Technical Journal* 51 (1972), 1 233–1 268.
- [11] Kob, M., Krämer, S., Prévot, A., Triep, M., Brücker, C., 2005, Acoustic measurement of periodic noise generation in a hydrodynamical vocal fold model, *Proceedings of Forum Acusticum, Budapest, 2005*, pp. 2 731–2 736.
- [12] Link, G., *A Finite Element Scheme for Fluid-Solid-Acoustics Interactions and its Application to Human Phonation*, Ph.D. thesis, Der Technischen Fakultät der Universität Erlangen-Nürnberg, Erlangen, 2008.
- [13] Lucero, J., Optimal glottal configuration for ease of phonation, *Journal of Voice* 12 (2) (1998), 151–158.
- [14] Martin, D., *Finite element library Mélina*, Université de Rennes, <http://perso.univ-rennes1.fr/daniel.martin/melina/>.
- [15] Nomura, T., Hughes, T. J., An arbitrary Lagrangian-Eulerian finite element method for interaction of fluid and a rigid body, *Computer methods in applied mechanics and engineering* 95 (1992), 115–138.
- [16] Pelorson, X., Hirschberg, A., van Hassel, R., Wijnands, A., Theoretical and experimental study of quasisteady flow separation within the glottis during phonation. Application to a modified two-mass model, *Journal of the Acoustical Society of America* 96 (6) (1994), 3 416–3 431.

P. Šidlof et al. / Applied and Computational Mechanics 4 (2010) 121–132

- [17] Scherer, R. C., Shinwari, D., De Witt, K. J., Zhang, C., Kucinski, B. R., Afjeh, A. A., Intraglottal pressure profiles for a symmetric and oblique glottis with a divergence angle of 10 degrees, *Journal of the Acoustical Society of America* 109 (4) (2001), 1 616–1 630.
- [18] Šidlof, P., Fluid-structure interaction in human vocal folds, Ph.D. thesis, Charles University in Prague, 2007.
- [19] Šidlof, P., Doaré, O., Cadot, O., Chaigne, A., Horáček, J., Finite element modeling of airflow in vibrating vocal folds, *Proceedings of International Conference on Voice Physiology and Biomechanics – ICVPB, Tampere, 2008*.
- [20] Šidlof, P., Švec, J. G., Horáček, J., Veselý, J., Klepáček, I., Havlík, R., Geometry of human vocal folds and glottal channel for mathematical and biomechanical modeling of voice production, *Journal of Biomechanics* 41 (2008), 985–995.
- [21] Thomson, S. L., Mongeau, L., Frankel, S. H., Aerodynamic transfer of energy to the vocal folds. *Journal of the Acoustical Society of America* 113 (2005), 1 689–1 700.
- [22] Titze, I. R., The human vocal cords: A mathematical model, Part II, *Phonetica* 29 (1974).
- [23] Titze, I. R., *Principles of Voice Production*, National Center for Voice and Speech, Denver, 2000.
- [24] Turek, S., *Efficient solvers for incompressible flow problems: An algorithmic and computational approach*, Springer-Verlag, Berlin, 1999.
- [25] Vilain, C. E., Pelorson, X., Fraysse, C., Deverge, M., Hirschberg, A., Willems, J., Experimental validation of a quasi-steady theory for the flow through the glottis. *Journal of Sound and Vibration* 276 (2004), 475–490.
- [26] Zanartu, M., Mongeau, L., Wodicka, G., Influence of acoustic loading on an effective single mass model of the vocal folds, *Journal of the Acoustical Society of America* 121 (2) (2007), 1 119–1 129.
- [27] Zhang, Z., Neubauer, J., Berry, D., Physical mechanisms of phonation onset: a linear stability analysis of an aeroelastic continuum model of phonation, *Journal of the Acoustical Society of America* 122 (4) (2007), 2 279–2 295.
- [28] Zörner, S., Numerical study of the human phonation process by the Finite Element Method, *Proceedings of the International Conference on Acoustics NAG/DAGA, Rotterdam, 2009*, 1 718–1 721.

Computers & Fluids 80 (2013) 290–300



Contents lists available at SciVerse ScienceDirect

Computers & Fluids

journal homepage: www.elsevier.com/locate/complfluid

Parallel CFD simulation of flow in a 3D model of vibrating human vocal folds

Petr Šidlof^{a,b,*}, Jaromír Horáček^a, Václav Řidký^b^aAcademy of Sciences of the Czech Republic, Institute of Thermomechanics, Dolejškova 5, 182 00 Prague 8, Czech Republic^bTechnical University of Liberec, NTI FM, Studentská 2, 461 17 Liberec, Czech Republic

ARTICLE INFO

Article history:

Received 15 September 2011
 Received in revised form 7 February 2012
 Accepted 8 February 2012
 Available online 17 February 2012

Keywords:

Numerical simulation
 Vocal folds
 Glottal airflow
 Finite volume method
 Parallel CFD

ABSTRACT

Accurate computation of highly unsteady and massively separated airflow in human vocal folds during phonation, which is fundamental for the understanding and modeling of the aeroacoustic processes involved in human voice production, requires CFD simulations on large 3D dynamic meshes. This work presents a 3D model of flow past vibrating vocal folds solved by cell-centered finite volume method, verification of the solver on a benchmark cylinder cross-flow problem, grid dependence study and parallel scalability results obtained on a heterogeneous Linux computational cluster with 12 Intel Xeon dual-processor dual-core and 17 AMD Opteron dual-processor single-core nodes. Transient computations on dynamic meshes with up to 3.2 M elements were performed on two geometries modeling convergent and divergent glottis with an angle of 20 degrees. In the results, the jet deflection angle, flow rate, glottal velocity and pressure, drag and lift force and jet contours (including phase-averaged data) are compared for these two configurations.

© 2012 Elsevier Ltd. All rights reserved.

1. Introduction

Human phonation is a complex process involving fluid–structure and fluid–acoustic interactions. Voice is created by passage of the expired airflow through a narrow constriction called *the glottis* [1]. This constriction is formed by the vocal folds, located in the larynx. The vocal folds are two symmetric soft tissue structures fixed between the thyroid cartilage and arytenoid cartilages. They are composed of the thyroarytenoid muscle and ligament covered by mucosa. Under certain conditions (subglottal pressure, glottal gap, longitudinal tension in the thyroarytenoid muscle and ligament) the vocal folds can start to oscillate and close the channel periodically. The dominant sound source in the glottis is associated with the oscillating volume flow, which determines the fundamental frequency of human voice [2]. In some cases, especially when the vocal folds are abducted (e.g. in breathy phonation), the acoustic consequence of the dipole sound sources due to unsteady forces exerted by the vocal folds on the fluid may also grow important [3]. The acoustic signal generated in the glottal region is further modulated by the vocal tract, radiated from the mouth, and perceived as voice. However, during recent years it has been emphasized that this source-filter theory of phonation is valid only as a first approx-

imation: the elastic oscillations of the vocal folds are two-way coupled not only to the airflow, but also to subglottal and supra-glottal acoustics.

From the fluid-mechanical point of view, human larynx can be seen as an approximately planar nozzle with time-varying clearance. However, the vocal fold vibration patterns present also longitudinal components [1,4], which disrupt the dominantly planar character of the geometry. The longitudinal shape of the nozzle has been recently shown to have an incidence on the flow field [5]. The airflow coming from the trachea accelerates in the convergent part of the glottis. Near the narrowest cross-section, airflow separates from the surface of the vocal folds due to adverse pressure gradient and forms a jet. The glottal jet, which is essentially planar, but might vary in intensity along the anterior–posterior axis in the proximity of the glottis, pulsates due to vocal fold oscillations. The jet inclination angle, jet core flow velocity and the position of the flow separation point are highly sensitive to the geometry of the vocal folds (which is, in real subjects, never perfectly symmetric), to the position within the oscillation cycle and magnitude of the subglottal pressure. Further downstream of the glottis, the jet interacts with laryngeal walls and supraglottal large-scale vortical structures, which leads to a complex 3D flow field.

The knowledge of the glottal flow patterns is important for the understanding of the fundamental processes of the voice production, but also in applied research, e.g. in development of voice prostheses for laryngectomized patients [6]. However, the vocal folds are hardly accessible and so direct *in vivo* flow measurements are

* Corresponding author at: Academy of Sciences of the Czech Republic, Institute of Thermomechanics, Dolejškova 5, 182 00 Prague 8, Czech Republic. Tel.: +420 26605 3135; fax: +420 28658 4695.

E-mail address: sidlof@it.cas.cz (P. Šidlof).

hardly possible. Thus, most experimental data on the laryngeal airflow has been obtained using physical models. There is a large number of experimental papers using hot-wire probes and discrete pressure probes (Barney et al. [7], Alipour and Scherer [8], Scherer et al. [9], Shinwari et al. [10]) and more recently using laser visualization techniques and Particle Image Velocimetry (PIV). These include results obtained on static vocal fold models (e.g. Erath and Plesniak [11,12], Li et al. [13]), externally driven models (Triep et al. [14], Kucinski et al. [15], Krane et al. [16], Erath and Plesniak [17]) and self-oscillating models (Thomson et al. [18], Neubauer et al. [19], Becker et al. [20], Šidlof et al. [21], Horáček et al. [22], Krebs et al. [23]). A comprehensive overview of the physical vocal fold models used in voice research is given in a recent paper of Kniesburges et al. [24].

Due to the difficulties encountered in both *in vivo* and *in vitro* measurements, there have always been efforts to develop mathematical models. The cornerstone of mathematical modeling of human phonation was set by Ishizaka and Flanagan [25], who developed a simple mass-spring model coupled to potential quasi-1D airflow. Although this may seem a serious oversimplification of the real physiological situation, the model proved very useful and its variants (e.g. Lucero [26], Pelorson et al. [27], Story and Titze [28], Sciamarella and d'Alessandro [29], Horáček et al. [30], Zhang [31], Yang et al. [4]) are widely used up to present. The main advantage of these models is that the equations may be solved either analytically, or using simple and very fast numerical methods for ordinary partial differential equations, making it possible to perform nearly real-time simulations on current computers. However, since these models do not provide much information on the glottal airflow, increasing effort has been devoted to numerical solution of the 2D or 3D Navier–Stokes equations on computational domains approximating the glottal channel. These include studies with fixed vocal folds (Suh and Frankel [32,33], Larson and Müller [34], Mihaescu et al. [35], Schwarze et al. [36]), forced vocal fold oscillation (Alipour et al. [37], Renotte et al. [38], Zhao et al. [3], Alipour and Scherer [39], Bae and Moon [40], Sciamarella and Quéré [41], Punčochářová-Požžková et al. [42], Mattheus and Brücker [5], Zheng et al. [43]) and models with the airflow fully coupled to elastic tissue oscillations (de Oliveira Rosa et al. [44], Thomson et al. [18], Tao and Jiang [45], Luo et al. [46], Link et al. [47], Zheng et al. [48], Sváček [49]). Only a few of these computational studies [44,32,33,35,36,5] solve the flow field in 3D, and most of them on a static geometry. One of the most complex approaches to phonation modeling was recently published in the works of Zheng et al. [50,51] and Seo and Mittal [52], who use the immersed boundary method for incompressible low-Mach number flow coupled to a finite element solver for the viscoelastic tissue to calculate the 3D flow field and flow-induced vibrations of the vocal folds including glottal closure and contact forces. Using the aerodynamic–acoustic splitting technique, the acoustic field is then calculated by solving linearized perturbed compressible equations. An extensive overview of the computational vocal fold models can be found in a recent review paper of Alipour et al. [53].

The Reynolds numbers found in airflow past vocal folds range from 1000 up to about 5000–10,000 [17]. This implies that the subglottal flow may be laminar. However, Neubauer et al. [19] showed that near the glottal region, transition from laminar to turbulent flow occurs and that the supraglottal flow field, dominated by separated jet flow and recirculation, is rather turbulent. Numerical computation of such transitory, highly unsteady airflow with massive separation is problematic. The Reynolds-Averaged Navier–Stokes (RANS) turbulence modeling is used rather marginally [38,33]. Some recent papers [32,35,36] claim that RANS approach for modeling of human phonation is inadequate and employ Large Eddy Simulations (LES). However, still many authors [37,44,39,18,40,41,34,47,42,49] use a “laminar” model, actually a

Direct Numerical Simulation (DNS) on a largely insufficient mesh. This approach was adopted within the current study, too.

During the years of the efforts to model human phonation in all its complexity, it has become clear that accurate computation of the airflow in human vocal folds during the phonation process, which is fundamental for the understanding of the aeroacoustic processes involved in voice production, requires CFD simulations on large 3D dynamic meshes. This work presents a 3D model of airflow past vibrating vocal folds, verification of the numerical scheme used, parallel scalability tests and results of numerical simulations of incompressible airflow on a dynamic meshes consisting of 500 K to 3.2 M cells. The scalability tests and computations were run on a heterogeneous Linux computational cluster with 12 Intel Xeon two-processor dual-core nodes and 17 AMD Opteron two-processor single-core nodes.

2. Methods

2.1. Mathematical model, geometry and boundary conditions

For low Mach number flows known in human phonation, the glottal airflow can be modeled by unsteady incompressible Navier–Stokes equations. In strong conservation form suitable for further finite volume discretization, the equations read

$$\nabla \cdot \mathbf{u} = 0$$

$$\frac{\partial \mathbf{u}}{\partial t} + \nabla \cdot (\mathbf{u}\mathbf{u}) - \nabla \cdot \nu \nabla \mathbf{u} - \frac{1}{\rho} \nabla p = 0, \quad (1)$$

where \mathbf{u} , p and ρ are fluid velocity, pressure, and density, respectively, and ν is kinematic viscosity.

The geometry of the model vocal folds used in this study is based on the widely used parametric shape “M5”, proposed by Scherer et al. [9,54]. The “M5” model is piecewise linear with rounded corners, and provides an easily parametrizable approximation of the vocal fold shape during oscillation. The 2D section of the computational domain is depicted in Fig. 1. In real human phonation, the vocal folds are known to exhibit convergent–divergent shaping during the oscillation cycle [55]. In current simulation, two elementary cases were investigated for the sake of simplicity: convergent vocal folds (angle $\psi = 20^\circ$) and a divergent configuration with $\psi = -20^\circ$. The thickness $T_{VF} = 7.3$ mm of the vocal folds (physiologically, the inferior–superior dimension), height $H = 5.5$ mm (medial–lateral dimension, normal to the sagittal plane) and length $L = 12$ mm of the vocal folds (anterior–posterior dimension, normal to the coronal plane, not seen in Fig. 1) were set to match average physiological values found in male subjects. The subglottal channel length was set to $T_0 = 0.4 T_{VF}$, the supraglottal channel length is $T_1 = 5.4 T_{VF}$. In both configurations, the vocal folds vibrate in the medial–lateral direction symmetrically with one degree of freedom and frequency $f = 100$ Hz, leaving a minimum glottal gap $g_{min} = 2 * 0.1$ mm and maximum glottal opening $g_{max} = 2 * 0.9$ mm.

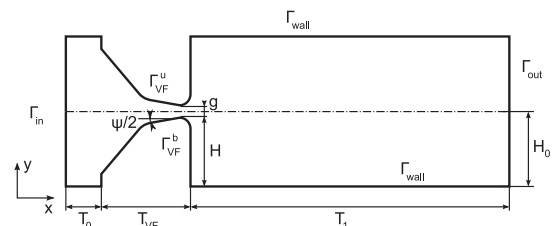


Fig. 1. 2D (coronal) section of the computational domain with vocal folds in zero position. The length T_1 of the supraglottal channel is not in scale.

When modeling human phonation, the boundary conditions can have crucial effect on the solution. To mimic the real physiological conditions, the airflow in the model is driven by constant pressure difference between the inlet Γ_{in} and outlet Γ_{out} of the domain (i.e. constant lung pressure and zero relative pressure at outlet). At the fixed channel walls Γ_{wall} and moving vocal fold surfaces Γ_{VF} a Neumann condition $\partial p / \partial n = 0$ was prescribed. The boundary conditions for the velocity field were set as follows: $\partial \mathbf{u} / \partial n = 0$ at Γ_{in} , no-slip condition $\mathbf{u} = 0$ at Γ_{wall} . At Γ_{VF} , the flow velocity is equal to the velocity of the moving vocal fold surface. Due to the presence of large vortical structures convected downstream of the glottis up to the outlet of the computational domain and consequent back-flow to the domain destabilizing the numerical solution, it was necessary to introduce a stabilized outflow condition at Γ_{out} : $\partial \mathbf{u} / \partial n = 0$ when velocity direction points outward of the domain, $\mathbf{u} = 0$ otherwise. This condition does not interfere with the prescribed pressure difference between inlet and outlet.

2.2. Mesh and mesh partitioning

The meshes used in the computations were constructed from an unstructured isotropic triangular 2D mesh extruded into third dimension. Some computations were also tested on meshes with locally refined elements in the narrow glottal region. However, the tests showed only minor improvements for a rather high price: due to continuity equation, the narrow glottal region is also the place, where the flow velocities and local Courant numbers $Co = u \Delta t / \Delta x$ are the highest. Thus, refining even a small number of elements (characteristic dimension Δx) between the vocal folds limits severely the attainable timestep Δt and causes a significant global increase in computational cost. The detailed view on the glottal region of the coarsest and finest mesh used in the grid-dependence testing and simulations (see Section 3.2) is depicted in Fig. 2.

To partition the mesh for the parallel computation, two different algorithms were tested: *scotch* [56] and *metis* [57]. The quality of the mesh decomposition was compared in terms of subdomain element number (important for load balance) and number of processor faces (influencing processor communication). The results are summarized in Section 3.3.

2.3. Numerical solution

The numerical solution of the airflow in the glottal channel with moving walls was implemented in OpenFOAM [58], an object-oriented open-source set of libraries programmed in the C++ language. OpenFOAM is based on the finite volume method in cell-centered approach on arbitrarily unstructured meshes.

The incompressible Navier–Stokes equations on a moving computational mesh were solved numerically using modified PISO

algorithm [59] with an extra loop of substep iterations and variable under-relaxation. The algorithm allows for automatic timestepping and is designed to achieve convergence for larger time-steps (i.e. large Courant numbers). However, the tradeoff with an increased CPU time for the substep iteration caused that for the current problem the algorithm performed comparably to the standard PISO solver. The discretization schemes were as follows: first-order Euler implicit for the time derivative, total variation diminishing (TVD) scheme for the convective term, central differencing scheme (CDS) with explicit nonorthogonal correction for the diffusion term.

The computational domain changes in time due to vocal fold oscillations. Since the vocal folds do not collide and close the channel completely in current simulations, it is not necessary to introduce topological changes to the mesh and the mesh is simply deformed. The coordinates of the element vertices in a new time-step are found by solving Laplace equation for the mesh velocity \mathbf{w} with spatially variable diffusivity γ :

$$\nabla \cdot (\gamma \nabla \mathbf{w}) = 0, \quad (2)$$

with boundary conditions given by zero mesh velocity at $\Gamma_{in} \cup \Gamma_{out} \cup \Gamma_{wall}$, prescribed velocity on the moving vocal fold surfaces Γ_{VF} and zero normal derivative on the front and back walls (here, the mesh is allowed to “slip” freely). The diffusivity γ decreases exponentially with distance from the vocal fold surfaces. Due to significant element distortion and consequent loss of element orthogonality between the moving vocal folds, one outer loop of nonorthogonal correctors was utilized within the modified PISO algorithm to guarantee stability of the computation.

The resulting linear system for the momentum was solved by bi-conjugate gradient method (PBiCG) with diagonal-based incomplete LU (DILU) preconditioning. For the pressure predictor and corrector steps, faster convergence was obtained using a geometric–algebraic multigrid (GAMG). The cell motion Laplace equation was solved by diagonal incomplete-Cholesky (DIC) preconditioned conjugate gradient method.

3. Results

3.1. Code verification

The accuracy of the code in the case of low Reynolds number separated channel flow was verified using a widely cited benchmark study published electronically by Turek and Schäfer [60]. This paper summarizes the quantitative results of 17 research groups using various computational methods to solve a benchmark problem of cross-flow over a cylinder, particularly of a 2D unsteady flow over a fixed circular cylinder at $Re = 100$ with a parabolic inflow velocity condition. The following global quantities are tracked and compared between the results of all the research groups:

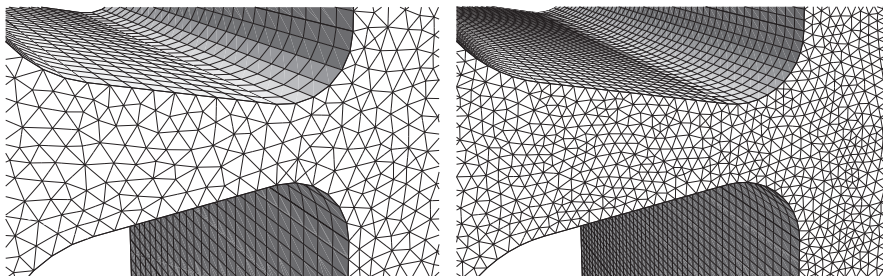


Fig. 2. Detailed view on the glottal region of the computational meshes: the coarsest mesh S_1 (550 k elements), the finest mesh S_6 (3.2 M elements).

frequency of separation (vortex shedding) f , Strouhal number St , maximum drag and lift coefficient c_{Dmax} and c_{Lmax} over one period $[t_0, t_0 + 1/f]$ and pressure difference $\Delta p(t)$ between the front and end point of the cylinder at $t = t_0 + 1/2f$. The initial time t_0 corresponds to the state when c_L is maximum, the definitions of the Strouhal number and drag and lift coefficients are as follows:

$$St = \frac{Df}{\bar{U}}, \quad (3)$$

$$c_D = \frac{2F_D}{\rho \bar{U}^2 D}, \quad c_L = \frac{2F_L}{\rho \bar{U}^2 D}, \quad (4)$$

where D is the cylinder diameter, \bar{U} the mean inflow velocity and F_D and F_L are the drag and lift forces

$$F_D = \int_S \left(\rho v \frac{\partial u_t}{\partial n} n_y - p n_x \right) dS, \quad (5)$$

$$F_L = - \int_S \left(\rho v \frac{\partial u_t}{\partial n} n_x - p n_y \right) dS.$$

Here u_t denotes the tangential velocity on the cylinder surface S , n_x and n_y are the components of the unit normal vector. The numerical results of the current algorithm calculated on a triangular mesh with 380 k elements are compared in Table 1 against the benchmark results published in [60], which contain also some (incomplete) experimental data. The table shows a good agreement with a maximum difference of about 6% against the mean values published in the benchmark study.

3.2. Grid dependence

The dependence of the results on the computational mesh has been tested for the convergent geometry on six isotropic grids S_1 – S_6 , composed of 550 k to 3.2 M prismatic elements. Since no turbulence and no boundary layer model was used in the calculations, it can be expected that the results change slightly with mesh refinement due to capture of finer and finer scales of turbulence, better resolution of the boundary layer and flow separation. Theoretically, the grid convergence would be best proved by solving stationary Navier–Stokes equations on static geometry with non-moving vocal folds. However, due to flow separation and Coanda effect, even in this simplified case a stationary solution of the glottal airflow is physically unstable already at low and moderate Reynolds numbers. This is caused by vortex shedding and jet reattachment to one of the channel walls, where the direction of the jet may swap in time. Thus, the results of full unsteady simulations over a time $t = 0.025$ s with moving vocal folds have been compared. Table 2 summarizes the sizes of the meshes S_1 – S_6 and computational times needed to perform these grid-dependence tests. These tests were run on different number and type of computational nodes, in order to load the cluster optimally.

Fig. 3 shows the pressure at a probe location 1 mm downstream of the glottis in the mid-glottal plane during first three vocal fold oscillation cycles. The vibration period is 0.01 s, with first maximum vocal fold approach at $t_1 = 0.0025$ s and maximum glottis opening at $t_2 = 0.0075$ s. Using meshes with more than 2 M elements, the spurious oscillations smooth out and the pressure waveforms do not show significant variations.

An important global parameter, which can be calculated from the flow field, is the aerodynamic (drag and lift) force:

$$F_x = \int_{\Gamma_{VF}^b} \tau_{1j} n_j dS \quad (6)$$

$$F_y = \int_{\Gamma_{VF}^b} \tau_{2j} n_j dS,$$

exerted on the vocal fold surface, where n_j are the components of the unit outer normal vector,

$$\tau_{ij} = \rho \left[v \left(\frac{\partial u_i}{\partial x_j} + \frac{\partial u_j}{\partial x_i} \right) - p \delta_{ij} \right] \quad (7)$$

is the stress tensor and δ_{ij} is the Kronecker symbol. Figs. 4 and 5 compare the horizontal and vertical forces on the bottom vocal fold calculated on the meshes S_1 – S_6 . The results computed on coarse meshes show much more variation in the case of the horizontal (drag) force, mainly in the opening phase of the glottis. This is the phase where a new jet develops and where the transglottal pressure drop, which is a dominant factor governing the drag force, is newly established. Apparently, the coarse meshes are not sufficient to capture this phenomenon and significant error is introduced in the opening phase.

3.3. Parallel performance

The CFD simulations were run on a computational cluster *Hydra* at the Technical University of Liberec – a heterogeneous cluster consisting of 12 Dell PowerEdge 1950 nodes (each one with two Intel Xeon 5140 dual-core processors, 1333 FSB, 4 MB shared L2-cache) and 17 Sun Fire V20z nodes (two single-core AMD Opteron 252 processors per node), running Linux CentOS. The nodes are interconnected by 1 Gbps network.

For running solvers in parallel, the OpenFOAM library uses the domain decomposition method and OpenMPI implementation of the MPI standard. Fig. 6 shows the decomposition of the computational domain into eight subdomains using *scotch* and *metis* libraries. The quality of these decompositions can be compared using Table 3, which summarizes the ratio of minimum and maximum number of cells per processor (ideally 1 for best load balance), and maximum and total number of processor faces (the less processor faces, the less interprocessor communication) for decompositions into 2–32 subdomains. The table suggests that in this particular case, *scotch* produces better decomposition in terms of interprocessor communication, but is outperformed by *metis* in terms of load balance (at least for lower number of subdomains). However, the final computational times do not show significant difference. As the *scotch* library is preferred in OpenFOAM due to licensing reasons, it was the choice in all further computations.

Fig. 7 shows the decomposition into 16 subdomains. In this case, the bottom left subdomain (yellow in the color version) is disconnected. Although this situation, which occurs both in *scotch* and *metis* decompositions, is known to produce instabilities in certain CFD codes, here it does not influence the computation negatively.

When running parallel CFD computations on a multicore heterogeneous architecture, for good scaling it is highly important how the computational threads are allocated on individual computational nodes, processors and processor cores. The Intel Xeon and

Table 1

Global parameters computed on the benchmark problem – results of the current study vs. results of 17 research groups published in [60].

	St [1]	c_{Dmax} [1]	c_{Lmax} [1]	Δp [Pa]
Current study	0.298	3.26	0.938	2.44
Reference data [60] (computational)	0.295–0.305	3.22–3.24	0.990–1.01	2.46–2.50
Reference data [60] (experimental)	0.284–0.290	N/A	N/A	N/A

Table 2
Computational meshes used in calculations – number of elements, number of points, numbers of layers in z- (anterior–posterior) direction, element size in x/y direction, computer time to simulate 0.025 s.

Mesh	NElements	NPoints	Layers	Elem. size (mm)	Comp. time/loaded cores
S ₁	550 k	290 k	25	0.23	32 h @ 4× AMD
S ₂	1.1 M	580 k	32	0.18	58 h @ 4× AMD
S ₃	1.6 M	840 k	36	0.16	55 h @ 8× AMD
S ₄	2.1 M	1.1 M	40	0.15	51 h @ 8× Intel 29 h @ 16× Intel
S ₅	2.7 M	1.4 M	43	0.139	67 h @ 8× Intel
S ₆	3.2 M	1.7 M	45	0.131	95 h @ 8× Intel

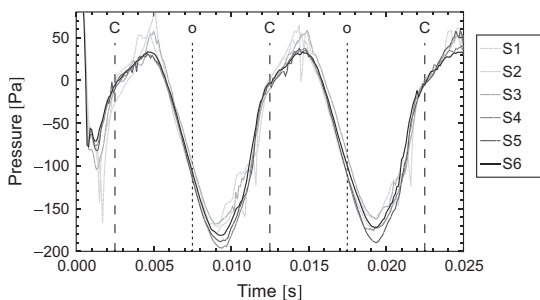


Fig. 3. Pressure at a location 1 mm downstream of the glottis calculated on meshes S₁–S₆. Dashed lines indicate the time instants of maximum glottis opening (o) and closure (C).

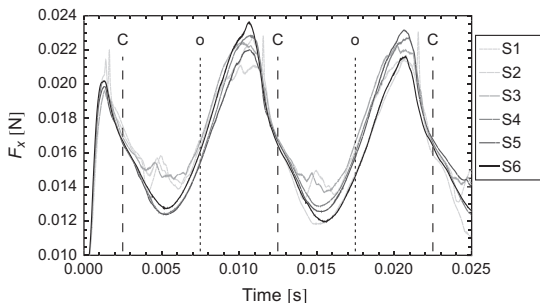


Fig. 4. Drag force on the bottom vocal fold calculated on meshes S₁–S₆. Dashed lines indicate the time instants of maximum glottis opening (o) and closure (C).

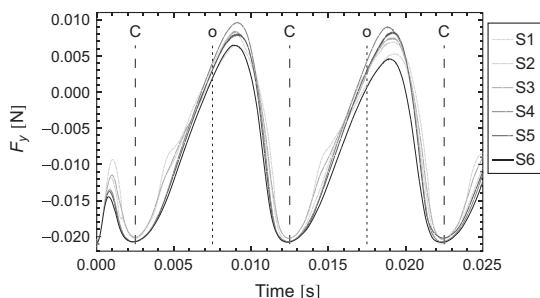


Fig. 5. Lift force on the bottom vocal fold calculated on meshes S₁–S₆. Dashed lines indicate the time instants of maximum glottis opening (o) and closure (C).

AMD Opteron nodes composing the *Hydra* cluster have different architectures and manufactures, and show slightly different

performance – for a serial run on one core, one timestep of the test computation requires 83 s on Intel processor and 87 s on AMD. Thus, all the parallel tests were run exclusively on one kind of architecture.

Fig. 8 summarizes the strong speedup results for various thread-to-core allocation schemes. For the dual-processor dual-core Intel nodes the computation scales best when only one processor and one core per node are allocated (blue¹ solid line) – the speedup is close to linear. The results for the case of two allocated cores on two processors of each node (red dashed line) are only slightly worse. When all the four cores of a node are loaded, the performance significantly drops. This is most likely caused by the fact that the Intel Xeon 5140 dual-core processors have a shared front side bus (FSB), which forms a bottleneck in this architecture.

On the dual-processor single-core AMD nodes, the parallel runs in the 2–2 thread-to-core allocation scheme (red dashed line in Fig. 8) outperform the 1–1 case for higher numbers of subdomains. One possible explanation is that unlike the Intel Xeon symmetric multiprocessing, where multiple processors are connected to a single shared main memory via external Northbridge chips, multiprocessor AMD Opteron systems are an example of a NUMA (non-uniform memory access) architecture: each CPU can access its own RAM with fast access times over an on-die integrated memory controller, and communicates with other CPUs and the I/O subsystem directly using natively implemented high-bandwidth links. This can lead to better multiprocessor scaling than in the older Intel Xeon systems. As a consequence, the computation run on four nodes and eight CPUs runs faster than that on eight nodes and eight CPUs, since the memory bandwidth is not limiting and there is less of the slow communication between the nodes.

3.4. Results of the transient simulations

In the following, the results of two transient simulations of glottal airflow are presented. The first case was the convergent vocal fold geometry with a fixed convergence angle of $\psi = 20^\circ$ (denoted further as CVG), computed over 20 periods of vibration ($t = 0.2$ s). The second configuration with divergent vocal folds ($\psi = -20^\circ$, DVG) was run over 8.5 periods ($t = 0.085$ s). In both cases, the simulations were run with a variable timestep, adjusted automatically by the solver to insure that the Courant–Friedrichs–Lewy (CFL) condition is satisfied. Depending on the maximum local Courant number (which occurs in the glottal gap and is dependent on the glottal opening), the timestep ranged from $1 - 5 \times 10^{-6}$ s on the mesh S₄ with 2.1 M elements (and a mesh with identical parameters in the divergent configuration). The airflow was driven by constant pressure difference $\Delta p = 300$ Pa, corresponding to soft phonation. On 16 Intel Xeon processor cores, the computation over 20 periods of vibration required 10.2 days of wall-clock time and 160 GB of disk space to store the results for further analysis.

¹ For interpretation of color in Figs. 6–16, the reader is referred to the web version of this article.

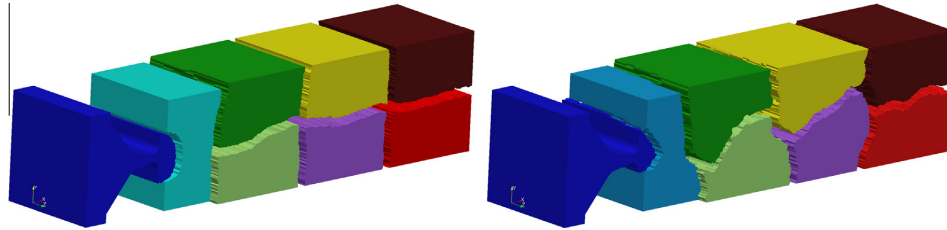


Fig. 6. Decomposed domain (eight subdomains) using *scotch* (left) and *metis* (right) libraries.

Table 3
Domain decomposition: *scotch* vs. *metis*.

Subdomains	Min/max cells per processor ratio		Max/total processor faces	
	Scotch	Metis	Scotch	Metis
2	0.988	0.999	3326/3326	3881/3881
4	0.981	0.998	6642/9859	7929/11,841
8	0.963	0.942	6378/21,177	7914/25,194
16	0.954	0.959	5384/34,569	6634/39,620
32	0.953	0.943	4946/56,953	5600/64,718

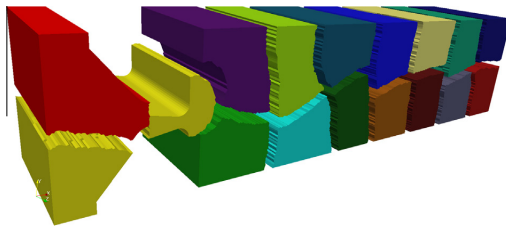


Fig. 7. Decomposed domain (16 subdomains) using *scotch*.

Fig. 9 shows examples of the velocity magnitude and pressure fields (CVG case) at time $t = 40$ ms, which corresponds to 50% of the closing phase. The same time instant is captured in Fig. 10 in x -normal sections. The figures demonstrate how the glottal jet, which is aligned with the anterior–posterior axis close downstream of the glottis, gradually loses its planar character. One of the important features known to occur in the separated airflow in the supraglottal region is that the jet tends to skew from the straight direction. In some studies ([11,61]) this behavior is attributed to the Coanda effect, other authors (e.g. Zheng et al. [51])

show that jet skewing can be the result of interaction with downstream flow structures. In any case, it is interesting to postprocess the calculated velocity fields and compute the jet deflection angle during several vocal fold vibration periods.

From the simulation data, the jet deflection angle α was evaluated in the mid-coronal plane. Differently to the jet deflection measure used in [43,5], it was defined as

$$\alpha = \arctan\left(\frac{y_{max}}{d_x}\right), \tag{8}$$

where y_{max} is the (vertical) distance of the jet core from the sagittal midplane, and $d_x = 1$ mm the (horizontal) distance of the probe line where the maximum velocity was evaluated from the superior vocal fold surface. In this way, the angle α measures the deviation of the jet from the straight direction, rather than the direction of the jet core velocity vector. For the cases when the jet is not curved, both definitions coincide. The results for the convergent and divergent geometries are in Fig. 11.

After a short initial transient, the jet deflection develops a clear, approximately periodic pattern with natural inter-cycle variability. The jet deflection is much higher for the divergent configuration. In both cases, the jet skews most in the proximity of glottal closure. This effect is in well agreement with the authors' previous

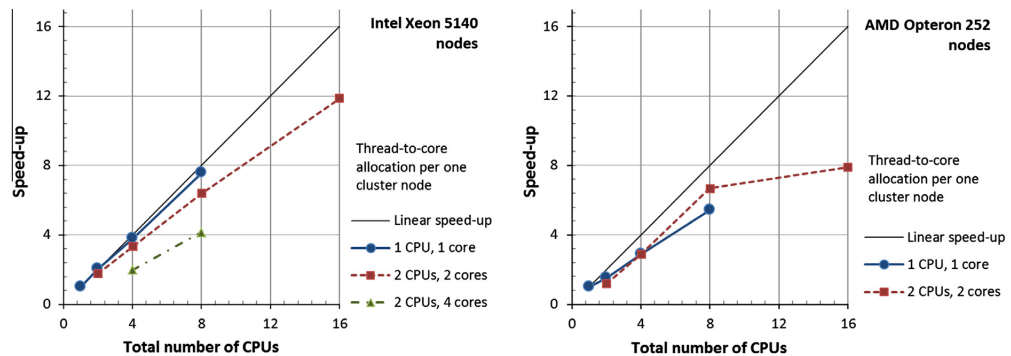


Fig. 8. Strong speedup on nodes with Intel Xeon and AMD Opteron processors at different thread-to-core allocation schemes.

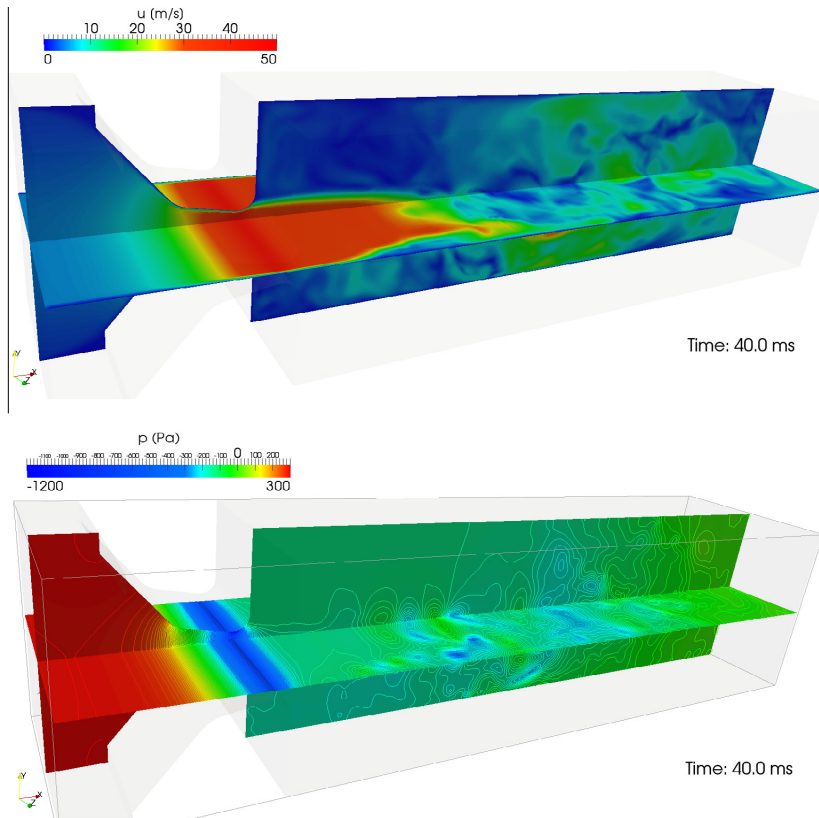


Fig. 9. Velocity magnitude and pressure fields (with 10 Pa isolines) in two sections, middle of the closing phase.

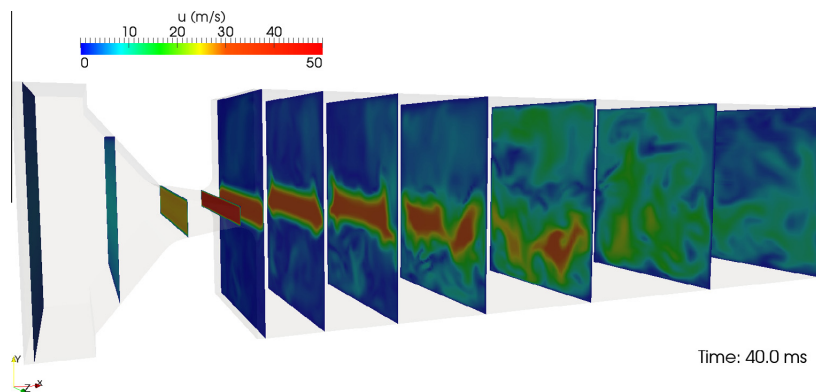


Fig. 10. Velocity magnitude field in x-normal sections, middle of the closing phase.

experimental findings [21], even though these were obtained on a self-oscillating synthetic vocal fold model with different vocal fold geometry.

The behavior of the glottal jet further downstream of the glottis can be seen from Figs. 12 and 13, which show its contour in four phases of vocal fold vibration: middle of the closing phase (0.75 T), maximum glottis closure (0 T), middle of the opening phase (0.25 T), fully open vocal folds (0.5 T). The isocontours were

calculated from instantaneous velocity fields in the 8th period of vibration, and from the phase-averaged velocity fields

$$\bar{U}(x, t) = \frac{1}{N-1} \sum_{i=1}^{N-1} u(x, t + iT), \tag{9}$$

where N is number of the periods calculated (CVG: $N = 20$, DVG: $N = 8$) and $T = 0.01$ s is the vibration period. The first period was

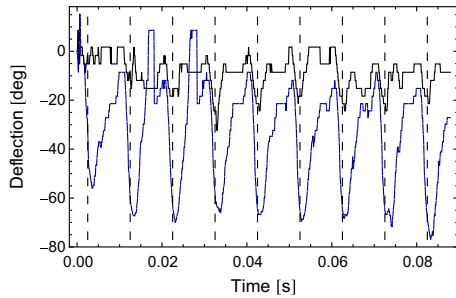


Fig. 11. Deflection of the glottal jet during first eight vocal fold oscillation cycles for the convergent (black, solid line) and divergent (blue, dashed line) geometries. Vertical dashed lines indicate the time instants of maximum glottis closure.

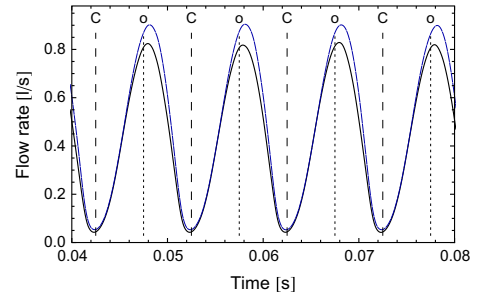


Fig. 14. Glottal flow rate for the convergent (black solid line) and divergent (blue dashed line) shape. Vertical dashed lines indicate the time instants of maximum glottis opening (o) and closure (C).

skipped to omit the initial transient effects. The phase-averaged results show that the jet skews systematically to the bottom, with interesting 3D effects near the side walls of the rectangular channel – in both configurations, the jet gets thicker further from the coronal midplane. In the divergent case during glottis opening, the jet is so curved that it hits the bottom channel wall not far from the glottis and splits into two parts, one of them recirculating back to the glottal region, forming a large-scale vortex and interacting with the newly developed jet. Further downstream of the glottis, the jet disperses and forms complex 3D structures.

The glottal flow rate, calculated as a surface integral of the momentum flux at the inlet boundary T_{in} , together with pressure and velocity x -component at a probe located on the glottal midline 1 mm downstream of the superior vocal fold surface, are shown in Figs. 14 and 15. The flow being modeled as incompressible, the flow rate in any cross-section (including the narrowest cross-section in glottis) must be identical due to continuity equation. The flow rate waveform is only slightly skewed to the right, practically in phase with vocal fold motion, and does not differ significantly in the convergent and divergent glottal configurations. The leakage flow present during the maximum approach of the

vocal folds is about 0.042 l/s, 5.1% of the peak flow rate. The probed waveforms in Fig. 15 reveal that the maximum jet velocity appears at about 62% (CVG) and 64% (DVG) of the vocal fold closing phase.

Although the current model implements forced vocal fold vibration only, it is interesting to calculate the forces acting on the vocal fold surfaces. The x - and y -component of the aerodynamic force (6) exerted on the bottom vocal fold is plotted in Fig. 16 for convergent and divergent glottis. The figure shows that the vocal fold is pressed towards the supraglottal region by an oscillating, but steadily positive drag force with a mean value $F_x = 0.0175$ N (CVG) and $F_x = 0.0185$ N (DVG). The pressure and viscous drag force components were calculated separately, the dominant one being pressure drag (about 20–50 times higher than viscous drag). Theoretically, in the case of complete vocal fold closure and flow blockage, the viscous drag would be zero and the subglottal pressure $p = 300$ Pa and zero supraglottal pressure would induce a pressure drag $F_x = 0.019$ N, which is close to the simulated mean value. This means that in the current case, pressure recovery is very weak and that there is a zone of negative pressure in the near subglottal region in the closing phase. The highest drag occurs almost in the same phase as the maximum jet velocity, i.e. in 66% (CVG) and

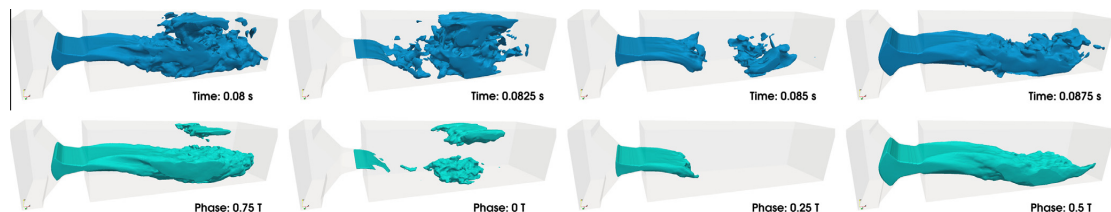


Fig. 12. Shape of the glottal jet for the convergent vocal folds in four phases of vocal fold motion. Instantaneous (top) and phase-averaged (bottom) fields – velocity magnitude isosurface (at value $U = 10$ m/s).

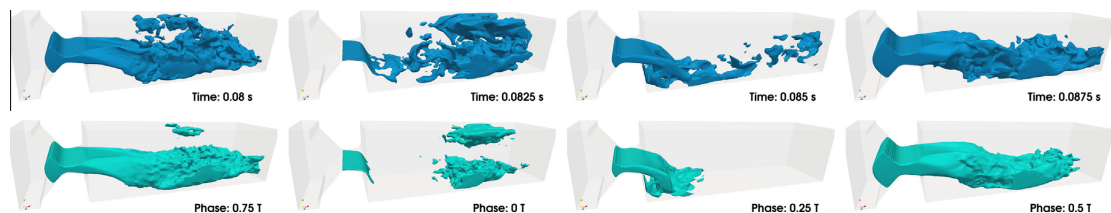


Fig. 13. Shape of the glottal jet for the divergent vocal folds in four phases of vocal fold motion. Instantaneous (top) and phase-averaged (bottom) fields – velocity magnitude isosurface (at value $U = 10$ m/s).

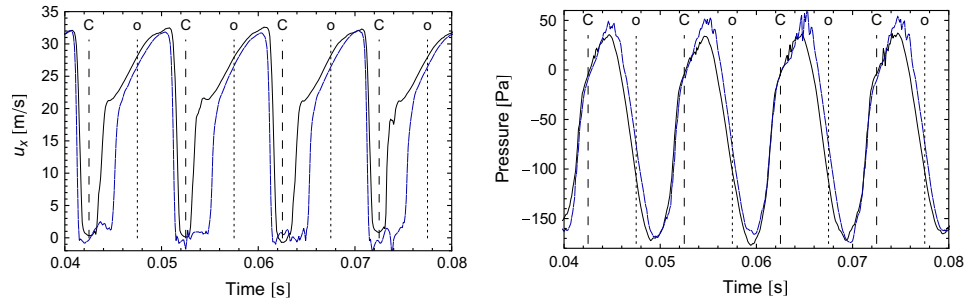


Fig. 15. Velocity x-component (left) and pressure (right) 1 mm downstream of the vocal folds for the convergent (black solid line) and divergent (blue dashed line) shape. Vertical dashed lines indicate the time instants of maximum glottis opening (o) and closure (C).

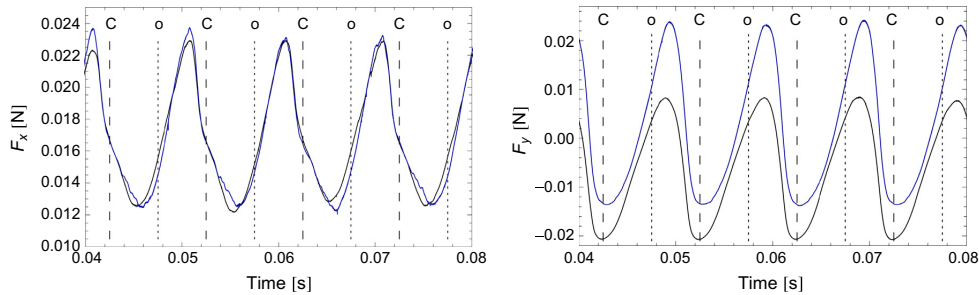


Fig. 16. Aerodynamic force exerted on the bottom vocal fold in the convergent (black solid line) and divergent (blue dashed line) glottis: x-component (drag force – left), y-component (lift force – right). Dashed vertical lines indicate the time instants of maximum glottis opening (o) and closure (C).

65% (DVG) of the vocal fold closing phase, the lowest drag at 53% (CVG) and 71% (DVG) of the opening phase.

As expected, the lift force F_y is negative (i.e. pressing the vocal folds apart) throughout larger part of the vibration cycle for the convergent case and mostly positive (pushing the vocal folds together) in the divergent configuration. Again, the lift force is constituted mostly of the pressure component; the amplitude of the viscous lift is about ten times lower. The lift force is lowest shortly before or shortly after maximum vocal fold approach (96% of the closing phase – CVG, 5% of the opening phase – DVG) and culminates at 32% (CVG) and 38% (DVG) of the closing phase. Historically, vocal fold oscillations were explained by Bernoulli effect: high flow velocity in glottis induces low pressure, which pushes vocal folds together; when the flow interrupts, pressure increases and presses the vocal folds apart. The plot of the lift force in Fig. 16 shows that this trivial explanation can be understood as the first approximation of the glottal physics, but that it is not entirely correct. The unsteady glottal aerodynamics are much more complex and the aerodynamic force is not necessarily in phase with vocal fold vibration, especially when the glottis has divergent shape.

4. Conclusions and discussion

A 3D finite volume model of glottal flow on a dynamic mesh with forced vocal fold oscillations was developed. The model aims for parallel resolution of glottal aerodynamics on fine 3D computational meshes. The algorithm was verified using benchmark computational data on flow over a static circular cylinder. Further, the grid dependence of the results was studied on six computational meshes composed of 550 k to 3.2 M elements.

In vocal fold and glottal flow modeling, a precise quantitative validation is always problematic, since the direct flow field

measurements in living subjects are almost impossible and the design of physical vocal fold models brings numerous technical complications. However, the current results are in good qualitative agreement with the data published in other computational papers, and with known physiological limits. When interpreting the data computed by the current model, it is necessary to keep in mind that the model geometry is simplified with regard to real larynx, and that the flow field in the very proximity of the outlet of the domain Γ_{out} may be influenced by the presence of the stabilized boundary condition for the velocity. A perfectly correct approach would be to situate the outlet much further downstream of the glottis. However, this would significantly increase the size of the mesh and the required CPU power.

During vibration of the vocal folds in the current model, a small gap is always left in between, leaving certain leakage flow where the real vocal folds would be completely closed (at least in most cases of the chest register). Optionally, the airflow can be artificially interrupted when the glottal gap drops below a limit value (not done in current simulations). This is a common choice in the body-conformal mesh-based computational models, in order to avoid dealing with topological changes of the mesh. The numerical instabilities often encountered on meshes with large deformations arise from the fact that the elements can get highly distorted (depending on the type of the elements used and on the method for updating of the grid point coordinates). When deformed uniaxially, the triangle-based prismatic elements used in the current mesh loose orthogonality in the intraglottal region and require employing nonorthogonal correctors, increasing the computational cost for one timestep and possibly introducing numerical errors. To circumvent this problem, a different type of mesh is currently tested based on unstructured hexahedral, surface-adapted block-refined meshes with high resolution in the medial–lateral direction and lower resolution in the inferior–superior direction. An

alternative to the body-conformal mesh-based methods are the immersed boundary solvers employed, e.g. in studies of Sciamarella and Quéré [41] and Luo et al. [46], Zheng et al. [43], Seo and Mittal [52], where a fixed Cartesian grid is used and the movement of the fluid–solid boundary is modeled.

The results of the 3D simulations show that the supraglottal flow dynamics are governed by complex interaction of a planar jet, channel boundaries and large-scale coherent vortices slowly propagating downstream. From practical reasons, 2D simplified flow models are still widely used in phonation modeling. The current results demonstrate that the 2D approximations can hold reasonably in the proximity of the glottis, where the flow field is forced to be mostly two-dimensional by the channel geometry. Thus, the reduction to 2D geometry, e.g. in models of the flow-induced vibrations of the vocal folds can spare much of the computational cost while not introducing significant error, especially if the flow separation point is predicted accurately. However, the 2D flow models substantially depart from reality further downstream of the flow separation point, where complex 3D vortex structures develop from the shear layer of the glottal jet. When the supraglottal aeroacoustics are of interest, a full 3D model should be used.

The current study also summarizes the results of parallel scalability tests run on Intel Xeon 5140 and AMD Opteron 252 nodes of a small computational cluster. The tests prove nearly linear scaling up to 16 cores, and show that the difference between the UMA architecture of the older Intel Xeon systems and the NUMA architecture of the AMDs leads to different requirements on the thread-to-core allocation schemes: while on the Intel nodes, the optimal configuration is to allocate only one thread per computational node, the AMD nodes are not much sensitive and in certain cases perform better when both processors are fully loaded. This conclusion is not valid universally, in the newer Intel Xeon systems (i.e. Intel Nehalem architectures) the shared FSB was replaced by a point-to-point processor link called QPI (QuickPath Interconnect) and the memory access shifted to NUMA, too. The current work intends to be a first step to massively parallel glottal flow computations on large clusters and supercomputers, which could provide new insight into the aerodynamics of human voice production.

Acknowledgments

The research has been supported by the Czech Science Foundation, project P101/11/0207 *Coupled problems of fluid and solid mechanics – nonlinear aeroelasticity*, within the research plan AV0220760514.

References

- [1] Titze IR. Principles of voice production. Prentice Hall; 1994.
- [2] McGowan R. An aeroacoustic approach to phonation. *J Acoust Soc Am* 1988;83(2):696–704.
- [3] Zhao W, Zhang C, Frankel S, Mongeau L. Computational aeroacoustics of phonation, part i: computational methods and sound generation mechanisms. *J Acoust Soc Am* 2002;112(5 Pt 1):2134–46.
- [4] Yang A, Lohscheller J, Berry DA, Becker S, Eysholdt U, Voigt D, et al. Biomechanical modeling of the three-dimensional aspects of human vocal fold dynamics. *J Acoust Soc Am* 2010;127(2):1014–31.
- [5] Mattheus W, Brücker C. Asymmetric glottal jet deflection: differences of two- and three-dimensional models. *J Acoust Soc Am* 2011;130(6):EL373–9.
- [6] Thomson S, Tack J, Verkerke G. A numerical study of the flow-induced vibration characteristics of a voice-producing element for laryngectomized patients. *J Biomech* 2007;40:3598–606.
- [7] Barney A, Shadle C, Davies P. Fluid flow in a dynamic mechanical model of the vocal folds and tract. i. Measurements and theory. *J Acoust Soc Am* 1999;105(1):444–55.
- [8] Alipour F, Scherer RC. Characterizing glottal jet turbulence. *J Acoust Soc Am* 2006;119(2):1063–73.
- [9] Scherer R, Shinwari D, Witt KD, Zhang C, Kucinschi B, Afjeh A. Intraglottal pressure profiles for a symmetric and oblique glottis with a divergence angle of 10°. *J Acoust Soc Am* 2001;109(4):1616–30.
- [10] Shinwari D, Scherer R, Dewitt K, Afjeh A. Flow visualization and pressure distributions in a model of the glottis with a symmetric and oblique divergent angle of 10°. *J Acoust Soc Am* 2003;113(1):487–97.
- [11] Erath B, Plesniak M. The occurrence of the Coanda effect in pulsatile flow through static models of the human vocal folds. *Exp Fluids* 2006;41:735–48.
- [12] Erath B, Plesniak M. The occurrence of the Coanda effect in pulsatile flow through static models of the human vocal folds. *J Acoust Soc Am* 2006;120(2):1000–11.
- [13] Li S, Scherer R, Wan M, Wang S, Wu H. The effect of glottal angle on intraglottal pressure. *J Acoust Soc Am* 2006;119(1):539–48.
- [14] Triep M, Brücker C, Schröder W. High-speed PIV measurements of the flow downstream of a dynamic mechanical model of the human vocal folds. *Exp Fluids* 2005;39:232–45.
- [15] Kucinschi B, Scherer R, Dewitt K, Ng T. An experimental analysis of the pressures and flows within a driven mechanical model of phonation. *J Acoust Soc Am* 2006;119(5 Pt. 1):3011–21.
- [16] Krane M, Barry M, Wei T. Unsteady behavior of flow in a scaled-up vocal folds model. *J Acoust Soc Am* 2007;122(6):3659–70.
- [17] Erath B, Plesniak M. An investigation of asymmetric flow features in a scaled-up driven model of the human vocal folds. *Exp Fluids* 2010;49(1):131–46.
- [18] Thomson S, Mongeau L, Frankel S. Aerodynamic transfer of energy to the vocal folds. *J Acoust Soc Am* 2005;118(3 Pt 1):1689–700.
- [19] Neubauer J, Zhang Z, Miraghaie R, Berry D. Coherent structures of the near field flow in a self-oscillating physical model of the vocal folds. *J Acoust Soc Am* 2007;121(2):1102–18.
- [20] Becker S, Knieburgs S, Müller S, Delgado A, Link G, Kaltenbacher M, et al. Flow-structure–acoustic interaction in a human voice model. *J Acoust Soc Am* 2009;125(3):1351–61.
- [21] Šidlof P, Doaré O, Cadot O, Chaigne A. Measurement of flow separation in a human vocal folds model. *Exp Fluids* 2011;51(1):123–36.
- [22] Horáček J, Uruha V, Radolf V, Veselý J, Bula V. Airflow visualization in a model of human glottis near the self-oscillating vocal folds model. *Appl Comput Mech* 2011;5:21–8.
- [23] Krebs F, Silva F, Sciamarella D, Artana G. A three-dimensional study of the glottal jet. *Exp Fluids*, 1–15. doi:10.1007/s00348-011-1247-3.
- [24] Knieburgs S, Thomson SL, Barney A, Triep M, Šidlof P, Horáček J, et al. In vitro experimental investigation of voice production. *Curr Bioinform* 2011;6(3):305–22.
- [25] Ishizaka K, Flanagan J. Synthesis of voiced sounds from two-mass model of the vocal cords. *The Bell Syst Tech J* 1972;51:1233–68.
- [26] Lucero J. Dynamics of the two-mass model of the vocal folds: equilibria, bifurcations, and oscillation region. *J Acoust Soc Am* 1993;94(6):3104–11.
- [27] Pelorson X, Hirschberg A, van Hassel R, Wijnands A, Auregan Y. Theoretical and experimental study of quasisteady-flow separation within the glottis during phonation. application to a modified two-mass model. *J Acoust Soc Am* 1994;96(6):3416–31.
- [28] Story B, Titze I. Voice simulation with a body-cover model of the vocal folds. *J Acoust Soc Am* 1995;97(2):1249–60.
- [29] Sciamarella D, d'Alessandro C. On the acoustic sensitivity of a symmetrical two-mass model of the vocal folds to the variation of control parameters. *Acta Acustica United with Acustica* 2004;90:746–61.
- [30] Horáček J, Šidlof P, Švec JG. Numerical simulation of self-oscillations of human vocal folds with Hertz model of impact forces. *J Fluids Struct* 2005;20(6):853–69.
- [31] Zhang Z. Influence of flow separation location on phonation onset. *J Acoust Soc Am* 2008;124(3):1689–94.
- [32] Suh J, Frankel S. Numerical simulation of turbulence transition and sound radiation for flow through a rigid glottal model. *J Acoust Soc Am* 2007;121(6):3728–39.
- [33] Suh J, Frankel S. Comparing turbulence models for flow through a rigid glottal model. *J Acoust Soc Am* 2008;123(3):1237–40.
- [34] Larsson M, Müller B. Numerical simulation of confined pulsating jets in human phonation. *Comput Fluids* 2009;38:1375–83.
- [35] Mihaescu M, Khosla SM, Murugappan S, Gutmark EJ. Unsteady laryngeal airflow simulations of the intra-glottal vortical structures. *J Acoust Soc Am* 2010;127(1):435–44.
- [36] Schwarze R, Mattheus W, Klostermann J, Brücker C. Starting jet flows in a three-dimensional channel with larynx-shaped constriction. *Comput Fluids* 2011;48(1):68–83.
- [37] Alipour F, Fan C, Scherer RC. A numerical simulation of laryngeal flow in a forced-oscillation glottal model. *Comput Speech Lang* 1996;10:75–93.
- [38] Renotte C, Bouffouix V, Wilquem F. Numerical 3d analysis of oscillatory flow in the time-varying laryngeal channel. *J Biomech* 2000;33(12):1637–44.
- [39] Alipour F, Scherer RC. Flow separation in a computational oscillating vocal fold model. *J Acoust Soc Am* 2004;116(3):1710–9.
- [40] Bae Y, Moon YJ. Computation of phonation aeroacoustics by an ins/pce splitting method. *Comput Fluids* 2008;37(10):1332–43.
- [41] Sciamarella D, Quéré PL. Solving for unsteady airflow in a glottal model with immersed moving boundaries. *Euro J Mech B/Fluids* 2008;27:42–53.
- [42] Punčochářová-Porížková P, Kozel K, Horáček J. Simulation of unsteady compressible flow in a channel with vibrating walls – influence of the frequency. *Comput Fluids* 2011;46(1):404–10.

- [43] Zheng X, Mittal R, Bielamowicz S. A computational study of asymmetric glottal jet deflection during phonation. *J Acoust Soc Am* 2011;129(4):2133–43.
- [44] de Oliveira Rosa M, Pereira J, Grellet M, Alwan A. A contribution to simulating a three-dimensional larynx model using the finite element method. *J Acoust Soc Am* 2003;114(5):2893–905.
- [45] Tao C, Jiang J. Mechanical stress during phonation in a self-oscillating finite-element vocal fold model. *J Biomech* 2007;40(10):2191–8.
- [46] Luo H, Mittal R, Zheng X, Bielamowicz SA, Walsh RJ, Hahn JK. An immersed-boundary method for flow-structure interaction in biological systems with application to phonation. *J Comput Phys* 2008;227(22):9303–32.
- [47] Link G, Kaltenbacher M, Breuer M, Döllinger M. A 2d finite-element scheme for fluid–solid–acoustic interactions and its application to human phonation. *Comput Meth Appl Mech Eng* 2009;198:3321–34.
- [48] Zheng X, Bielamowicz S, Luo H, Mittal R. A computational study of the effect of false vocal folds on glottal flow and vocal fold vibration during phonation. *Ann Biomed Eng* 2009;37(3):625–42.
- [49] Sváček P. Numerical approximation of flow induced vibrations of channel walls. *Comput Fluids* 2011;46(1):448–54.
- [50] Zheng X, Xue Q, Mittal R, Beilamowicz S. A coupled sharp-interface immersed boundary-finite-element method for flow-structure interaction with application to human phonation. *J Biomech Eng* 2010;132(11):111003.
- [51] Zheng X, Mittal R, Xue Q, Bielamowicz S. Direct-numerical simulation of the glottal jet and vocal-fold dynamics in a three-dimensional laryngeal model. *J Acoust Soc Am* 2011;130(1):404–15.
- [52] Seo JH, Mittal R. A high-order immersed boundary method for acoustic wave scattering and low-Mach number flow-induced sound in complex geometries. *J Comput Phys* 2011;230(4):1000–19.
- [53] Alipour F, Brucker C, Cook D, Gommel A, Kaltenbacher M, Mattheus W, et al. Mathematical models and numerical schemes for the simulation of human phonation. *Curr Bioinform* 2011;6(3):323–43.
- [54] Scherer RC, Shinwari D, Witt KJD, Zhang C, Kucinschi BR, Afjeh AA. Intraglottal pressure distributions for a symmetric and oblique glottis with a uniform duct. *J Acoust Soc Am* 2002;112(4):1253–6.
- [55] Titze IR. The physics of small-amplitude oscillation of the vocal folds. *J Acoust Soc Am* 1988;83(4):1536–52.
- [56] Chevalier C, Pellegrini F. Pt-scotch: a tool for efficient parallel graph ordering. *Parall Comput* 2008;34(6–8):318–31.
- [57] Karypis G, Kumar V. A fast and high quality multilevel scheme for partitioning irregular graphs. *SIAM J Scient Comput* 1998;20:359–92.
- [58] The OpenFOAM foundation. OpenFOAM User Guide; 2011 <<http://www.openfoam.org/docs/user/>>.
- [59] Ferziger JH, Peric M. Computational methods for fluid dynamics. Springer; 2001.
- [60] Turek S, Schäfer M. Recent benchmark computations of laminar flow around a cylinder; 1996 205 citations <<http://www.mathematik.tu-dortmund.de/lsi/iii/cms/papers/SchaeferTurek1996.pdf>>.
- [61] Tao C, Zhang Y, Hottinger D, Jiang J. Asymmetric airflow and vibration induced by the Coanda effect in a symmetric model of the vocal folds. *J Acoust Soc Am* 2007;122(4):2270–8.

Biomechanics and Modeling in Mechanobiology manuscript No.
(will be inserted by the editor)

A hybrid approach to computational aeroacoustics of human voice production

Šidlof P. · Zörner S. · Hüppe A.

Received: 18 October 2013 / Accepted: 2 September 2014

Abstract The aeroacoustic mechanisms in human voice production are complex coupled processes, which are still not fully understood. Here, a hybrid numerical approach is presented to analyze the sound generation in human voice production. First, the fluid flow is solved using a parallel finite volume CFD solver on a fine computational mesh covering the larynx. The CFD simulations are run for four geometrical configurations: both with and without false vocal folds, and with fixed convergent or convergent-divergent motion of the medial vocal fold surface. Subsequently, the aeroacoustic sources and propagation of the sound waves are calculated using Lighthill's analogy or acoustic perturbation equations on a coarse mesh covering the larynx, vocal tract and radiation region near the mouth. Aeroacoustic sound sources are investigated in the time and frequency domain to determine their precise origin and correlation with the flow field. The acoustic wave propagation from the larynx and vocal tract into the free field is solved by the finite element method. Two different vocal tract shapes are considered and modeled according to MRI vocal tract data of the vowels /i/ and /u/. The spectra of the radiated sound evaluated from the acoustic simula-

tion show good agreement with the formant frequencies known from human subjects.

Keywords computational aeroacoustics · parallel CFD · human voice · biomechanics · vocal folds · ventricular folds

1 Introduction

In everyday life, people are surrounded by a variety of sources generating disruptive noise, which can even be hazardous to health if certain sound pressure levels are exceeded. Two major sources of noise are mechanical vibration (e.g., vehicle engines, industrial machines and mechanisms) and turbulent airflow (airplanes, jet engines, aerodynamic vehicle noise, ventilators or air conditioning systems). However, some sources of flow-induced sound are desirable – this is the case when considering wind musical instruments or the human voice.

Human voice production is a process involving flow-induced vibration of the vocal folds, which are multi-layered soft tissue structures located in the larynx. A detailed overview of human voice production mechanisms from the physiological and fluid-mechanical point of view is given in the works of Titze (2006) and Mittal et al (2013), respectively. Here it is sufficient to state that the sound in the human larynx is generated by a complex interaction between a pulsating air jet, induced by expiration from lungs and formed by the vibrating vocal folds, and supraglottal turbulent structures. In a first approximation, the vocal tract acts as a filter of the acoustic pressure perturbations generated in the larynx, forming different vowels depending on its shape. Despite all efforts to date, the full details of the sound production mechanisms are yet to be entirely understood.

Šidlof P.
Technical University of Liberec
Studentská 2, 461 17 Liberec, Czech Republic
E-mail: petr.sidlof@tul.cz

Šidlof P.
Academy of Sciences of the Czech Republic
Institute of Thermomechanics
Dolejšková 5, 182 00 Prague 8, Czech Republic

Zörner S., Hüppe A.
Vienna University of Technology
Institute of Mechanics and Mechatronics
Wiedner Hauptstraße 8–10, 1040 Vienna, Austria

One way to analyze voice generation is to model the fundamental physical phenomena mathematically using partial differential equations and solve them numerically with the assistance of simulation tools. An extensive review of numerical models of human phonation can be found in (Alipour et al 2011).

In the field of aeroacoustics in the human vocal tract, the computational methods gain even more importance, since direct flow and acoustic measurements within the vocal tract are invasive and therefore hardly possible. One approach to computational aeroacoustics is the direct solution of the compressible Navier-Stokes equations, which capture both fluid dynamic and acoustic phenomena. This approach was used, e.g., in the studies of Zhao et al (2002) and Zhang et al (2002), where the compressible Navier-Stokes equations were solved on an axisymmetric 2D geometry. To characterize the different sources, the analogy of Ffowcs-Williams-Hawkings was used. The authors concluded that the main source is of a dipolar kind, induced by the net force exerted by the surface of the vocal folds onto the fluid.

However, direct numerical simulation of aeroacoustic problems has specific drawbacks. Firstly, the aerodynamic and acoustic pressure fields have dramatically different length scales, with differences easily reaching the orders of 10^3 – 10^5 . This leads to very different requirements on the grid element size for the fluid-dynamic and acoustic fields. Moreover, most of the sound generation processes are located close to the flow constriction formed by the vocal folds (called glottis), and so considerable computational power would be wasted when solving the fluid-dynamic fields in the whole vocal tract. This is why the hybrid methods, solving the flow and acoustic fields separately, represent a viable option in computational aeroacoustics.

A hybrid aeroacoustic approach for the simulation of voice production was used, e.g., in the work of Bae and Moon (2008), where the perturbed compressible equations were solved on a 2D geometry with acoustic sources from incompressible Navier-Stokes equations. Fully three-way fluid-solid-acoustic coupling was presented by Link et al (2009), who used Lighthill's acoustic analogy to calculate the acoustics. A recent study of Seo and Mittal (2011) followed by Tian et al (2014) employs the immersed boundary method for incompressible low-Mach number flow coupled to a finite element solver for the viscoelastic tissue and a hydrodynamic-acoustic splitting technique and linearized perturbed compressible equations to compute the acoustic field.

The vibration of the real human vocal folds is flow-induced. However, the fully coupled fluid-structure simulations, e.g., (Link et al 2009; Seo and Mittal 2011; Feistauer et al 2013) always suffer from a lack of accu-

rate geometrical and material properties of the living tissues. This is due to the fact that the parameters are highly subject-specific, and also because most of the vocal fold tissue measurements, e.g., (Zörner et al 2010; Kelleher et al 2013), are still hardly applicable in vivo to precisely determine the vocal fold material parameters during abduction. As shown in the paper of Zörner et al (2013), the full fluid-structure interaction solution can be approximated by prescribed vocal fold motion, provided that the boundary conditions are set properly. In this way, the problem is circumvented and also considerable computational resources are spared. This approach is also adopted in the current study.

For the present paper, a CFD model of flow past the vibrating vocal folds, modeled by incompressible Navier-Stokes equations and solved numerically in parallel on a fine 3D computational mesh covering the larynx, yields the fluid dynamical data. Further, two variants of acoustic analogies for the computation of flow-induced sound generated in the larynx are presented. From the CFD results, aeroacoustic source terms are calculated using Lighthill's acoustics analogy and a perturbation-based approach. The propagation of the sound waves is then calculated using the finite element method on a coarser 3D mesh also comprising the vocal tract and acoustic radiation region near the mouth. This enables the investigation of the impact of different geometries and vocal fold vibration patterns.

2 CFD model of the glottal flow

2.1 Mathematical model

The airflow through the vocal folds is modeled by the Navier-Stokes equations on a time-dependent 3D geometry. Since the flow velocities found in typical human phonation are usually below $Ma = 0.2$, the incompressible Navier-Stokes equations in strong conservation form are used, given by

$$\begin{aligned} \nabla \cdot \mathbf{u} &= 0, \\ \frac{\partial}{\partial t} \mathbf{u} + \nabla \cdot (\mathbf{u}\mathbf{u}) - \nu \Delta \mathbf{u} + \frac{1}{\rho_0} \nabla p &= 0. \end{aligned} \quad (1)$$

Here \mathbf{u} denotes flow velocity, p fluid dynamic pressure, ρ_0 is air density and ν kinematic viscosity. The boundary conditions imposed on the pressure and velocity fields were chosen to approximate the real physiological conditions: the airflow in the model is driven by a constant pressure difference between the inlet and the outlet of the domain (i.e., constant lung pressure

and zero relative pressure at the outlet). The pressure condition at the inlet is applied on the total pressure

$$p_0 = p + \frac{1}{2} \rho (\mathbf{u} \cdot \mathbf{u}). \quad (2)$$

At the outlet, the fluid-dynamic pressure $p = 0$ is prescribed and on the channel walls $\partial p / \partial \mathbf{n} = 0$. The boundary conditions for the velocity field were set as follows: $\partial \mathbf{u} / \partial \mathbf{n} = 0$ at the inlet, where \mathbf{n} is the unit outer normal, and no-slip condition $\mathbf{u} = 0$ on the fixed walls. On the vocal fold surfaces, the flow velocity is calculated according to the velocity of the moving vocal fold. Due to the presence of large vortical structures convected downstream of the glottis up to the outlet of the computational domain and consequent backflow to the domain destabilizing the numerical solution, it was necessary to introduce a stabilized outflow condition at the outlet of the domain: $\partial \mathbf{u} / \partial \mathbf{n} = 0$ if the velocity direction points outward from the domain and $\mathbf{u} = 0$ otherwise.

2.2 Geometry

The computational domain for the fluid flow consists of a short straight subglottal region of length $T_0 = 2.8$ mm, the vocal folds of length $T_{VF} = 7.2$ mm, optionally ventricles and false vocal folds (FVFs, also called ventricular folds), and a supraglottal region of total length $T_1 = 40$ mm (see Fig. 1). Note that for practical reasons the larynx is not oriented consistently with respect to its physiological position, i.e. the laryngeal channel "length" is actually aligned with the inferior-superior direction. The height (medial-lateral dimension) of the laryngeal channel is $2 * H_0 = 12.0$ mm. To avoid geometrical complexities, the cross-section of the glottal channel in the current model is rectangular with thickness of 12 mm – the shape does not change along the anterior-posterior axis.

The geometry of the model vocal folds used in this study is specified according to the parametric vocal fold shape description "M5" proposed by Scherer et al (2001). The "M5" model is piecewise linear with rounded corners; as compared to real vocal fold geometry, the model is considerably simplified (Šidlof et al 2008). However, it is widely used since it provides an easily parameterizable 2D approximation of the vocal fold surface geometry, the major variable being the medial surface convergence angle ψ (defined usually as positive for divergent vocal folds, and as negative for convergent configuration).

Regarding the geometry of the false vocal folds, it is more difficult to find relevant quantitative data in the literature. In the current model, the FVFs were

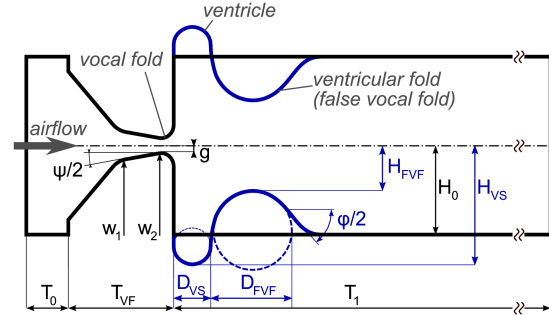


Fig. 1: Geometric model of the human larynx in coronal section. Model without (black) and with (blue) FVFs. The length of the supraglottal channel is not to scale.

approximated by a shape described by Agarwal et al (2003), where two large datasets obtained by lamina-graphic measurements of living subjects were processed, parametrized and quantified. According to the data published in this paper, the radius of the ventricle was set to $D_{VS}/2 = 1.25$ mm, the radius of the false vocal fold to $D_{FVF}/2 = 6.3$ mm and the FVF superior surface divergence angle to $\varphi = 110^\circ$. The height (medial-lateral span) within the ventricle is $2 * H_{VS} = 16$ mm, the gap between the false vocal folds $2 * H_{FVF} = 6$ mm.

During the CFD simulation, the vocal folds oscillate, thus deforming the computational domain. The kinematics of the vocal folds were programmed to allow for two-degrees-of-freedom, convergent-divergent motion of each of the vocal folds, with prescribed sinusoidal displacement of the inferior and superior vocal fold margins in the medial-lateral direction

$$\begin{aligned} w_1(t) &= A_1 \sin(2\pi ft + \xi) \\ w_2(t) &= A_2 \sin(2\pi ft), \end{aligned} \quad (3)$$

where f is the frequency of vibration and ξ the phase difference. The coordinates (3) determine uniquely the glottal half-gap g and the medial surface convergence angle ψ (see Fig. 1). During oscillation, the inferior, medial and superior vocal fold surfaces remain straight, and the connecting radii correspond exactly to the "M5" shape definition of Scherer et al (2001), so that the shape is smooth without sharp edges. In this way, the basic convergent-divergent motion of the real vocal folds is mimicked, whilst still keeping the kinematic model simple.

In order to assess the influence of the individual geometric and kinematic parameters, four configurations were used for the CFD simulations (see Tab. 1). In all

Table 1: Overview of the parameters of the geometric configurations C1, C1F, C2 and C2F: presence of the false vocal folds, amplitudes A_1 , A_2 and phase difference ξ between the inferior and superior vocal fold margin, medial surface convergence angle ψ , minimum and maximum glottal half-gap g (see also Fig. 1 and eqn. (3)).

	C1	C1F	C2	C2F
FVFs	no	yes	no	yes
A_1	0.4 mm	0.4 mm	0.3 mm	0.3 mm
A_2	0.4 mm	0.4 mm	0.3 mm	0.3 mm
ξ	0	0	$\pi/2$	$\pi/2$
ψ	-20°	-20°	$-24^\circ \dots 24^\circ$	$-24^\circ \dots 24^\circ$
g_{min}	0.1 mm	0.1 mm	0.2 mm	0.2 mm
g_{max}	0.9 mm	0.9 mm	0.72 mm	0.72 mm

cases, the vibration of the upper and lower vocal folds was symmetric with respect to the medial plane.

In simulations C1 and C1F, the vocal folds move with a single degree of freedom and a fixed convergence angle $\psi = -20^\circ$. In C2 and C2F, the motion of the model captures the basic kinematic features of the real vocal folds. Based on the values listed by Titze (2006) and the data measured by Boessenecker et al (2007) using high-speed imaging of excised human larynges, the phase shift between the inferior and superior margin of the vocal folds was set to $\pi/2$. Due to the stability problems caused by severe mesh deformation, the amplitudes A_1 and A_2 of the inferior and superior vocal fold margin were set lower than in C1 and C1F. Physiologically, this corresponds to insufficient glottal closure. The letter 'F' in the acronym denotes the presence or absence of the false vocal folds.

2.3 CFD mesh

The computational domain and the mesh are depicted in Fig. 2 (for configuration C1F). The mesh is unstructured triangular and isotropic in the coronal plane, extruded in a structured way to the third dimension. The grid was generated using a free mesh generator *gms*h (Geuzaine and Remacle 2009), with element characteristic length 0.15 mm in the coronal plane and 0.3 mm in the medial-lateral direction for the undeformed mesh. For the parallel CFD simulations, the mesh is partitioned using the scotch algorithm (Chevalier and Pellegrini 2008). More details on mesh generation and partitioning can be found in previous work of the author (Šidlof et al 2013).

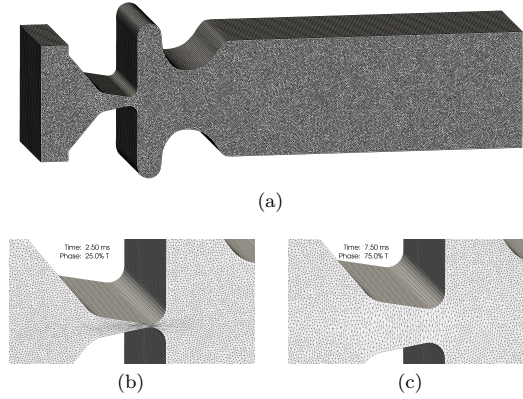


Fig. 2: (a) Full view of the CFD computational domain and undeformed mesh composed of 2.4M prismatic elements for case C1F. (b) Maximum closure and (c) maximum opening phases within the vocal fold vibration cycle.

2.4 Implementation and numerical solution

The numerical solution of the airflow in the glottal channel with moving walls was implemented in *OpenFOAM*, an object-oriented open-source set of libraries programmed in the C++ language. *OpenFOAM* is based on the finite volume method in collocated cell-centered approach on arbitrarily unstructured meshes. The incompressible Navier-Stokes equations on a moving computational mesh were solved numerically using a modified PISO algorithm (Ferziger and Peric 2002). In contrast to the standard PISO algorithm, it has a substep iteration loop: multiple cycles over the same timestep with the last iteration results (optionally under-relaxed) used as an initial guess for the next substep iteration. The current simulation used two substep iterations with the under-relaxation factor $\alpha = 1$ (i.e., no under-relaxation).

The discretization schemes were as follows: first-order implicit Euler for the time derivative, total variation diminishing (TVD) scheme with a limiter function

$$\Phi(r) = \max(0, \min(2r, 1)) \quad (4)$$

for the convective term, and central differencing scheme (CDS) with nonorthogonal correction for the diffusion term. The timestep Δt is adjusted automatically during the transient solution so that the maximum local Courant number is kept below a predefined limit. The

Courant number on unstructured 3D meshes is calculated as

$$Co = \frac{1}{2} \frac{\sum_f |\Phi_f|}{\Delta V} \Delta t, \quad (5)$$

where $\Phi_f = A_f (\mathbf{u}_f \cdot \mathbf{n}_f)$ is the velocity flux normal to face f with surface A_f of the cell with volume ΔV .

The computational domain changes in time due to vocal fold oscillations. Since the vocal folds do not collide and close the channel completely in current simulations, it is not necessary to introduce topological changes to the mesh, instead it is simply deformed. The coordinates of the element vertices in a new timestep are found by solving an auxiliary Laplace equation

$$\nabla \cdot (\gamma \nabla \mathbf{w}) = 0 \quad (6)$$

for the mesh velocity \mathbf{w} with spatially variable diffusivity γ . Boundary conditions are set to $\mathbf{w} = 0$ at the inlet, outlet, top and bottom walls, prescribed mesh velocity on the moving vocal fold surfaces and $\partial \mathbf{w} / \partial \mathbf{n} = 0$ on the lateral walls where the mesh is allowed to “slip” freely. Two strategies for the distribution of the diffusivity γ were tested: $\gamma = \text{const}$ and γ decreasing exponentially with distance from the vocal fold surfaces. The former approach was used in the simulations, the latter caused grid connectivity errors in certain cases. Due to significant element distortion and consequent loss of element orthogonality between the moving vocal folds, one outer loop of nonorthogonal correctors was utilized within the modified PISO algorithm to guarantee stability of the computation. The nonorthogonal correction strategy within the current finite volume discretization is described in detail by Jasak (1996). Unlike the discretization of the temporal, convective and diffusive terms, the nonorthogonal correctors are treated explicitly. In test simulations with static vocal folds, the nonorthogonal correctors were not needed. The resulting implicit scheme allowed the use of a higher Courant number limit $Co < 5$. With the moving grid, the numerical scheme acquires explicit character and the timestep has to be limited so that the CFL condition $Co < 1$ is satisfied.

The resulting linear system for momentum was solved using the bi-conjugate gradient method with diagonal-based incomplete LU preconditioning. For the pressure predictor and corrector steps, faster convergence was obtained using a geometric multigrid solver, using an *OpenFOAM*-specific cell agglomeration algorithm and a conjugate gradient-type method for solution of the coarsest level matrix. The Laplace equation (6) for the mesh motion was discretized using central differences

and solved using the diagonal incomplete-Cholesky preconditioned conjugate gradient method. The auxiliary problem (6) must be solved for each timestep. In the current simulation setup, the solution of the Laplace equation caused a computational overhead of about 10 % for the case C1 and C1F, and 20 % for C2 and C2F.

Before running the CFD simulations for the aeroacoustic computations, the accuracy of the code was verified on a benchmark case of 2D unsteady separated cylinder cross-flow at low Reynolds numbers. The maximum differences found in the frequency of vortex shedding, Strouhal number and maximum and minimum drag and lift coefficients were about 6% in comparison to the mean benchmark values (Šidlof et al 2013).

For parallelization of the CFD simulations, *OpenFOAM* employs the domain decomposition method. The strong and weak scaling tests were performed on a shared-memory parallel supercomputer SGI Altix UV 100. The parallel scaling results, published and discussed in detail in (Šidlof et al 2013a), show a strong speedup of about 28x on 40 computational cores, which makes the current CFD simulations on computational meshes with about 2.5 M elements feasible on this small parallel supercomputer. The weak parallel efficiency (with a fixed job-per-core size of 120 k elements) showed a drop to 50% on 50 cores. As pointed out by Rivera et al (2011), the MPI communication routines in *OpenFOAM* may cause an important overhead for a higher number of MPI tasks, when the multigrid solver is used. However, this is only one possible explanation, as the parallel performance analysis and optimization for massive parallelization in *OpenFOAM* is still a matter of intense ongoing research.

2.5 CFD results

Figures. 3–7 show the results of the CFD simulations in four geometrical configurations C1, C1F, C2 and C2F (see Tab. 1). In all cases, the initial conditions, boundary conditions for pressure and velocity and also the frequency of vibration $f = 100$ Hz are identical. The airflow is driven by a constant pressure difference $\Delta p_0 = 360$ Pa between the inlet and the outlet (where p_0 is the total pressure (2)), corresponding to soft phonation. Contrary to prescribed flow velocity, which is often used as a boundary condition at the inlet, a pressure gradient assures a natural development of the flow which ensures that appearing frequencies can be traced back to the vocal fold vibration and are not directly induced by inflow conditions (Zörner et al 2013).

The grid dependence was analyzed in the previous study (Šidlof et al 2013) on six isotropic meshes composed of 550 k to 3.2 M elements. The grid sensitivity

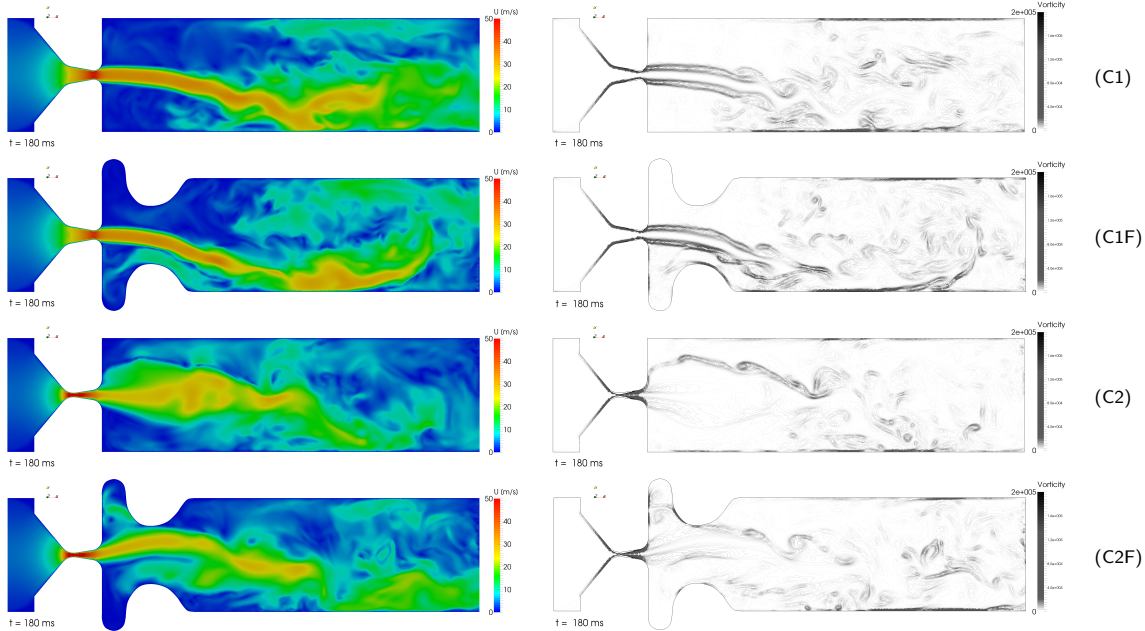


Fig. 3: Flow field in the mid-coronal section in the 19th period of vibration, middle of the vocal fold closing phase, simulations C1, C1F, C2 and C2F. Velocity magnitude (left), vorticity magnitude contours (right).

was tested for a local value of pressure shortly downstream of the glottis, and for two integral quantities: drag and lift forces exerted by the airflow on the vocal folds. It has been shown that for this type of simulation a mesh consisting of approximately 2.4 M elements is sufficient.

For the purpose of subsequent aeroacoustic computations, a CFD simulation over at least 20 periods of vocal fold vibration ($t = 0.2$ s) was needed to obtain sufficient resolution in the sound spectra. The simulation run required about 4600 core-hours and a disk space of about 160 GB to store the velocity, pressure and mesh displacement fields in $20 * 100 = 2000$ timesteps.

The flow field in a mid-coronal section is illustrated in Fig. 3, which shows the velocity magnitude and vorticity magnitude contours for all configurations. The time instant $t = 0.18$ s corresponds to the middle of the closing phase in the 19th period of vibration, close to the phase when the glottal jet is most intensive. The regions of high vorticity are located mainly on the medial surfaces of the vocal folds, in the shear layer of the jet and in the place where the jet interacts with the supraglottal channel wall. It can be seen that within the divergent phase of the vocal fold motion in C2 and

C2F, the shear layer of the jet is wider and induces less vorticity than in C1 and C1F.

In all simulations, the jet is deflected to one side of the channel during most of the vocal fold oscillation period. As remarked by Mittal et al (2013), this should not be hastily attributed to the Coanda effect (as is quite often the case in the voice biomechanics community). The direction of the pulsating glottal jet is actually affected by a variety of complex phenomena, some of which are discussed further. The jet deflection angle was evaluated by locating the maximum of the mid-coronal velocity profile taken at $x = 1$ mm downstream of the glottis and plotted in Fig. 4.

The jet deflection angle is higher in C1F than in C1, reaching up to -75° near the maximum vocal fold closure. In the case of fixed vocal fold convergence angle (C1 and C1F), the jet deflection angle is generally biased downwards. In C2F, the jet flaps during the oscillation period and the jet deflection angle oscillates between positive and negative values.

According to our understanding and analysis of the results, the deflection angle is influenced by three major effects. First, by interaction with recirculating flows, which play a dominant role particularly when the glottal jet momentum is low, i.e. near glottal closure. This

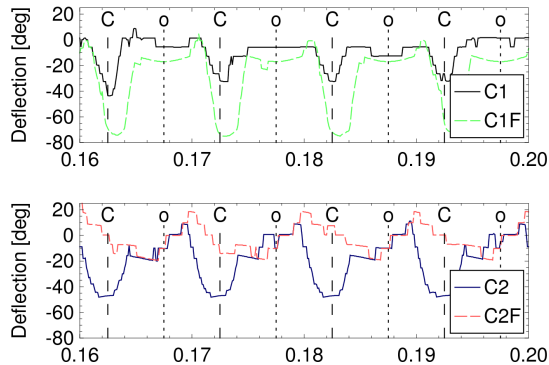


Fig. 4: Glottal jet deflection angle within four periods of vocal fold vibration for the four cases C1, C1F, C2 and C2F. Vertical dashed lines indicate the time instants of maximum glottis opening (o) and closure (C).

behavior was also observed in the PIV measurements on two different synthetic vocal fold models of Pickup and Thomson (2009) and Sidlof et al (2011). The constriction formed by the false vocal folds and the additional volume of the ventricle induce different backflow and vortex patterns, which deflect the jet significantly more in C1F than in the case C1 with a straight supraglottal channel.

The large-scale supraglottal vortices and recirculating flows in the simulations C2/C2F with convergent-divergent motion are very different from those in the configurations C1/C1F. Thus, the influence of the false vocal folds on the jet deflection angle for this type of vocal fold kinematics is different from the previous two simulations. Again, the jet skews most near the glottal closure in C2. However, in the case with false vocal folds (C2F), the jet deflection angle is generally lower than in C2 and its maximum and minimum lie in the middle of the closing phase and in about 3/4 of the opening phase, respectively.

Second, the jet also skews as a result of supraglottal pressure distribution, which is affected by the presence or absence of the false vocal folds. When the vocal folds are divergent (C2 and C2F), the jet separates and deflects already on the medial surfaces due to adverse pressure gradient. As the grid resolution is not sufficient to capture the intraglottal jet shear layer and vortex structures, in this case the jet skewing may be attributed to the Coanda effect.

Fig. 5 shows the pressure distribution along glottal midline. The pressure drop within the glottis in the presence of the FVFs (C1F) compared to case C1 is lower due to the slightly lower flow rate, as can be seen in Fig. 6. The pressure distribution in cases C2/C2F

is different, since in this time instant the glottis has a divergent shape and the minimum glottal gap is smaller. Here, the pressure minimum is located further from the superior margin $x = 0$ and the pressure drop is lower in C2F, since the flow rate in the middle of the closing phase is slightly higher than in C2.

The time history of the flow rate in Fig. 6 reveals that the false vocal folds in the current simulations cause a slight decrease in peak flow rate in C1/C1F and slight increase of the minimum flow rate in C2/C2F. The effect of the FVFs on the transglottal flow resistance and flow rate has already been investigated in several studies. Most of them (Zheng et al 2009; Li et al 2007) show that the presence of the ventricular folds tends to decrease flow resistance and increase flow rate. However, there are also works which have found the contrary (Alipour et al 2007). As pointed out by Bailly et al (2008), the effect of the FVFs can be highly sensitive to the geometry, particularly to the ratio

$$\eta = \frac{2g}{2H_{FVF}} \quad (7)$$

between the true vocal fold gap and false vocal fold gap (see Fig. 1). Agarwal (2004) demonstrated that a noticeable decrease in translaryngeal flow resistance can be seen for $\eta = 2 \dots 6$ and the results of Li et al (2007) show that the influence of FVFs is already insignificant above $\eta > 1.5$. In the current simulations, the FVF gap is higher, yielding $\eta = 3.3 \dots 30$.

Fig. 6 also shows that the flow rate in cases C2/C2F has lower amplitude compared to C1/C1F, and the minimum is at about 30 % of the peak value. This is caused by the settings of the vocal fold motion kinematic model (see also Tab. 1). The convergent-divergent motion induces a kink in the flow rate waveform at the end of the closing phase.

The geometry of the current simplified model is rectangular. Fig. 7 demonstrates a mid-sagittal section the transition of the velocity field, which has planar characteristics in the subglottal region and shortly downstream of the glottis, to a complex fully 3D flow field further in the supraglottal region. The jet in the case C1F seems to be shorter than in C1, but only due to the fact that it skews more and leaves the visualization plane earlier. In fact, the current numerical simulations suggest that the false vocal folds do not have a significant effect on the jet length. The jet in C2F is bent in the transverse plane, making it appear split in two in the sagittal section.

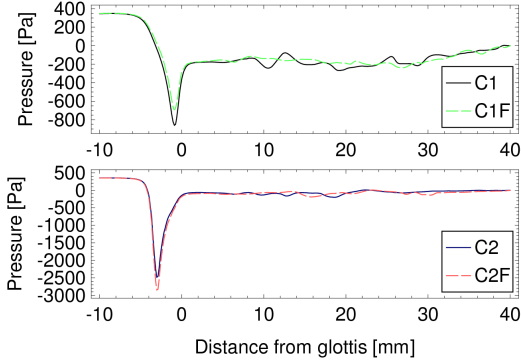


Fig. 5: Pressure distribution along glottal midline for the four simulations, middle of the closing phase ($t = 180$ ms).

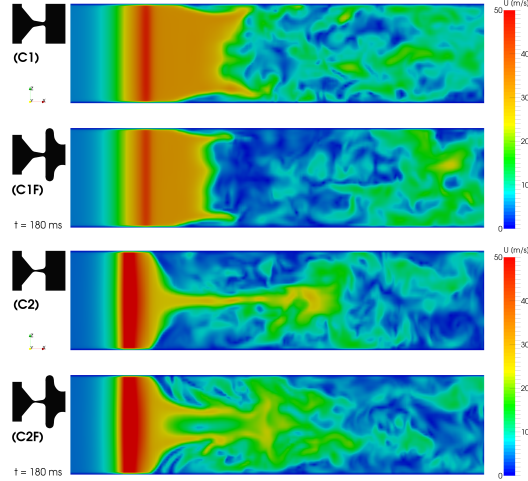


Fig. 7: Velocity magnitude in the mid-sagittal section for the four simulations C1, C1F, C2 and C2F, 19th period of vibration, middle of the closing phase.

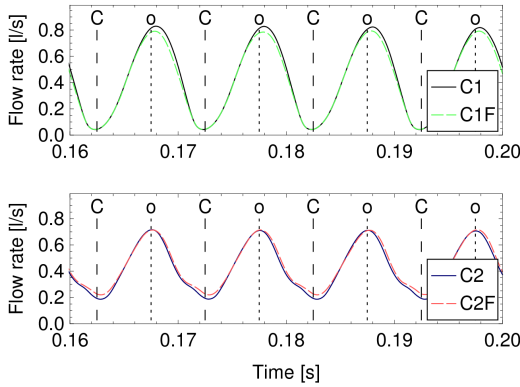


Fig. 6: Flow rate within glottis for the four cases C1, C1F, C2, C2F. Vertical dashed lines indicate the time instants of maximum glottis opening (o) and closure (C).

3 Aeroacoustics

3.1 Geometry of the vocal tract and computational procedure

The geometric model used for the aeroacoustic simulation consists of the larynx, the vocal tract and an acoustic propagation region in which the radiated sound is monitored (see Fig. 9a). The vocal tract model is attached to the larynx and consists of multiple frustums concatenated one after another. The number of frustums and their radii determine the resulting sound radiating from the artificial mouth. The cross sections (so-called area functions) were taken from works of Story et al (1996), who acquired 3D vocal tract shapes of particular

vowels and consonants by means of magnetic resonance imaging (MRI). Thereby, 18 vocal tract configurations were discussed, each being divided into single segments with a length of about 3.97 mm. Two of these shapes are used in this work, representing the vowels /i/ (“heed”) and /u/ (“who”). The vocal tract for /i/ consists of 44 segments and for /u/ of 46 segments, resulting in a length of approximately 17.5 cm and 18.25 cm, respectively. The area of the vocal tract segments as a function of distance from the larynx for both models is plotted in Fig. 8. As the vocal tracts are attached to the outflow of the CFD domain, the rectangular flow domain is an additional volume to the measured data of Story et al (1996). Therefore, an error is introduced as the first frustum is positioned 40 mm (T_1) downstream of the glottis – its actual location. The geometric difference has an effect on the acoustics and will be discussed in Sec. 3.5. The transition from the rectangular outflow to the circular inlet of the vocal tract is made by a volume, which has a square base and gradually changes to a circle along the center axis. At the end of the vocal tract, the mouth, an acoustic propagation region ($2.5 \times 2.5 \times 2.5 \text{ cm}^3$) is added to capture the jump of acoustic impedance due to the transition from the relatively small volume of the vocal tract to an open domain.

The acoustic domain consists of three subdomains (Fig. 9a). The first subdomain is the acoustic source region, where the fluid simulation is performed and in which the flow induced sources are computed. Directly attached to it is the vocal tract, which acts as an acoustic

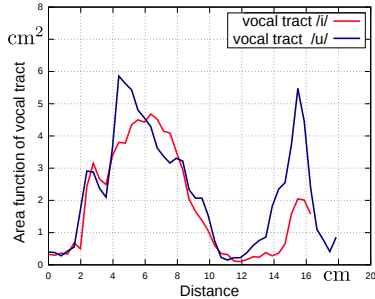


Fig. 8: Area of vocal tract segment as a function of distance from the larynx model.

filter, followed by an acoustic propagation region. As the finite element method is nodal based and *OpenFOAM* is cell-centered, the data is interpolated onto the nodes using VTK (The Visualization Toolkit, Schroeder and Martin (2004)). The grid size used in the flow simulation (characteristic length 0.15 mm) is unnecessarily small for computation of acoustic wave propagation. Therefore, to preserve acoustic energy, the acoustic sources are conservatively interpolated (see Kaltenbacher (2007)) onto a coarser grid. The mesh is composed of hexahedral elements with a characteristic length of 0.2 mm (see Fig. 9b) and gradually coarsens from the source region to the propagation region to a characteristic length of 1.3 mm. According to Kaltenbacher (2007), this element size leads to a correct frequency resolution of up to 12 kHz – assuming that 20 linear finite elements per wave length are required to adequately resolve the acoustic wave. Once the acoustic sources are determined, the sound propagation is computed on the whole acoustic domain, consisting of the larynx (fluid flow – source region), the vocal tract and the propagation regions. For the acoustic simulation a timestep value of 10^{-5} s has proven to be sufficient for the considered frequency range of up to 3.5 kHz.

In the following sections two approaches towards hybrid aeroacoustic computations are presented: Lighthill’s analogy and a perturbation-based approach. Within this setup it is possible to utilize hybrid schemes, since we assume minor back reaction of the acoustic field onto the flow field. This has the advantage that the vocal tract may be varied while the sources based on the flow field remain the same. Therefore, we only need one flow simulation to determine the source terms and are able to perform multiple acoustic simulations, each carried out on different vocal tract geometries. To solve the partial differential equations, the finite element method (FEM) is employed in both Lighthill’s and perturbation-based approach. These methods are all implemented in our

in-house research code *CFS++*, which was used for the following aeroacoustic simulations.

For a better overview, the case names C1 ... C2F are given a suffix to characterize which kind of acoustic simulation is being referred to: i and u for vocal tract /i/ and /u/, respectively, and PE and LH for perturbation equations and the Lighthill approach, respectively. For example case C1F_u_PE would be the acoustic simulation for the case C1F with vocal tract /u/ utilizing the perturbation equations.

All channel walls are considered to be hard reflecting and perfectly matched layers (PML) are located at the inflow (1 cm in front of the glottis) and surrounding the propagation region (see Fig. 9a) to avoid backscattering of acoustic waves – according references are made for each aeroacoustic method. The PML is 5 mm thick at the inlet and 6 mm thick in normal direction to the propagation region.

To solving the resulting algebraic system of equations we utilize the direct sparse solver library PARDISO (Schenk and Gärtner. 2004). PARDISO is a direct solver which is perfectly suited for the simple wave equation since the resulting matrix of the linear system only needs to be factorized once per simulation. However, computational costs are not an issue for the acoustic equations, since the mesh is considerably coarser than for the CFD and the equations are linear.

3.2 Lighthill’s analogy

The Lighthill approach (Lighthill 1952) reformulates the compressible Navier-Stokes equations into an inhomogeneous wave equation

$$\frac{1}{c^2} \frac{\partial^2 p'}{\partial t^2} - \Delta p' = \frac{\partial^2}{\partial x_i \partial x_j} T_{ij} \quad (8)$$

with the speed of sound c , acoustic pressure p' and the Lighthill tensor

$$T_{ij} = \underbrace{\rho u_i u_j}_{\text{Reynolds stress}} - \underbrace{\tau_{ij}}_{\text{Viscous stress}} + \underbrace{(p' - c^2 \rho') \delta_{ij}}_{\text{Heat conduction}} \quad (9)$$

which acts as a source term for the wave equation. In (9), τ_{ij} is the stress tensor, ρ' the acoustic density and δ_{ij} the Kronecker delta. For high Reynolds numbers the viscous stress and stresses caused by heat conduction terms may be neglected (Lighthill 1952), since in regions of ambient temperature the contribution of heat conduction is of the same order as the viscous term. This leads to the approximation

$$T_{ij} \approx \rho u_i u_j . \quad (10)$$

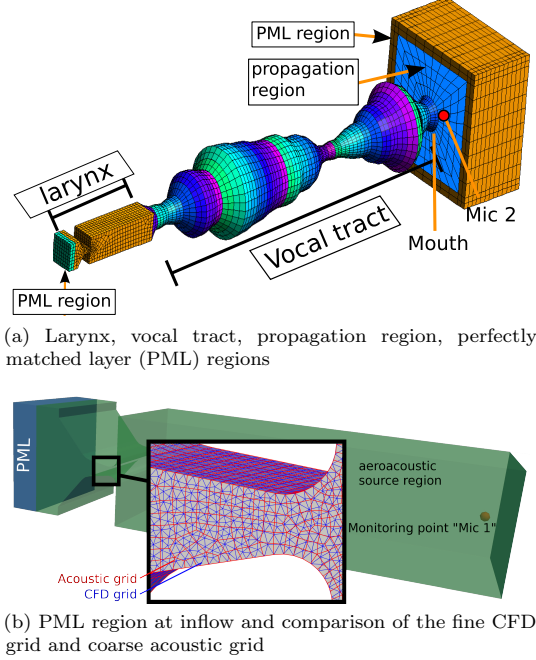


Fig. 9: Geometry and mesh for the acoustic simulation.

Lighthill's derivation assumes a scenario in which the source region is surrounded by a large volume of fluid at rest. Therefore the computed pressure has to be regarded as a superposition of acoustic and hydrodynamic pressure inside the source region. Only for monitoring points far away from the turbulent flow can the obtained pressure be regarded as acoustic.

For the perfectly matched layers (see Fig. 9a) the formulation as introduced by Kaltenbacher et al (2013) is applied. For further details and numerical implementation, we refer to Kaltenbacher (2007).

The Newmark scheme is employed to solve the second derivative in time. In order to employ the FEM to discretize the space derivatives, the boundary value problem (8) is required in a weak formulation. To achieve this, equation (8) is multiplied by an appropriate test function and is integrated over the whole domain Ω . The necessary test function ψ is chosen from the Sobolev space

$$H^1 := \{ \psi(\cdot) \in L^2(\Omega) \mid \partial\psi(\mathbf{x})/\partial x_i \in L^2(\Omega), \forall \mathbf{x} \in \Omega \} \quad (11)$$

with L^2 the space of square integrable functions. The variational formulation is then given as

$$\begin{aligned} \int_{\Omega} \frac{1}{c^2} \frac{\partial^2 p'}{\partial t^2} \psi \, dx - \int_{\Omega} \Delta p' \psi \, dx \\ = \int_{\Omega} \nabla \cdot (\nabla \cdot \mathbf{T}) \psi \, dx. \end{aligned}$$

Applying Green's integral theorem on the second derivatives in space results in

$$\begin{aligned} \int_{\Omega} \frac{1}{c^2} \frac{\partial^2 p'}{\partial t^2} \psi \, dx + \int_{\Omega} \nabla p' \cdot \nabla \psi \, dx \\ = - \int_{\Omega} (\nabla \cdot \mathbf{T}) \cdot (\nabla \psi) \, dx. \end{aligned}$$

An advantage of the FEM with regard to Lighthill's analogy, is the order reduction of the spatial derivative of the Lighthill tensor due to the integration by parts. As we assume hard reflecting walls ($\partial p'/\partial n = 0$) at the vocal tract and larynx, the boundary integral arising from the integration by parts is zero.

The infinite-dimensional space (11) is replaced by finite-dimensional subspace $V_h \subset H^1$ and a basis $\{\varphi_1, \dots, \varphi_N\}$ of V_h is selected, with N the number of FE nodes in the computational domain. Thereby, the unknown pressure is approximated by

$$p'(t, x) \approx p'_h(t, x) = \sum_{i=1}^N p'_i(t) \varphi_i(x). \quad (12)$$

Verification for the presented method was published by Kaltenbacher et al (2010), in which simulation and experimental results of the acoustic field induced by flow around a cylinder are compared. Additionally, they examine the acoustics of co-rotating vortex pairs, for which an analytic solution exists. Both verification examples were in good agreement.

3.3 Perturbation equation

In contrast to Lighthill's (LH) approach, the perturbation equation (PE) approach takes mean flow effects into account. This system of PDEs can be derived directly from the governing equations of fluid dynamics based on conservation of mass, momentum and energy as well as the state equations of the fluid. The fundamental idea is to introduce a splitting of the compressible field variables, pressure p^c , velocity \mathbf{u}^c and density ρ^c into mean and fluctuating parts. For pressure and velocity this reads as

$$p^c = \bar{p} + p' \quad ; \quad \mathbf{u}^c = \bar{\mathbf{u}} + \mathbf{u}' \quad (13)$$

It is essential for the validity of this ansatz that the perturbation quantities are much lower than the mean quantities (i.e. $p' \ll \bar{p}$). A direct application of (13) to the governing equations of fluid dynamics leads to the linearized Euler equations (LEE) as used in Bailly and Juvé (2000). Although the mean components of the flow field are excluded from the solution, the perturbation quantities cannot be regarded as acoustic quantities. Therefore, the splitting is pushed one step further by formally separating hydrodynamic and acoustic quantities. For the velocity field, this splitting is based on the fact that the incompressible part of the velocity field is purely solenoidal $\nabla \cdot \mathbf{u}^v = 0$, whereas the acoustic components are irrotational $\nabla \times \mathbf{u}^a = 0$. Thereby we obtain

$$\mathbf{u}^c = \bar{\mathbf{u}} + \mathbf{u}' = \bar{\mathbf{u}} + \mathbf{u}^v + \mathbf{u}^a. \quad (14)$$

A similar ansatz can be applied for the other field variables. Based on the assumptions of incompressible homentropic CFD data, this approach leads to a system of partial differential equations describing the aeroacoustic field in terms of acoustic pressure p^a and acoustic particle velocity \mathbf{u}^a as

$$\begin{aligned} \frac{\partial}{\partial t} p^a + \rho c^2 \nabla \cdot \mathbf{u}^a + \nabla \cdot (p^a \bar{\mathbf{u}}) &= -\frac{\partial}{\partial t} p - \bar{\mathbf{u}} \cdot \nabla p, \\ \frac{\partial}{\partial t} \mathbf{u}^a + (\mathbf{u}^a \cdot \nabla) \bar{\mathbf{u}} + (\bar{\mathbf{u}} \cdot \nabla) \mathbf{u}^a + \frac{1}{\rho} \nabla p^a &= 0. \end{aligned} \quad (15)$$

Here, the right hand side of the first equation in (15) is determined with the help of the CFD results, which provides the incompressible variables p and, by time averaging, the mean flow field $\bar{\mathbf{u}}$.

This approach of splitting the perturbation quantities was initially used by Ewert and Schröder (2003) to derive the *Acoustic Perturbation Equations* (APE), which can be given in different variations for specific flow situations. The system (15) is closely related to the APE-2 system and the detailed derivation can be found in Hüppe (2014) and Hüppe and Kaltenbacher (2012a), in which also a stabilized finite element scheme is provided, which enables efficient computations in the time domain. Thereby, the first order time derivative is discretized by the trapezoidal rule. To avoid reflections from the domain boundary, we use a perfectly matched layer (PML) formulation given in (Hüppe and Kaltenbacher 2012b) which is valid under the assumption of vanishing mean flow inside the damping layer.

3.4 Acoustic Sources

McGowan (1988) investigated the sound generation mechanisms of phonation from a fluid mechanical point

of view. He introduced the vorticity-velocity interaction force, which is identical to the Lamb vector \mathbf{L} apart from the density constant (see eqn. (16)). To derive a relationship between this force and sound production, McGowan stated, based on Powell (1964), that the derivative of the Lighthill tensor \mathbf{T} may be approximated by the divergence of the Lamb vector,

$$\frac{\partial^2 \mathbf{T}_{ij}}{\partial x_i \partial x_j} \approx \rho \nabla \cdot \mathbf{L} = \rho \nabla \cdot ((\nabla \times \mathbf{u}) \times \mathbf{u}). \quad (16)$$

We use this approach to investigate the sound sources and compare them to the source terms given by the perturbation equation in (15).

Applying the Fast Fourier Transform (FFT) we analyze all source terms for the fundamental frequency (100 Hz) producing tonal sound and a frequency of 1425 Hz inside the broadband noise region of the spectrum. Isosurfaces of the sources for both frequencies are displayed in Fig. 10. For each approach the results are normed to their maximum value. The plot of the source terms indicates that the dominant source of the fundamental frequency is clearly found inside the glottis and the highest amplitudes are found in a thin layer right above the surface of the vocal folds. These are induced by the net force acting onto the surface of the vocal folds, also found by Zhao et al (2002). This effect is especially visible when considering the divergence of the Lamb vector, as the isosurface for the value 0.4 is found directly on the surface of the vocal folds. Also a thin region of acoustic sources can be found downstream on the top and bottom of the supraglottal wall. Considering (16), these source regions can be explained by high velocity gradients in the vicinity of the wall, which arise due to a large scale vortex deflecting the jet in combination with the no-slip boundary condition.

For the non harmonic frequency 1425 Hz, we display the acoustic sources in Fig. 10c and Fig. 10d. In this case, the sources are concentrated in the vortical decay region. In the case of the divergence of the Lamb vector the shear layer of the jet stream originating from the glottis also generates visible acoustic sources – an isosurface value decreased by one order of magnitude was necessary for proper visualization. In both cases, the sound sources are caused by vortices in the supraglottal region, as can be deduced by comparison to the flow field (Fig. 3). Fig. 10 also shows that they are more than one order of magnitude lower than the sources inside the glottis. This conclusion is consistent with the findings of Zhao et al (2002).

As a comparison between the cases C1, C1F, C2 and C2F, the acoustic sources for the PE equation are depicted in the time domain by contour surfaces in

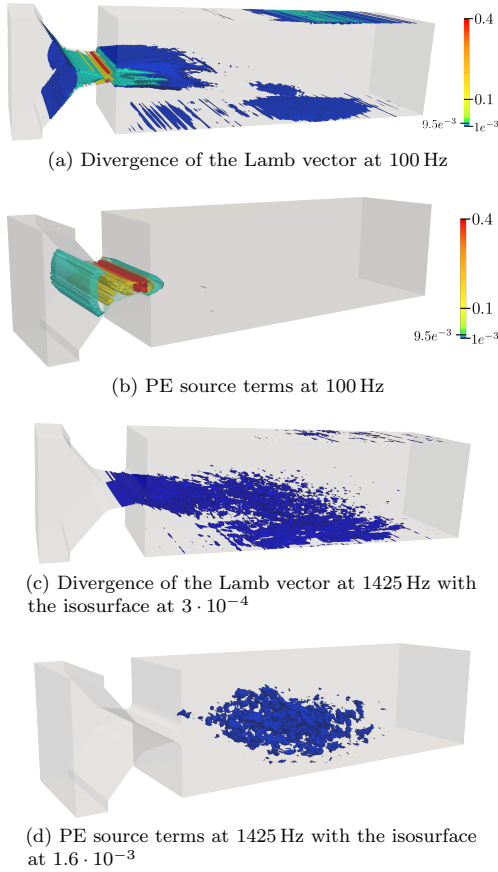


Fig. 10: Acoustic sources for case C1, comparing the two approaches in frequency domain at the fundamental frequency of 100 Hz and a non-harmonic frequency of 1425 Hz. (Results have been normed to their maximum value)

Fig. 11 for the time instant 180 ms, which is the same time as for the vorticity plots in Fig. 3. In all four figures the source term has been normalized to the maximum amplitude of C2_PE, which had the highest value. For the cases C1_PE and C1F_PE, the pattern is very similar. They show the highest value at the glottis outflow and smaller values of acoustic sources are additionally found in the turbulent region of the jet. As for C2_PE and C2F_PE, source terms with high amplitudes are present along the length of the whole glottis region. In contrast to C1_PE and C1F_PE, contour surfaces with lower threshold are only found in the first half of the supraglottal region. This can be explained by the vorticity plot in Fig. 3, which suggests a much lower vorticity magnitude for C2_PE C2F_PE case and

also reveals that the jet does not impinge as far as in C1 and C1F. Correlation between vortices and source distribution can clearly be seen when comparing Fig. 11 and Fig. 3.

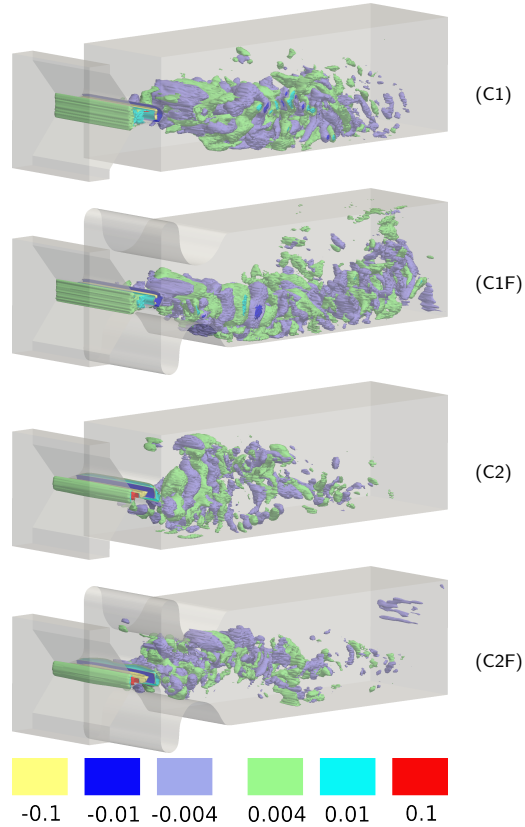


Fig. 11: Acoustic PE sources in the time domain at time instant 180 ms, middle of the vocal fold closing phase for simulations C1, C1F, C2 and C2F.

The impact and further analysis of the four cases on the acoustics is discussed in the next section.

3.5 Acoustic results

Inside the flow domain, as stated by Lighthill (1952), the Lighthill’s analogy does not distinguish between acoustic and hydrodynamic fluctuation quantities. Therefore, as expected, for a monitoring point “Mic 1” inside the flow domain 3.99 cm downstream of the glottis (see Fig. 9b) this analogy gives a much higher sound pressure level (SPL) inside the flow region than for the PE, as can be seen in Fig. 12. The two aeroacoustic approaches

show a discrepancy over the whole frequency range. Calculations performed with the wave equation have significantly higher SPL, up to 20 dB for the fundamental frequency of 100 Hz. Furthermore, the envelope of the higher harmonic frequencies is different: for the frequency range of 0.5–2.5 kHz the wave equation stagnates at about 70–80 dB, whereas for the perturbation equation the SPL rises from about 55 dB–75 dB in the range of 0.5–1.3 kHz and then drops down to 50 dB at 2.5 kHz. As a result, higher harmonics are masked by broadband noise in the Lighthill’s analogy, but harmonics up to 700 Hz are visible for the PE.

As previously mentioned, the described differences in the obtained SPLs can be explained by the fact that the pressure computed using the Lighthill tensor as the acoustic source is superimposed by hydrodynamic quantities inside the source region. Thereby an interpretation of the SPL with respect to acoustics is hard to establish. This is not the case for the perturbation equations as flow and acoustic components of the field are separated right from the beginning of the derivation thus avoiding these effects.

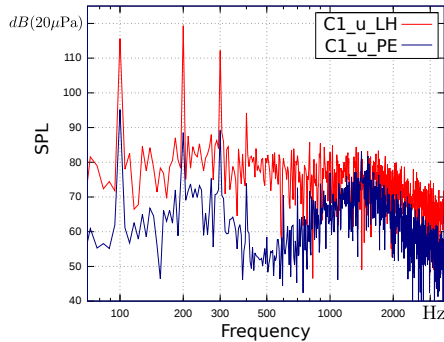


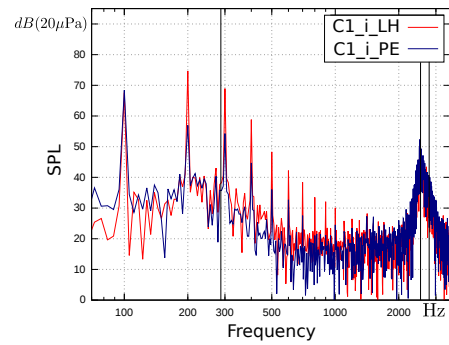
Fig. 12: Acoustic pressure at “Mic 1” for the simulations C1.u.LH and C1.u.PE

The sound spectrum evaluated at “Mic 2”, positioned 1 cm from the mouth (approx. 23 cm from the glottis) in the propagation region is given in Fig. 13 for the /i/ and /u/ vowels. The computed formant frequencies (local maxima of the spectral envelope, distinctive attributes of the individual vowels) are summarized in Tab. 2, and compared to the formant frequencies of the natural speech published by Story et al (1996). For both vowels the formants show a small deviation to natural speech, which can be explained by the additional volume of the CFD domain (see Sec. 3.1).

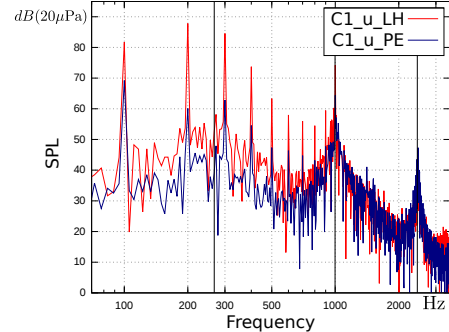
Fig. 13 also demonstrates the degree of agreement between the Lighthill’s and PE approach. All formants

Table 2: First three formants from natural speech as given by Story et al (1996) and simulated by our reproduced vocal tract for all CFD cases. Natural speech is denoted by superscript “N”, the simulated version by “S” (Lighthill’s analogy and PE are identical).

	/i/ ^N	/i/ ^S	/u/ ^N	/u/ ^S
F1	333 Hz	292 Hz	389 Hz	270 Hz
F2	2332 Hz	2538 Hz	987 Hz	1000 Hz
F3	2986 Hz	2749 Hz	2299 Hz	2484 Hz



(a) Acoustic pressure for vocal tract /i/



(b) Acoustic pressure for vocal tract /u/

Fig. 13: Acoustic sound spectra at a monitoring point “Mic 2” downstream of the mouth for both vocal tract models, comparing Lighthill’s acoustic analogy and the perturbation equations. Black vertical lines indicate the formants.

are identical in frequency and for all non harmonic frequencies the amplitudes are in good agreement. Nevertheless, the spectra show different amplitudes of the fundamental frequency 100 Hz and its harmonics. The higher amplitudes can be explained by the acoustic field at the monitoring point “Mic 1”, which is inside the flow field. Especially the second harmonic frequency has a 30 dB higher value for the Lighthill approach. Hydrodynamic fluctuating pressure superimposes the acoustic

pressure, which also leads to the increased results also at the second monitoring point “Mic 2”. As a result, all the following acoustic simulations are performed by the PE.

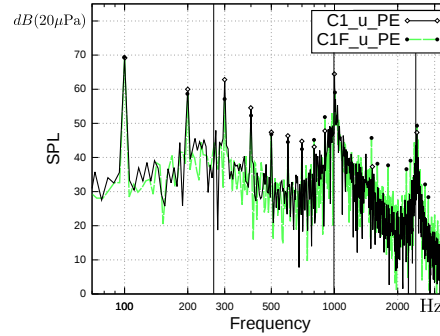
To assess the acoustic impact of the FVFs, we will focus on the results of the simulation domain representing the vocal tract /u/ at the recording point “Mic 2”. In Fig. 14 the observed frequency spectra are contrasted with the simulation without false vocal folds, distinguishing themselves only by the harmonics. Without FVFs, harmonics dominate other frequencies up to 1 kHz, whereas with FVFs they are clearly visible over the whole illustrated frequency range. This phenomena is noticeable when analyzing the acoustic sources in Fig. 15, in which they are plotted in the coronal plane at one of the harmonics (2.6 kHz). The figure reveals that by including the FVFs a significantly larger source region is generated, which is higher in amplitude. Comparing C2_u.PE and C2F_u.PE the inclusion of the false vocal folds has the same effect on the amount of pronounced harmonics, but mainly found below 1.3 kHz. However, for C1F_u.PE the increase in amplitude of the harmonics, holds for the whole examined frequency range.

The set of simulations also allows comparison of the cases with different vocal fold motion, C1F_u.PE and C2F_u.PE. Fig. 16 depicts the FFT of the acoustic signal at the monitoring point “Mic 2”. Harmonic frequency only differs about 2–3 dB except at 300 Hz where C2F_u.PE is 8 dB higher. Above 800 Hz the harmonics in C2F_u.PE are not distinguishable from non harmonics, whereas in C1F_u.PE harmonics are still identifiable. However, non harmonic frequencies in C2F_u.PE are up to 10 dB lower in amplitude compared to the case C1F_u.PE – the same holds, when comparing C1_u.PE with C2_u.PE. The reason for this can be found by analyzing the sources in Fig. 11 and the vorticity in Fig. 3.

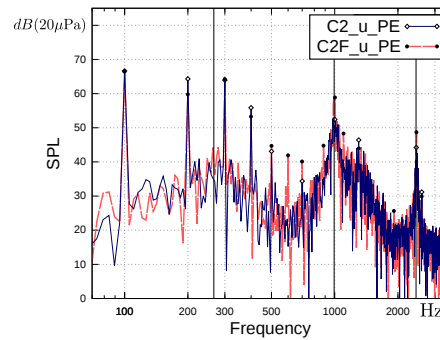
The fundamental frequency, as shown earlier, has the origin inside the glottis and, as Fig. 11 indicates, these source terms are pronounced for both cases. In contrast, non harmonic acoustic frequencies are suppressed for the C2F_u.PE case. These frequency components are created due to turbulence, as shown earlier (see Fig. 10), and compared to the C1 and C1F cases, the vorticity exhibits significantly lower magnitudes (see Fig. 3), hence the suppressed frequencies.

4 Conclusions

We have developed an aeroacoustic model of human voice production. The CFD model, based on unsteady incompressible Navier-Stokes equations in 3D, is one-way coupled with an aeroacoustic solver, *CFS++*. The



(a) Acoustic pressure of C1_u.PE and C1F_u.PE



(b) Acoustic pressure of C2_u.PE and C2F_u.PE

Fig. 14: Acoustic sound spectra calculated by the perturbation equations at a monitoring point “Mic 2” for the vocal tract model /u/. Harmonics are emphasized with the symbol \diamond (without FVFs) and \bullet (with FVFs).

flow field is solved on a time-dependent computational domain, deformed by the vibration of the vocal folds.

To resolve the fine scales of turbulence of the highly unsteady and separated airflow within the 3D vocal fold channel, a sufficiently fine computational grid has to be used, resulting in relatively high computational demands. The CFD simulations were run in parallel on a small shared-memory SGI Altix UV supercomputer, using the domain decomposition method and SGI implementation of the MPI standard.

The CFD simulations were performed in four different geometrical configurations, allowing us to assess the influence of the false focal folds and of the convergent-divergent motion of the vocal folds. The jet formed in the glottis is affected by a combination of supraglottal pressure distribution and recirculation flow patterns. The effect of the false vocal folds on the flow rate and on the jet deflection angle was shown to be ambiguous for the two types of vocal fold motion. When the vocal fold medial surface exhibits convergent-divergent shape-

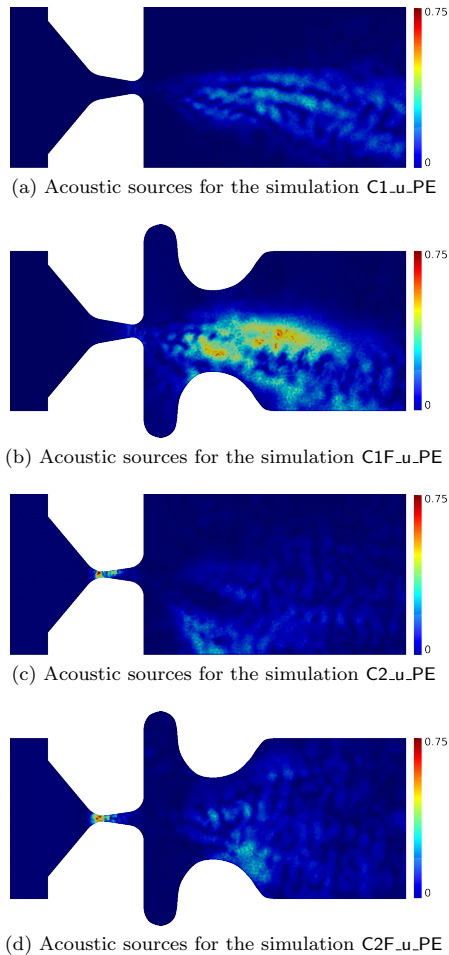


Fig. 15: Acoustic sources in the frequency domain of the acoustic perturbation equation at 2.6 kHz. Normed to the maximum value found for the C2F_u_PE.

ing, the intraglottal pressure profile is different with impact on the jet shear layer, which is wider during the divergent phase, produces less vorticity and thereby suppresses higher acoustical frequencies.

Concerning acoustics, two acoustic field calculations were tested: Lighthill's analogy and the linearized acoustic perturbation equations. As expected from the theoretical analysis, the Lighthill's analogy showed a 20 dB overestimation of SPL inside the source region, which may be related to the fact that pressure computed by Lighthill's wave equation must be seen as a superposition of acoustic and hydrodynamic pressure. For a recording point in the acoustic propagation region good agreement between these two approaches was achieved.

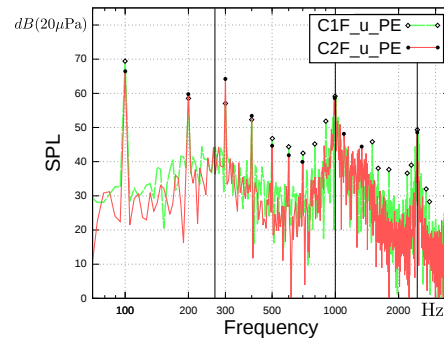


Fig. 16: Acoustic sound spectra at a monitoring point "Mic 2", comparing C1F_u_PE and C2F_u_PE. Black vertical lines indicate the formants.

The simulated formant frequencies for the /i/ and /u/ vowels compared well with the formant frequencies measured on human subjects. Furthermore, the simulations suggest that the false vocal folds induce an amplification of higher harmonics in the radiated acoustic field. When convergent-divergent VF vibration was compared to the oscillation with fixed convergence angle of the medial surface, a reduction of the non harmonic frequency content was found.

The current model contains numerous simplifications with respect to the complex physiology of human voice production. However, we have shown that a reduced model, well balanced with respect to modeling complexity and computational cost, can contribute to a better understanding of the aeroacoustic sound generation mechanisms in phonation.

Acknowledgements The research has been supported by the Czech Science Foundation, project P101/11/0207, and by the Austrian Science Fund under grant no. I 532-N20. The support of the Czech and Austrian agencies for international cooperation and mobility within ICM OeAD - MŠMT (project No. CZ 09/2013 - 7AMB13AT006), which helps the effective cooperation of the authors, is also gratefully acknowledged. The CFD simulations were run on the facilities of the Supercomputing center of the CTU in Prague.

References

- Agarwal M, Scherer R, Hollien H (2003) The false vocal folds: shape and size in frontal view during phonation based on laminagraphic tracings. *J Voice* 17(2):97–113,doi: 10.1016/S0892-1997
- Agarwal M (2004) The false vocal folds and their effect on translaryngeal airflow resistance. Ph.D. thesis, Bowling Green State University.
- Alipour F, Jaiswal S, Finnegan E. (2007) Aerodynamic and acoustic effects of false vocal folds and epiglottis in excised larynx models. *Ann Otol Rhinol Laryngol* 116(2):135–144

- Alipour F, Brucker C, D Cook D, Gommel A, Kaltenbacher M, Mattheus W, Mongeau L, Nauman E, Schwarze R, Tokuda I, Zörner S (2011) Mathematical models and numerical schemes for the simulation of human phonation. *Curr Bioinform* 6(3):323–343, doi: 10.2174/157489311796904655
- Bae Y, Moon YJ (2008) Computation of phonation aeroacoustics by an INS/PCE splitting method. *Comput Fluids* 37(10):1332–1343, doi: 10.1016/j.compfluid.2007.12.002
- Bailly C, Juvé D (2000) Numerical solution of acoustic propagation problems using linearized Euler equations. *AIAA J* 38:22–29, doi: 10.2514/2.949
- Bailly L, Pelorson X, Henrich N, Ruty N (2008) Influence of a constriction in the near field of the vocal folds: physical modeling and experimental validation. *J Acoust Soc Am* 124(5):3296–3308, doi: 10.1121/1.2977740
- Boessenecker A, Berry DA, Lohscheller J, Eysholdt U, Döllinger M (2007) Mucosal Wave Properties of a Human Vocal Fold. *Acta Acust United Ac* 93(5):815–823
- Chevalier C, Pellegrini F (2008) PT-scotch: A tool for efficient parallel graph ordering. *Parallel Comput* 34(6-8):318–331, doi: 10.1016/j.parco.2007.12.001
- Ewert R, Schröder W (2003) Acoustic perturbation equations based on flow decomposition via source filtering. *J Comput Phys* 188(2):365–398, doi: 10.1016/S0021-9991(03)00168-2
- Feistauer M, Hasnedlová-Prokopová J, Horáček J, Kosík A, Kučera V. (2013) DGFEM for dynamical systems describing interaction of compressible fluid and structures. *J Comput Appl Math* 254:17–30, doi: 10.1016/j.cam.2013.03.028
- Ferziger JH, Peric M (2002) Computational methods for fluid dynamics. Springer-Verlag Berlin Heidelberg, doi: 10.1007/978-3-642-56026-2
- Geuzaine C. and Remacle J.F. (2009) Gmsh: a three-dimensional finite element mesh generator with built-in pre- and post-processing facilities. *Int J Numer Meth Eng* 79(11), 1309–1331
- Hüppe A (2014) Spectral finite elements for acoustic field computation (Measurement-, Actuator-, and Simulation-technology). Ph.D. thesis, Shaker Verlag GmbH, doi: 10.2370/9783844024609
- Hüppe A, Kaltenbacher M (2012a) Spectral finite elements for computational aeroacoustics using acoustic perturbation equations. *J Comput Acoust* 20(02):1240,005 1–13, doi: 10.1142/S0218396X1240005X
- Hüppe A, Kaltenbacher M (2012b) Stable matched layer for the acoustic conservation equations in the time domain. *J Comput Acoust* 20(01):1250,004, doi: 10.1142/S0218396X11004511
- Jasak H (1996) Error Analysis and Estimation for the Finite Volume Method with Applications to Fluid Flows. Ph.D. thesis, Imperial College of Science, Technology and Medicine, London.
- Kaltenbacher B, Kaltenbacher M, Sim I (2013) A modified and stable version of a perfectly matched layer technique for the 3-d second order wave equation in time domain with an application to aeroacoustics. *J Comput Phys* 235(0):407–422, doi: 10.1016/j.jcp.2012.10.016
- Kaltenbacher M (2007) Numerical simulation of mechatronic sensors and actuators. Springer-Verlag Berlin Heidelberg, doi: 10.1007/978-3-540-71360-9
- Kaltenbacher M, Escobar M, Ali I, Becker S (2010) Numerical simulation of flow-induced noise using LES/SAS and Lighthill’s acoustics analogy. *Int J Numer Meth Fl* 63(9):1103–1122, doi: 10.1002/fld.2123
- Kelleher J, Siegmund T, Du M, Naseri E, Chan R (2013) Empirical measurements of biomechanical anisotropy of the human vocal fold lamina propria. *Biomech and Model in Mechan* 12(3):555–567, doi: 10.1007/s10237-012-0425-4
- Li S, Wan M, Wang S (2007) The Effects of the False Vocal fold Gaps in a Model of the Larynx on Pressures Distributions and Flows. *Digital Human Modeling*. Springer-Verlag Berlin Heidelberg, 147–156, doi: 10.1007/978-3-540-73321-8_18
- Lighthill M (1952) On sound generated aerodynamically. I. general theory. *Proceedings of the Royal Society of London*, Series A, Mathematical and Physical Sciences 211(1107):564–587, doi: 10.1098/rspa.1952.0060
- Link G, Kaltenbacher M, Breuer M, Döllinger M (2009) A 2D finite-element scheme for fluid-solid-acoustic interactions and its application to human phonation. *Comput Method Appl M* 198:3321–3334, doi: 10.1016/j.cma.2009.06.009
- McGowan R (1988) An aeroacoustic approach to phonation. *J Acoust Soc Am* 83(2):696–704, doi: 10.1121/1.396165
- Mittal R, Erath BD, Plesniak MW (2013) Fluid dynamics of human phonation and speech. *Annu Rev Fluid Mech* 45(1):437–467, doi: 10.1146/annurev-fluid-011212-140636
- Pickup BA, Thomson SL (2009) Influence of asymmetric stiffness on the structural and aerodynamic response of synthetic vocal fold models. *J Biomech* 42(14):2219–2225, doi: 10.1016/j.jbiomech.2009.06.039
- Powell A (1964) Theory of vortex sound. *J Acoust Soc Am* 36(1):177–195, doi: 10.1121/1.1918931
- Rivera O, Furlinger K and Kranzlmüller D (2011) Investigating the Scalability of OpenFOAM for the Solution of Transport Equations and Large Eddy Simulations. *Proceedings of the 11th International Conference on Algorithms and Architectures for Parallel Processing - Part II*:121–130
- Schenk O, Gärtner K (2004) Solving unsymmetric sparse systems of linear equations with PARDISO. *Future Gener Comp Sy* 20(3):475–487, doi: 10.1016/j.future.2003.07.011
- Scherer R, Shinwari D, Witt KD, Zhang C, Kucinschi B, Afjeh A (2001) Intraglottal pressure profiles for a symmetric and oblique glottis with a divergence angle of 10 degrees. *J Acoust Soc Am* 109(4):1616–1630, doi: 10.1121/1.1333420
- Schroeder W, Martin K, (2004) *The Visualization Toolkit*. C. D. Hansen and C. R. Johnson, editors. Elsevier
- Seo JH, Mittal R (2011) A high-order immersed boundary method for acoustic wave scattering and low-Mach number flow-induced sound in complex geometries. *J Comput Phys* 230(4):1000–1019, doi: 10.1016/j.jcp.2010.10.017
- Šidlof P, Švec JG, Horáček J, Veselý J, Klepáček I, Havlík R (2008) Geometry of human vocal folds and glottal channel for mathematical and biomechanical modeling of voice production. *J Biomech* 41(5):985–995, doi: 10.1016/j.jbiomech.2007.12.016
- Šidlof P, Doaré O, Cadot O, Chaigne A (2011) Measurement of flow separation in a human vocal folds model. *Exp Fluids* 51(1):123–136, doi: 10.1007/s00348-010-1031-9
- Šidlof P, Horáček J, Řídký V (2013) Parallel CFD simulation of flow in a 3D model of vibrating human vocal folds. *Comput Fluids* 80:290–300, doi: 10.1016/j.compfluid.2012.02.005
- Šidlof P, Zörner S, Hüppe A (2013a) Numerical simulation of flow-induced sound in human voice production. *Procedia Engineering* 61:333–340, doi: 10.1016/j.proeng.2013.08.024
- Story BH, Titze I, Hoffman EA (1996) Vocal tract area functions from magnetic resonance imaging. *J Acoust Soc Am* 100(1):537–554, doi: 10.1121/1.415960
- Tian FB, Dai H, Luo H, Doyle JF, Rousseau B (2014) Fluid-structure interaction involving large deformations: 3D simulations and applications to biological systems. *J Comput Phys* 258:451–469, doi: 10.1016/j.jcp.2013.10.047

- Titze IR (2006) *The Myoelastic aerodynamic theory of phonation*, 1st edn. National Center for Voice and Speech
- Zhang C, Zhao W, Frankel S, Mongeau L (2002) Computational aeroacoustics of phonation, part II: Effects of flow parameters and ventricular folds. *J Acoust Soc Am* 112(5 Pt 1):2147–2154, doi: 10.1121/1.1506694
- Zhao W, Zhang C, Frankel S, Mongeau L (2002) Computational aeroacoustics of phonation, part I: Computational methods and sound generation mechanisms. *J Acoust Soc Am* 112(5 Pt 1):2134–2146, doi: 10.1121/1.1506693
- Zheng X, Bielamowicz S, Luo H, Mittal R (2009) A Computational Study of the Effect of False Vocal Folds on Glottal Flow and Vocal Fold Vibration During Phonation. *Ann Biomed Eng* 37(3):625–642, doi: 10.1007/s10439-008-9630-9
- Zörner S, Kaltenbacher M, Lerch R, Sutor A, Döllinger M (2010) Measurement of the elasticity modulus of soft tissues. *J Biomech* 43(8):1540–1545, doi: 10.1016/j.jbiomech.2010.01.035
- Zörner S, Kaltenbacher M, Döllinger M (2013) Investigation of prescribed movement in fluid-structure interaction simulation for the human phonation process. *Comput Fluids* 86:133–140, doi: 10.1016/j.compfluid.2013.06.031

4.4 PIV measurements of flow in physical vocal fold models

4.4.1 Overview and context

The numerical modeling of airflow in human vocal folds has always been complemented by attempts to investigate the glottal flow and pressure fields experimentally. However, due to the inaccessibility of the vocal folds, direct in vivo flow measurements are mostly restrained to monitoring the instantaneous flow rate at lips and nostrils by means of the Rothenberg mask ([Hertegard and Gauffin, 1992](#)). To obtain deeper understanding of the laryngeal fluid dynamics, flow measurements can be performed either using excised animal model larynges – usually canine ([Alipour and Scherer, 2006](#), [Khosla et al., 2008](#), [Alipour and Finnegan, 2013](#)), or excised human larynges ([Alipour et al., 1996b](#), [Tsai et al., 2009](#)). A thorough overview of the measurements using excised larynges can be found in ([Dollinger et al., 2011](#)). Although the excised larynx measurements are the closest approximation to the real physiological situation, this approach brings numerous complications. The tissues have to be treated carefully, with quick post-mortem measurements preferable compared to freezing and rethawing procedures, which usually influence the mechanical properties and thus the vibration of the vocal folds. The real larynges have very complicated geometry, which is highly subject-specific. Moreover, due to ethical concerns and related regulations the access to animal and especially human excised larynges is very limited, and the measurements have to be performed in close cooperation with persons skilled in pathology.

The second way of experimental investigation of flow in human vocal folds is the usage of physical vocal fold models. These models are usually further from the real laryngeal physiology, but the geometry and material properties are better defined and the measurements more repeatable. The models can be also upscaled while retaining dynamic similarity with the real vocal folds (i. e. by using a fluid with higher viscosity), which can improve the spatial resolution e. g. when using global imaging methods or discrete pressure measurements. The list of physical models of vocal folds is immense, a thorough review paper on this topic was published by [Kniesburgs et al. \(2011\)](#). If we restrict ourselves to studies using laser visualization and velocity field measuring techniques, they can be divided into three categories: works using models, where the vocal folds do not oscillate ([Shinwari et al., 2003](#), [Erath and Plesniak, 2006a,b](#), [Kucinski et al., 2006a](#)), models with forced vocal fold oscillation using rotating cams or driven stepper motors ([Triep et al., 2005](#), [Kucinski et al., 2006b](#), [Krane et al., 2007](#), [Triep and Brücker, 2010](#)) and self-oscillating synthetic models fabricated from soft silicon or polyurethane mixtures ([Neubauer et al., 2007](#), [Becker et al., 2009](#), [Drechsel and Thomson, 2008](#)).

4.4.2 Author's contributions to flow field measurements in vocal fold synthetic models

The author's own PIV measurements of the supraglottal velocity fields using physical models of vocal folds are summarized in two papers reprinted in the following section. The first paper, published in *Acta Technica* (journal without impact factor) reports on coherent structures downstream of a life-sized polyurethane model with latex cover layer, developed in the Institute of Thermomechanics. The vocal folds were attached to a transparent vocal tract model, where the flow field was measured by PIV and further analyzed by Proper Orthogonal Decomposition (POD).

The second paper reprinted from *Experiments & Fluids* describes the mechanical vibration, acoustic and flow field measurements obtained using a 4:1 scaled synthetic self-oscillating vocal fold model, developed by the author himself in cooperation with Olivier Doaré and Olivier Cadot from École Nationale Supérieure de Techniques Avancées, Paris. The phase-locked flow field measurements with high spatial resolution were used to quantify the position of the flow separation point during vocal fold oscillation.

Reprints

- J. Horáček, P. Šidlof, V. Uruba, J. Veselý, V. Radolf, and V. Bula. Coherent structures in the flow inside a model of the human vocal tract with self-oscillating vocal folds. *Acta Technica*, 55:327–343, 2010
- P. Šidlof, O. Doaré, O. Cadot, and A. Chaigne. Measurement of flow separation in a human vocal folds model. *Experiments in Fluids*, 51(1):123–136, 2011

Coherent structures in the flow inside a model of the human vocal tract with self-oscillating vocal folds¹

JAROMÍR HORÁČEK^{2,3}, PETR ŠIDLOF², VÁCLAV URUBA²,
JAN VESELÝ², VOJTĚCH RADOLF², VÍTĚZSLAV BULA²

Abstract. The measurement of the airflow in a specially developed 1 : 1 scaled complex physical model of the voice production is described. This model consists of simplified models of the trachea, the self-oscillating vocal folds and the vocal tract with acoustical spaces that correspond to the vowel [a:]. The measurement set-up enabled to use the Particle Image Velocimetry (PIV) method for description of the airflow-pattern and synchronous vocal fold vibration visualization, acoustic and pressure measurements. The results are presented for the subglottal pressure and airflow rates in the range of normal human phonation. Especially, Coanda effect of the glottal jet and coherent structures showing large eddies in the glottal region of the vocal tract are studied.

Key words. Biomechanics of voice, voice production modeling, PIV method, coherent structures.

1. Introduction

Voice production is a complex physiological process, which involves several basic factors like airflow coming from the lungs, vocal-folds vibration and acoustic resonances of the cavities of the human vocal tract [1]. The airflow is given by the air pressure in lungs. Primary pressure fluctuations arise in the human larynx as a result of the flow induced vocal folds vibration. The acoustic resonant spaces, formed by the air cavities upstream the vocal folds,

¹The research was supported by the Grant Agency of the Czech Republic by project No. 101/08/1155 “Computer and physical modelling of vibroacoustic properties of human vocal tract for optimization of voice quality”.

²Institute of Thermomechanics, Academy of Sciences of the Czech Republic, Dolejšková 5, Praha 182 00, Czech Republic

³E-mail: jaromirh@it.cas.cz

modify the sound and codetermine its final quality. The self-oscillating vocal folds, excited by the airflow, generate a primary laryngeal tone whose fundamental frequency corresponds to the vibration frequency of the vocal folds. In the airways above the vocal folds, i.e. in the vocal tract, the acoustic resonant phenomena modify the spectrum of the primary laryngeal tone. However, an exact physical mechanism changing the airflow energy into the acoustic energy in the glottis is not properly known yet.

Biomechanical modeling of the voice production is based on general physical principles of fundamental disciplines of mechanics (vibration and dynamics of compliant bodies, fluid dynamics and acoustics). The computational modeling can be carried out only approximately. The mathematical models must be verified experimentally, partly by a clinical *in vivo* investigation but mostly on physical models *in vitro*. This is especially important when some physical quantities or parameters are neglected in the theoretical solution, such as the fluid viscosity, turbulence or interaction of the vocal tract acoustics with the vibration of the vocal folds.

Because the investigation of the airflow pattern in the glottis region *in vivo* is problematic, the measurements of the flow characteristics and regimes are provided on various physical models. A number of experiments were performed for flows in 2D rigid *in vitro* models of the glottis (see e.g. [2]–[4]), where mainly static pressure measurements were carried out for different geometries of the glottal region. Such experiments concentrated on the effects of the channel asymmetry and shape (convergent, liplike and divergent). Later, similar studies were provided with vibrating replicas that mimicked the vocal folds motion like a rigid body [5]–[7].

Recently, Particle Image Velocimetry (PIV) technique enabled new possibilities in such studies [8]–[17]. The unsteady respiratory airflow during inspiration and expiration in a 3D complex model of the human airway cavities created from CT images including the vocal and nasal tracts, larynx, trachea and lungs was studied in [8]; no vocal fold vibrations exist in this case.

PIV studies [9]–[11] of the 3D water flows behind a driven 3:1 scaled-up model of the opening and closing glottis took into account the influence of the ventricular folds and irregularity of the glottal closure. Similar PIV measurements in [12] were focused on Coanda effect in the jet of the airflow in a scaled-up driven model of the vocal folds modeled by a moving rigid body. The airflow-structure-acoustic interaction on a 4:1 scaled-up model of the glottis shaped by one self-oscillating vocal fold with two-degrees of freedom while the other vocal fold was unmovable was studied in [13] and [14].

Sophisticated and more realistic 1:1 scaled experiments were performed by Neubauer et al. [15] studying the coherent structures in a free air jet near self-oscillating vocal folds. Influence of a vocal folds asymmetry on skewing of the glottal free jet was studied by Pickup & Thomson [16] using self-oscillating vocal folds made of two-layer silicon rubber modeling the vocal fold body and

cover. Becker et al. [17] modeled a full fluid-structure-acoustic interaction in a test rig using self-oscillating polyurethane model of the vocal folds and taking into account influence of a simplified vocal tract model on the air jet focusing on Coanda effect.

The present study describes the developed 1:1 scaled complex physical model of the voice production in humans that consists of the trachea, the self-oscillating vocal folds and the vocal tract with acoustical spaces corresponding to the vowel [a:]. The time-resolved PIV method was used for instantaneous velocity field evaluation. The vibrating vocal folds during oscillation were recorded by a high-speed camera in the same instants as the airflow velocity patterns. The results are presented for measurements performed within a physiological range of mean airflow rate, subglottal pressure and fundamental frequency of the vocal folds vibrations.

2. Measurement set-up

The scheme of the all instrumentation and of the test rig is shown in Fig. 1. The airflow was coming from a pressure vessel (PV-17) joint to a central compressor. Prior to the measurement, the storage tank (ST-2) was filled with the smoke particles coming from the generator DANTEC High Volume Liquid Seeding Generator 10F03 (GEN-1), or for tracing particles the cigarette smoke was used instead of the generator. Then the corresponding valve was closed. The mean airflow rate in the main measurement line was controlled by the digital flow controller AALBORG DFC4600 (DFC-3 and PC1-4) and measured by the float flow meter (FM-20). Before entering the glottal region of the model with the mounted vocal folds (VF-6), the subglottal pressure in the model of the trachea (SUB-18) was measured by the special dynamic semiconductor pressure transducers IT AS CR (PT-5) mounted on the channel wall. The trachea was modeled by a Plexiglas tube (length 23 cm and inner diameter 25.5 mm). The PIV laser sheet (LAS-PIV-7) was focused on a part of the vocal tract model (VT-19), which was observed by the PIV high-speed camera (CAM-PIV-11). The self-oscillating vocal folds were synchronously recorded by the other high-speed PIV camera (CAM-IM-12). The microphone of the sound level meter B&K 2239 (B&K SLM-13) was installed in the distance of 30 cm from the outlet of the vocal tract model. The time signals from the pressure transducers and microphone were measured by the B&K measurement system Pulse 10 with Controller Module MPE 7537 A (PULSE-14) controlled by a computer (PC-15). The computer (PC4-21) was used for recording the vocal folds model vibrations by the high-speed camera.

The time-resolved PIV method was used for instantaneous velocity field evaluation. The measuring system DANTEC consists of PIV Laser Unit New Wave Research Pegasus (Nd:YLF, cylindrical optics, double head, wavelength

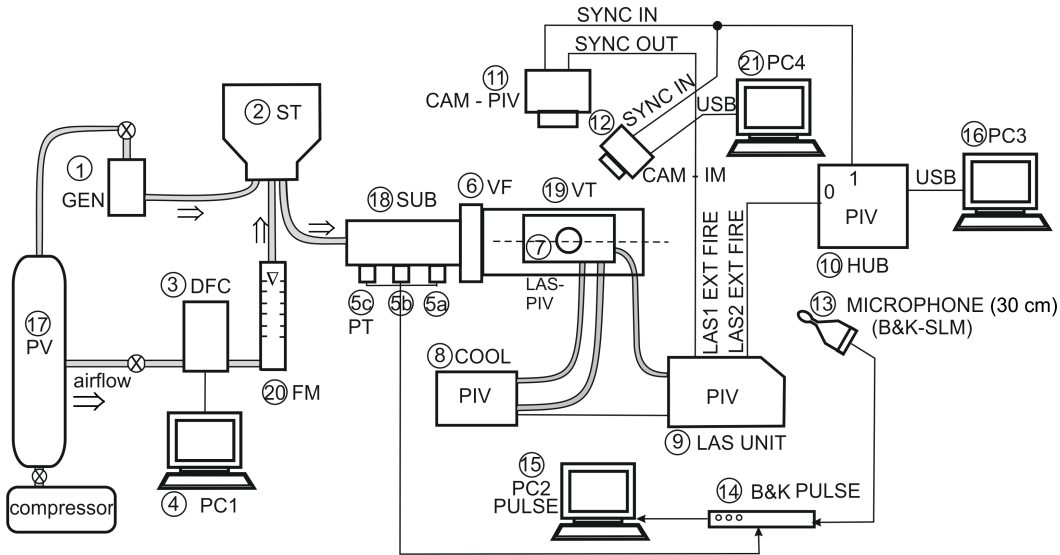


Fig. 1. Scheme of the measurement set-up

527 nm, frequency up to 10 kHz, shot energy 10 mJ for 1 kHz) (LAS UNIT-9), two high-speed CCD cameras NanoSense MkIII Nikon AF micro Nikkor 60 mm, aperture $f/5.6$, focused at distance cca 15 cm, with maximal resolution 1280×1024 pixels and corresponding maximal frequency 500 double-frames per second, Cooler Thermo Electron corporation NESLAB MERLIN M33 (COOL-8), DANTEC IDTX-Streaming timing HUB (HUB-10). The camera memory 4 GB represents 1635 full resolution double-frames. The maximal frequency of the camera is limited by data rate so that it could be augmented by reducing the resolution. In the experiments, we used reduced resolution with maximal possible frequency, and 1000 consecutive snapshots were acquired. The main computer Dell Precision PIV S690 with 8 core Xeon 3.73 GHz and 4GB RAM (PC3-16) controlled the complete PIV system. The software Dynamics Studio ver. 3 was used for both data acquisition and velocity-fields evaluation by application of the adaptive correlation method.

3. Vocal folds and vocal tract models

The shape and dimensions of the vocal folds model are shown in Fig. 2. The vocal folds skin was made of a latex thin cover layer filled by a compound prepared from polyurethane elastomer VytaFlex™ consisted of parts A and B and the softener So-Flex mixed in the ratio 1:1:3. The vocal folds model was joined to the model of the subglottal spaces.

A simplified 2D Plexiglas model of the human vocal tract was developed from the 3D finite element models designed from magnetic resonance images

FLOW INSIDE A MODEL OF HUMAN VOCAL TRACT

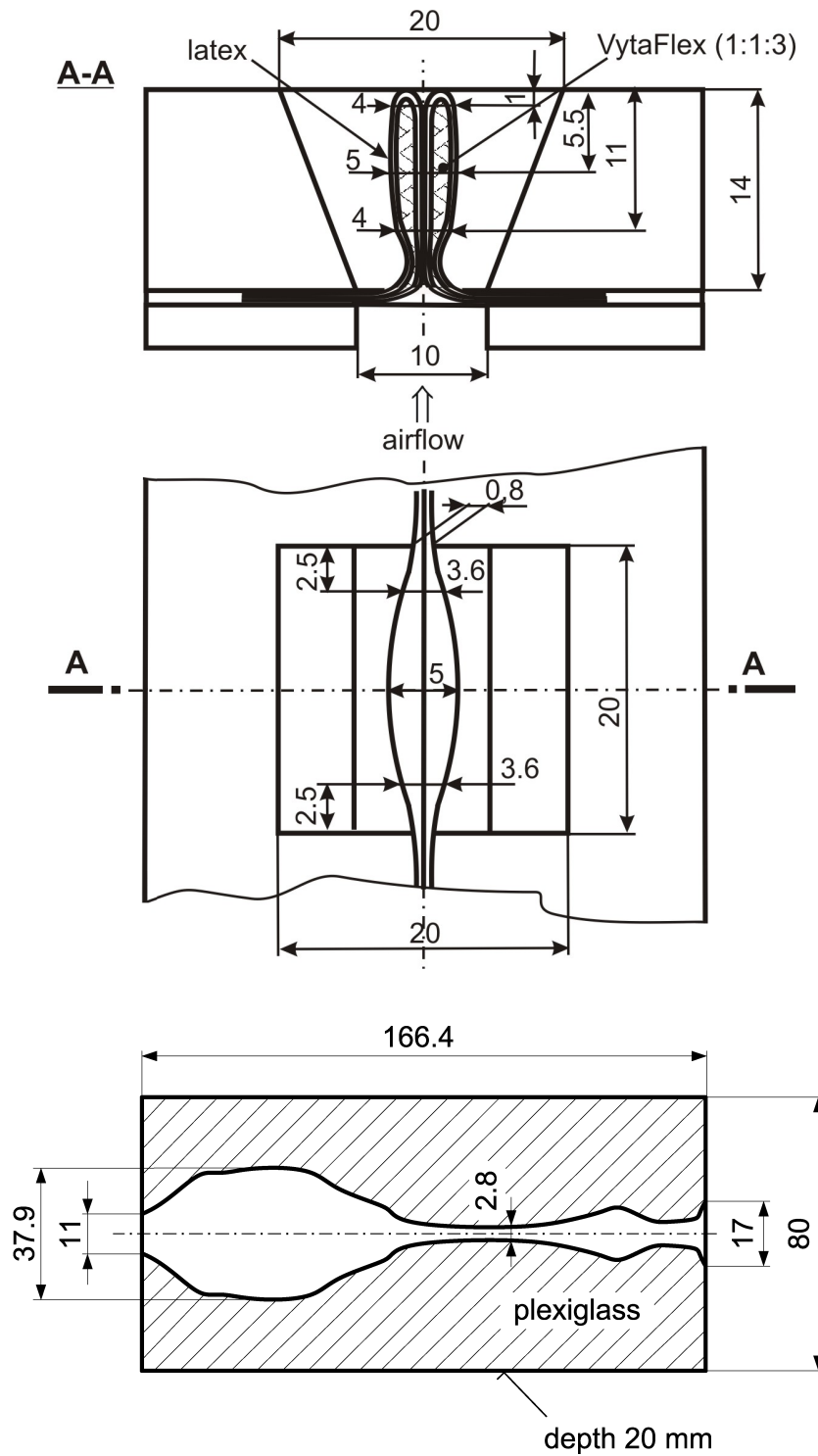


Fig. 2. Schemes of the models; *upper picture*: the vocal folds mounted in a supporting frame, *lower picture*: the vocal tract for vowel [a:]

of the subject during phonation [18]. To ensure their correspondence, the 2D and 3D models have the same areas in the cross-sections along the vocal tract. The shape of the 2D vocal tract model for the vowel [a:] is sketched in Fig. 2. The model begins with a simple model of the laryngeal cavity near the ventricular folds and ends at the lips modeling the mouth cavity. This 2D model covered by another two plane-parallel Plexiglas walls enabled the airflow visualization by the PIV method.

The photos in Fig. 3 show the measurement set-up including a detail of the voice producing model consisted of the subglottal, the vocal folds and the vocal tract parts.

4. Identification of coherent structures by orthogonal decomposition method

The Proper Orthogonal Decomposition (POD) method was introduced in the context of turbulence by Lumley [19] as an objective definition of what was previously called big eddies and which is now widely known as coherent structures. Convergence of the series of eigenmodes is very fast in the flows in which large coherent structures contain a major fraction of the total kinetic energy, e.g. the pseudo-periodical vortex streets in wakes.

The Bi-Orthogonal Decomposition (BOD) method represents an extension of the POD method. While POD analyzes data in spatial domain, the BOD performs spatiotemporal decomposition. Aubry et al. [20] presented the BOD as a deterministic analysis tool for complex spatiotemporal signals. First, a complete decomposition in two-dimensional space and time was performed. These decompositions were based on two-point temporal and spatial velocity correlations. A set of orthogonal spatial (topos) and temporal (chronos) eigenmodes are to be computed allowing the expansion of the velocity field. The BOD method analyzes a deterministic space–time signal (e.g. velocity) $\mathbf{u}(\mathbf{x}, t)$, which is decomposed as follows:

$$\mathbf{u}(\mathbf{x}, t) = \sum_{k=1}^N \lambda_k \overline{\varphi_k(\mathbf{x})} \psi_k(t) . \quad (1)$$

The bar denotes complex conjugate, $\varphi_k(\mathbf{x})$ are spatial eigenfunctions so-called toposes, $\psi_k(t)$ are temporal eigenfunctions so-called chronoses, λ_k are the common eigenvalues and N is number of the PIV snapshots.

Global flow energy can be written as

$$E_G = \sum_{k=1}^N \lambda_k^2 , \quad (2)$$

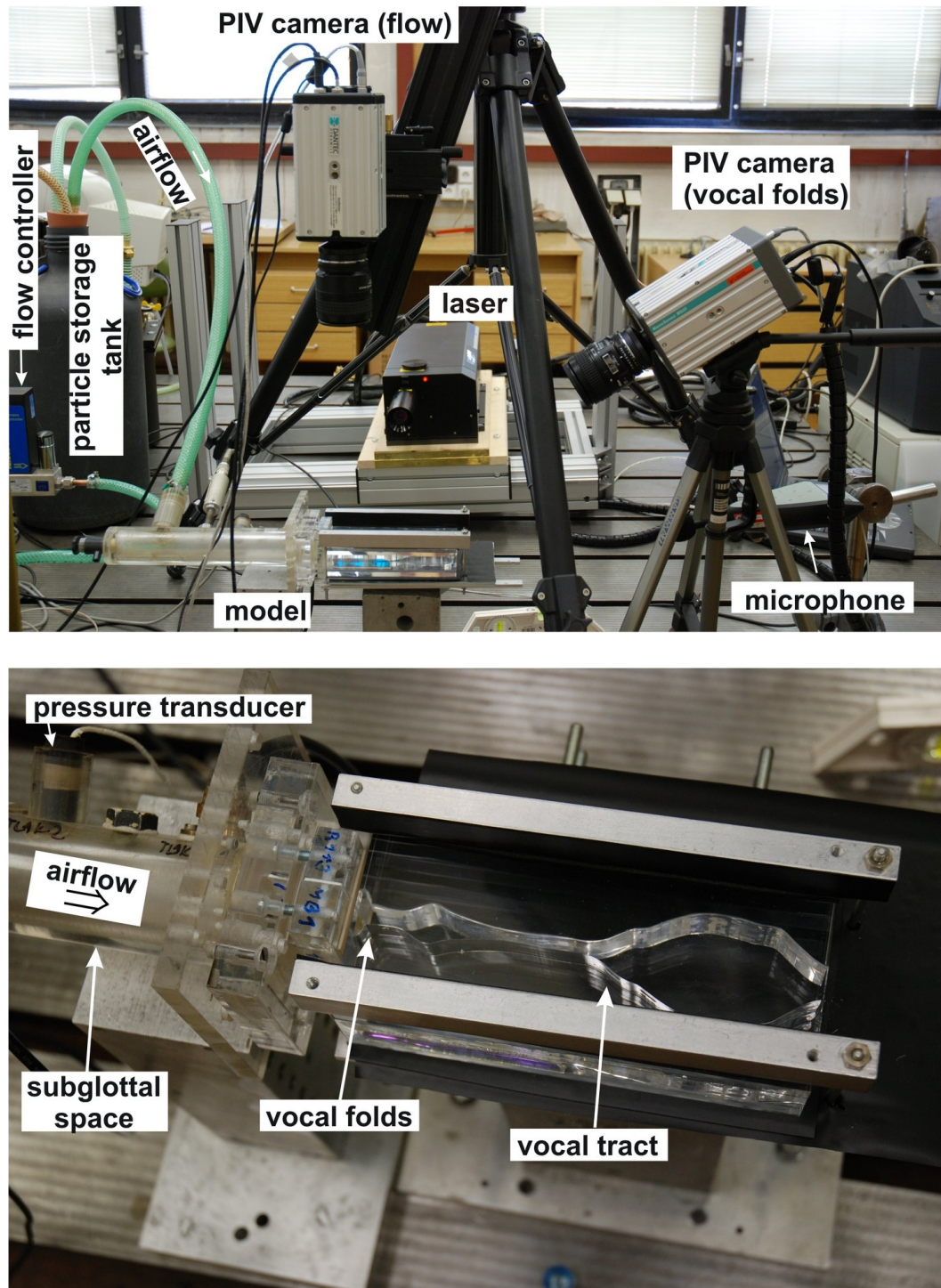


Fig. 3. Measurement set-up; *upper picture*: general view, *lower picture*: detail of the model

and a cumulative sum of energy showing the relative importance of each topois given by

$$E_k = \sum_{j=1}^k \lambda_j^2 / E_G, \quad k = 1, 2, \dots, N. \quad (3)$$

It should be noticed that the BOD introduces a time–space separation in the velocity field expansion. While the classic orthogonal decomposition POD is based on full two-point space–time correlations and entails space and time-dependent eigenmodes, BOD is closer to analytical and numerical studies where the velocity field is naturally expanded over products of spatial functions and temporal functions.

Detailed description of the POD and BOD methods and a mathematical background is given e.g. in paper [21].

5. Results

The results are presented here for the mean airflow rate $Q_{\text{mean}} = 0.25$ l/s, the fundamental frequency of the vocal folds self-oscillation $F0 = 158$ Hz, the time difference between two laser-pulses $\Delta t = 6 \mu\text{s}$ and the laser frequency $f_{\text{las}} = 1582$ Hz.

The microphone and subglottal pressure signals are shown in Fig. 4 together with the spectrum of the microphone signal and the glottal gap width evaluated from the series of the images of the vibrating vocal folds in the cross-section plane where the flow visualization by PIV was performed. The signals are not perfectly periodic, because the vocal fold vibrations were not exactly repeatable in each oscillation cycle and the sampling frequency of the high-speed camera was not sufficient due to the limits of the frequency range of the PIV system. The fundamental frequency of the acoustic and pressure signals was $F0 = 158$ Hz with many higher harmonics, and the sound pressure level (SPL) measured at the distance 30 cm in front of the lips model was 75.9 dB. In addition to the formant frequencies at about $F1 \cong 650$ Hz, $F2 \cong 1$ kHz, $F3 \cong 3$ kHz and $F4 \cong 4$ kHz detected in the microphone spectrum, which approximately agree with the computed values of the formant frequencies, some other parasitic resonant frequencies of an unknown origin can be seen in the spectrum near 1.5 and 2.5 kHz.

It should be noted that the beginning and end of the closing and opening phases of the glottis motion were not observed at the exactly identical times along the vocal folds model. This could emphasize 3D effects in the flow in the vocal tract.

The airflow velocity patterns evaluated from the PIV measurement in the laryngeal and epiglottis part of the vocal tract model during one vocal fold oscillation period are shown in Fig. 5. The denoted images ($i = 1$ –11) and

FLOW INSIDE A MODEL OF HUMAN VOCAL TRACT

335

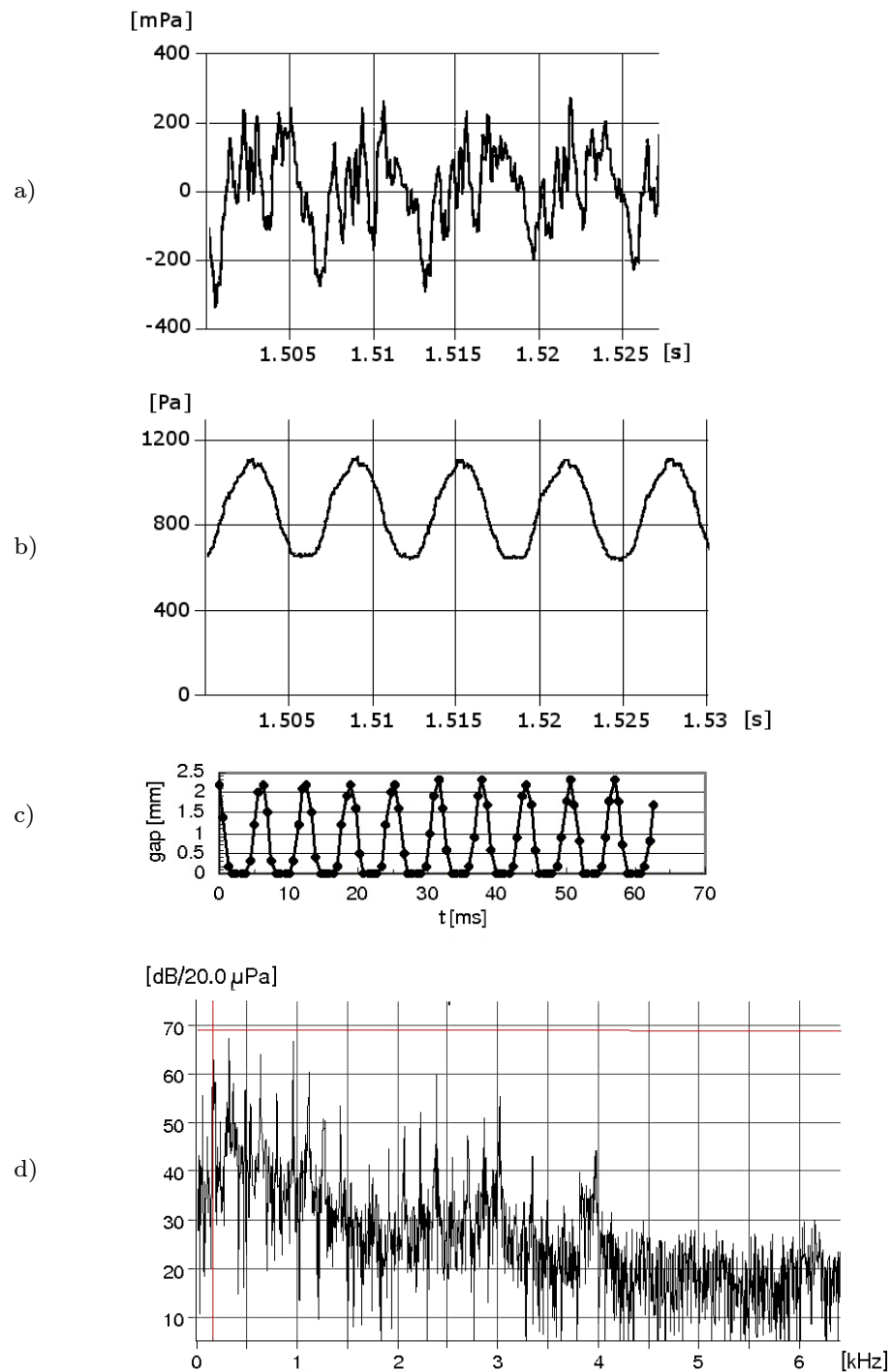
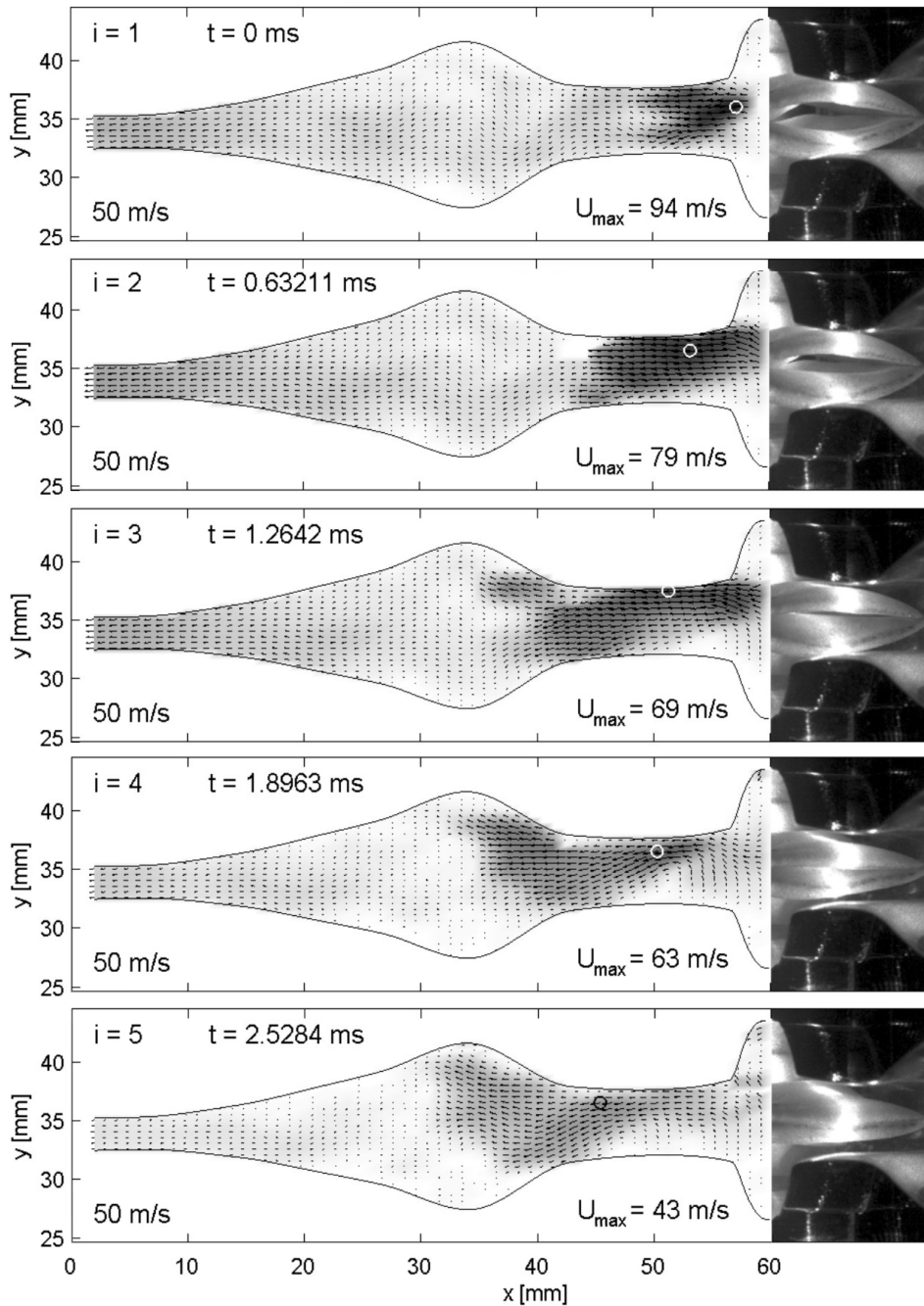


Fig. 4. Measured signals; a) microphone signal (radiated sound from the vocal tract), b) subglottal pressure measured by the pressure transducer in the model of the trachea, c) changes of glottal gap width measured at the middle cross-section of the vibrating vocal folds, d) FFT spectrum of the microphone signal

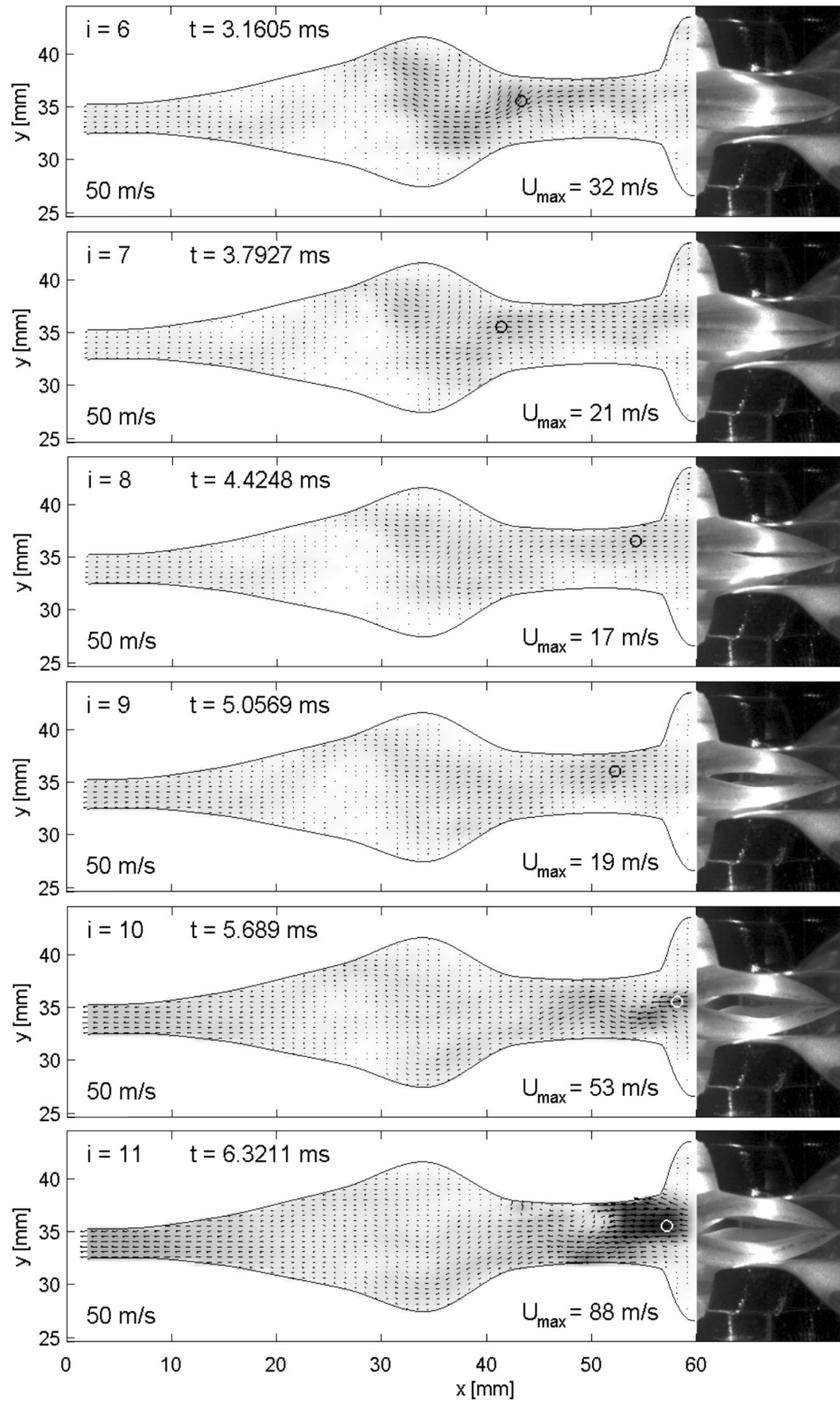


Continued >

Fig. 5. Airflow velocities measured near the glottal region and vibration of the vocal folds model in $i = 1-11$ time instants during one oscillation cycle; the air flows from the right to the left and the absolute values of the velocity vectors are highlighted by a gray intensity scaling; the vibrating vocal folds are shown on the right side of each picture

FLOW INSIDE A MODEL OF HUMAN VOCAL TRACT

337



338

J. HORÁČEK ET AL.

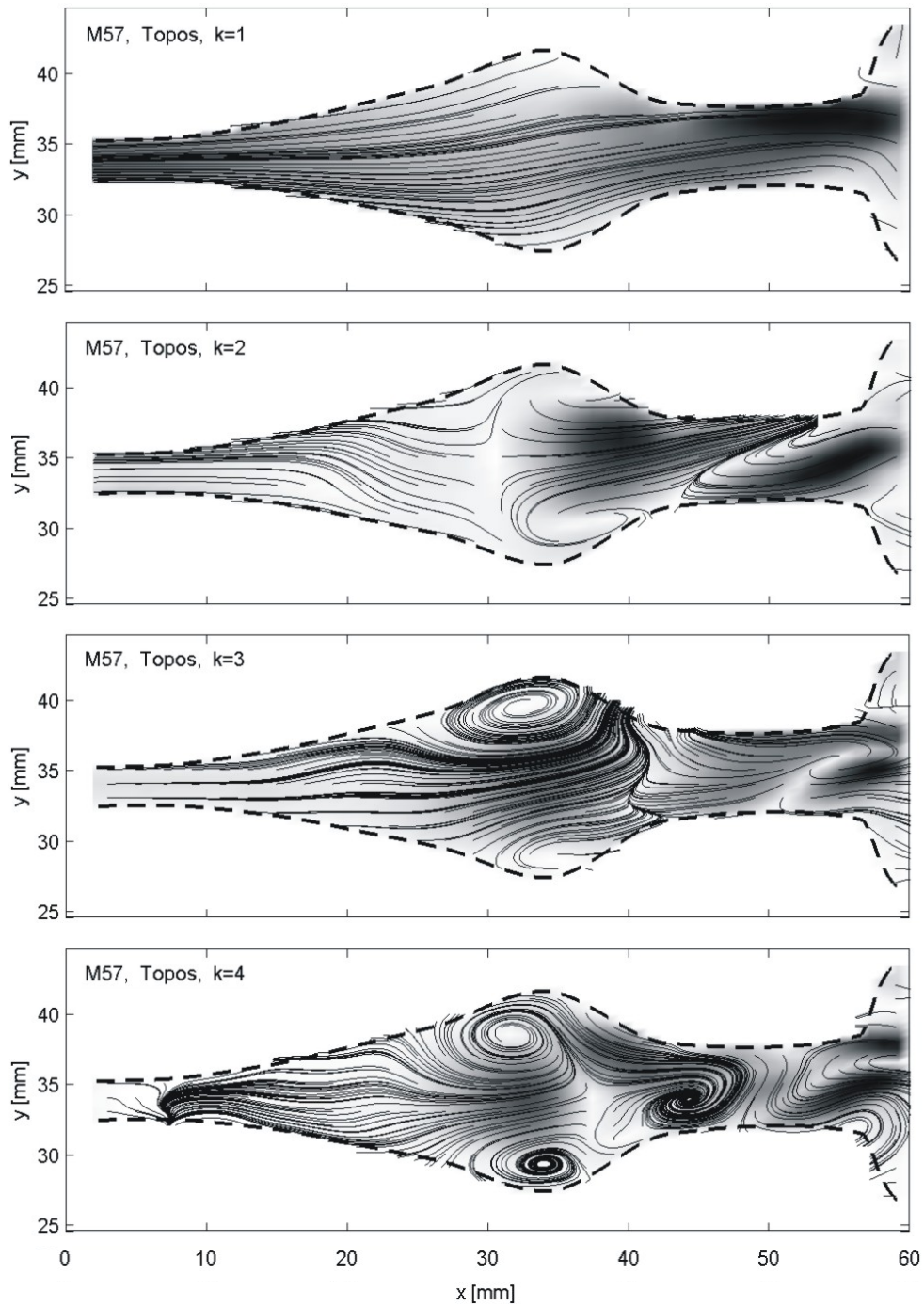


Fig. 6. First four toposes; the air flows from right to left and the absolute values of the topos vectors are highlighted by a gray intensity scaling

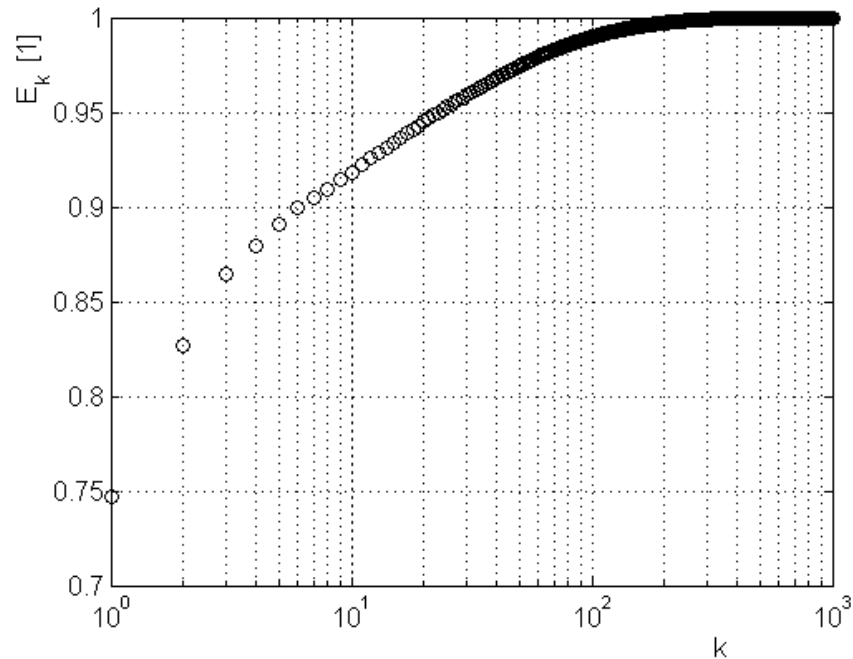


Fig. 7. Cumulative energy of the flow

time instants exactly correspond to the sampling frequency of the glottal gap width as shown in Fig. 4. The images $i = 1-11$ of the vibrating vocal folds recorded at the same time instants are added to the right-hand side of each airflow velocity pattern. A small circle on each image denotes the position of the point with the maximum value of the airflow velocity evaluated at each time instant. The maximum airflow velocities about 90 m/s are observed in the jet near the vocal folds outlet during the maximum glottis opening (see the images $i = 1$ and $i = 11$ in Fig. 5). The flow is asymmetric; the jet is skewed and predominantly attached to the upper wall of the channel resembling the Coanda effect.

The coherent structures evaluated in the flow field are shown in Fig. 6, where first four toposes $\varphi_k(x, y)$ ($k = 1, 2, 3, 4$) are presented using a streamline display pattern. The corresponding cumulative flow energy E_k for individual modes ($k = 1, 2, \dots, 1000$) and first four chronoses $\psi_k(t)$ associated with the toposes ($k = 1, 2, 3, 4$) are shown in Figs. 7 and 8, respectively.

The first six orthogonal spatial eigenmodes (toposes $\varphi_k(x, y)$, $k = 1, 2, \dots, 6$) represent about 90 % of total kinetic energy (see Fig. 7). This means that a few lower order, high-energy modes could capture principal properties of the entire flow. The first topos ($k = 1$) contains nearly 75 % of the flow energy and represents more or less the mean flow. The second topos ($k = 2$) having about 8 % of energy forms a strong jet detecting the Coanda effect when the jet can attach randomly the upper or lower wall of the channel. The third topos ($k = 3$)

with about 3.8 % of flow energy represents a strong large vortex situated on the left side from the model of the ventricular folds sitting at the upper wall in the epilaryngeal part of the vocal tract model. The vortex dimensions are comparable with the height (cross-section) of the channel (see, the streamline pattern for $k = 3$ in Fig. 6). Just before entering the model of the mouth cavity in the narrowest part of the vocal tract model the large vortices disappear and the flow is getting nearly uniform. The topos $k = 4$ containing about 1.5 % of the total flow energy shows formation of the smaller vortices.

The direction of the each term of the velocity vector in the sum in (1) is given by the topos multiplied by the corresponding chronos, which can have either positive or negative instantaneous value. The first chronos shown in Fig. 8 has only positive values and the positive constant mean value characterizes the pulsating mean flow velocity magnitude. The second chronos can be characterized as a time process with strong fundamental vibration frequency $F0$ and higher harmonics. The higher toposes are characterized by the higher level of the random component and the stronger higher harmonics.

Large eddies of a size comparable with the channel height were clearly noticeable in the airflow velocity patterns in the model of the mouth cavity. The first topos measured in this part of the vocal tract that contains about 87 % of the flow energy is shown in Fig. 9. The airflow was here permanently attached to one wall of the channel forming the Coanda effect in the jet coming from the narrow epilaryngeal part. It should be noted that for the flow visualization in the mouth cavity model another setting of the experiment had to be arranged due to limited dimensions of the field of view, which can be measured by the used PIV system.

6. Conclusion

The results of the PIV measurements of the airflow in the human vocal tract model and analyses of the coherent flow structures show large vortices with dimensions comparable with the channel cross-section above the ventricular folds and Coanda effect with the flapping air jet coming from the vibrating glottis. The vortices disappear in the narrowest epilaryngeal part of the vocal tract where the flow is uniform. Considerable 3D effects of the glottal flow were observed in the vocal tract, especially near the vibrating vocal folds and for higher airflow rates. Large eddies of a size comparable with the channel height were observed in the model of the mouth cavity.

The results are qualitatively in a good agreement with the recent experimental studies of unsteady flows near the oscillating glottis, focused, however, mainly on the flapping jet where no vocal tract forming the shape of the channel was modeled.

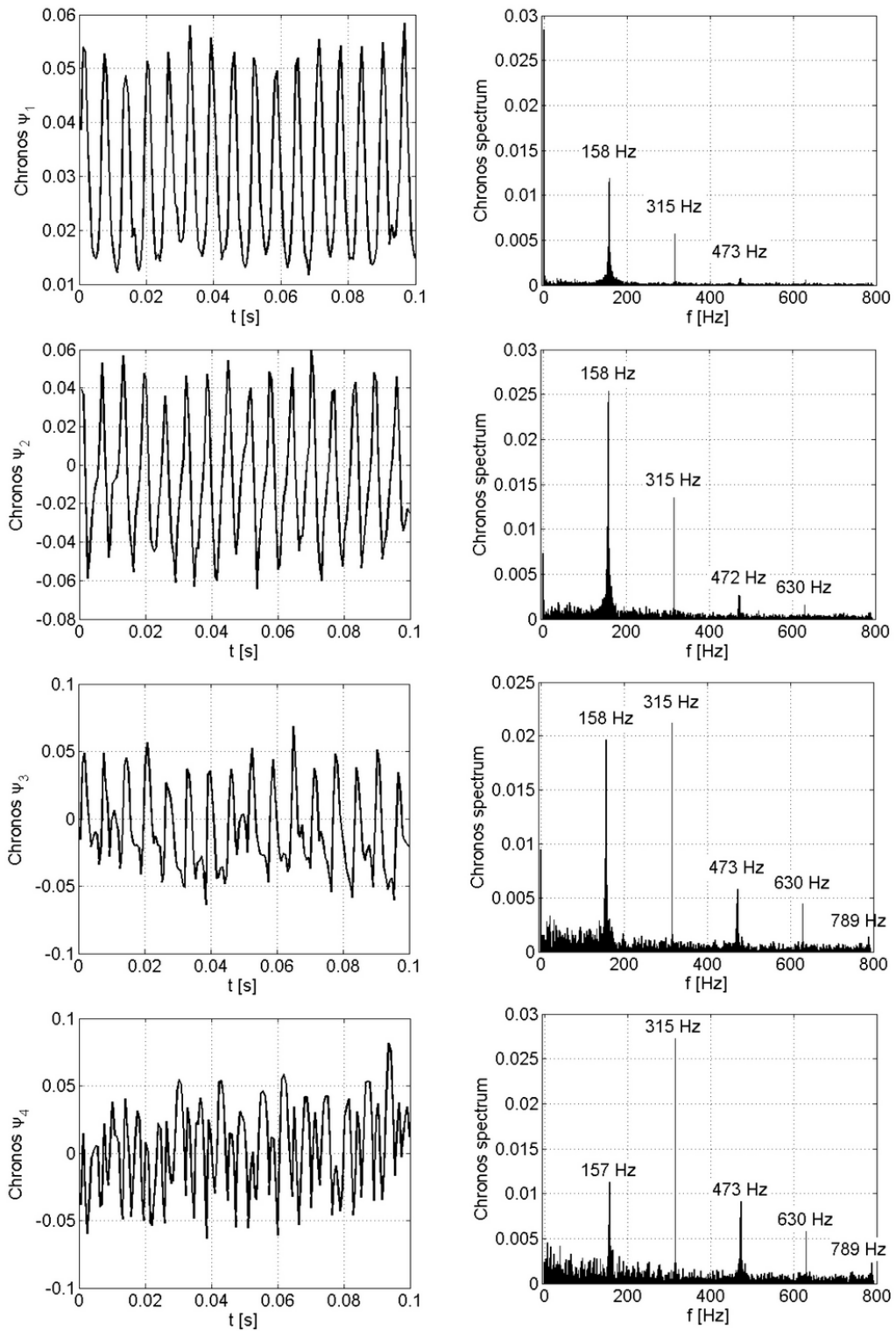


Fig. 8. First four chronoses in time and frequency domain

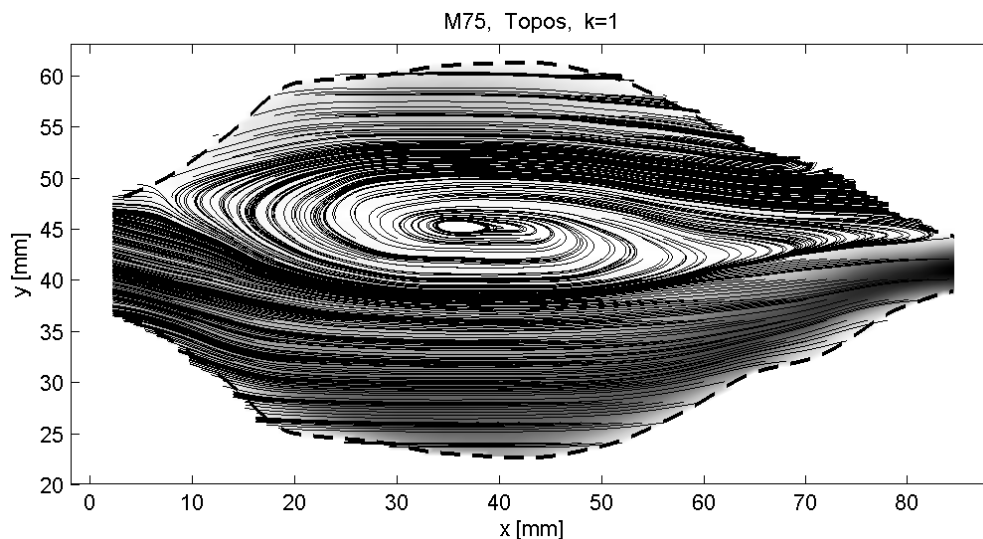


Fig. 9. First topos in the mouth cavity model; the air flows from right to left and the absolute values of the topos vectors are highlighted by a gray intensity scaling

References

- [1] I. R. TITZE: *Principles of voice production*. National Center for Voice and Speech, Iowa City 2000.
- [2] R. C. SCHERER, D. SHINWARI, K. J. DE WITT, C. ZHANG, B. R. KUCINSCHI, A. A. AFJEH: *Intraglottal pressure profiles for a symmetric and oblique glottis with an divergence angle of 10 degrees*. *J. Acoustical Soc. Amer.* *109* (2001), 1616–1630.
- [3] G. D. J. HOFMANS, G. GROOT, M. RANUCCI, G. GRAZIANI, A. HIRSCHBERG: *Unsteady flow through in-vitro models of the glottis*. *J. Acoustical Soc. Amer.* *113* (2003), 1658–1675.
- [4] D. SHINWARI, R. C. SCHERER, K. J. DEWITT, A. A. AFJEH: *Flow visualization and pressure distributions in a model of the glottis with a symmetric and oblique divergent angle of 10 degrees*. *J. Acoustical Soc. Amer.* *113* (2003), 487–496.
- [5] M. DEVERGE, X. PELORSON, C. VILAIN, P. LAGREE, F. CHENTOUF, J. WILLEMS, A. HIRSCHBERG: *Influence of collision on the flow through in-vitro rigid models of the vocal folds*. *J. Acoustical Soc. Amer.* *114* (2003), 3354–3362.
- [6] B. ERATH, M. PLESNIAK: *The occurrence of the Coanda effect in pulsatile flow through static models of the human vocal folds*. *Experim. Fluids*, *41* (2006), 735–748.
- [7] B. R. KUCINSCHI, R. C. SCHERER, K. J. DEWITT, T. T. M. NG: *An experimental analysis of the pressures and flows within a driven mechanical model of phonation*. *J. Acoustical Soc. Amer.* *119* (2006), 3011–3021.
- [8] S. K. KIM, S. K. CHUNG: *Investigation on the respiratory airflow in human airway by PIV*. *J. Visualization* *12* (2009), 259–266.
- [9] CH. BRÜCKER, M. TRIEP, W. MATTHEUS, R. SCHWARZE: *Pulsating jet generated by a driven glottis-shaped orifice*. Proc. 2nd International Conference on Jets, Wakes and Separated Flows, Berlin (Germany), Sept. 16–19, 2008, Technical University of Berlin.
- [10] M. TRIEP, W. MATTHEUS, M. STINGL, C. BRÜCKER: *Three-dimensional unsteady flow nature in the vocal tract during human phonation*. NAG/DAGA 2009 International

- Conference on Acoustics, Rotterdam (Netherlands), March 23–26, 2009 (M. M. Boone, ed.), TU-Delft, 1741–1743.
- [11] C. KIRMSE, M. TRIEP, C. BRÜCKER, M. DÖLLINGER, M. STINGL: *Experimental flow study of modeled regular and irregular glottal closure types*. Logopedics Phoniatrics Vocology 35 (2010), 45–50.
- [12] B. ERATH, M. PLESNIAK: *Investigation of asymmetric flow features in a scaled-up driven model of the human vocal folds*. Experiments in Fluids (2010), doi 10.1007/s00348-009-0809-0.
- [13] P. ŠIDLOF: *Fluid-structure interaction in human vocal folds*. PhD thesis, Faculty Math. Phys., Charles University in Prague, 2007.
- [14] P. ŠIDLOF, J. HORÁČEK: *Mathematical and physical modeling of flow-induced vibrations of human vocal folds*. Flow induced vibration (I. Zolotarev, J. Horáček, eds.), Institute of Thermomechanics AS CR, v.v.i., Prague 2008, 141–146.
- [15] J. NEUBAUER, Z. ZHANG, R. MIRAGHAIE, D. A. BERRY: *Coherent structures of the near field flow in a self-oscillating physical model of the vocal folds*. J. Acoustical Soc. Amer. 121 (2007), 1102–1118.
- [16] B. A. PICKUP, S. L. THOMSON: *Influence of asymmetric stiffness on the structural and aerodynamic response of synthetic vocal fold models*. J. Biomechanics 42 (2009), 2219–2225.
- [17] S. BECKER, S. KNIESBURGES, S. MÜLLER, A. DELGADO, G. LINK, M. KALTENBACHER, M. DÖLLINGER: *Flow-structure-acoustic interaction in human voice model*. J. Acoustical Soc. Amer. 125 (2009), 1351–1361.
- [18] T. VAMPOLA, J. HORÁČEK, J. ŠVEC: *FE modeling of human vocal tract acoustics. Part I: Production of Czech vowels*. Acta Acustica united with Acustica 94 (2008), 433–447.
- [19] J. L. LUMLEY: *The structure of inhomogeneous turbulent flows*. Atmospheric turbulence and radio wave propagation (A. M. Yaglom, V. I. Tatarsky, eds.), Nauka, Moskva 1967, 166–178.
- [20] N. AUBRY, R. GUYONNET, R. LIMA: *Spatiotemporal analysis of complex signals: Theory and applications*. J. Statist. Phys. 64 (1991), 683–739.
- [21] V. URUBA, M. KNOB: *Application of the orthogonal decomposition methods*. 22nd Symposium on anemometry (Z. Chára, L. Klaboch, eds.), Holany–Litice (Czech Republic), June 2008, Institute of Hydrodynamics AS CR, v.v.i., Prague 2008, 103–108.

Received November 7, 2010

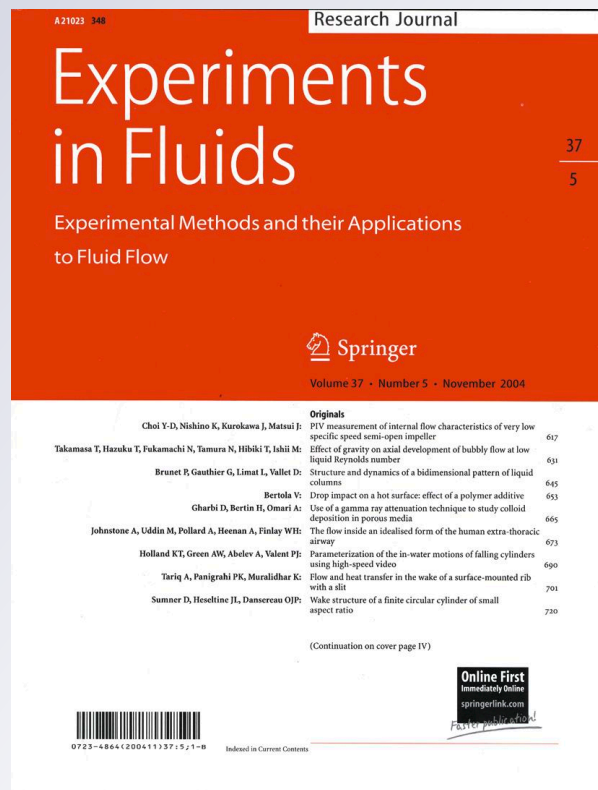
Measurement of flow separation in a human vocal folds model

*Petr Šidlof, Olivier Doaré, Olivier Cadot
& Antoine Chaigne*

Experiments in Fluids
Experimental Methods and their
Applications to Fluid Flow

ISSN 0723-4864
Volume 51
Number 1

Exp Fluids (2011) 51:123-136
DOI 10.1007/
s00348-010-1031-9



Author's personal copy

Exp Fluids (2011) 51:123–136
DOI 10.1007/s00348-010-1031-9

RESEARCH ARTICLE

Measurement of flow separation in a human vocal folds model

Petr Šidlof · Olivier Doaré · Olivier Cadot ·
Antoine Chaigne

Received: 10 February 2010 / Revised: 18 November 2010 / Accepted: 14 December 2010 / Published online: 7 January 2011
© Springer-Verlag 2011

Abstract The paper provides experimental data on flow separation from a model of the human vocal folds. Data were measured on a four times scaled physical model, where one vocal fold was fixed and the other oscillated due to fluid–structure interaction. The vocal folds were fabricated from silicone rubber and placed on elastic support in the wall of a transparent wind tunnel. A PIV system was used to visualize the flow fields immediately downstream of the glottis and to measure the velocity fields. From the visualizations, the position of the flow separation point was evaluated using a semiautomatic procedure and plotted for different airflow velocities. The separation point position was quantified relative to the orifice width separately for the left and right vocal folds to account for flow asymmetry. The results indicate that the flow separation point remains close to the narrowest cross-section during most of the vocal fold vibration cycle, but moves significantly further downstream shortly prior to and after glottal closure.

1 Introduction

Human voice is created by expiring air from the lungs through a narrow constriction called *the glottis*. This constriction is formed by the vocal folds, located in the larynx.

The vocal folds (also called the vocal cords) are two symmetric soft tissue structures fixed between the thyroid cartilage and arytenoid cartilages. Basically they are composed of the thyroarytenoid muscle and ligament covered by mucosa. Under certain conditions (subglottal pressure, glottal width, longitudinal tissue tension), the vocal folds can start to oscillate and in regular phonation close the channel periodically, thus creating disturbances of the pressure field. These pressure disturbances are further filtered by the vocal tract, radiated from the mouth, and perceived as voice.

The concept of fluid–structure–acoustic interaction between the airflow, elastic vocal folds, and sub- and supraglottal acoustic spaces relies on knowledge of aerodynamics in the larynx. However, due to periodic closure of the glottal channel during vocal fold vibration and inherent unsteadiness of the airflow, the aerodynamic effects in the larynx are very complex. In spite of the progress in fundamental research of human voice production during recent years, some features of the glottal flow are not yet fully understood, one of them being flow separation from the vocal fold surfaces.

From the fluid-mechanical point of view, the human larynx can be seen as a nearly planar nozzle with time-varying clearance. In the convergent part, the airflow accelerates. Near the narrowest cross-section, airflow separates due to adverse pressure gradient and forms a jet (see Fig. 1). Although flow separation in divergent ducts has been intensively studied, usable criteria predicting flow separation are known only for simple cases. Fox and Kline (1962) published performance maps for straight and conical diffusers: in these cases, the most important factors are the area ratio, divergence angle, and inlet boundary layer blockage. Generally, the authors show that the boundary layer does not separate and the flow remains attached to

P. Šidlof (✉)
Institute of Thermomechanics,
Academy of Sciences of the Czech Republic,
Dolejšková 5, 182 00 Prague 8, Czech Republic
e-mail: sidlof@it.cas.cz

O. Doaré · O. Cadot · A. Chaigne
Unité de Mécanique (UME), ENSTA Paris Tech,
Chemin de la Hunière, 91761 Palaiseau cedex, France

Author's personal copy

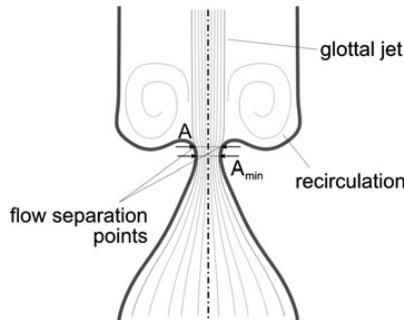


Fig. 1 Symmetric airflow in the glottis (idealization). Physiological orientation—flow in the inferior-to-superior direction

both walls only for low divergence half-angles (less than 10° for short diffusers, less than 1° for long ones). As the divergence angle increases, the flow shifts to transitory stall and further to bistable stall, when the flow separates from one wall only. For even higher divergence angles and diffuser lengths, there is jet flow, where the mainstream almost ignores the walls and passes at nearly constant area.

For the much more complex case of flow past human vocal folds, however, there are no general criteria predicting where exactly the flow separation takes place, as this can be influenced by many factors: interaction of the jet with supraglottal turbulent and vortical structures; flow interruption during glottal closure and formation of the new jet when the glottis reopens; whether the boundary layer has enough time to develop, etc. Yet, the information on the flow separation position is essential, e.g., in simplified computational models of phonation, where the airflow is usually modeled by Bernoulli or Euler equations. These models, still widely used due to their computational efficiency, require prior knowledge of the separation point position to obtain realistic pressure distributions along the vocal folds.

In the field of voice production research, the importance of the flow separation point movement was assessed theoretically in the paper of Krane and Wei (2006). Zhang (2008) showed in his sensitivity study that the flow separation location has significant impact on the eigenmode-coupling effect of the flow-induced stiffness, which he regards as a primary mechanism of phonation onset. He concludes that the high sensitivity to the flow separation location indicates to the need for phonation models to be capable of accurate prediction of flow separation.

In the simplified computational models of phonation, the position of the separation point is either fixed to the superior margin of the vocal folds (Story and Titze 1995; Horáček et al. 2005; Zanartu et al. 2007; Zhang et al. 2007) or supposed to move along the divergent part of the glottis. In this case, its position is usually specified using a

semiempirical criterion, which states that the jet separates at the position where the channel cross-section A reaches

$$A/A_{\min} = FSC, \quad (1)$$

where A_{\min} is the minimum glottal cross-section (see Fig. 1) and FSC is a constant which can be called “flow separation coefficient”. In different published papers, various values of FSC are used: Deverge et al. (2003) sets $FSC = 1.2$ (based on the pioneer work of Pelorson et al. (1994) and private communication with Liljencrants), the model of Lucero (1998) assumes $FSC = 1.1$. In their comparative study, Decker and Thomson (2007) tested different values of the flow separation coefficient: $FSC = 1.2$ and $FSC = 1.47$ (according to finite volume computations of Alipour et al. (1996) and Alipour and Scherer (2004)). Recently, Cisonni et al. (2008) published data on the flow separation point coefficient computed by inverse simplified flow models. According to their results, the coefficient remains almost constant with a value $FSC = 1.08$ when a Poiseuille model is employed, or oscillates in the range $FSC = 1.02$ – 1.07 when a Bernoulli model is used.

It appears that a criterion for flow separation position expressed by Eq. (1) approximately holds for steady or quasi-steady flow, but its validity for intrinsically unsteady pulsating flow past vibrating vocal folds is questionable. Vilain et al. (2004) discusses this issue and proposes to solve the glottal flow alternatively by Thwaites’ method within the boundary layer. This is done by Hirtum et al. (2005), whose simplified Navier–Stokes solver predicts $FSC = 1.2$ – 1.75 .

The next controversial issue is that the criterion (1) implicitly assumes that the glottal flow is symmetric with regard to glottal mid-plane and that it separates at the same location on the right and left vocal folds. However, many of the recent works on glottal airflow dynamics, both computational and experimental, show that in reality the behavior of the glottal jet is more complex and strongly asymmetric. During vocal fold vibration, the location where the airflow separates might move down- and upstream considerably.

Hofmans et al. (2003), solving the Navier–Stokes equations by the “viscous vortex blob” method, obtained $FSC = 1.2$ for a narrow glottis and $FSC = 1.4$ – 1.6 for widely abducted vocal folds. The finite volume computations of Alipour and Scherer (2004) yielded $FSC = 1.1$ – 1.9 . Thomson et al. (2005) were among the first to include fluid–structure interaction in a FEM model and compared the computational results with experiments on a true-scale rubber physical model, but did not investigate flow separation. The paper of Suh and Frankel (2007), who solved the Favre-filtered compressible Navier–Stokes equations in 3D by finite element method, was focused on flow–acoustic

Author's personal copy

Exp Fluids (2011) 51:123–136

125

interaction. Tao et al. (2007), using the Flotran solver coupled to a 2-mass model programmed in ANSYS APDL, pointed out that the asymmetry of the driving force on the vocal folds and their displacement asymmetry can reach 11%. Recently, Sciamarella and Quéré (2008) analyzed the flow past vibrating rigid vocal folds using a multigrid finite difference method and showed that the mobility of the flow separation point is nontrivial and only rarely quasi-static. The flow separation coefficient, which was evaluated, ranged between $FSC = 1.0$ – 1.3 .

Before the laser flow measurement methods were available, the experimental papers on glottal aerodynamics, e.g., Barney et al. (1999) and Alipour and Scherer (2006), used hot-wire anemometry to measure flow velocity, or discrete pressure taps to obtain pressure distributions (Scherer et al. 2001). Neither of these methods provides sufficient spatial resolution to evaluate the position of the flow separation point. Shinwari et al. (2003), using a 7.5 times scaled plexiglass static model with vocal folds in different configurations, measured pressure distributions and obtained, among others, some quantitative data on flow separation in terms of distance from the minimal cross-section. For various transglottal pressures, the separation point was at 0.23 cm on the vocal fold, where the flow was attached, and at 0.02 cm on the opposite one.

With the development of laser flow visualization techniques and PIV, the possibilities of flow field measurements extended considerably. First, glottal flow visualizations and PIV measurements were published by Triep et al. (2005), who used a three times scaled hydrodynamic setup, and Erath and Plesniak (2006a, b) on a static 7.5 times life-size vocal fold model. Kucinski et al. (2006) confronted his Fluent computations with pressure and flow rate measurements on a mechanically driven physical model, but did not assess velocity fields. Li et al. (2006) used a similar technique (with a static physical model) and tried to evaluate the flow separation points, although only qualitatively. Like Triep et al. (2005), Krane et al. (2007) made measurements on an externally driven model of the human glottis in a water channel, which operated at lower frequencies.

An extensive PIV data set on glottal flow was published by Neubauer et al. (2007), who used a life-sized model of Thomson et al. (2005) and quasi-phase-locked PIV to measure near-field flow structures. The paper provides detailed data on jet core velocity, jet inclination angle, and also on the flow separation point, however only qualitatively. The paper of Becker et al. (2009) is focused on elucidation of the mechanisms of sound production in the larynx. The authors used a synthetic life-sized self-oscillating vocal fold model. Their results demonstrate the existence of the Coanda effect in phonation. Erath and

Plesniak (2010) published a study on asymmetric flow features in the glottis. Using an externally driven 7.5 times life-sized model precisely mimicking vocal fold oscillation, they quantify jet skewing in the divergent part of the glottis and deduce implications of flow asymmetries on sound production. In a recent paper, Triep and Brücker (2010) used an improved experimental setup equipped with time-resolved PIV to show that the supraglottal flow field is highly 3D. Their results also show that the presence of the ventricular folds decreases the pressure loss and stabilizes the jet during the divergent phase.

In spite of the considerable amount of data published on supraglottal velocity fields, there seems to be a lack of measurements with sufficient resolution to draw systematic conclusions regarding airflow separation in human phonation. This paper presents an experimental study providing quantitative data on the position of the flow separation point during vocal fold vibration. The glottal airflow in a physical self-oscillating vocal fold model was visualized using a phase-locked PIV system. The location of the flow separation point was evaluated from the visualizations by a semiautomatic procedure.

2 Methods

2.1 Vocal fold model

A new physical model of human vocal folds was designed for the current study. The model was proposed as a vocal-fold-shaped element vibrating in a rectangular channel. Unlike most of the physical models reported in previous works, in this case, the vocal fold vibration was flow-induced, not externally forced. The shape of the vocal folds that has been most widely used in mathematical and physical modeling of human voice seems to be model “M5”, proposed by Scherer et al. (2001, 2002) and used, among others, in theoretical and experimental studies by him, Thomson et al. (2005), or Erath and Plesniak (2006a). The geometry of the “M5” model is piecewise linear with rounded corners. It is based on data from X-ray databases and provides an easily parametrizable approximation of the vocal fold shape during oscillation. In this work, the authors decided to specify the shape of the model vocal folds according to their own measurements of excised female human larynges in prephonatory position. The description of the methods used and a detailed quantitative specification of the vocal fold shape measured can be found in Šidlof et al. (2008). The shape was described by a piecewise cubic spline. Unlike the “M5” model, the shape is not composed of straight segments, but changes the curvature continuously. In the region where flow separation takes place (in the divergent part, downstream of the

Author's personal copy

narrowest cross-section), the radius of curvature is approximately 5.4 mm (which scales to 1.35 mm lifeseize).

The model vocal folds were cast using RTV-II type 69199 two-compound silicone rubber. In the configuration presented here, the upper vocal fold was fixed to the channel wall in order to avoid asymmetric modes of vibration and situations where the vocal folds vibrate with significantly different amplitudes or even dissimilar frequencies. The second silicone vocal fold, glued on a light rigid support, was mounted on four flat springs into the wall of the channel. The prephonatory adduction of the vocal folds can be set precisely by two adjusting screws.

The physical dimensions of the real human larynx are very small, making the design of a life-sized physical model a very difficult issue. In order to perform high-resolution measurements on a mechanical model with well-defined properties, the physical model was scaled up by a factor of four. Table 1 summarizes the important dimensional and dimensionless parameters of the real larynx and the physical model, particularly the Reynolds and Strouhal numbers

$$Re = \frac{U_0 L}{\nu}, \quad St = \frac{fL}{U_0} \quad (2)$$

based on the mean subglottal velocity U_0 , kinematic viscosity ν , fundamental frequency of vibration f and vocal fold thickness L (see Fig. 2).

The elasticity of the vocal folds is modeled mainly by the stiffness of the flat springs. As shown in Fig. 4, each spring was clamped to a rigid beam on one side and screwed to the rigid support of the vocal fold on the other. The dimensions ($85 \times 10 \times 0.5$ mm) and material (brass alloy, Young modulus 100 GPa) of the springs were designed so that the first natural frequency of the system matched the desired scaled frequency. After fabrication, the force-deflection curve of the springs was measured. Within the operational limits, the response was roughly linear (slightly hardening under heavier loads), with stiffness about 200 N/m per one spring. The stiffness of the

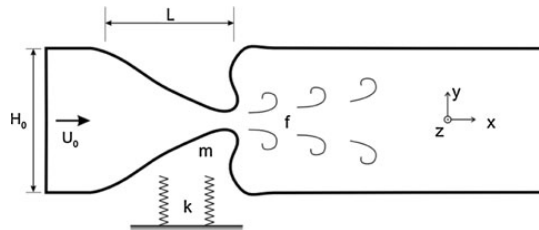


Fig. 2 Overview of the important dimensional parameters: channel height H_0 , inlet flow velocity U_0 , characteristic length (vocal fold thickness) L and frequency f , mass m and stiffness k

silicone rubber itself would be too large to allow self-sustained oscillation with the desired frequency and plays important role during vocal fold collisions only.

The elastic support gives the vocal fold three degrees of freedom. The first is the “heaving” (10) mode of vibration, where the vocal fold translates along the y -axis (see Fig. 2 for orientation of the coordinate system). In the second, “rocking” (11) mode, the mass rotates about the z -axis. The elastic support itself does not block the third, undesired, “torsional” (20) mode, where the vocal fold rotates about the x -axis. Frequency analysis of the impulse response shows that the natural frequency of the largely dominant heaving mode is 11.0 Hz. The second highest peak in the spectrum (about 20 dB lower than the first one) at 21.9 Hz belongs to the torsional mode. The high-speed camera recordings of flow-induced vibration revealed, however, that the torsional mode is suppressed by collisions against the opposite vocal fold and most likely also by the aerodynamic damping, since this mode did not occur even for vibration without collisions at low flow rates. The rocking mode manifests as an indistinct peak at 38 Hz. As a result, the flow-induced vibration occurs slightly above the first natural frequency and has mostly the character of the first (10) mode.

2.2 Experimental setup

The vocal fold model was mounted in a plexiglass wind tunnel. A centrifugal fan regulated by a frequency inverter drives the flow through a honeycomb screen into a long circular channel intended to suppress the inlet turbulence (see Figs. 3, 4). Further, the channel cross-section contracts smoothly by factor $f \approx 6$ into a rectangular 100×40 mm inlet of the measuring section with the vocal folds. Downstream of the vocal folds, the channel continues 40 cm to simulate the vocal tract and terminates freely into ambient air.

To allow free motion of the vocal fold, there has to be a small gap between the vocal fold and the channel walls. The leakage flow at the inferior margin (left edge in Fig. 3)

Table 1 Comparison of the relevant dimensional and dimensionless parameters: mean subglottal velocity U_0 , channel height H_0 , vocal fold thickness L , oscillation/vortex shedding frequency f , transglottal pressure Δp , Reynolds and Strouhal number Re and St

	Real larynx	Physical model
U_0 (m/s)	1–10	1.4–2.5
H_0 (mm)	10–20	40
L (mm)	10	40
f (Hz)	100–400	10–14
Δp (Pa)	200–2,000	50–250
Re	600–6,000	3,000–6,000
St	0.1–1	0.2–0.3

Author's personal copy

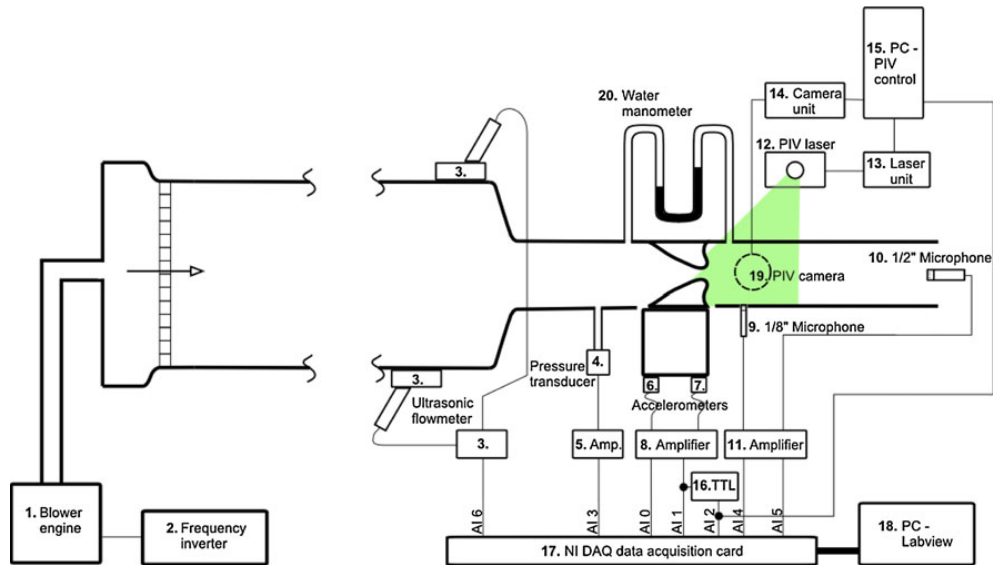


Fig. 3 Diagram of the experimental setup used for the measurements of vocal fold vibration and for visualization of the supraglottal flow. 1 Rietschle Thomas centrifugal fan (2,200 W, $\Delta p_{max} = 29$ mbar, $Q_{max} = 2,770$ m³/h). 2 Omron Sysdrive 3G3MV frequency inverter (380 V, 0–60 Hz). 3 GE Panametric GC 868 ultrasonic gas flowmeter. 4 Validyne DP15TL dynamic pressure transducer (steel membrane 0.125 PSI FS). 5 Validyne CD23 amplifier. 6, 7 Brüel&Kjær 4507C accelerometers. 8 Brüel&Kjær Nexus conditioning amplifier type 2692 (frequency bandpass 1 Hz–1 kHz). 9 G.R.A.S. 1/8" condenser microphone type 4138, G.R.A.S. preamplifier type 26AJ. 10 G.R.A.S.

1/2" prepolarized free field microphone type 40BE, G.R.A.S. preamplifier type 26AJ. 11 Brüel&Kjær Nexus conditioning amplifier type 2690. 12 New Wave Research PIV laser SOLO 3–15. 13 New Wave Research SOLO III laser unit. 14 LaVision Imager PRO camera unit. 15 PC-2proc Intel Xeon, software Davis v7. 16 Philips PM5715 TTL/pulse generator. 17 National Instruments NI DAQpad-6015 data acquisition card. 18 PC-software NI LabView v7.1. 19 LaVision Imager PRO camera (1,600 × 1,200 pixel, Canon macro TV zoom lens). 20 Kimo water manometer (precision 0.5 mm H₂O (5 Pa))

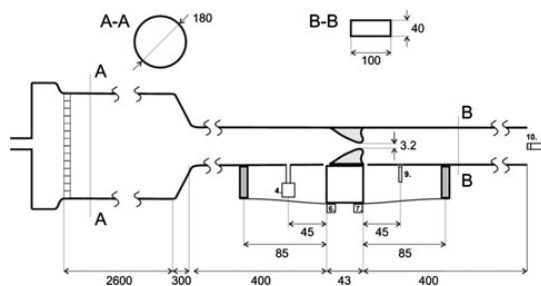


Fig. 4 Schematic of the vocal fold model and important dimensions of the wind tunnel (in millimeters)

was blocked by a thin membrane. Since the mean supraglottal pressure in the model was close to atmospheric pressure, the leakage at the superior margin was not important. The airflow along the side walls, which could not be completely avoided, did not significantly influence the supraglottal velocity fields measured in the channel mid-plane.

The setup was equipped with accelerometers (Brüel&Kjær 4507C), mounted below the apex and leading edge of

the vocal fold to record vocal fold vibration. The frequency spectra of the acceleration signal were used to detect the frequency of vibration of the vocal fold. To capture the subglottal pressure including the DC part of the signal, dynamic pressure transducers (Validyne DP15TL, steel membrane 0.125 PSI FS) were used. Two microphones (G.R.A.S. 1/8" condenser microphone type 4138 mounted flush with the wall, G.R.A.S. 1/2" prepolarized free field microphone type 40BE located at the channel exit) recorded the supraglottal dynamic pressure and the radiated acoustic pressure. To measure the mean flow in the channel, an ultrasonic gas flowmeter (GE Panametric GC 868) was fixed near the downstream end of the circular channel. The diagram in Fig. 3 shows the locations and wiring of transducers used. The important dimensions are summarized in Fig. 4.

The PIV system consisted of a Nd:YAG laser (New Wave Research Solo III, maximum repetition rate 15 Hz, 120 mJ), laser unit, and the PIV camera and unit (La Vision Imager PRO, 1,600 × 1,200 pix, max. 15 frames/s). The flow was seeded from an olive oil atomizer upstream of the honeycomb screen. The camera lens (Canon macro TV zoom), fixed 1.5 cm from the plexiglass wall, had a field of view of about 60 × 45 mm, providing spatial

Author's personal copy

resolution of the raw camera frames of 0.037 mm/pix. The PIV settings were as follows: delay between pulses 20 μ s, interrogation area 32×32 pix, 50% overlap. In order to remove the laser sheet reflections on the vocal fold surface, the raw images were preprocessed using sliding background image subtraction. The postprocessing options consisted of multi-pass correlation, peak validation, median filtering and smoothing.

The laser and camera were triggered by a rectified signal from one of the accelerometers. Hence, the system was phase-locked with the vocal fold vibration to measure the velocity fields at precisely defined phases of the oscillation cycle. Due to the low repetition frequency of the laser system (15 Hz), only one pulse could be generated per one oscillation cycle. The phase difference between the laser and vocal fold oscillation was set in such a way that during 40 subsequent periods of vibration, 40 camera frames were recorded, covering the whole oscillation cycle. The setup of the optics allowed recording the 2D flow field immediately downstream of the glottis. Due to oil particle deposition on the walls, frequent cleaning was necessary between experimental runs to preserve sufficient image sharpness.

2.3 Determination of the flow separation point from the recorded camera frames

Traditionally, the term “flow separation point” used in simplified models of glottal flow assumes that the glottal flow is symmetric with regard to the glottis midline, as depicted in Fig. 1. In this case, it is sufficient to quantify the separation point position by the glottal area at the critical place. However, flow visualizations and PIV measurements on physical models, as well as computational flow simulations based on finite element or finite volume codes, show that this is rarely the case: the glottal jet tends to attach to one of the vocal fold surfaces and significantly skews from the glottis midline position (see Fig. 5 for a schematic representation of the flow pattern).

Such asymmetric flow was observed in measurements presented in this paper, too. Therefore, it was necessary to introduce a suitable coordinate system to describe the position of the “left” and “right” separation point independently, still allowing to correlate the new results to previously used criteria for flow separation.

First, the narrowest cross-section was located (defined by the left and right VF apex in Fig. 6). The line is not necessarily perpendicular to the channel, because during vibration the apex of the vocal fold moves slightly in the horizontal direction (that is, in the inferior–superior direction in physiological orientation). Then, the “left” and “right” flow separation coefficients FSC_L and FSC_R can be defined simply as the distance of the respective flow

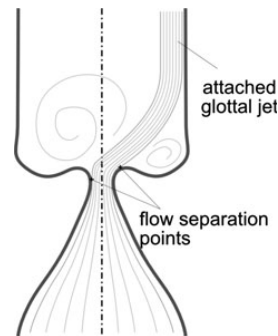


Fig. 5 Asymmetric flow in the glottis. Physiological orientation—flow in the inferior-to-superior direction

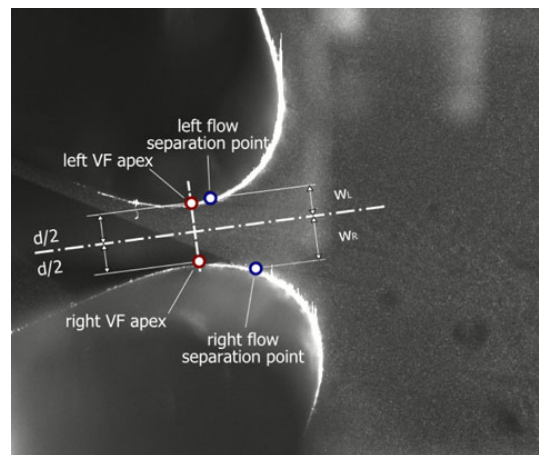


Fig. 6 Definition of the flow separation coefficient. Experimental configuration—flow direction from the left to the right

separation point from the axis divided by half of the orifice width:

$$FSC_L = \frac{w_L}{d/2}, \quad FSC_R = \frac{w_R}{d/2}. \quad (3)$$

Such a description is a generalization of the symmetrical definition (1). If the vocal fold vibration and supraglottal velocity field were perfectly symmetrical with regard to the glottal axis, the definitions would be equivalent.

In principle, the position of the flow separation point may be evaluated from the vector fields calculated by the PIV method. However, in the PIV velocity field, a single vector is computed typically from a 32×32 pixel “interrogation” area, which means that the resolution of the vector field is much lower than the resolution of the original image. Moreover, the vector represents a statistical mean of particle velocities within the interrogation area.

Author's personal copy

Exp Fluids (2011) 51:123–136

129

Consequently, the vector fields tend to smooth out small-scale turbulent effects and large velocity gradients.

However, when the optical setup is properly focused and the glottal area well illuminated by the laser sheet, it is possible to exploit directly the raw camera double-frames, which provide more detailed information on the small-scale flow features, although not quantitative. When the two camera frames are played consecutively in image analysis software, the boundary between the fast moving particles within the glottal jet and almost immobile particles in the supraglottal area becomes clearly evident. Figure 7 shows the raw camera frame and the computed PIV velocity field. The still figure cannot display the motion of the particles used to locate the separation points, but provides a basic insight into what flow scales are lost in the PIV field. Using this technique, it is possible to discern the glottal jet contour and the position of the flow separation point with an accuracy on the order of 0.1 mm. Even when taking into account the possible error introduced by the partly subjective character of the method, the uncertainty of the position of the flow separation point is well below 0.5 mm (0.12 mm lifesize). In the rare cases where the glottal jet was not clearly recognizable, the position of the separation point was not recorded and the value was rejected.

Technically, the evaluation procedure of the flow separation point was as follows (performed using high-speed camera image analysis software Olympus i-SPEED 2):

- the images were calibrated using the known height of the channel
- for each phase of the vocal fold oscillation, the position of the “left” and “right” flow separation point and of the vocal fold apex was located manually,
- the coordinates of the four points were recorded by the software and the left and right flow separation coefficients were calculated automatically according to Eq. (3).

3 Results

3.1 Dynamic and acoustic measurements

Although it was not the primary objective of this study to measure the dynamic response of the structure to flow excitation and the sound signal, these results help understand the dynamic and acoustic properties of the system. The vibration of the vocal fold is shown in Fig. 8. The figure depicts nine phases of an oscillation cycle from measurement 012, a case of regular vocal fold vibration with a collision in each cycle. The third phase (top right) is in the maximum glottis opening. The eighth phase (bottom,

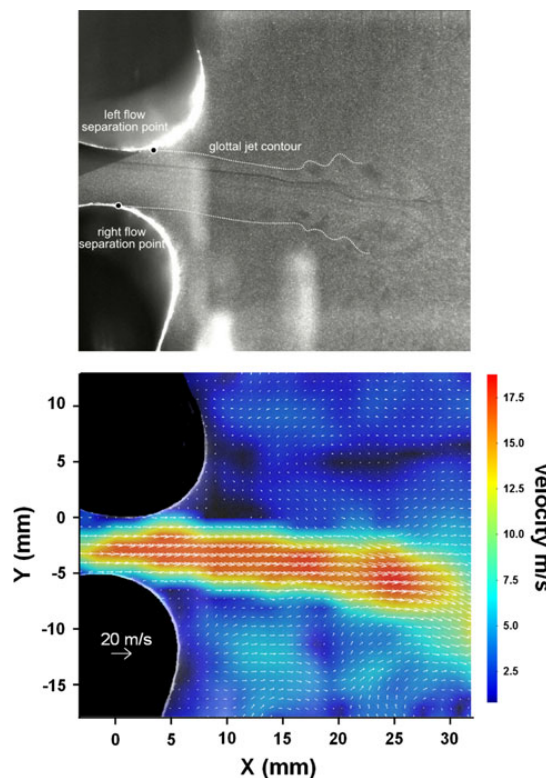


Fig. 7 Raw image recorded by the PIV camera (first frame of the double-frame) showing the positions of seeding particles (*top*). When played consecutively with the second frame, the glottal jet contours and the position where the jet separates from the vocal fold surface are clearly visible. Instantaneous vector velocity field computed by PIV (*bottom*). Measurement 012 ($Re = 5,400$), regular vocal fold vibration with a collision in each cycle. Frequency of vibration 13.2 Hz

in the middle) was taken in the middle of the of the contact period, where the vocal folds approached most. This phase also reveals the maximum deformation of the vocal folds.

Figures 9 and 10 show the waveforms and spectra of the vocal fold acceleration, subglottal pressure, supraglottal pressure, and radiated acoustic pressure. The mechanical vibration for the lower flow rate (Fig. 9) is nearly sinusoidal. The non-harmonic spectral frequency of 78.5 Hz, significant also in the spectrum of the subglottal pressure, corresponds probably to subglottal acoustic resonance. In the waveforms of the microphone signals, strong broadband noise is present, caused by turbulence in the supraglottal region.

The accelerometer waveform for $Re = 5,400$ (Fig. 10) clearly shows the vocal fold collisions, which are visible as peaks on the positive half-waves. The acoustic signals are well correlated with the vocal fold motion and have a

Author's personal copy

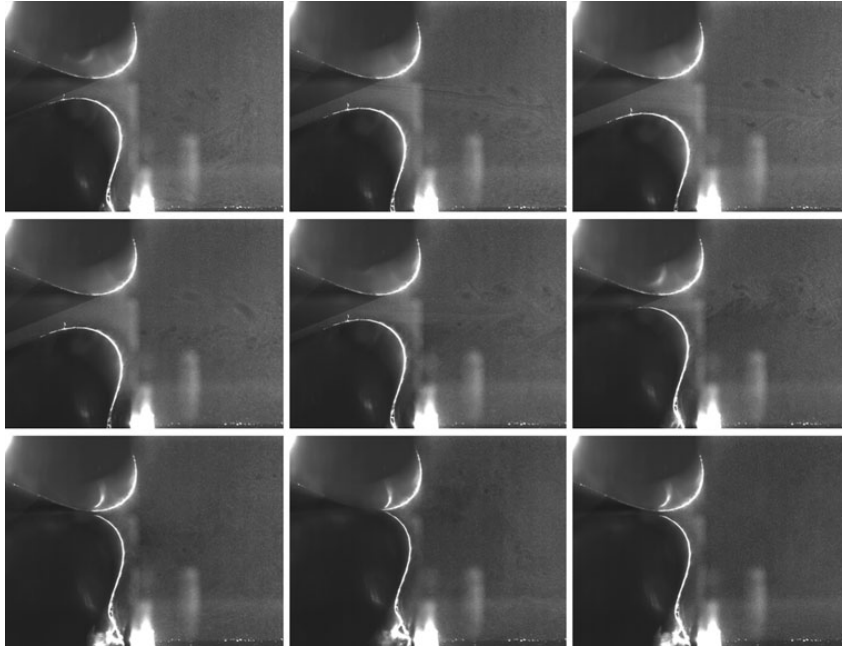


Fig. 8 Flow-induced vibration of the vocal fold—nine phases of an oscillation cycle. Measurement 012 ($Re = 5,400$), regular vocal fold vibration with a collision in each cycle. Frequency of vibration 13.2 Hz

periodic structure with harmonic frequencies in their spectra. The subglottal pressure appears to include less noise, but this is probably caused by the fact that unlike measuring microphones, the dynamic pressure transducer used was unable to capture high-frequency components. It is apparent that in the configuration used, the best signal to trigger the PIV system is the acceleration, which has best periodicity and signal-to-noise ratio.

3.2 Flow visualizations and PIV measurements

Figure 11 shows a typical velocity field downstream of the glottis evaluated by the PIV method. The vocal folds in the left part of the figure were masked out to show better their contours and to remove meaningless vectors. The vector plot reveals the glottal jet, which separates from the vocal fold surfaces and enters into the supraglottal domain. The jet is skewed to the right in this particular case. This tendency was observed throughout all the measurement sets, supporting the assumption that the Coanda effect is present in human phonation. In some of the measurements, the direction of the jet axis switched occasionally. However, the jet skewed preferentially to the right as in this case, probably due to slight asymmetry in the geometry of the left and right vocal folds, and possibly also due to the fact that the left (upper) vocal fold was fixed, while the right

(bottom) one vibrated. In the region between the right vocal fold surface and the jet, a large recirculation vortex can be seen.

The flow visualizations (accompanied by acoustic and dynamic measurements) were performed systematically for increasing flow rates. These ranged from the lowest possible airflow able to induce self-sustained vocal fold oscillations up to the highest values realistic in human phonation.

3.3 Position of the flow separation point

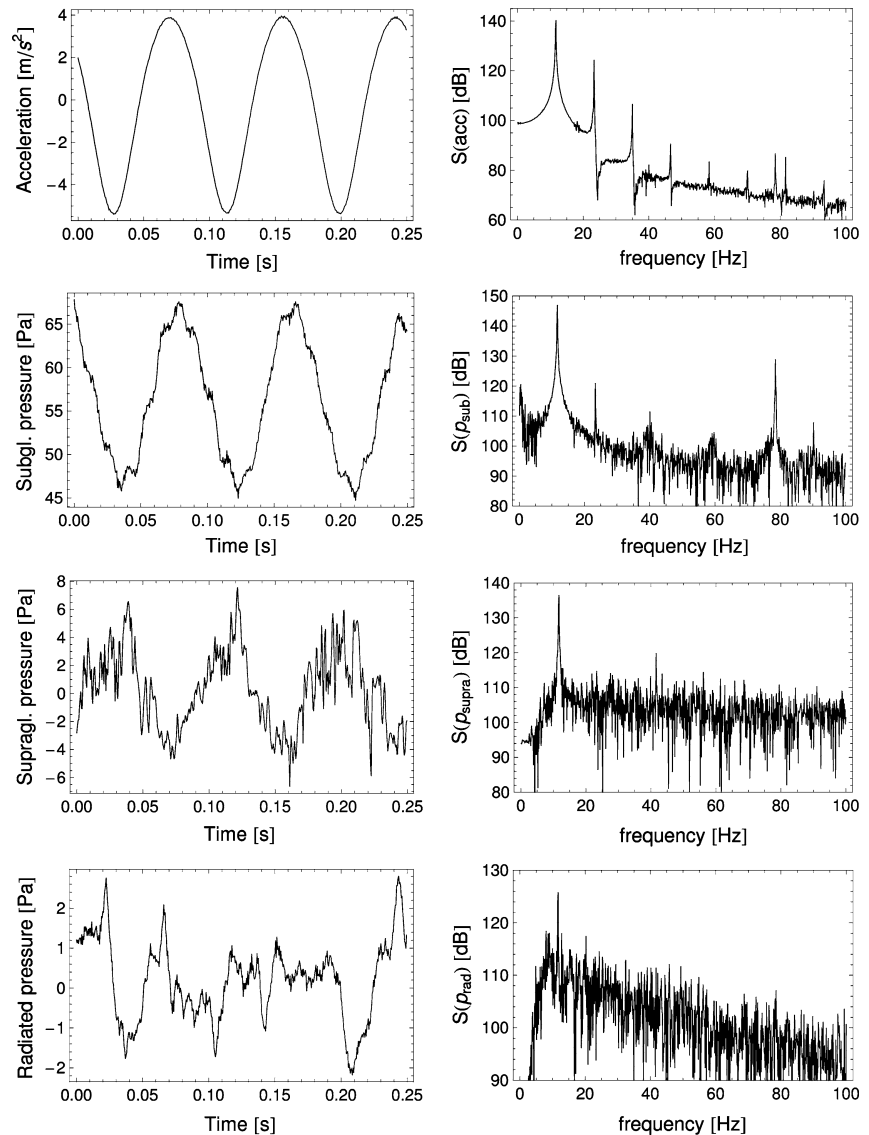
The essence of this work is quantification of the flow separation point locations during vocal fold vibration, as explained in Sect. 2.3. During phonation, the glottal velocity field is not perfectly periodic and the location of the flow separation point in a specific phase can vary over subsequent cycles of vibration. Due to the highly arduous procedure of evaluation of the separation point, it is impossible to provide proper statistical information. However, it is important to assess the fluctuation of the flow separation point position at least in one case. For this purpose, four measurements recorded at identical conditions (Reynolds number $Re = 5,400$, vocal fold vibrations with collisions) were analyzed. In order to superimpose the results of these measurements, where the frequency of

Author's personal copy

Exp Fluids (2011) 51:123–136

131

Fig. 9 Waveforms (*left*) and frequency spectra (*right*) of the acceleration, subglottal pressure, supraglottal pressure and pressure radiated at the channel exit. Measurement 002 ($Re = 3,500$), vocal fold vibration without a collisions. Frequency of vibration 11.7 Hz



vibration varied slightly (<0.1 Hz) and the double-frames were not taken in exactly identical phases, it was necessary to extract in each case precisely one period, align the four measurements, interpolate and resample the data.

The results in Fig. 12 show that during most of the vibration cycle, the flow separation coefficients have low variation. Near glottal closure, the data are much more scattered. This is caused by the fact that when the vocal folds collide and the jet is interrupted, the flow is highly nonstationary and the decaying or evolving jet is more susceptible to interactions with turbulent structures. In certain measurements, it was even observed that the jet

changes direction over subsequent cycles and attaches to the left or right vocal fold in a random way.

In the following, the results of flow separation point measurements for three flow rates are presented. Figure 13 summarizes the results for $Re = 3,500$, flow rate $Q = 5.5$ L/s, transglottal pressure difference $\Delta p = 45$ Pa, frequency of vibration $f = 10.9$ Hz (corresponding to $Q = 1.4$ L/s, $\Delta p = 720$ Pa and $f = 173$ Hz lifesize). As can be seen from the orifice width plot in the right, in this case, the vocal folds did not collide throughout the oscillation cycle. Such vocal fold vibration can be observed in certain types of breathy phonation.

Author's personal copy

Fig. 10 Waveforms (*left*) and frequency spectra (*right*) of the acceleration, subglottal pressure, supraglottal pressure and pressure radiated at the channel exit. Measurement 012 ($Re = 5,400$), regular vocal fold vibration with a collision in each cycle. Frequency of vibration 13.2 Hz

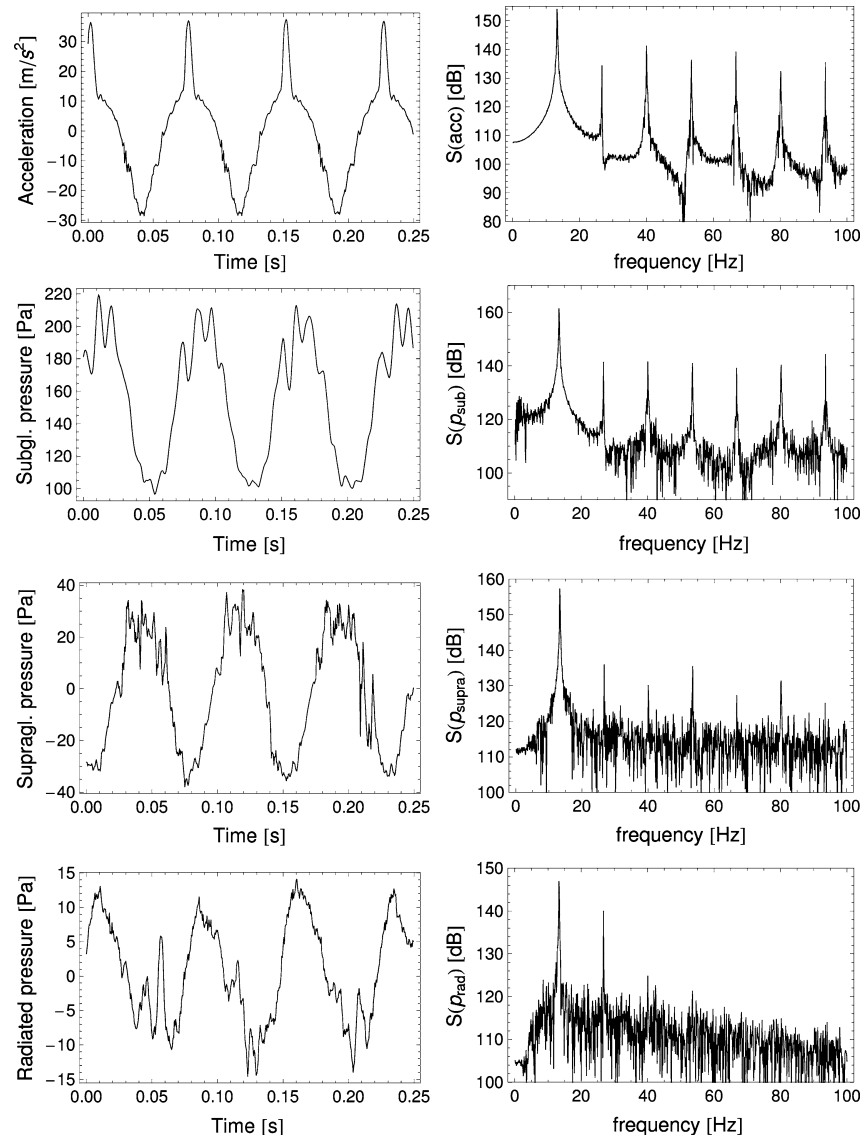


Figure 13 also shows the development of the left and right flow separation coefficients during 40 phases of the vocal fold oscillation cycle. The opening and closing phases are separated by dashed lines. The vocal folds approximate the most between frames #5–7, where the opening phase begins (see the orifice width plot in Fig. 13). In a large part of the oscillation period, both left and right flow separation coefficients stay between 1.0 and 1.5. Near glottal closure and reopening, however, the FSC_R sharply increases up to about 5.5. This is a quantification of an effect, which can be seen almost universally in all measurements—when the glottal gap gets very narrow, the jet

weakens and tends to attach to one of the vocal fold surfaces (in this case, the right one). Since the airflow separates very far from the narrowest cross-section, the separation coefficients reach much higher values than usually assumed.

The effect is even more prominent in cases where the vocal folds collide and the glottal gap closes. Figure 14 shows the flow separation coefficients and orifice width for $Re = 5,400$, $Q = 8.58$ L/s, $\Delta p = 150$ Pa and $f = 13.4$ Hz (which correspond to $Q = 2.1$ L/s, $\Delta p = 2,400$ Pa and $f = 214$ Hz lifesize). Again, when the glottis is wide open, the flow separation coefficient is close to 1.1, increases to

Author's personal copy

Exp Fluids (2011) 51:123–136

133

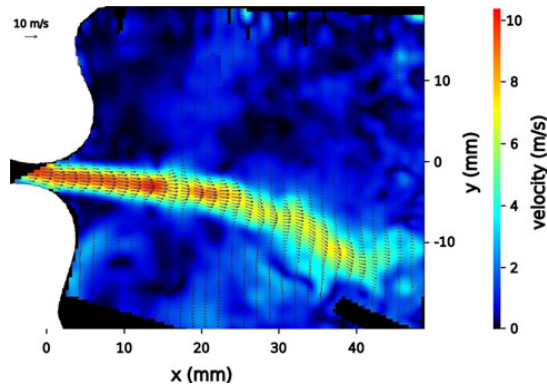


Fig. 11 Typical instantaneous flow velocity field downstream of the glottis. Measurement 002d ($Re = 3,500$, without glottal closure), middle of the closing phase

about 1.5 in the middle of the opening/closing phases, and sharply rises up to 20 near vocal fold contact. The jet was attached mostly to the right vocal fold, but the left separation coefficient near the glottis opening increased up to values around 5, as in previous cases. Figure 15 proves that the increase in the FSC near glottal closure is not caused by the fact, that the glottal gap d (denominator in equation 3) is small: the distance of the flow separation point from the vocal fold apex itself increases, too. This shows that the airflow separates further downstream, than when the glottis is wide open.

For the case shown in Fig. 16 ($Re = 6,600$, $Q = 10.4\text{L/s}$, $\Delta p = 230\text{Pa}$, $f = 13.8\text{Hz}$, corresponding to $Q = 2.6\text{L/s}$, $\Delta p = 3,600\text{Pa}$ and $f = 220\text{Hz}$ lifesize), FSC_R has a plateau at 1.12 and shortly before glottal closure sharply rises up to 20. The FSC_L data are more scattered, but show similar behavior.

The physical model vibrated well for a broad range of higher airflow velocities, also. The quantified data on flow separation showed very similar behavior even for these high velocities. Nevertheless, since these flow rates are beyond the physiologically relevant limits, the results are not shown here.

4 Discussion and conclusions

The main objective of this paper was to provide experimental quantitative data on glottal aerodynamics and namely on the position of the flow separation point during phonation. A physical, four times scaled vocal fold model was designed to perform the measurements. The geometry of the vocal folds was based on measurement of excised human larynges in phonation position and is slightly different from the “M5” approximation commonly used in modeling studies.

The authors believe that in order to get representative experimental data on the aerodynamics of human phonation using physical models, it is desirable that the model be self-oscillating, rather than externally driven. However, the requirement of a self-excited system brings numerous complications and technical limitations. First of all, the physical model does not provide enough free parameters (e.g., the subglottal velocity U_0) to be set independently, and thus, it cannot be ensured that the dynamic similarity of the model and the real larynx is perfect. In current measurements, nevertheless, the pertinent Reynolds and Strouhal numbers lie within the bounds encountered in human phonation.

From the same reason, the flow-induced vibration of the vocal fold model is not precisely identical with that found in the real larynx. The convergent–divergent shaping of the glottis is not mimicked by the model to the extent that can be reached in externally driven models: the current model vibrates dominantly in the 10 mode and it mostly resembles the “convergent” M5 geometry. Therefore, the results are relevant e.g., for glottal opening or for situations close to breathy voice, where the subglottal pressure is not high, prephonatory glottal diameter nonzero and where there is strong reason to believe that the glottal shape changes from divergent to convergent shortly before closing. However, considering that the shape of the medial surface of the real vocal folds during vibrations can be more complex (not strictly straight convergent or straight divergent as in the M5 model), the authors assume that the results on flow

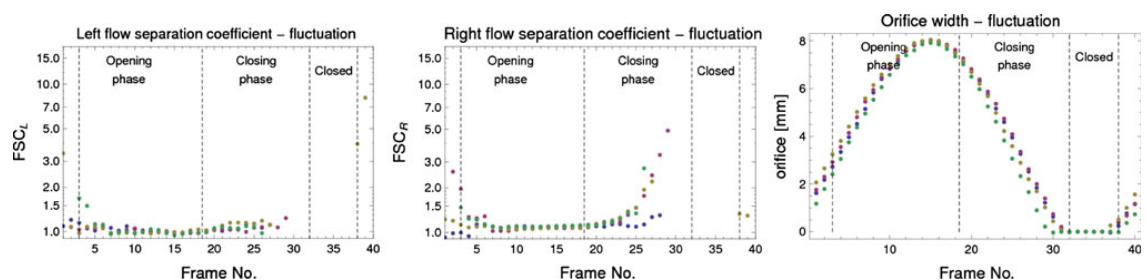


Fig. 12 Fluctuation of the left and right flow separation coefficients and of the orifice width. Measurements 012s-w ($Re = 5,400$, with glottal closure). Dashed lines delimit the boundaries of vocal fold vibration phases (opening phase, closing and closed phase)

Author's personal copy

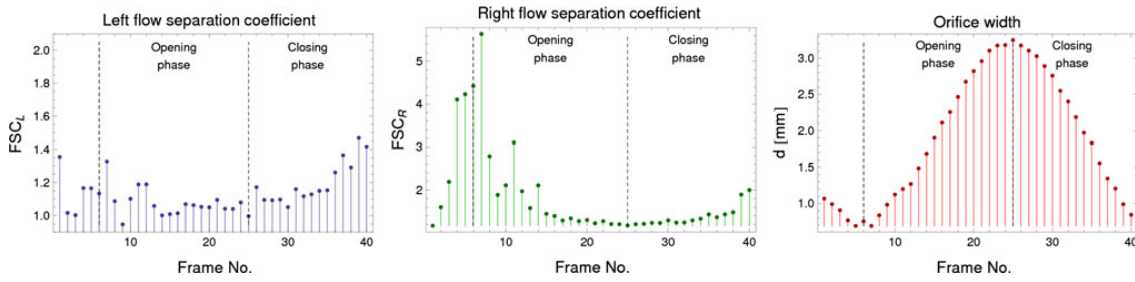


Fig. 13 Measurement 002c ($Re = 3,500$, without glottal closure), one oscillation cycle. *Left* and *right* flow separation coefficient, orifice width

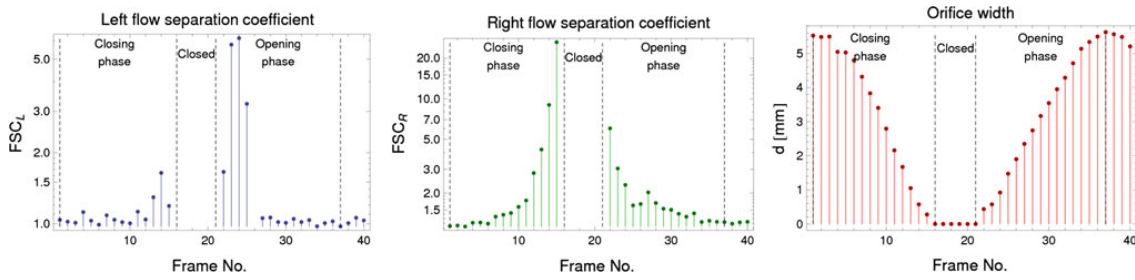


Fig. 14 Measurement 012v ($Re = 5,400$, with glottal closure), one oscillation cycle. *Left* and *right* flow separation coefficient, orifice width

Fig. 15 Measurement 012v ($Re = 5,400$, with glottal closure), one oscillation cycle. Distance of the *left* and *right* flow separation point from the vocal fold apex

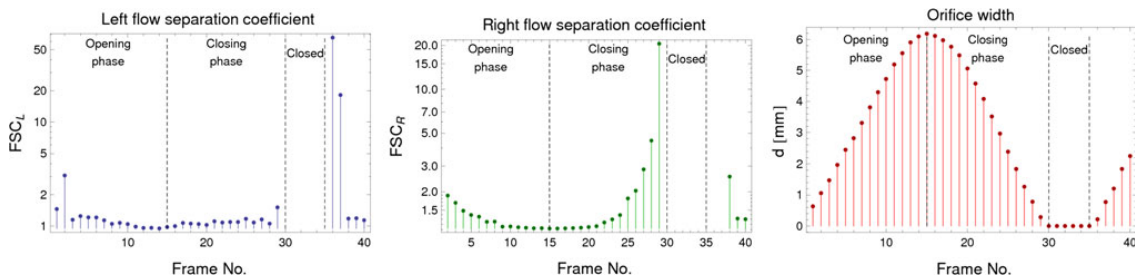
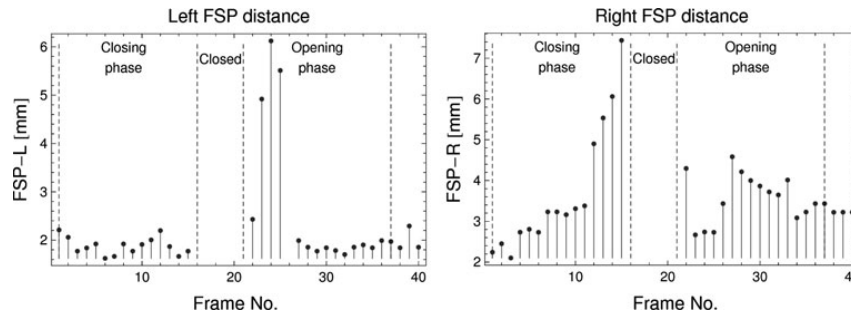


Fig. 16 Measurement 017c ($Re = 6,600$, with glottal closure), one oscillation cycle. *Left* and *right* flow separation coefficient, orifice width

Author's personal copy

Exp Fluids (2011) 51:123–136

135

separation locations measured using the model with a curved shape can have certain relevance to the other cases of phonation, too.

It should be also noted that the flow rates in the model are rather high relative to values known from human phonation and the duration of the phase when the vocal folds are closed (which is usually quantified by the *closed quotient*, CQ) lies in the lower bound of values encountered during loud speech. Nevertheless, the experience from other self-oscillating physical models (Pelorson et al. 1994; Thomson et al. 2005; Becker et al. 2009) shows that it is difficult to design a system behaving identically to the real vocal larynx, and even using approximate physical models, important and relevant results can be obtained.

The physical model was equipped with accelerometers monitoring vocal fold vibration. To measure the dynamic pressures and acoustic signals in the sub- and supraglottal spaces, pressure transducers and microphones were mounted in the setup. A PIV system synchronized with the vocal fold vibration was used to visualize the supraglottal airflow and to evaluate the position of the flow separation points along the vocal fold surfaces during their vibration. The airflow in the glottis can be to first approximation considered as two-dimensional: one may assume that the flow velocity does not change significantly along the length of the vocal folds (i.e., along the anterior–posterior axis z , see Fig. 2) in the very proximity of the glottis. This is not true further downstream, where turbulent structures dominate the flow field. The vorticity, aligned originally along the z -axis, interacts with the velocity field and creates inevitably a 3D velocity field. But when focused on the flow separation from the vocal fold surface, it is possible to draw meaningful data from PIV measurements in the coronal (x – y) plane.

In simplified glottal flow models based on Bernoulli or Euler equations where flow separation is taken into account, the position of the flow separation point is commonly considered as constant with respect to the narrowest cross-section. This implicitly assumes that the airflow is symmetric and separates at the same location from the left and right vocal fold. In current work, a modified criterion for flow separation (left and right flow separation coefficient—FSC), generalizing the classical criterion, was proposed. The results suggest that the usage of the classical flow separation criterion with constant values ranging between 1.1 and 1.5 is quite plausible, at least for the part of the oscillation cycle where the vocal folds are not too close together. Shortly before and after glottis closure, however, the aerodynamic effects are apparently much more complex and the criterion does not hold any more. The measured values of FSC demonstrate a general trend: shortly prior to and after glottal closure, either of the coefficients sharply increases, i.e., the glottal jet separates

much further downstream of the narrowest cross-section. This is consistent with the qualitative results of Neubauer et al. (2007), who observed that during glottis opening, the jet is attached to the VF wall and strongly curved.

In a perfectly symmetrical glottal channel, the supra-glottal flow field is bistable: the glottal jet does not remain symmetric, but tends to attach to either side of the channel. In the experiments, one of the directions was always preferential, although not exclusively. It seems that this was caused by minor asymmetries of the geometry, rather than by the fact that one of the model vocal folds was static. The same behavior was observed in the study of Erath and Plesniak (2010), who showed that even minor geometric irregularities cause the jet to skew to one of the directions with a high probability.

The physiological analogy to the current experimental setup would be unilateral vocal fold paralysis. The fact that one of the vocal folds in the model does not vibrate limits to certain extent the applicability of the results to real phonation. The current study is focused primarily on glottal aerodynamics and specifically dynamics of the glottal jet, which should not be largely different from the situation in the real larynx. Moreover, there have been even more dissimilar arrangements successfully used in experimental studies with synthetic and excised larynges, e.g., the hemilarynx configuration (one vocal fold colliding against symmetry plane). As long as a physical model representing all the important qualities of the real human larynx at once is not available, it is worth using approximate models that inevitably differ from reality in certain aspects.

The techniques used in this study for determining the location of flow separation were relatively laborious and time-consuming and required perfect adjustment of the experimental setup, in particular clean and well-focused optics. As some of the measurements did not provide sufficient contrast and resolution, only three measurements were evaluated. Even though these do not represent a comprehensive statistical data set, the authors believe that the results provide important new quantitative information, which cannot be found in the current literature.

In subsequent studies, several construction details and measurement techniques could be further improved. The state-of-the-art of the current PIV laser and camera systems, for instance, would allow a time-resolved measurement.

The current experimental setup does not contain a model of ventricular folds. It can be speculated what the influence of the ventricular folds on the position of the flow separation point is: depending on their distance from the vocal folds, they might both straighten the glottal flow axially or make it skew laterally even more. The authors believe it is a good starting point to obtain experimental data not biased by the presence of the ventricular folds. However, in the

Author's personal copy

future, it would be appropriate to perform a parametric study with various ventricular fold shapes and locations and determine their effect on supraglottal aerodynamics. With these modifications, the experimental setup could provide even more systematic and precise data on airflow separation and help to enlighten some of the fundamental aspects of human phonation.

Acknowledgments The research has been financially supported by the Grant Agency of the Academy of Sciences of the Czech Republic, project KJB200760801 *Mathematical modeling and experimental investigation of fluid–structure interaction in human vocal folds*, research plan AV0Z20760514. The support of ENSTA ParisTech, who provided the experimental background, is also gratefully acknowledged.

References

- Alipour F, Scherer RC (2004) Flow separation in a computational oscillating vocal fold model. *J Acoust Soc Am* 116(3):1710–1719
- Alipour F, Scherer RC (2006) Characterizing glottal jet turbulence. *J Acoust Soc Am* 119(2):1063–1073
- Alipour F, Fan C, Scherer RC (1996) A numerical simulation of laryngeal flow in a forced-oscillation glottal model. *Comput Speech Lang* 10:75–93
- Barney A, Shadle C, Davies P (1999) Fluid flow in a dynamic mechanical model of the vocal folds and tract. i. measurements and theory. *J Acoust Soc Am* 105(1):444–455
- Becker S, Kniesburges S, Müller S, Delgado A, Link G, Kaltenbacher M, Döllinger M (2009) Flow-structure-acoustic interaction in a human voice model. *J Acoust Soc Am* 125(3):1351–1361
- Cisonni J, Hirtum AV, Pelorson X, Willems J (2008) Theoretical simulation and experimental validation of inverse quasi-one-dimensional steady and unsteady glottal flow models. *J Acoust Soc Am* 124(1):535–545
- Decker G, Thomson S (2007) Computational simulations of vocal fold vibration: Bernoulli versus Navier-Stokes. *J Voice* 21(3):273–284
- Deverge M, Pelorson X, Vilain C, Lagrée P, Chentouf F, Willems J, Hirschberg A (2003) Influence of collision on the flow through in-vitro rigid models of the vocal folds. *J Acoust Soc Am* 114(6 Pt 1):3354–3362
- Erath B, Plesniak M (2006) The occurrence of the Coanda effect in pulsatile flow through static models of the human vocal folds. *Exp Fluids* 41:735–748
- Erath B, Plesniak M (2006) The occurrence of the Coanda effect in pulsatile flow through static models of the human vocal folds. *J Acoust Soc Am* 120(2):1000–1011
- Erath B, Plesniak M (2010) An investigation of asymmetric flow features in a scaled-up driven model of the human vocal folds. *Exp Fluids*. doi:10.1007/s00348-009-0809-0
- Fox R, Kline S (1962) Flow regime data and design methods for curved subsonic diffusers. *Trans ASME J Basic Eng* 84:303–312
- Hirtum AV, Pelorson X, Lagrée P (2005) In vitro validation of some flow assumptions for the prediction of the pressure distribution during obstructive sleep apnoea. *Med Biol Eng Comput* 43:162–171
- Hofmans G, Groot G, Ranucci M, Graziani G, Hirschberg A (2003) Unsteady flow through in-vitro models of the glottis. *J Acoust Soc Am* 113(3):1658–1675
- Horáček J, Šidlof P, Švec JG (2005) Numerical simulation of self-oscillations of human vocal folds with Hertz model of impact forces. *J Fluids Struct* 20(6):853–869
- Krane M, Wei T (2006) Theoretical assessment of unsteady aerodynamic effects in phonation. *J Acoust Soc Am* 120(3):1578–1588
- Krane M, Barry M, Wei T (2007) Unsteady behavior of flow in a scaled-up vocal folds model. *J Acoust Soc Am* 122(6):3659–3670
- Kucinschi B, Scherer R, Dewitt K, Ng T (2006) An experimental analysis of the pressures and flows within a driven mechanical model of phonation. *J Acoust Soc Am* 119(5 Pt 1):3011–3021
- Li S, Scherer R, Wan M, Wang S, Wu H (2006) The effect of glottal angle on intraglottal pressure. *J Acoust Soc Am* 119(1):539–548
- Lucero J (1998) Optimal glottal configuration for ease of phonation. *J Voice* 12(2):151–158
- Neubauer J, Zhang Z, Miraghaie R, Berry D (2007) Coherent structures of the near field flow in a self-oscillating physical model of the vocal folds. *J Acoust Soc Am* 121(2):1102–1118
- Pelorson X, Hirschberg A, van Hassel R, Wijnands A, Auregan Y (1994) Theoretical and experimental study of quasisteady-flow separation within the glottis during phonation. Application to a modified two-mass model. *J Acoust Soc Am* 96(6):3416–3431
- Scherer R, Shinwari D, Witt KD, Zhang C, Kucinschi B, Afjeh A (2001) Intraglottal pressure profiles for a symmetric and oblique glottis with a divergence angle of 10 degrees. *J Acoust Soc Am* 109(4):1616–1630
- Scherer RC, Shinwari D, Witt KJD, Zhang C, Kucinschi BR, Afjeh AA (2002) Intraglottal pressure distributions for a symmetric and oblique glottis with a uniform duct. *J Acoust Soc Am* 112(4):1253–1256
- Sciamarella D, Quére PL (2008) Solving for unsteady airflow in a glottal model with immersed moving boundaries. *Eur J Mech B Fluids* 27:42–53
- Shinwari D, Scherer R, Dewitt K, Afjeh A (2003) Flow visualization and pressure distributions in a model of the glottis with a symmetric and oblique divergent angle of 10 degrees. *J Acoust Soc Am* 113(1):487–497
- Šidlof P, Švec JG, Horáček J, Veselý J, Klepáček I, Havlík R (2008) Geometry of human vocal folds and glottal channel for mathematical and biomechanical modeling of voice production. *J Biomech* 41(5):985–995
- Story B, Titze I (1995) Voice simulation with a body-cover model of the vocal folds. *J Acoust Soc Am* 97(2):1249–1260
- Suh J, Frankel S (2007) Numerical simulation of turbulence transition and sound radiation for flow through a rigid glottal model. *J Acoust Soc Am* 121(6):3728–3739
- Tao C, Zhang Y, Hottinger D, Jiang J (2007) Asymmetric airflow and vibration induced by the Coanda effect in a symmetric model of the vocal folds. *J Acoust Soc Am* 122(4):2270–2278
- Thomson S, Mongeau L, Frankel S (2005) Aerodynamic transfer of energy to the vocal folds. *J Acoust Soc Am* 118(3 Pt 1):1689–1700
- Triep M, Brücker C (2010) Three-dimensional nature of the glottal jet. *J Acoust Soc Am* 127(3):1537–1547. doi:10.1121/1.3299202
- Triep M, Brücker C, Schröder W (2005) High-speed PIV measurements of the flow downstream of a dynamic mechanical model of the human vocal folds. *Exp Fluids* 39:232–245
- Vilain C, Pelorson X, Fraysse C, Deverge M, Hirschberg A, Willems J (2004) Experimental validation of a quasi-steady theory for the flow through the glottis. *J Sound Vib* 276:475–490
- Zanartu M, Mongeau L, Wodicka G (2007) Influence of acoustic loading on an effective single mass model of the vocal folds. *J Acoust Soc Am* 121(2):1119–1129
- Zhang Z (2008) Influence of flow separation location on phonation onset. *J Acoust Soc Am* 124(3):1689–1694. doi:10.1121/1.2957938
- Zhang Z, Neubauer J, Berry D (2007) Physical mechanisms of phonation onset: a linear stability analysis of an aeroelastic continuum model of phonation. *J Acoust Soc Am* 122(4):2279–2295

Chapter 5

Application: Flutter instability of airfoils with two degrees of freedom

5.1 Introduction

A second application of fluid dynamics on moving geometries, where the author has been active in recent years, is the external aviation aerodynamics, namely investigation of the flutter instability of airfoils. Flutter is a dynamic instability of an elastic structure coupled to airflow, caused by the interaction between elastic, inertial and aerodynamic forces. In simple words, flutter may occur at certain flow velocities and structural natural vibration frequencies, when the energy is transferred from the airflow to the structure and the internal damping is not able to absorb it. This can lead to vibration of an aircraft component with exponentially increasing amplitudes and catastrophic consequences. Thus, the aircraft components (wings, flaps and ailerions, stabilators, elevons and rudders) must be designed and tested not only to sustain dynamic loads induced by mechanical accelerations and air turbulence during take-off, cruise and landing, but also to ensure that within design flight conditions, the aircraft components may never encounter dynamic flow-induced instability.

There are more types of aeroelastic instabilities – e. g. coupled-mode flutter, panel flutter, stall flutter, buffeting or galloping. In general, flutter instability is a complex nonlinear phenomenon which is not yet fully understood in all the aspects. In current days, the flight flutter testing is performed at a number of discrete test points arranged in increasing order of dynamic pressure and airflow velocity. The number of these test points required to clear the flutter envelope of an airplane is quite high - for example about 500 for the F-14 fighter plane, or 260 for the Gulfstream II civil airplane (Kehoe, 1995). In between the test points, the data is interpolated, which might be questionable considering the high nonlinearity of the flutter phenomena. In exceptionally rough weather conditions or in some cases of gross human error during aircraft service, the airplane may still encounter the instable regime during flight. This is why the aircraft disasters caused by flutter-induced structural disintegration are not limited to the early days of aviation (e. g. the Cody Float-plane Verona airliner crash in 1919, Lockheed L-188 Electra flight 542 crash in 1959, or Northwest Orient Airlines Flight 710 disaster in 1960, all of them killing everyone aboard), but also to recent history. A notable example is the 1997 Maryland airshow accident, where a F117 stealth jet fighter crashed before the eyes of the spectators after a part of its left wing broke off the fuselage due to elevon-wing flutter caused by missing fasteners.

The research of the author concentrates on the classical and stall flutter of airfoils with two degrees of freedom. In order to understand the classical flutter, it is useful to derive the linearized analytical equations describing the coupled-mode flutter instability. This is done in the following section.

5.2 Classical theory of airfoil aeroelastic instability

The fundamental principles of the static (divergence-type) and dynamic (flutter-type) instability of aeroelastic systems can be shown on an example of a 2D airfoil supported by a linear spring with stiffness k_y and a torsional spring with torsional stiffness k_α (see Fig.5.1). The airfoil has two degrees of freedom (DOF) - vertical shift (plunge) with a coordinate y , and rotation (pitch) about the elastic axis EA, measured by the angle of attack α , and is subject to airflow with freestream velocity U . The horizontal motion of the airfoil is blocked. This 2DOF kinematic model is a commonly used approximation of a real 3D aircraft wing or stabilator, with the pitch and plunge DOF representing the torsion and bending of the lifting surface, respectively.

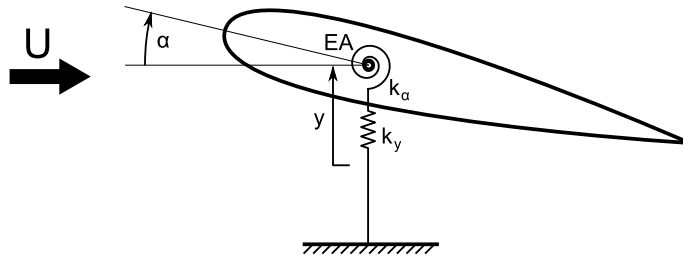


Figure 5.1: Approximation of an airfoil by a model with two degrees of freedom. The elastic axis (EA) is constrained to move only vertically.

When interested in the onset of the flutter-type instability, one might restrain the analysis to small angles, $\alpha \ll 1$. Then, the equations of motion of the system take a simple form

$$\begin{aligned} m \ddot{y} + S_\alpha \ddot{\alpha} + k_y y &= L_y \\ S_\alpha \ddot{y} + I_\alpha \ddot{\alpha} + k_\alpha \alpha &= M, \end{aligned} \quad (5.1)$$

where m , S_α and I_α is the mass, static moment and moment of inertia of the airfoil with respect to the elastic axis. L_y is the vertical component of the total aerodynamic force and M the moment of the aerodynamic forces with respect to the elastic axis. The calculation of the latter two depends on the aerodynamic theory used. In full generality, they are given by the integration of the stress tensor \mathbb{T} or stress vector $\boldsymbol{\tau} = \mathbb{T} \cdot \mathbf{n}$ over the surface of the airfoil Γ

$$\begin{aligned}
L_y &= \int_{\Gamma} \tau_2 dS = \int_{\Gamma} \sum_{j=1}^2 \mathbb{T}_{2j} n_j dS, \\
M &= \int_{\Gamma} \sum_{j,k=1}^2 \varepsilon_{3jk} \tau_j x_k dS = \int_{\Gamma} \sum_{j,k,l=1}^2 \varepsilon_{3jk} \mathbb{T}_{jl} n_l x_k dS = \\
&= \int_{\Gamma} \sum_{l=1}^2 \left(\mathbb{T}_{1l} n_l x_2 - \mathbb{T}_{2l} n_l x_1 \right) dS, \tag{5.2}
\end{aligned}$$

with \mathbf{n} the unit outer normal vector to the airfoil surface and ε_{ijk} the Levi-Civita symbol. The stress tensor \mathbb{T} is a function of the unsteady pressure and velocity fields $p(t, x)$ and $\mathbf{u}(t, x)$ according to the constitutive relation for the Newtonian fluids

$$\mathbb{T}_{ij} = -p \delta_{ij} + \mu \left(\frac{\partial u_i}{\partial x_j} + \frac{\partial u_j}{\partial x_i} \right), \tag{5.3}$$

where δ_{ij} stands for the Kronecker delta, and μ the dynamic fluid viscosity. Equations (5.2, 5.3) can be used in a full numerical simulation of the Navier-Stokes equations in 2D or 3D, which, however, does not give an analytical expression for the critical flow velocity, and which can be highly computationally expensive. For the purpose of the flutter onset prediction, a linearized aerodynamic force and moment approximation

$$\begin{aligned}
L_y &= C_L q S \\
M &= L_y e + C_{MAC} q S c \tag{5.4}
\end{aligned}$$

might be used (Dowel, 1978). Here $C_L = C_{L_0} + \frac{\partial C_L}{\partial \alpha} \alpha$ is the Taylor expansion of the coefficient for small angles α , $q = \rho U^2 / 2$ is the dynamic pressure, ρ the air density, e is the distance of the elastic axis from the aerodynamic axis (point on the airfoil, with respect to which the aerodynamic forces have zero moment), and c and S the airfoil chord and surface, respectively. C_{L_0} , C_{MAC} and $\frac{\partial C_L}{\partial \alpha}$ are dimensionless constants dependent on the airfoil shape and character of the airflow (subsonic or supersonic). For symmetric airfoils in incompressible airflow, $C_{L_0} = C_{MAC} = 0$. Equation (5.1) then reads

$$\begin{aligned}
m \ddot{y} + S_\alpha \ddot{\alpha} + k_y y - q S \frac{\partial C_L}{\partial \alpha} \alpha &= 0 \\
S_\alpha \ddot{y} + I_\alpha \ddot{\alpha} + k_\alpha \alpha - q S e \frac{\partial C_L}{\partial \alpha} \alpha &= 0, \tag{5.5}
\end{aligned}$$

which is a second-order system of ordinary differential equations for the generalized coordinates y and α . Unlike equations (5.1) with a general form of aerodynamic forces, equations (5.5) are now linear. For the stability analysis we will assume a solution

$$\mathbf{V}(t) = \mathbf{V}_0 e^{\omega t}, \quad \mathbf{V}(t) = \begin{pmatrix} y(t) \\ \alpha(t) \end{pmatrix}, \quad \mathbf{V}_0 = \begin{pmatrix} y_0 \\ \alpha_0 \end{pmatrix} \quad (5.6)$$

and analyze the real and imaginary parts of the complex frequency ω . Substituting (5.6) into (5.5) and rearranging into matrix form yields

$$\begin{pmatrix} m\omega^2 + k_y & S_\alpha \omega^2 - qS \frac{\partial C_L}{\partial \alpha} \\ S_\alpha \omega^2 & I_\alpha \omega^2 + k_\alpha - qS e \frac{\partial C_L}{\partial \alpha} \end{pmatrix} \begin{pmatrix} y_0 \\ \alpha_0 \end{pmatrix} e^{\omega t} = \mathbf{0}. \quad (5.7)$$

For the existence of nontrivial solution of (5.7) it is necessary that the determinant of the matrix is zero. Introducing notation

$$A \equiv mI_\alpha - S_\alpha^2 \quad (5.8)$$

$$B \equiv m \left(k_\alpha - qS e \frac{\partial C_L}{\partial \alpha} \right) + k_y I_\alpha + S_\alpha qS \frac{\partial C_L}{\partial \alpha} \quad (5.9)$$

$$C \equiv k_y \left(k_\alpha - qS e \frac{\partial C_L}{\partial \alpha} \right) \quad (5.10)$$

one can write the equation for the determinant

$$A\omega^4 + B\omega^2 + C = 0. \quad (5.11)$$

Solving (5.11) yields

$$\omega^2 = \frac{-B \pm \sqrt{B^2 - 4AC}}{2A} \quad (5.12)$$

where the signs of the coefficients A, B, C determine the character of the solution. A is positive for any mass distribution in the airfoil. It can be shown (Dowel, 1978) that C is also positive for all the relevant conditions. The coefficient B can be both positive and negative. Then we can consider two cases:

1. $B > 0$

If $B^2 - 4AC > 0$, ω^2 is real and negative and thus ω is pure imaginary, which corresponds to stable oscillations. When $B^2 - 4AC < 0$, however, ω^2 is complex and at least one root ω will

have a positive real part. The oscillation of the airfoil is an exponentially growing harmonic function. This type of instability is called **flutter**. The condition

$$B^2 - 4AC = 0 \quad (5.13)$$

thus represents the boundary between the stable and unstable oscillations and can be used to calculate the explicit value of the critical dynamic pressure q_F and velocity U_F for the onset of the flutter-type instability.

2. $B < 0$

For $q = 0$ (zero flow velocity $U = 0$) the coefficient B is positive. It turns negative only for sufficiently big values of q . However, since $A > 0, C > 0$, the condition (5.13) would be satisfied prior to this, and so these cases do not have to be considered.

It should be noted that the results presented above are relevant only for the largely simplified approximation of the aerodynamic forces (5.4), which is approximately valid for a flat plate or slender symmetric airfoil under potential airflow and low angles of attack. The aerodynamic force and moment are functions of the angle of attack α only, do not account for viscosity, turbulence, flow separation or history effects.

There is a number of aerodynamic theories of various complexity, which can be used for better approximation of the aerodynamic forces. One possibility is to use the quasi-1D Euler equations for the flow. For the purpose of stability boundary evaluation (assuming small angles of attack $\alpha \ll 1$ and deflections $y \ll 1$ and the same form of solution (5.6) as previously), equations (5.1) can be rewritten in matrix form with the right-hand side formulated in terms of added aerodynamic mass, stiffness and damping matrices \mathbb{M}_2 , \mathbb{K}_2 and \mathbb{B}_2 (see e. g. [Horáček et al. \(1997\)](#)):

$$\mathbb{M} \ddot{\mathbf{V}} + \mathbb{K} \mathbf{V} = \rho (\mathbb{M}_2 \dot{\mathbf{V}} + \mathbb{B}_2 \dot{\mathbf{V}} + \mathbb{K}_2 \mathbf{V}) \quad (5.14)$$

\mathbb{M} and \mathbb{K} are the structural mass and stiffness matrices formed from coefficients in equation (5.1). Rearranging (5.14) into the space of 4×4 matrices yields

$$\begin{pmatrix} \mathbb{I} & \mathbb{O} \\ \mathbb{O} & \mathbb{M} - \rho \mathbb{M}_2 \end{pmatrix} \begin{pmatrix} \dot{\mathbf{V}} \\ \ddot{\mathbf{V}} \end{pmatrix} = \begin{pmatrix} \mathbb{O} & \mathbb{I} \\ \mathbb{K} - \rho \mathbb{K}_2 & -\rho \mathbb{B}_2 \end{pmatrix} \begin{pmatrix} \mathbf{V} \\ \dot{\mathbf{V}} \end{pmatrix}, \quad (5.15)$$

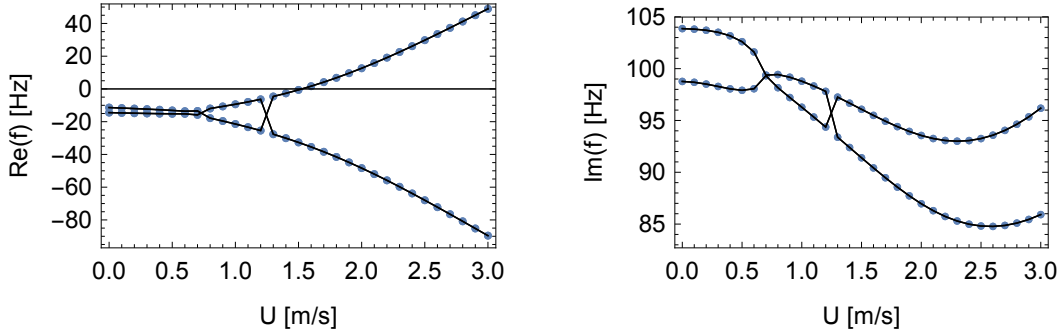
where \mathbb{I} and \mathbb{O} are identity and zero matrices, respectively. By left-multiplying (5.15) by the inverse matrix $(\mathbb{M} - \rho \mathbb{M}_2)^{-1}$ we get

$$\begin{pmatrix} \dot{\mathbf{V}} \\ \ddot{\mathbf{V}} \end{pmatrix} = \mathbb{A} \begin{pmatrix} \mathbf{V} \\ \dot{\mathbf{V}} \end{pmatrix}, \quad \mathbb{A} = \begin{pmatrix} \mathbb{O} & \mathbb{I} \\ (\mathbb{M} - \rho \mathbb{M}_2)^{-1} (\mathbb{K} - \rho \mathbb{K}_2) & -\rho (\mathbb{M} - \rho \mathbb{M}_2)^{-1} \mathbb{B}_2 \end{pmatrix} \quad (5.16)$$

Assuming a harmonic solution (5.6) and substituting into (5.16) yields an eigenvalue problem

$$(\mathbb{A} - \omega \mathbb{I}) \begin{pmatrix} y_0 \\ \alpha_0 \\ \omega y_0 \\ \omega \alpha_0 \end{pmatrix} = \mathbf{0}. \quad (5.17)$$

The added aerodynamic mass, damping and stiffness matrices \mathbb{M}_2 , \mathbb{B}_2 and \mathbb{K}_2 are functions of the freestream velocity U and vanish for $U = 0$. Evaluating the eigenvalues ω of (5.17) for increasing values of the flow velocity U and analyzing whether the real part of the complex frequency ω is positive or negative then determines whether the system is in the stable region and where are the stability boundaries, i. e. critical flow velocities for flutter onset. An example of a flutter boundary evaluation by one of the author's own codes is plotted in Fig. 5.2. In this example, it can be seen that the critical flow velocity lies close to $U = 1.5$ m/s. For a supercritical velocity $U = 1.6$ m/s, exponentially growing oscillations with a frequency of 95.48 Hz will occur.



$$U = 1.5 \text{ m/s} : f = \{-32.66 + 91.39 i, -32.66 - 91.39 i, -0.59 + 96.07 i, -0.59 - 96.07 i\}$$

$$U = 1.6 \text{ m/s} : f = \{-35.43 + 90.42 i, -35.43 - 90.42 i, 1.68 + 95.48 i, 1.68 - 95.48 i\}$$

Figure 5.2: Real and imaginary parts of the complex eigenfrequency $f = \frac{\omega}{2\pi}$ for the increasing flow velocity U .

As already mentioned, the most complex approach to flutter prediction is the full numerical simulation of the 2D or 3D Navier-Stokes equations coupled to the structural equations of motion, i. e. numerical solution of nonlinear partial differential equations on a computational domain deformed in time due to airfoil motion and evaluation of the aerodynamic forces by (5.2). This approach does not permit analysis in frequency domain for fast stability boundary computation. However, it allows predicting also different types of aeroelastic instabilities, e. g. the stall flutter occurring when the airflow separates from the airfoil surfaces at high angles of attack.

5.3 Author's contributions to computational and experimental investigation of airfoil flutter

The results of author's research of flow-induced instability of airfoils are given in the following two reprints. The work was done within a project which started in 2013 in close cooperation between the Technical University of Liberec and Institute of Thermomechanics of the Academy of Sciences of the Czech Republic. The first paper, published in the proceedings of the conference Experimental Fluid Mechanics 2013 (EPJ Web of Conferences, 2014) describes the two-degree-of-freedom NACA0015 airfoil model, which has been redesigned, equipped with sensors, mounted into a wind-tunnel and tuned to exhibit self-oscillations within a certain range of inflow velocities. The paper also summarizes the first results of the dynamic measurements of flow-induced airfoil vibrations.

After the stability boundaries for the flutter-type instability were mapped, a new set of measurements was realized. This time, the experimental setup was complemented by an interferometric system for the measurements of the unsteady flow field, fully synchronized with the dynamic and pressure measurements. The methodology for the evaluation of the interferometric images and the results of this set of measurements are reported in the second paper, presented in a symposium on Fluid-structure interaction in Anaheim, CA, USA and published in proceedings of the ASME Pressure Vessels & Piping 2014 Conference.

Reprints

- P. Šidlof, M. Štěpán, V. Vlček, V. Řidký, D. Šimurda, and J. Horáček. Flow past a self-oscillating airfoil with two degrees of freedom: measurements and simulations. *EPJ Web of Conferences*, 67:02108, 2014a
- P. Šidlof, V. Vlček, M. Štěpán, J. Horáček, M. Luxa, D. Šimurda, and J. Kozánek. Wind tunnel measurements of flow-induced vibration of a NACA0015 airfoil model. In *Proceedings of the ASME 2014 PVP Conference - symposium Fluid-structure interaction*, Anaheim, CA, USA, 2014b

EPJ Web of Conferences 67, 02108 (2014)

DOI: 10.1051/epjconf/20146702108

© Owned by the authors, published by EDP Sciences, 2014

Flow past a self-oscillating airfoil with two degrees of freedom: measurements and simulations

Petr Šidlof^{1,2a}, Martin Štěpán¹, Václav Vlček², Václav Řídký¹, David Šimurda² and Jaromír Horáček²

¹Technical University of Liberec, NTI FM, Studentská 2, 461 17 Liberec, Czech Republic

²Academy of Sciences of the Czech Republic, Institute of Thermomechanics, Dolejškova 5, 182 00 Prague 8

Abstract. The paper focuses on investigation of the unsteady subsonic airflow past an elastically supported airfoil for subcritical flow velocities and during the onset of the flutter instability. A physical model of the NACA0015 airfoil has been designed and manufactured, allowing motion with two degrees of freedom: pitching (rotation about the elastic axis) and plunging (vertical motion). The structural mass and stiffness matrix can be tuned to certain extent, so that the natural frequencies of the two modes approach as needed. The model was placed in the measuring section of the wind tunnel in the aerodynamic laboratory of the Institute of Thermomechanics in Nový Knín, and subjected to low Mach number airflow up to the flow velocities when self-oscillation reach amplitudes dangerous for the structural integrity of the model. The motion of the airfoil was registered by a high-speed camera, with synchronous measurement of the mechanic vibration and discrete pressure sensors on the surface of the airfoil. The results of the measurements are presented together with numerical simulation results, based on a finite volume CFD model of airflow past a vibrating airfoil.

1 Introduction

In aerospace engineering, fluid-structure interaction can play a very important and potentially dangerous role: under certain circumstances, the coupling between flow and structure may lead to unstable exponentially increasing oscillations. The classical example is the flutter instability of airfoils, which occurs for systems with two degrees of freedom when the critical flow velocity is surpassed [1]. The consequent large-amplitude oscillations can result in destruction of the elastic part due to low-cycle fatigue [2], with possibly catastrophic consequences. Thus, the importance of theoretical and experimental analysis of the aeroelastic phenomena in these applications cannot be placed in doubt.

The purpose of this study is the research of the flow-induced vibration of airfoils using interferometry and CFD. The current paper presents the results of first wind-tunnel measurements of a newly reconstructed model of a NACA0015 airfoil with two degrees of freedom (DOF) – pitching (rotation about the elastic axis) and plunging (vertical translational motion). The results are compared to numerical simulations of airflow past an airfoil, whose motion is prescribed based on the kinematic data identified from the measurements.

2 State-of-the-art

The majority of experimental works dealing with 2-DOF vibration of airfoils is still limited to the simplified case of forced (externally excited) vibration [3–13]. The standard method for the measurement of the flow field in the proximity of the vibrating profile is the Particle Image Velocimetry (PIV), complemented with local pressure measurements using pressure probes. The usage of interferometric or schlieren methods has not yet been published in this specific context, although these methods are well suited especially for the case of higher subsonic, transonic and supersonic velocities where the PIV method is hardly applicable. Moreover, the interferometric measurements can provide pressure field data for the calculation of the forces and moments acting on the airfoil. The drawback of the interferometric approach – the assumption of the isentropic flow in the calculation of the pressure field – can be minimized by concurrent pneumatic measurements used to calculate correction factors.

The interferometric images provide results, whose precision is proportional to the test section width and flow velocity (the number of interferometric fringes increases linearly with the light path length, and also with the Mach number). The PIV and interferometric methods can be seen as complementary, since with the increasing

^a Corresponding author: petr.sidlof@tul.cz

Mach number the difficulties of a typical PIV setup generally grow, but the applicability of the interferometric method is not influenced and the precision of the results evaluated from the fringes increases.

3 Experimental setup

3.1 Physical design

The experimental setup, which can be seen in figure 1, builds on previous experience obtained in the Institute of Thermomechanics in the years 2006-2012, when self-oscillating models of the NACA0015 and DCA18% airfoils with two degrees of freedom were designed and the methodology of the measurements developed [14–16].

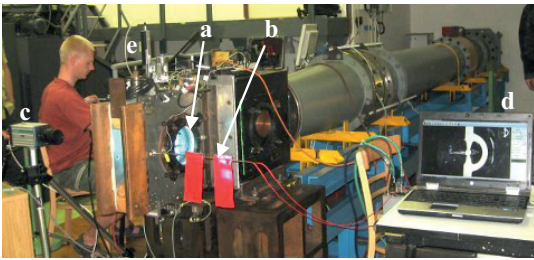


Figure 1. Overall view of the experimental setup. The illuminated measuring section with the airfoil (a), Prandtl tube (b), high-speed camera (c) and its controlling PC (d), and the deflection sensor (e).

A model of a symmetric NACA0015 airfoil with a chord length of 65 mm and width of 80 mm was placed in a 80x210 mm test section of a vacuum wind tunnel in the laboratory of the Institute of Thermomechanics in Nový Knín. The supporting frame of the airfoil allows two degrees of freedom – vertical shift (plunge) and rotation about elastic axis (pitch), which is located at 1/3 of the chord length (see figure 2). The translation stiffness is realized by adjustable flat springs, the torsional stiffness comes from a thin torsion bar inside the profile. For higher flow velocities and pitching amplitudes, this bar is highly dynamically loaded and prone to destruction.

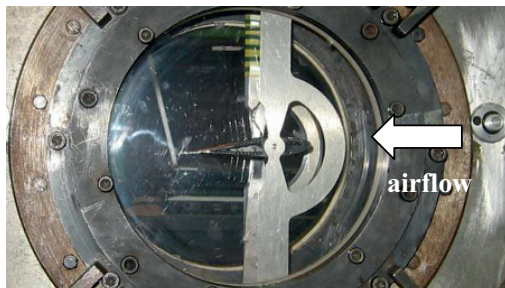


Figure 2. Side view of the measuring section with the airfoil and its support with two degrees of freedom (vertical shift – plunge, and rotation about the elastic axis – pitch).

During first preliminary measurements, the torsion bar underwent rupture due to excessively high pitching amplitudes, destroying also the cables and some of the sensors inside the airfoil. Certain parts of the model had to be remanufactured, and the guiding mechanism was also slightly improved. The total mass of the dynamic system can now be tuned by mounting additional masses onto the moving frame. In this way, the eigenfrequency of the plunging mode can be shifted apart from the torsional mode eigenfrequency. From the theoretical point of view, this should postpone the flutter onset to higher flow velocities.

Prior to wind tunnel measurements, the natural frequencies and damping ratios of the system with various values of additional masses attached was measured and identified in laboratory [17]. For the system with all three additional masses of $m = 350$ g, the eigenfrequency of the translational mode is 17.7 Hz, about 2-3 Hz lower than without the additional masses. The natural frequency of the rotational mode is 24.8 Hz and should not depend on the additional masses.

3.2 Sensors and wiring

The airfoil is equipped with six miniature pressure transducers Freescale MPXH6115 mounted flush with the airfoil surface – three on the top surface, three on the bottom. Due to damage of the model during previous measurements, only two sensors (V1h and V2h, both on the top surface) remained functional. The signal from the transducers, which have built-in preamplifiers, leads off the measuring section by a flexible bundle of wires designed for high mechanical loads.

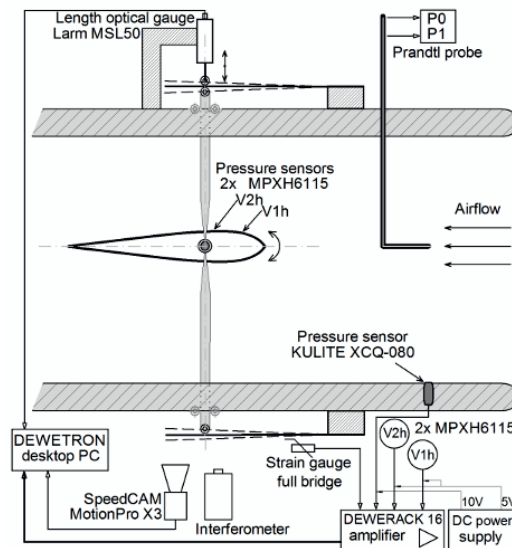


Figure 3. Schematic of the airfoil model and sensor wiring. In the real setup, the high-speed camera (SpeedCAM X3) is oriented perpendicularly to the figure plane.

The vertical deflection of the airfoil is measured by a Larm MSL50 optical length gauge (see figure 3). The

EFM 2013

dynamic range of this sensor was found to be insufficient for very high amplitudes (the limit arises from exceeding the maximum allowed linear velocity), and so an additional strain gauge bridge was mounted on the bottom flat spring and calibrated to provide a redundant signal of the vertical deflection.

The measuring section of the wind tunnel is equipped by a Prandtl tube, measuring the static pressure p_l and total pressure p_0 . The Prandtl tube is connected to a pressure scanner wired to a PC, which registers the pressures and evaluates the Mach number using relation

$$Ma = \sqrt{\frac{2}{\kappa - 1} \left(\left(\frac{p_l}{p_0} \right)^{\frac{1-\kappa}{\kappa}} - 1 \right)}. \quad (1)$$

Here $\kappa = c_p/c_v$ is the heat capacity ratio, for ideal diatomic gas equal to 7/5. The flow velocity can be then calculated as

$$u = Ma \sqrt{\kappa RT}, \quad (2)$$

where $R = 287.1 \text{ J} \cdot \text{kg}^{-1} \cdot \text{K}^{-1}$ is the specific gas constant for dry air and T is the absolute local static temperature calculated from the ambient temperature T_0 as

$$T = T_0 \left(1 + \frac{\kappa - 1}{2} Ma^2 \right)^{-1}. \quad (3)$$

The signals from the airfoil pressure transducers, strain gauge bridge and optical length gauge sensor are digitized, monitored online and stored by a Dewetron software system.

In standard configuration, the flow field around the airfoil is measured by Mach-Zehnder interferometer and a high-speed camera. Due to technical issues, the interferometer was not mounted during this set of measurements. To monitor the airfoil motion (the vertical deflection is measured by the length gauge, but for the pitch angle there is currently no sensor installed on the model), a high-speed camera (NanoSense MKIII, maximum resolution 1280x1024 pixels @1000 Hz) and a special light source were mounted in the perpendicular direction, using the same optical access as the interferometric setup. The camera is triggered from the Dewesoft module, which ensures perfect synchronisation of the pressure and deflection measurements with the high-speed camera frames. The region of interest was set to a rectangle 756x700 pixel to spare disk storage and to save time during the transfer of data from the camera to the PC, which was the most time-consuming operation during the measurement.

4 Numerical model

The CFD model is described in detail in [18]; here it is sufficient to state that the model is based on cell-centred finite volume discretization of incompressible Navier-Stokes equations solved on a moving mesh. Two variants of the model are used: a fully 3D model, and a much

computationally cheaper 2D model used for fast testing and preliminary analysis. The numerical code uses the *OpenFOAM* package, which is available as a free open-source software under the GNU general public licence. The motion of the airfoil is prescribed as a 2-DOF harmonic oscillation, with kinematic data identified from the experimental results.

Most of the CFD simulations were run in parallel on a SGI Altix UV 100 shared-memory supercomputer of the Supercomputing Centre of the Czech Technical University in Prague. This shared-memory machine is built on the cache coherent non uniform memory access (cc-NUMA) architecture and offers 12 6-core Intel Xeon Nehalem processors, with 8 GB per core RAM. The nodes are interconnected by the SGI NUMalink 5 interconnects, providing low latency and 15 GB/s bandwidth through two 7.5 GB unidirectional links. The *OpenFOAM* library is compiled using standard *gcc*, and the parallel solvers run via SGI MPT implementation of the MPI standard.

5 Results

5.1 Evaluation of the airfoil motion from the high-speed camera images

The measurement was performed for 32 cases: four configurations of additional masses and various values of inlet flow velocities. In all cases, first the airfoil was forced an initial deflection of $y = 3 \text{ mm}$. Once the flow velocity in the wind tunnel was adjusted as needed, the high-speed camera started recording and shortly afterwards the airfoil was released.

During the 32 measurements, altogether more than 30 000 frames were recorded by the high-speed camera. The position of the airfoil in all these frames (vertical shift and pitch angle) were evaluated after the wind tunnel measurements using the positions of three key points (see figure 4), which were tracked automatically using *Olympus i-Speed Advanced* software suite. On a standard laptop, the software was able to process about 10 frames per second.

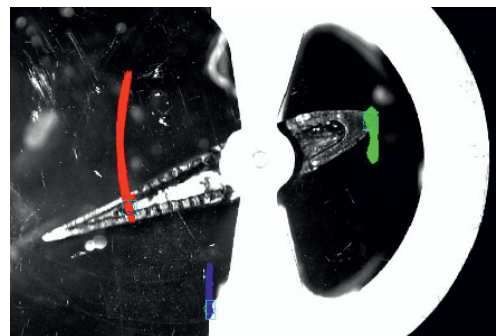


Figure 4. Points tracked automatically by the Olympus i-Speed software.

Figures 5, 6 show the time history of the pitch angle (positive nose-up) and vertical deflection (positive upwards) for two cases selected out of the 32

measurements, both in configuration #4, with all additional masses attached ($m = 350$ g). Figure 5 demonstrates a case where the flow velocity is subcritical. From the initial deflection ($y = 3$ mm, pitch = 2°), the vertical displacement oscillates with exponential attenuation to zero. As the two modes are coupled (the elastic axis is not located in the centre of gravity), a short transient in the pitching mode is excited, too.

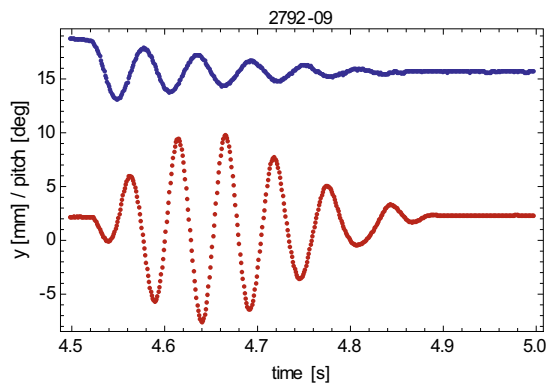


Figure 5. Vertical deflection (blue) and pitch (red) of the airfoil in time, configuration #4. Measurement 2792-09, $Ma = 0.1$: subcritical flow velocity.

The offset of the vertical deflection waveform does not have physical meaning; it is caused by an arbitrary position of the coordinate system origin when processing the camera frames. The offset of the pitch waveform (dark red) of about 2° corresponds to a real initial inclination of the airfoil, caused by imperfect adjustment of the torsion bar.

When the flow velocity is increased (measurements 2792-13, 2792-26..31 – not shown here), the behaviour of the system remains qualitatively the same, but the damping factor decreases due to negative damping contribution from the aerodynamic damping matrix. A measurement at a supercritical flow velocity, when the flutter instability is present, is demonstrated in figure 6. In this case, the real part of the complex frequency is not negative any more, and within the validity of a linear approximation the amplitudes of the oscillations would exponentially grow until system destruction. Due to nonlinearities of the system (both mechanical and aerodynamic), the amplitudes eventually stabilize at a finite value.

To visualize the amplitudes and phase differences between the two modes, the airfoil motion can be also displayed in phase plane. Tab. 1 reports the phase plots of all the cases measured, with vertical displacement y on the bottom axis and pitch angle on the left axis. In the cases where the system reached the flutter instability, the frequency and amplitudes of both modes are listed in the table, too. For configurations #1, 2 and 3, no measurements were performed beyond the lowest flow velocity able to trigger the flutter instability in order not to destroy the model: it was not known a priori, whether the vibration amplitude stabilizes due to system

nonlinearities earlier, than the torsion bar breaks. The last measurements in configuration #4, however, recorded the system behaviour at several supercritical flow velocities up to $Ma = 0.2$.

In general, from the data given in Tab. 1 it can be concluded that the current model behaves in a predictable way, consistent with the classical theory of 2-DOF aeroelastic systems. The flutter instability occurs at certain critical flow velocity, with a frequency in between the natural frequencies of the mechanical system (in our case somewhat closer to the frequency of the translational mode). When additional mass is applied to the frame, increasing the corresponding translational natural frequency and widening the gap between the two frequencies, the flutter instability is postponed to higher flow velocities. The effect is, however, not very distinct: the critical flow velocity for configuration #1 ($m = 0$ g) is $Ma = 0.145$, for configuration #4 ($m = 350$ g) flutter occurs at $Ma = 0.160$. When the flow velocity is increased beyond the critical value, the oscillation amplitudes grow significantly (from $7.1^\circ / 0.81$ mm at $Ma = 0.16$ to $17.9^\circ / 4.27$ mm at $Ma = 0.2$ for cfg. #4), with a very slight increase in the flutter frequency (18.6 Hz to 18.9 Hz).

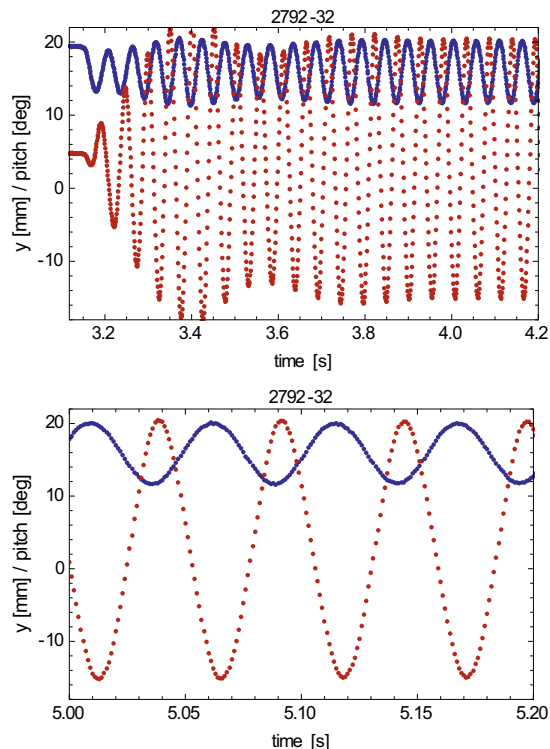


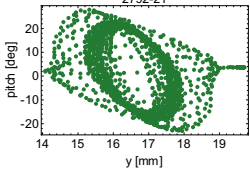
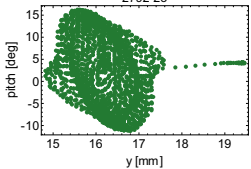
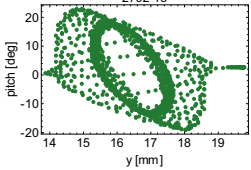
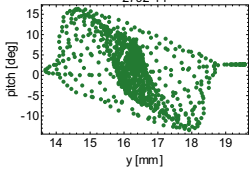
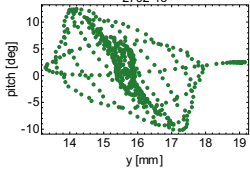
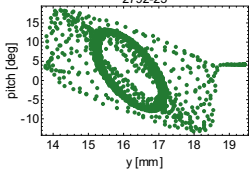
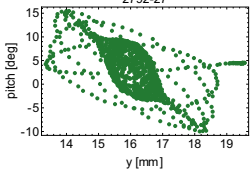
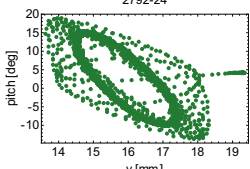
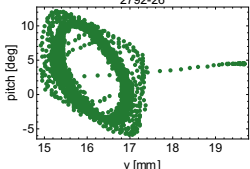
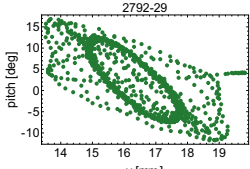
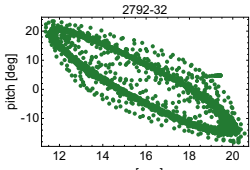
Figure 6. Vertical deflection (blue) and pitch (red) of the airfoil in time, configuration #4. Measurement 2792-32, $Ma = 0.2$: supercritical flow velocity – flutter.

EFM 2013

Table 1. Plots of the airfoil motion in phase plane for different configurations (additional masses m) and Mach numbers Ma . For supercritical flow velocities, frequency and amplitudes of both modes are included.

Ma [-]	configuration #1 ($m=0$ g)	configuration #2 ($m=70$ g)	configuration #3 ($m=210$ g)	configuration #4 ($m=350$ g)
0				
0.05				
0.1				
0.125				
0.130				
0.135				
0.140				

^a Corresponding author: petr.sidlof@tul.cz

Ma [-]	configuration #1 ($m=0$ g)	configuration #2 ($m=70$ g)	configuration #3 ($m=210$ g)	configuration #4 ($m=350$ g)
0.145	 <p>Flutter frequency: 21.8 Hz Pitch amplitude: 18.8° Plunge amplitude: 1.17 mm</p>			
0.150				 <p>Flutter frequency: 21.2 Hz Pitch amplitude: 16.0° Plunge amplitude: 1.05 mm</p>
0.155				 <p>Flutter frequency: 19.7 Hz Pitch amplitude: 10.2° Plunge amplitude: 0.89 mm</p>
0.160				<p>Flutter frequency: 20.0 Hz Pitch amplitude: 12.5° Plunge amplitude: 1.38 mm</p> <p>Flutter frequency: 18.6 Hz Pitch amplitude: 7.1° Plunge amplitude: 0.81 mm</p>
0.170				 <p>Flutter frequency: 18.8 Hz Pitch amplitude: 10.1° Plunge amplitude: 1.34 mm</p>
0.200				 <p>Flutter frequency: 18.9 Hz Pitch amplitude: 17.9° Plunge amplitude: 4.27 mm</p>

EFM 2013

5.2 Pressure measured on the airfoil surface

In the current set of measurements, due to technical complications it was unfortunately not possible to install the interferometric setup. Thus, the only measurements of the flow field are the signals from the discrete pressure sensors mounted on the surface of the oscillating airfoil. The relatively cheap MPXH6115 miniature pressure sensors provided unexpectedly good and accurate signals: prior to wind tunnel measurements, they were verified against a high-end Kulite XCQ-080 pressure transducer, with no significant discrepancy in amplitude and phase up to at least 1 kHz.

The time history of the pressure from these two sensors is shown in figure 7 for two cases, both in the flutter regime. The ambient atmospheric pressure was 98.32 kPa. As can be seen from comparison with figure 6, the maximum static pressure occurs very close to the time instant of minimum pitch angle, and vice versa. The amplitude of the static pressure oscillations is significantly higher for sensor V1h, located closer to the airfoil leading edge. The minimum static pressure registered in measurement #2792-25 ($Ma = 0.155$) is about -4.3 kPa rel., in measurement #2792-32 ($Ma = 0.2$) about -8.1 kPa rel.

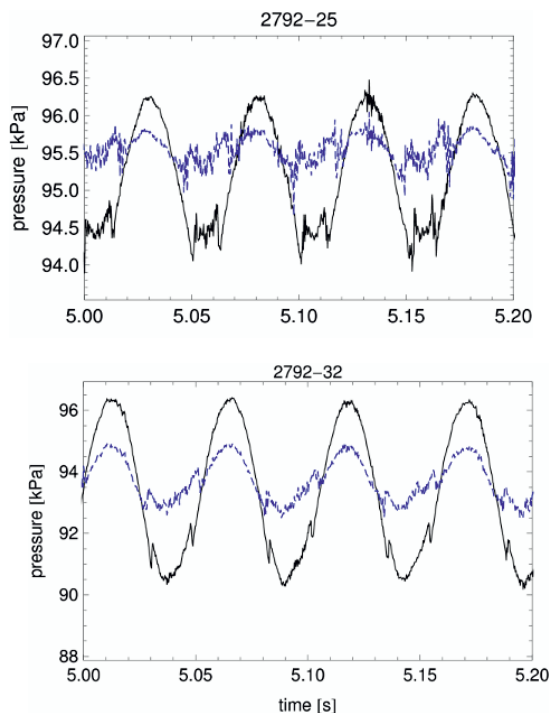


Figure 7. Static pressure measured at two pressure probes installed flush with the airfoil surface during flutter. Top: measurement 2792-25 (configuration #3, $Ma = 0.155$) Bottom: measurement 2792-32 (configuration #4, $Ma = 0.2$) — signal V1h (12 mm from leading edge, 18% of chord) - - - signal V2h (31 mm from leading edge, 47% of chord)

5.3 Numerical simulation results

The numerical simulations were run using the simplified 2D model, with the airfoil kinematic data and inlet Mach numbers matching values of measurements #2792-25 and #2792-32. The frequencies and amplitudes of the oscillation modes are listed in Tab. 1. For #2792-25, the phase lag of the pitching mode behind the plunging mode was identified to 1.182π , in #2792-32 it was 1.134π . Figure 8 shows the simulated pressure field for a time instant approximately in the middle of the 6th period of vibration, where the vertical deflection of the airfoil passes through zero position (cf. figure 9).

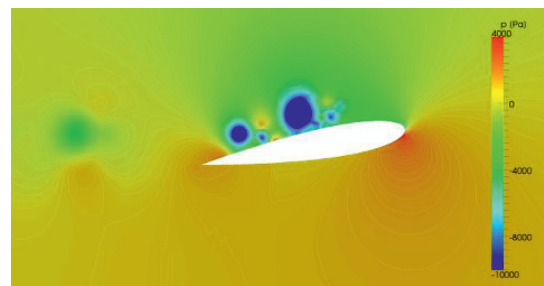


Figure 8. Simulated pressure field for the case 2792-32 ($Ma = 0.2$), $t = 0.2875$ s (6th period). Pressure isolines by 100 Pa. Zero level corresponds to atmospheric pressure.

The pitching angle being 9.85° , the highest pressure (about 4 kPa) is located on the bottom surface near the leading edge. On the top surface, the airflow separates and forms a highly turbulent separation region, with vortex structures forming zones of very low pressure. As the simulation is performed in 2D, the vortex dynamics are completely different from the real 3D case. In particular, the vortex structures cannot interact and change orientation, and thus disperse with a much slower rate than they would in 3D. This is a known drawback of the 2D simulations; the predictions of the 2D model in the separation region must be interpreted cautiously.

The time history of the pressure in two probes (V1h, V2h), located at the places where the pressure transducers are mounted on the physical model, are shown in figure 10. These results can be directly compared to the values measured in the wind tunnel and displayed in figure 7. As expected, the pressure maxima correspond to the time instants of minimum pitching angle (cf. figure 9 for the simulation #2792-32).

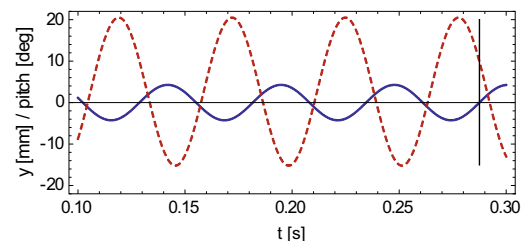


Figure 9. Time history of the plunge (—) and pitching angle (- - -) in the numerical simulation #2792-32 ($Ma = 0.2$). Vertical line in $t = 0.2875$ s.

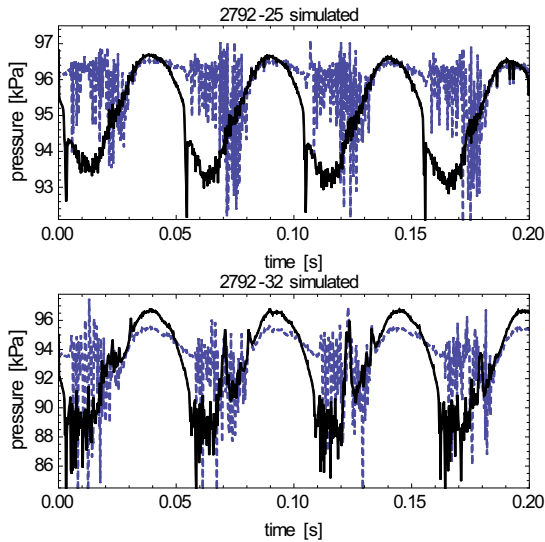


Figure 10. Simulated static pressure at two probes on the top surface of the airfoil, cases 2792-25 ($Ma = 0.155$) and 2792-32 ($Ma = 0.2$).

— probe V1h (12 mm from leading edge, 18% of chord)
 - - - probe V2h (31 mm from leading edge, 47% of chord)

In both simulations, the waveform of pressure probe V1h (in 18% of the chord length) compares very well to the measurement, only with the minimum values slightly lower and more influenced by pressure disturbances than the measured data. The pressure probe V2h is located at 47% chord. During almost half of the oscillation period (when pitching angles are positive), the probe already lies in the separation region. Thus, the pressure predictions of the numerical model are negatively influenced by the fact that the 2D simulation overestimates the turbulent pressure fluctuations, as discussed earlier. However, during negative pitching angles the V2h signal still compares well with the experiments.

6 Conclusions

Based on the previous experience and measurements of the authors, a physical model of a NACA0015 airfoil with two degrees of freedom has been modified and repaired, equipped with sensors and measured in a wind tunnel at various values of subcritical and supercritical flow velocities. The mechanical vibration and static pressure at two discrete locations of the upper airfoil surface were measured, with synchronous high-speed imaging of the airfoil motion. The stability boundaries for different values of additional masses (i.e., different eigenfrequencies of the plunging mode) have been identified, and the post-flutter behaviour of the system analysed. The results served well as a frame of reference for subsequent set of measurements, where an interferometric system was mounted. However, the interferometric data has not yet been processed and evaluated.

The measured signals from the pressure sensors have also been used as validation data for a concurrently

developed CFD model of airflow past an oscillating airfoil. The results of the numerical simulations match well in the regions of attached flow. However, at high angles of attack when the airflow separates, the 2D CFD predictions strongly overestimate the turbulent pressure fluctuations. In this separated flow regime, both numerical simulations and interpretation of the interferometric data remain a challenging goal for the future.

Acknowledgements

The research has been supported by the Czech Science Foundation, project 13-10527S "Subsonic flutter analysis of elastically supported airfoils using interferometry and CFD". We wish to acknowledge the support of the team of the Aerodynamic laboratory in Nový Knín, who helped during the wind tunnel measurements, and Dr. Jan Kozánek, who provided the identified complex eigenfrequencies of the model.

References

1. E.H. Dowell, Kluwer Academic Publishers, Dordrecht (1995)
2. A.N. Marques, C.F.C. Simoes, J.L.F. Azevedo, Journal of the Brazil Society of Mechanical Sciences and Engineering **27**, 4 (2006)
3. D. Poirel, Y. Harris, A.A. Benaissa, Journal of Fluids and Structures **24** (2008)
4. M.R. Soltani, F.R. Marzabadi, Transaction B: Mechanical Engineering **17**, 6 (2010)
5. H.H. Hilton, C.G. Merrett, SAE International Journal of Aerospace **4**, 2 (2011)
6. A. Garcia-Sagrado, T. Hynes, Journal of Fluids and Structures **30** (2012)
7. J.A. Rivera, B.E. Dansberry, R.M. Bennett, M.H. Durham, W.A. Silva, NASA Technical Memorandum 104072 (1991)
8. T. O'Neil, T.W. Strganac, Journal of Aircraft **35**, 4 (1998)
9. F.O. Carta, NASA Contractor Report 3172 (1979)
10. I. Fenercioglu, O. Cetiner, Journal of Fluids and Structures **31** (2012)
11. T. Prangemeier, D. Rival, C. Tropea, Journal of Fluids and Structures **26** (2010)
12. Y. Lian, M.V. Ol, W. Shy, AIAA Paper 2008-652, (2008)
13. A.R. Norizham, T. Andrienne, I.G. Dimidtriadis, AIAA Journal **49**, 10 (2011)
14. V. Vlček, J. Kozánek, I. Zolotarev, *International Conference on Vibration Problems*, Prague (2011)
15. V. Vlček, J. Kozánek, Acta Technica CSAV **56** (2011)
16. V. Vlček, J. Horáček, M. Luxa, J. Veselý, *International Conference on Flow Induced Vibration – FIV*, Prague (2008)
17. J. Kozánek, V. Vlček, I. Zolotarev, *Dynamical Systems – Theory and Applications*, Lodz (2013)
18. V. Řídký, P. Šidlof, *Experimental Fluid Mechanics*, Kutná Hora (2013)

Proceedings of the ASME 2014 Pressure Vessels & Piping Conference
 PVP2014
 July 20-24, 2014, Anaheim, California, USA

PVP2014-28294

**WIND TUNNEL MEASUREMENTS OF FLOW-INDUCED VIBRATION
 OF A NACA0015 AIRFOIL MODEL**

Petr Šidlof

Technical University of Liberec
 Studentská 2, 461 17 Liberec 1, Czech Republic
 Email: sidlof@it.cas.cz

Václav Vlček

Institute of Thermomechanics,
 Academy of Sciences of the Czech Republic
 Dolejškova 5, 182 00 Prague 8, Czech Republic

Martin Štěpán

Technical University of Liberec
 Studentská 2, 461 17 Liberec 1,
 Czech Republic

Jaromír Horáček

Institute of Thermomechanics,
 Academy of Sciences of the
 Czech Republic
 Dolejškova 5, 182 00 Prague 8,
 Czech Republic

Martin Luxa

Institute of Thermomechanics,
 Academy of Sciences of the
 Czech Republic
 Dolejškova 5, 182 00 Prague 8,
 Czech Republic

David Šimurda

Institute of Thermomechanics,
 Academy of Sciences of the Czech Republic
 Dolejškova 5, 182 00 Prague 8, Czech Republic

Jan Kozánek

Institute of Thermomechanics,
 Academy of Sciences of the Czech Republic
 Dolejškova 5, 182 00 Prague 8, Czech Republic

ABSTRACT

The paper reports on interferometric measurements of flow over a NACA0015 airfoil model during flutter limit cycle oscillations. The airfoil model is fixed on an elastic support allowing motion with two degrees of freedom – pitch and plunge. The structural mass and stiffness matrices can be tuned to certain extent, so that the eigenfrequencies of the two modes approach as needed. The model is equipped with dynamic pressure probes and sensors measuring the airfoil vertical position. The flow field around the airfoil was measured by Mach-Zehnder interferometer and registered using a high-speed camera synchronously with the mechanical vibration and pressure measurements. The Mach number of the incident airflow was gradually increased and the response of the aeroelastic system to initial impulse measured, until the flutter instability onset occurred. Flutter boundaries were evaluated for various additional masses attached (i.e., for various plunging mode eigenfrequencies), and post-critical behavior of the system investigated. The interferograms recorded by the high-speed camera were postprocessed, yielding pressure distribution around the airfoil during its vibration and an estimate of the

total aerodynamic force and energy transfer from the airflow to the structure.

NOMENCLATURE

n	index of refraction
λ	wave length of the interferometer light source
L	test section width
K	Gladston-Dale constant
ρ	local air density
p_0	Total pressure
p_1	Static pressure
Ma	Mach number
κ	Heat capacity ratio
c_p, c_v	Heat capacity at constant pressure / volume
R	Specific gas constant
T	Absolute local static temperature
T_0	Ambient temperature
m	Additional mass on the airfoil frame

INTRODUCTION

Fluid-structure interaction affects an increasing number of technical applications – stability of suspension bridges, towers, smokestacks and skyscrapers, vibration of steam turbine blades, flow in heat exchangers and nuclear reactors, or wind turbine blade, airfoil and helicopter rotor blade vibration. The coupling between the flow and the structure may lead to large-amplitude oscillations and result in destruction of the elastic part due to low-cycle fatigue. In aerospace engineering, fluid-structure interaction can play a very important and potentially dangerous role: under certain circumstances, the coupling between flow and structure may lead to unstable exponentially increasing oscillations. The classical example is the flutter instability of airfoils, which occurs for systems with two degrees of freedom when the critical flow velocity is surpassed [1].

The flutter instability, its boundaries and the aeroelastic response of a two-degree-of freedom (DOF) airfoil can be modeled and explained by simplified aeroelastic equations, where a linear mass-spring system is coupled to potential flow [2]. In more complex flow regimes, e. g. limit cycle oscillations with high angle of attack or stall flutter with massive flow separation, the simplified models cannot predict flow field accurately, and the airflow has to be modeled by Navier-Stokes equations. Turbulent flow has a three-dimensional character and so 3D simulations are preferable, but in a number of cases, two-dimensional models are still applied from practical reasons.

Many experimental works dealing with the 2-DOF vibration of airfoils, e.g. [3-7] are limited to the simplified case of forced, externally excited vibration. Poirel et al. [8] reports on self-sustained oscillations of a NACA0012 airfoil in pure pitch, Razak et al. [9] investigated flutter and stall flutter of a self-excited airfoil with pitch and plunge DOF.

The standard methods for the measurement of the flow field in the proximity of the vibrating profile are Hot-Wire Anemometry (HWA) and Particle Image Velocimetry (PIV), complemented with local pressure measurements using pressure probes. The usage of interferometric or Schlieren methods for unsteady airflow past vibrating structures is rather scarce, although these methods are well suited especially for the case of moderate and higher subsonic velocities, and also transonic and supersonic velocities where the PIV method is hardly applicable. The drawback of the interferometric approach – the assumption of isentropic flow in the calculation of the pressure field – can be minimized by concurrent pneumatic measurements used to calculate correction factors.

The interferometric images provide results, whose precision is proportional to the test section width and flow velocity: the number of interferometric fringes increases linearly with the light path length, and also with the Mach number. The PIV and interferometric methods can be seen as complementary, since with the increasing Mach number the difficulties of a typical PIV setup generally grow, but the applicability of the interferometric method is not influenced and the precision of the results evaluated from the fringes increases.

The purpose of this study is the research of flow-induced vibration of airfoils and measurement of the unsteady flow field around the airfoil using interferometric methods. The current paper presents the results of wind-tunnel measurements of flutter of a NACA0015 pitch-plunge airfoil.

DYNAMIC MODEL OF THE PITCH-PLUNGE AIRFOIL

The experimental setup builds on previous experience obtained in the Institute of Thermomechanics in the years 2006-2012, when self-oscillating models of the NACA0015 and DCA18% airfoils with two degrees of freedom were designed and the methodology of the measurements developed [10, 11].

For the wind tunnel measurements, a model of a symmetric NACA0015 airfoil with a chord length of 65 mm and

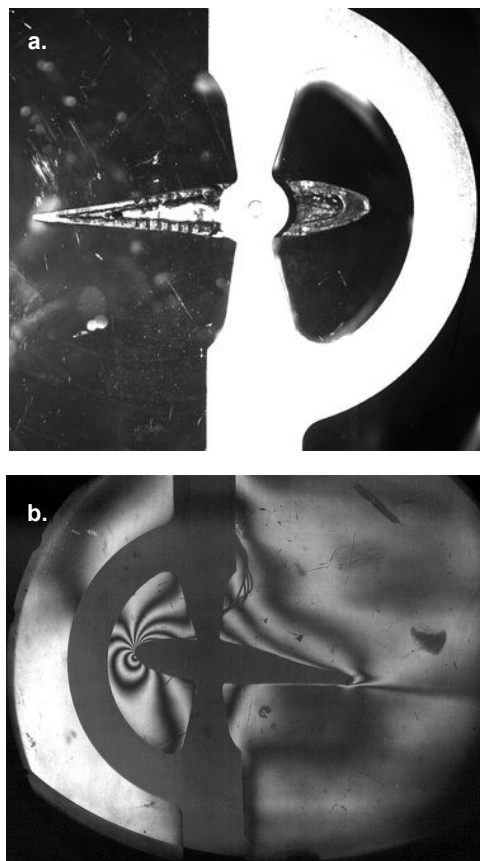


FIG. 1 MODEL OF THE NACA0015 AIRFOIL WITH TWO DEGREES OF FREEDOM IN THE VIEW OF A HIGH-SPEED CAMERA WITH STANDARD FRONTAL ILLUMINATION (a.), AND WITH INTERFEROMETRIC OPTICAL SETUP (b.)

width of 80 mm was manufactured. The supporting frame of the airfoil allows motion with two degrees of freedom – vertical shift (plunge) and rotation about elastic axis (pitch), which is located at 1/3 of the chord length. The model can be seen in Fig. 1, which shows high-speed camera frames in two measurement configurations: with standard frontal illumination by a standalone light source (a.), and with Mach-Zehnder interferometer installed (b.), rendering visible the interferometric fringes.

The translation stiffness of the model is realized by adjustable flat springs outside the test section, the torsional stiffness comes from a thin torsion bar inside the profile. For higher flow velocities and pitching amplitudes, this bar with a diameter of 1.6 mm is highly dynamically loaded and prone to destruction.

The total mass of the dynamic system can be tuned by mounting additional masses onto the moving frame. In this way, the eigenfrequency of the plunging mode can be shifted apart from the torsional mode eigenfrequency. From the theoretical point of view, this should postpone the flutter onset to higher flow velocities. The natural frequencies and damping ratios of the system with various values of additional masses attached were measured and identified in laboratory by Kozánek [12]. For the system with an additional mass of $m = 350$ g, the eigenfrequency of the translational mode is 17.7 Hz, about 2-3 Hz lower than without the additional masses ($m = 0$ g). The natural frequency of the rotational mode is 24.8 Hz and should not depend on the additional masses.

INTERFEROMETRIC SETUP

The airfoil model was fixed in a 80x210 mm test section of a suction-type wind tunnel in the Aerodynamic laboratory of the Institute of Thermomechanics in Nový Knín. The optical glasses in the sidewalls of the test section allow optical access for the optical measurement. The Mach-Zehnder interferometer was mounted over the wind tunnel (see Fig. 2).

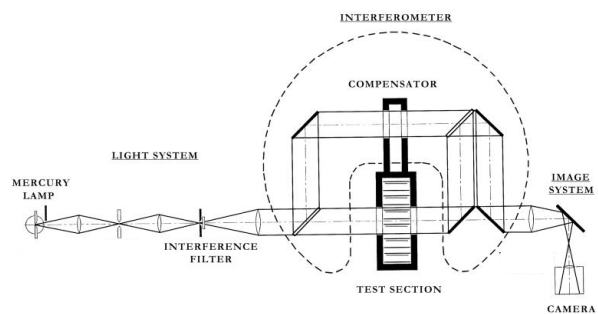
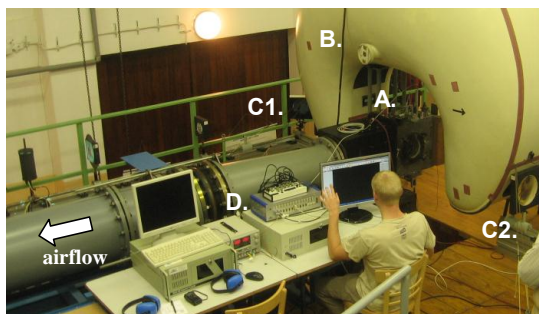


FIG. 2 WIND TUNNEL AND SCHEMATIC OF THE INTERFEROMETRIC SETUP: A. TEST SECTION WITH THE AIRFOIL MODEL, B. MACH-ZEHNDER INTERFEROMETER, C1. OPTICS BETWEEN THE MERCURY LAMP AND INTERFEROMETER, C2. OPTICS BETWEEN THE INTERFEROMETER AND HIGH-SPEED CAMERA, D. AMPLIFIERS AND DATA ACQUISITION HARDWARE

Due to space limitations, the collimated beam from the light source is reflected by mirror C1 into the interferometer B (see Fig. 2). The coherent power light is divided into two branches on the first semi-permeable mirror in the interferometer. The measuring branch passes through the test section and the comparative branch passes through a compensator. The interferometric image of the flow field in the test section with the airfoil appears on the second semi-permeable mirror. Slight refraction effects in the test section influence the phase differences between the two beams, thus forming an interference pattern. The interferometric image consists of dark and bright interferometric fringes. From the differences in times for a light beam to pass through a fluid in adjacent fringes (k) and ($k-1$), and from the wavelength of monochromatic light we may obtain relation for the difference in the index of refraction between the adjacent fringes:

$$(n)_k - (n)_{k-1} = \frac{\lambda}{L} \quad (1)$$

Here $\lambda = 435.8$ nm is the wave length of the monochromatic light employed. Through the empirical Gladstone-Dale equation a relation for the difference in density between adjacent fringes is obtained

$$(\rho)_k - (\rho)_{k-1} = \frac{\lambda}{LK} \quad (2)$$

L is the test section width, $K = 0.0002297 \text{ m}^3/\text{kg}$ is the Gladstone-Dale constant. As seen from eqn. (2), interferometry can be used for measuring the density differences between two points in the flow field. The interferometer can be set for an infinite interference fringe (which is used in this measurement) or for the finite fringe displacement method.

The interferograms, focused by optics C2, can be either visualized on a simple diffusion screen, or recorded by a still or high-speed camera. For the current measurements of the unsteady airflow past the oscillating airfoil, the unsteady interferograms were recorded using a high-speed camera (NanoSense MKIII, resolution 1280x1024 pixels @1000 Hz), aligned on the optical bench of the interferometer. The field of view of the camera was set to approximately 380x300mm, covering most of the visible flow field around the oscillating airfoil.

SENSORS AND ELECTRICAL CONNECTIONS

In addition to the interferometric setup for the flow field measurements, the model was equipped with various pressure sensors. One dynamic pressure transducer (Kulite XCQ-080) was mounted in the wall of the entry section to monitor the fast variations of the static pressure due to airfoil oscillation. For the measurement of the inflow velocity, a Prandtl tube measuring the mean value of the static pressure p_1 and total pressure p_0 was mounted shortly upstream of the test section. The Prandtl tube is connected to a pressure scanner wired to a PC, which registers the pressures and evaluates the Mach number using Eq. (3):

$$\text{Ma} = \sqrt{\frac{2}{\kappa - 1} \left(\left(\frac{p_1}{p_0} \right)^{\frac{1-\kappa}{\kappa}} - 1 \right)} \quad (3)$$

Here $\kappa = c_p/c_v$ is the heat capacity ratio, for ideal diatomic gas equal to 7/5. The flow velocity can be then calculated according to Eq. (4).

$$u = \text{Ma} \sqrt{\kappa R T} \quad (4)$$

Here $R = 287.1 \text{ J kg}^{-1} \text{ K}^{-1}$ is the specific gas constant for dry air and T is the absolute local static temperature calculated from the ambient temperature T_0 as shown in Eq. (5) below:

$$T = T_0 \left(1 + \frac{\kappa - 1}{2} \text{Ma}^2 \right)^{-1} \quad (5)$$

Further, the airfoil is equipped with six miniature dynamic pressure transducers Freescale MPXH6115 mounted flush with the airfoil surface. Three of the transducers are located on the upper surface, three on the lower one. Due to damage of the model during previous measurements, only two sensors (V1h and V2h, as shown in Fig. 3) remained functional. The signal from the transducers, which have built-in preamplifiers, leads out of the vibrating airfoil and out of the measuring section by a flexible bundle of wires designed for high mechanical loads.

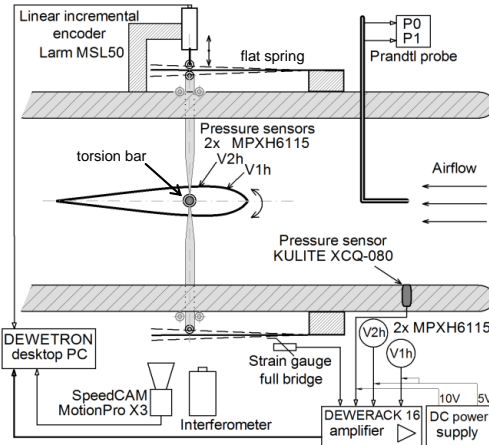


FIG. 3 SCHEMATIC OF THE TEST SECTION WITH THE AIRFOIL MODEL, SENSORS AND TRANSDUCERS

The vertical deflection of the airfoil is measured by a Larm MSL50 linear encoder. For higher plunging amplitudes, the dynamic range of this sensor is insufficient (the limit arises from exceeding the maximum allowed linear velocity). This is why an additional strain gauge bridge was mounted on the flat spring supporting the airfoil frame and calibrated to provide a redundant signal of the vertical deflection.

The signals from the airfoil pressure transducers, strain gauge bridge and the linear encoder are digitized, monitored online and stored by a Dewetron software system. The software includes a special module for triggering of the high-speed camera, which enables perfect synchronization of the recorded interferograms with the signals from all the sensors.

TABLE 1. EXPERIMENTAL CONDITIONS OF THE EVALUATED MEASUREMENTS: ADDED MASS m , PRESENCE OF THE INTERFEROMETRER, MACH NUMBER Ma

	m [g]	Intetfer.	Ma [1]	Remark
2792-15	73	no	0.15	critical
2792-21	0	no	0.145	critical
2792-25	215	no	0.155	critical
2792-26	359	no	0.16	critical
2810-2-23	0	yes	0.162	critical
2810-2-39	940	yes	0.218	critical
2810-2-45	940	yes	0.23	supercritical

RESULTS

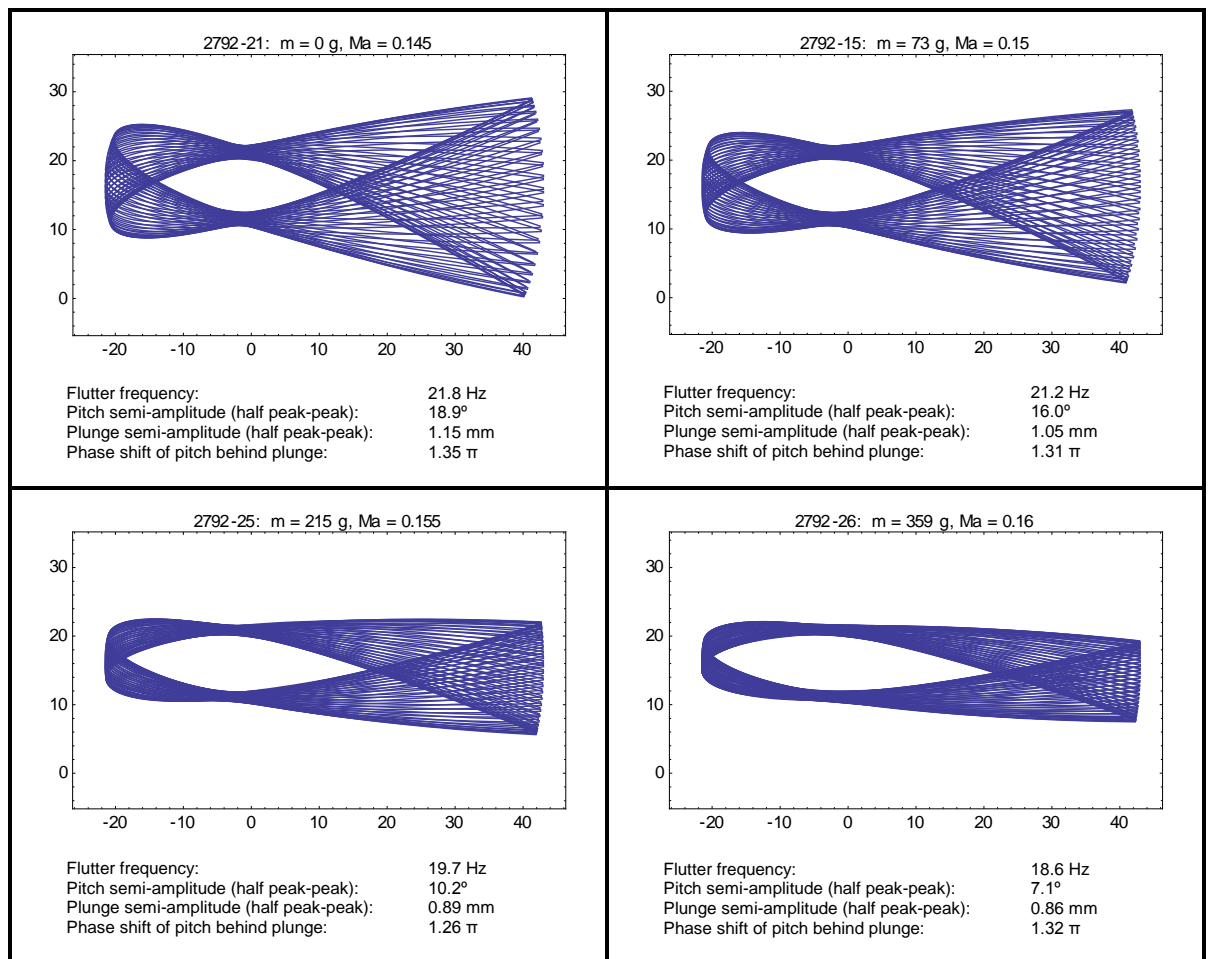
In the following, the results from two sets of measurements are summarized. The first set (2792-xx) was

realized without optical flow field measurements; the second one (2810-2-xx) was with Mach-Zehnder interferometer installed. Between the two measurements, the model had to be removed from the wind tunnel and disassembled. The eigenfrequencies of the model and the critical flow velocity for flutter onset is highly influenced by internal damping in the model, caused mainly by friction in the supports, bearings and model framework. Within the current setup, it is not possible to guarantee that the damping remains exactly the same after disassembly/assembly, negatively influencing the repeatability of the measurements. This is why the critical inflow velocity, for instance, was higher in the 2810-2 set than in the same

configuration within the previous measurement set. For clarity, the important experimental conditions of the measurements reported in this paper are summarized in Tab. 1.

The system being nonlinear, the initial conditions have to be kept constant, since they may influence the behavior of the system. For all measurements, the airflow was first set to a desired value. Then, the model was given an initial deflection (plunge) of 0.3 mm, released and left to vibrate freely in the airflow either with exponentially decreasing amplitudes (for subcritical flow velocities), or entering the flutter regime (for critical and supercritical flow velocities).

TABLE 2. VISUALIZATION OF THE FLUTTER OSCILLATION AND LIST OF VIBRATION PARAMETERS AT LIMIT CYCLE OSCILLATIONS NEAR CRITICAL FLOW VELOCITY FOR FOUR DIFFERENT VALUES OF ADDITIONAL MASS m



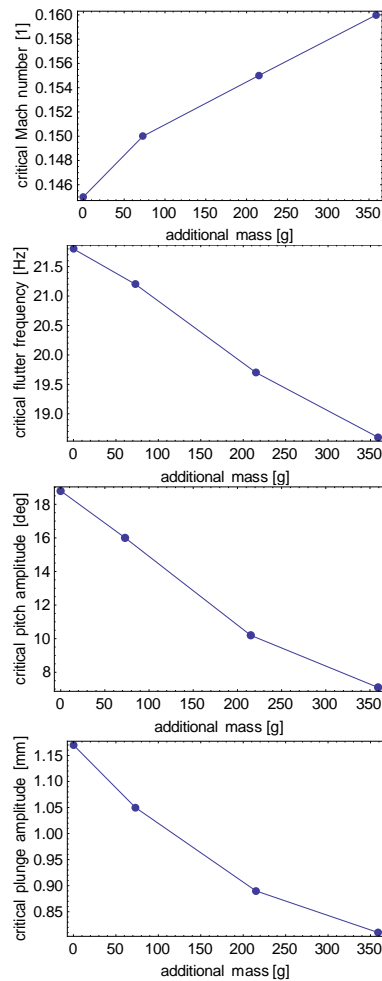


FIG. 4 STABILITY BOUNDARIES (CRITICAL FLOW VELOCITY FOR FLUTTER ONSET) AND LIMIT CYCLE PARAMETERS (FLUTTER FREQUENCY, PITCH AND PLUNGE SEMI-AMPLITUDE) AS A FUNCTION OF ADDITIONAL MASS

Stability boundaries

The critical flow velocities (Mach numbers Ma) for flutter onset for the case of four additional masses m attached to the airfoil frame are summarized in Tab. 2. The table also contains flutter frequencies, semi-amplitudes of the pitching and plunging modes (evaluated as a half of the peak-peak amplitude of the respective modes), phase difference between the plunging and pitching motion and graphical visualization of the limit

cycle oscillations. The visualization was done by plotting the airfoil contours, extracted from the high-speed camera frames, within one limit cycle. The critical Mach number was determined with a precision in the order of $Ma = 0.001$, i.e., below 1 m/s. The trends summarized in Tab. 2 are also shown graphically in Fig. 4. It can be seen that with increasing additional mass (decreasing eigenfrequency of the plunging mode) the critical flow velocity increases, which is in agreement with the linearized flutter theory.

However, during additional measurements 2810-2-23 and 2810-2-39, where bearings of the supporting frame have been slightly redesigned, it has been found that the mechanical damping of the system can influence the critical flow velocity more than the setting of the plunging mode eigenfrequency. The redesigned system having slightly higher damping, the critical flow velocity for $m = 0$ g increased to $Ma = 0.162$, for $m = 940$ g the system lost stability at $Ma = 0.218$.

From Fig. 4 it follows that the frequency of the flutter and amplitudes of both the pitching and plunging motion at critical flow velocity decrease with increasing additional mass. This is caused by the fact that the natural frequency of the plunging mode (about 20 Hz for $m = 0$ g and $Ma = 0$) gets further from the natural frequency of the pitching mode, which is 22 Hz for $Ma = 0$.

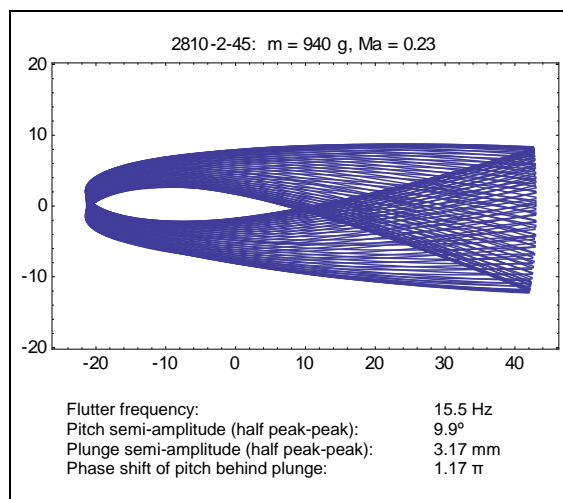
For all configurations, the pitching motion is phase-shifted behind the plunging motion by about 1.3π . The phase-shift does not seem to be influenced significantly by the additional mass.

Post-critical behavior of the system

When the airflow velocity is increased beyond the critical value, the amplitudes and the frequency of vibration generally increase up to certain limit, as was shown for certain configurations in [13]. In the current paper, the results obtained in measurement 2810-2-45 ($m = 940$ g, $Ma = 0.23$) are analyzed in detail. This measurement was performed for the highest velocity, where the flutter oscillation still occurred. For $m = 940$ g and inflow velocities higher than $Ma > 0.23$, the system regained stability due to high aerodynamic damping. During measurement 2810-2-45, the Mach-Zehnder interferometer was mounted and the unsteady interferograms recorded by the high-speed camera.

As summarized in Tab. 3, the frequency of vibration is 15.5 Hz. The airfoil vibrates with quite high plunging amplitude and moderate pitching amplitude, with the two modes out of phase similarly as in the previous measurements. Figs. 5, 6, and 7 show the time history of the plunging motion, pitching motion and signals from the pressure transducers, with detailed views on the transient stage (release from the initial deflection, onset of the flow-induced vibrations) and a period of stable oscillations. Data in Fig. 5 was taken from the linear encoder signal, Fig. 6 was evaluated from the high-speed camera frames.

TABLE 3. VISUALIZATION OF THE FLUTTER OSCILLATION AND LIST OF VIBRATION PARAMETERS FOR CASE 2810-2-45 AT A SUPERCRITICAL FLOW VELOCITY



Unlike the previous measurements with independent illumination [13], in this case, when the interferometer was mounted, the software was not able to track and evaluate the position of the airfoil in the camera frames automatically. Instead, the airfoil position had to be located manually, which deteriorated the precision of the pitching signal compared to previous automatically evaluated measurements. Fig. 5 shows that before reaching limit cycle oscillations, the airfoil oscillates about 12 periods with increasing amplitudes. The limit cycle oscillations are nearly sinusoidal both in pitch and plunge. The motion can be also visualized in phase plane, as has been done in [13] for the first set of measurements.

The signals from the pressure transducers are plotted in Fig. 7. Both probes are mounted on the upper surface of the airfoil: V1H close to the leading edge (in 18% of the chord), V2H further downstream in about middle of the chord. The semi-amplitude at V1H in the limit cycle oscillations is 2.1 kPa, at the downstream probe V2H about 0.5 kPa. The upstream pressure transducer is located in the region, where the airflow is mostly attached. V2H, on the other side, lies in the place where the airflow is massively separated, especially for high positive angles of attack and negative plunging velocities. This is why the data from V2H is more scattered, and unlike V1H, do not agree well with the results of numerical simulations [13].

For measurement 2810-2-45, the interferograms of one period of stable limit-cycle oscillations have been evaluated. The frame rate of the high-speed camera being 1000 fps and frequency of vibration $f = 15.5$ Hz, 65 frames per period were recorded. Eight frames are displayed in Tab. 4 together with the time instants, when the camera was triggered. The times

correspond precisely to the time base of the Dewetron data acquisition system, used for pressure and plunge motion measurements.

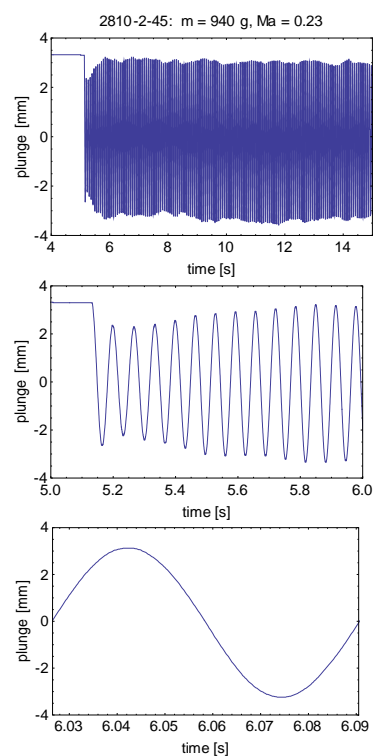


FIG. 5 TIME HISTORY OF THE PLUNGING MOTION (TOP), CLOSE-UP ON THE TRANSIENT (MIDDLE) AND STABLE (BOTTOM) STAGE

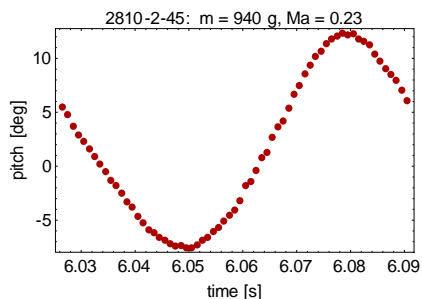


FIG. 6 TIME HISTORY OF THE PITCHING ANGLE – ONE PERIOD OF THE STABLE OSCILLATIONS

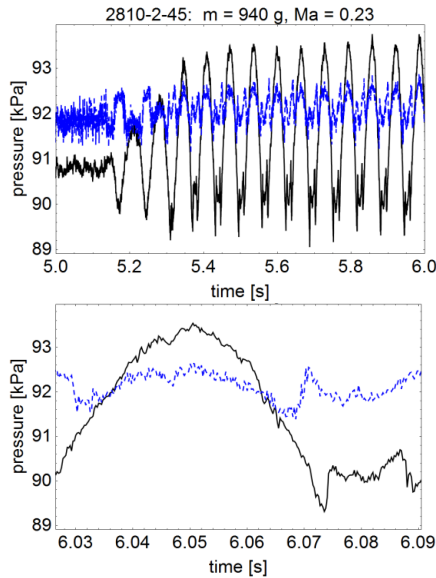


FIG. 7 STATIC PRESSURE MEASURED ON THE SURFACE OF THE AIRFOIL, TRANSIENT AND STABLE STAGE.
 — PROBE V1H (12 MM FROM LEADING EDGE, 18% OF CHORD)
 - - - PROBE V2H (31 MM FROM LEADING EDGE, 47% OF CHORD)

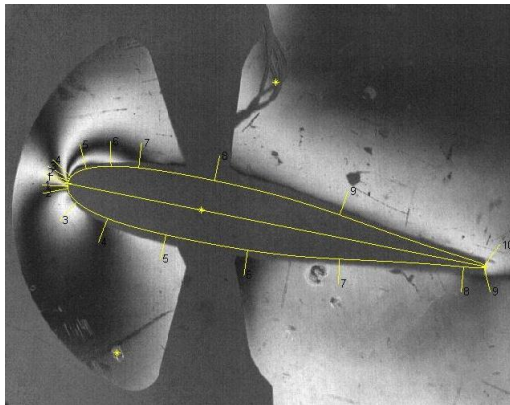


FIG. 8 EVALUATION OF A SAMPLE INTERFEROGRAM

Out of the full number of 65 frames from the vibration period, each second was evaluated using a procedure described in detail by Kozánek [11], yielding discrete density values at points where the interferometric fringes intersect the airfoil surface (see Fig. 8). Under the assumption of isentropic flow,

the aerodynamic pressure can be calculated from the evaluated density values.

Interpolation and numerical integration of the pressure over the upper and lower surface of the airfoil yields the total drag and lift force, exerted by the airflow on the vibrating airfoil [11]. The time history of the drag force is shown in Fig. 9 separately for the upper and lower airfoil surface. By comparison with Fig. 6 it can be seen that the drag on the lower and upper surface is almost precisely in-phase and out-of-phase with the angle of attack, respectively.

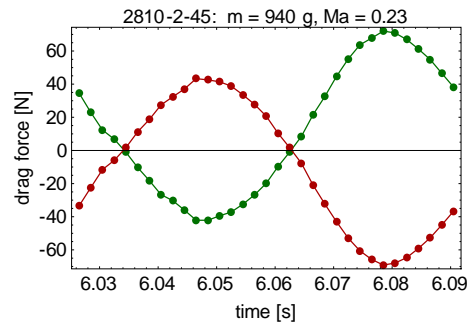


FIG. 9 DRAG FORCE COMPONENTS:
 — LOWER AIRFOIL SURFACE
 - - - UPPER AIRFOIL SURFACE

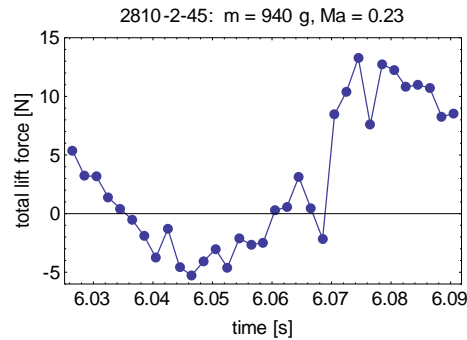
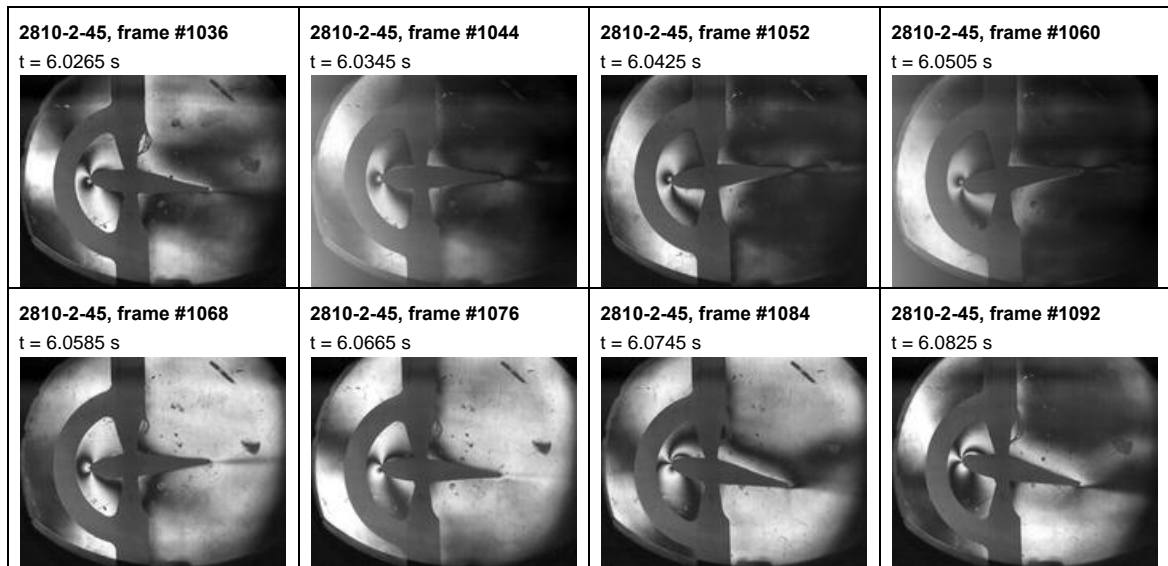


FIG. 10 TOTAL LIFT FORCE ON THE AIRFOIL

Fig. 10 shows the time history of the total lift force. Again, the waveform contains some noise, which is caused mainly by a low number of interferometric fringes apparent for this low Mach number flow. Plotting the total lift force against the plunge displacement yields a hysteresis loop (see Fig. 11), whose area corresponds to the energy transferred from the flow field to the vibrating structure through the plunging mode.

TABLE 4. INTERFEROGRAMS IN 8 PHASES OF ONE STABLE VIBRATION CYCLE



Numerical integration of the hysteresis loop in Fig. 11 using trapezoidal rule yields an energy of approximately 0.045 Joule per one oscillation cycle, giving a power of about 0.7 Watt. The energy is transferred from the flow to the airfoil by the pitching mode, too. However, to estimate this part, it would be necessary to calculate the total aerodynamic moment. For the current low flow velocities and consequent low resolution of the interferograms, the numerical integration does not provide results precise enough to perform these evaluations.

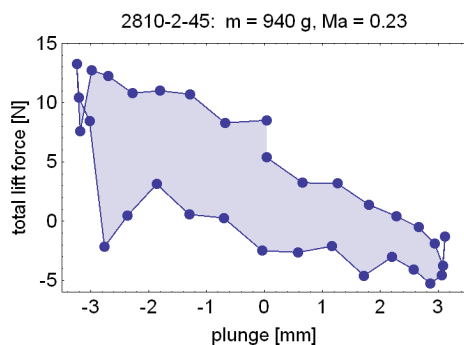


FIG. 11 ENERGY TRANSFERRED FROM THE AIRFLOW TO THE AIRFOIL THROUGH THE PLUNGING MODE

CONCLUSIONS

A physical model of an airfoil with two degrees of freedom has been designed, equipped with sensors and subjected to airflow in a subsonic suction-type wind tunnel. Using the current methods, it is possible to investigate the stability boundaries of the system, measure and analyze its dynamic behavior. The wind-tunnel has lateral optical access, and can be equipped with a Mach-Zehnder interferometer.

The stability boundaries of the current setup as a function of additional mass attached to the vibrating frame have been measured. For one case of a supersonic flow velocity, the waveforms of all the measured signals have been analyzed. For the same configuration, the interferograms have been evaluated and postprocessed, yielding the time-history of the drag and lift force exerted on the airfoil, and an estimate of the energy transfer from the airfoil to the structure.

In the current setup, no direct measurement of the pitching angle was possible. Instead, this had to be evaluated from the high-speed camera frames. Even though the mounting of such transducer represents a challenging task due to serious space limitations and rather violent dynamic conditions in the vibrating airfoil model, this is one of the priorities for subsequent measurements.

The accuracy of the pressure field evaluations from the unsteady interferograms increases with higher flow velocities, as more interferometric fringes are apparent on the high-speed camera frames. It has been shown that the method can be used

even for low flow velocities of about $Ma = 0.2$. For velocities above $Ma = 0.3 - 0.4$, the current airfoil model either oscillates with amplitudes so high that some components of the model might be destroyed (this is for the case of low additional mass, when the natural frequency of the pitching and plunging mode without airflow are close), or remains in the stable region where flutter does not occur (in the case of a high additional mass, natural frequencies of the two modes further apart).

In future, a new airfoil model will be manufactured, allowing for more precise tuning of the eigenfrequencies, equipped with pressure probes on both airfoil surfaces and with a pitching angle sensor. An in-house software is also being currently developed for semi-automatic evaluation of the density and pressure field from the unsteady interferograms.

ACKNOWLEDGMENTS

The research has been supported by the Czech Science Foundation, project 13-10527S *Subsonic flutter analysis of elastically supported airfoils using interferometry and CFD*.

REFERENCES

1. Naudasher, E. and Rockwell, D.: "Flow-Induced Vibrations", A. A. Balkema, Rotterdam, 1994.
2. Dowell, E. H.: "A Modern Course in Aeroelasticity", Kluwer Academic Publishers, Dordrecht, 1995.
3. O'Neil, T. and Strganac, T. W.: "Aeroelastic response of a rigid wing supported by nonlinear springs", *Journal of Aircraft*, 35, N. 4, 1998, pp. 616-622.
4. Lian, Y., Ol, M. V. and Shy, W.: "Comparative study of pitch-plunge airfoil aerodynamics at transitional Reynolds number". AIAA Paper 2008-652, 2008, 16 pp.
5. Soltani, M. R. and Marzabadi, F. R.: "Experimental investigation of transition on a plunging airfoil", *Transaction B: Mechanical Engineering*, 17, N. 6, 2010, pp. 468-479.
6. Prangemeier, T., Rival, D. and Tropea, C.: "The manipulation of trailing-edge vortices for an airfoil in plunging motion", *Journal of Fluids and Structures*, 26, 2010, pp. 193-204.
7. Fenercioglu, I., Cetiner, O.: "Categorization of flow structures around a pitching and plunging airfoil", *Journal of Fluids and Structures*, 31, 2012, pp. 92-102.
8. Poirel, D., Harris, Y. and Benaissa, A. A.: "Self-sustained aeroelastic oscillations of a NACA0012 airfoil at low-to-moderate Reynolds numbers", *Journal of Fluids and Structures*, 24, pp. 700-719.
9. Razak, N. A., Andrianne, T. and Dimidriadis, G.: "Flutter and stall flutter of a rectangular wing in a wind tunnel", *AIAA Journal*, 49, N. 10, 2011, Issue 10, pp. 2258-2271.
10. Vlček, V. and Kozánek, J.: "Preliminary interferometry measurements of a flow field around fluttering NACA0015 profile", *Acta Technica CSAV*, 56, 2011, pp. 379-387.
11. Kozánek, J., Vlček, V. and Zolotarev, I.: "The flow field acting on the fluttering profile, kinematics, forces and total moment", *International Journal of Structural Stability and Dynamics*, 13, N. 7, pp. 1340009-1-1340009-6.
12. Kozánek, J., Vlček, V. and Zolotarev, I.: "Vibrating profile kinematic in the start of flutter", *Dynamical systems – theory and applications*, Łódź, Poland, 2013.
13. Šidlof, P., Štěpán, M., Vlček, V., Řidký, V., Šimurda, D., Horáček, J.: "Flow past a self-oscillating airfoil with two degrees of freedom: measurements and simulations", EPJ Web of Conferences, 2014 (in press)

Chapter 6

Conclusion

Fluid dynamics is a fascinating scientific field with countless industrial applications. With the advent of affordable computing power in the second half of the 20th century, CFD simulations became a viable option for the investigation of various fluid flow problems. One might wonder whether the CFD would not replace challenging and expensive fluid dynamic measurements in foreseeable future. However, unlike e. g. computational solid mechanics, where it is nowadays in many cases perfectly feasible to use a computational mesh fine enough to reduce the error and uncertainty to an insignificant level, this is often not the case in CFD simulations.

For the ultimate numerical solution of the Navier-Stokes equations – so called Direct Numerical Simulation (DNS), it is essential that the mesh size be comparable with the size of the smallest turbulent eddies (and the time step with the inverse of highest frequencies). The DNS imposes prohibitive requirements on the required grid point number, which scales with $Re^{9/4}$ and which is largely beyond the potential of contemporary largest supercomputers even for moderate Reynolds numbers. For a typical airplane aerodynamics problem, for instance, the grid point number required for a DNS is in the order of 10^{16} . In present day, DNS has to be regarded as a research tool, not as a brute-force solution to engineering problems.

For turbulent flow simulations, almost all contemporary commercial CFD codes use Reynolds-Averaged Navier-Stokes (RANS) approach, where the influence of the turbulent eddies on the mean flow is modeled by certain approximation. The choice of turbulence models is immense. However, all the models were developed with specific assumptions and simplifications, none of them can be used universally and none of them is exact.

A promising class of methods called Large Eddy Simulations (LES), where the influence of large-scale anisotropic eddies induced by the geometry, boundary and initial conditions is solved, while the impact of the small, subgrid-scale and essentially isotropic vortices is modeled, has emerged during recent years and gains popularity not only in academia, but also in industry. In terms of computational cost and accuracy, LES can be seen as a compromise between RANS and DNS: the number of gridpoints for a correctly resolved LES of a given problem is much higher than that of a RANS simulation, but still far away from extreme requirements of DNS. The influence of the approximate subgrid-scale model on the global solution is generally lower than in the case of RANS. Nonetheless, it still introduces certain modeling error.

We see that even for the simple cases of flow problems, where the physics are completely known and exactly described by partial differential equations (i. e. incompressible single-phase

flow of perfectly Newtonian fluids), the Navier-Stokes equations cannot be solved numerically in a straightforward way due to practical constraints like the CPU performance, memory and cache size and memory bandwidth, and have to be complemented by approximate models, introducing additional and hardly quantifiable physical modeling error. In more complex situations, e. g. multiphase, non-Newtonian, reacting flow or combustion, even the mathematical model and the values of physical parameters are not known exactly. This is why no one could seriously suggest that the measurements in fluid flow problems are no longer needed. Both experimental and numerical approaches have their limitations and uncertainties, resource requirements and costs. In any case, most insight into a specific fluid flow problem can be gained when the numerical computations and experiments are used concurrently.

Bibliography

- J. Abbiss, T. Chubb, and E. Pike. Laser doppler anemometry. *Optics & Laser Technology*, 6: 249–261, 1974.
- R. Adrian. Particle-imaging techniques for experimental fluid mechanics. *Annual Review of Fluid Mechanics*, 23:261–304, 1991.
- F. Alipour, C. Fan, and R. C. Scherer. A numerical simulation of laryngeal flow in a forced-oscillation glottal model. *Computer Speech and Language*, 10:75–93, 1996a.
- F. Alipour, R. Scherer, and J. Knowles. Velocity distributions in glottal models. *Journal of Voice*, 10(1):50–58, March 1996b.
- F. Alipour and E. Finnegan. On the acoustic effects of the supraglottic structures in excised larynges. *The Journal of the Acoustical Society of America*, 133(5):2984–2992, 2013.
- F. Alipour and R. C. Scherer. Flow separation in a computational oscillating vocal fold model. *Journal of the Acoustical Society of America*, 116(3):1710–1719, September 2004.
- F. Alipour and R. C. Scherer. Characterizing glottal jet turbulence. *Journal of the Acoustical Society of America*, 119(2):1063–1073, February 2006.
- F. Alipour, C. Brucker, D. D Cook, A. Gommel, M. Kaltenbacher, W. Mattheus, L. Mongeau, E. Nauman, R. Schwarze, I. Tokuda, and S. Zorner. Mathematical models and numerical schemes for the simulation of human phonation. *Current Bioinformatics*, 6(3):323–343, 2011.
- Y. Bae and Y. J. Moon. Computation of phonation aeroacoustics by an ins/pce splitting method. *Computers & Fluids*, 37(10):1332 – 1343, 2008.
- K. J. Bathe. *Finite element procedures*. Prentice-Hall, 1996.
- S. Becker, S. Kniesburges, S. Müller, A. Delgado, G. Link, M. Kaltenbacher, and M. Döllinger. Flow-structure-acoustic interaction in a human voice model. *Journal of the Acoustical Society of America*, 125(3):1351–1361, March 2009.
- F. J. Blom. Considerations on the spring analogy. *International Journal for Numerical Methods in Fluids*, 32(6):647–668, March 2000.
- F. M. Bos. *Numerical simulations of flapping foil and wing aerodynamics*. PhD thesis, Technische Universiteit Delft, 2010.

- D. W. Bryer and R. Pankhurst. *Pressure-probe methods for determining wind speed and flow direction*. H.M.S.O, London, 1971.
- M. Bunch. *Dynamics of the singing voice*. Vienna: Springer-Verlag, 1982.
- S. H. Chue. Pressure probes for fluid measurement. *Progress in Aerospace Sciences*, 16:147–223, 1975.
- A. Cuerva and A. Sanz-Andrés. On sonic anemometer measurement theory. *Journal of Wind Engineering and Industrial Aerodynamics*, 88:25–55, 2000.
- T. A. Davis. UMFPack: unsymmetric multifrontal sparse LU factorization package. University of Florida, Gainesville, FL, USA, 2006. <http://www.cise.ufl.edu/research/sparse/umfpack/> [Online; accessed 29 November 2006].
- M. de Oliviera Rosa, J. Pereira, M. Grellet, and A. Alwan. A contribution to simulating a three-dimensional larynx model using the finite element method. *Journal of the Acoustical Society of America*, 114(5):2893–2905, November 2003.
- M. Dollinger, J. Kobler, D. A Berry, D. D Mehta, G. Luegmair, and C. Bohr. Experiments on analysing voice production: Excised (human, animal) and in vivo (animal) approaches. *Current Bioinformatics*, 6(3):286–304, 2011.
- J. Donea, A. Huerta, J.-P. Ponthot, and A. Rodríguez-Ferran. *Encyclopedia of Computational Mechanics*, volume 1, chapter 14 – Arbitrary Lagrangian-Eulerian Methods, pages 414–437. John Wiley & Sons, Ltd., 2004.
- E. Dowel. *A modern course in aeroelasticity*. Sijthoff & Noordhoff International Publishers B. V., Alphen aan den Rijn, 1978.
- J. S. Drechsel and S. L. Thomson. Influence of supraglottal structures on the glottal jet exiting a two-layer synthetic, self-oscillating vocal fold model. *Journal of the Acoustical Society of America*, 123:4434–4445, 2008.
- B. Erath and M. Plesniak. An investigation of jet trajectory in flow through scaled vocal fold models with assymetric glottal passages. *Experiments in Fluids*, 2006:735–748, August 2006a.
- B. Erath and M. Plesniak. The occurrence of the Coanda effect in pulsatile flow through static models of the human vocal folds. *Experiments in Fluids*, 41:735–748, 2006b.
- M. Feistauer. *Mathematical methods in fluid dynamics*. Longman, Harlow, 1993.
- M. Feistauer, J. Felcman, and I. Straškraba. *Mathematical and computational methods for compressible flow*. Clarendon Press, Oxford, 2003.
- M. Feistauer, J. Hasnedlová-Prokopová, J. Horáček, A. Kosík, and V. Kučera. DGFEM for dynamical systems describing interaction of compressible fluid and structures. *Journal Of Computational and Applied Mathematics*, 254:17–30, December 2013.
- J. H. Ferziger and M. Peric. *Computational Methods for Fluid Dynamics*. Springer-Verlag Berlin Heidelberg, December 2002.

- S. Hertegard and J. Gauffin. Acoustic properties of the Rothenberg mask. Technical Report 2-3, Royal Institute of Technology, Stockholm, Speech Transmission Laboratory, 1992.
- J. Heywood, R. Rannacher, and S. Turek. Artificial boundaries and flux and pressure conditions for the incompressible Navier-Stokes equations. *International Journal for Numerical Methods in Fluids*, 22:352–352, 1996.
- M. Hirano, S. Kurita, and T. Nakashima. The structure of the vocal folds. In K. Stevens and M. Hirano, editors, *Vocal Fold Physiology*, number 4, pages 33–43. University of Tokyo Press, Tokyo, 1981.
- J. Horáček, J. Veselý, and V. Uruba. Aeroelastic instability of a plate flexibly mounted in the channel wall (Aeroelastická nestabilita pružně uložené desky ve stěně kanálu, in Czech). *Engineering Mechanics*, pages 335–348, 1997.
- J. Horáček, P. Šidlof, and J. G. Švec. Numerical simulation of self-oscillations of human vocal folds with Hertz model of impact forces. *Journal of Fluids and Structures*, 20(6):853–869, August 2005.
- J. Horáček, P. Šidlof, V. Uruba, J. Veselý, V. Radolf, and V. Bula. Coherent structures in the flow inside a model of the human vocal tract with self-oscillating vocal folds. *Acta Technica*, 55: 327–343, 2010.
- K. Ishizaka and J. Flanagan. Synthesis of voiced sounds from two-mass model of the vocal cords. *The Bell System Technical Journal*, 51:1233–1268, 1972.
- R. I. Issa. Solution of the implicitly discretised fluid flow equations by operator-splitting. *Journal of Computational Physics*, 62(1):40 – 65, 1986.
- H. Jasak, H. G. Weller, and A. D. Gosman. High resolution NVD differencing scheme for arbitrarily unstructured meshes. *International Journal for Numerical Methods in Fluids*, 31:431–449, 1999.
- H. Jasak. *Error Analysis and Estimation for the Finite Volume Method with Applications to Fluid Flows*. PhD thesis, Imperial College of Science, Technology and Medicine, 1996.
- H. Jasak and Z. Tuković. Automatic mesh motion for the unstructured finite volume method. Unpublished manuscript, 2004.
- J. F. J.C. Kaimal. *Athmospheric Boundary Layer Flows: Their Structure and Measurement*. Oxford University Press, New York, 1994.
- M. W. Kehoe. A historical overview of flight flutter testing. Technical Report NASA Technical Memorandum 4720, National Aeronautics and Space Administration, 1995.
- S. Khosla, S. Murugappan, R. Lakhamraju, and E. Gutmark. Using particle imaging velocimetry to measure anterior-posterior velocity gradients in the excised canine larynx model. *The Annals of otology, rhinology, and laryngology*, 117(2):134–144, February 2008.
- S. Kniesburges, S. L. Thomson, A. Barney, M. Triep, P. Šidlof, J. Horáček, C. Brücker, and S. Becker. In vitro experimental investigation of voice production. *Current Bioinformatics*, 6 (3):305–322, September 2011.

- V. Kopecký. *Laserová anemometrie v mechanice tekutin*. Tribun EU, Brno, 2008.
- M. Krane, M. Barry, and T. Wei. Unsteady behavior of flow in a scaled-up vocal folds model. *Journal of the Acoustical Society of America*, 122(6):3659–3670, December 2007.
- B. R. Kucinschi, R. C. Scherer, K. J. DeWitt, and T. T. M. Ng. Flow visualization and acoustic consequences of the air moving through a static model of the human larynx. *Journal of Biomechanical Engineering*, 128(3):380–390, June 2006a.
- B. R. Kucinschi, A. A. Afjeh, and R. C. Scherer. On the application of the lattice boltzmann method to the investigation of glottal flow. *The Journal of the Acoustical Society of America*, 124(1):523, 2008.
- B. Kucinschi, R. Scherer, K. Dewitt, and T. Ng. An experimental analysis of the pressures and flows within a driven mechanical model of phonation. *Journal of the Acoustical Society of America*, 119(5 Pt 1):3011–3021, May 2006b.
- M. Larsson and B. Müller. Numerical simulation of confined pulsating jets in human phonation. *Computers & Fluids*, 38:1375–1383, 2009.
- G. Link, M. Kaltenbacher, M. Breuer, and M. Döllinger. A 2d finite-element scheme for fluid–solid–acoustic interactions and its application to human phonation. *Computer Methods in Applied Mechanics and Engineering*, 198:3321–3334, 2009.
- T. Liu and J. Sullivan. *Pressure and Temperature Sensitive Paints*. Springer, Berlin, Heidelberg, 2005.
- T. Liu, B. Campbell, S. Burns, and J. Sullivan. Temperature- and pressure-sensitive luminescent paints in aerodynamics. *Applied Mechanics Reviews*, 50:227–246, 1997.
- C. Lomas. *Fundamentals of Hot-Wire Anemometry*. Campridge University Press, Cambridge, 1986.
- J. Lucero. Dynamics of the two-mass model of the vocal folds: Equilibria, bifurcations, and oscillation region. *The Journal of the Acoustical Society of America*, 94(6):3104–3111, 1993.
- H. Luo, R. Mittal, X. Zheng, S. A. Bielamowicz, R. J. Walsh., and J. K. Hahn. An immersed-boundary method for flow-structure interaction in biological systems with application to phonation. *Journal of Computational Physics*, 227(22):9303–9332, 2008.
- W. Mattheus and C. Brücker. Asymmetric glottal jet deflection: Differences of two- and three-dimensional models. *The Journal of the Acoustical Society of America*, 130(6):EL373–EL379, 2011.
- Seika Measurement Technology. Principle of PIV, 2014. http://www.seika-mt.com/product/piv-en/Principle_of_PIV.html [Online; accessed 24 June 2014].
- The OpenFOAM Extend Project, 2014. <http://www.extend-project.de/> [Online; version foam-extend-3.0; accessed 16 September 2014].
- The OpenFOAM Foundation. OpenFOAM, 2014. <http://openfoam.org/> [Online; version 2.3.0; accessed 16 September 2014].

- M. Mihaescu, S. M. Khosla, S. Murugappan, and E. J. Gutmark. Unsteady laryngeal airflow simulations of the intra-glottal vortical structures. *Journal of the Acoustical Society of America*, 127(1):435–444, 2010.
- J. Neubauer, Z. Zhang, R. Miraghaie, and D. Berry. Coherent structures of the near field flow in a self-oscillating physical model of the vocal folds. *Journal of the Acoustical Society of America*, 121(2):1102–1118, February 2007.
- S. Patankar and D. Spalding. A calculation procedure for heat, mass and momentum transfer in three-dimensional parabolic flows. *International Journal of Heat and Mass Transfer*, 15(10):1787 – 1806, 1972.
- X. Pelorson, A. Hirschberg, R. van Hassel, A. Wijnands, and Y. Auregan. Theoretical and experimental study of quasisteady-flow separation within the glottis during phonation. application to a modified two-mass model. *Journal of the Acoustical Society of America*, 96(6):3416–3431, December 1994.
- A. Perry. *Hot-Wire Anemometry*. Clarendon, Oxford, 1982.
- P. Puncochářová-Požřzková, K. Kozel, and J. Horáček. Simulation of unsteady compressible flow in a channel with vibrating walls - influence of the frequency. *Computers & Fluids*, 46(1):404–410, July 2011.
- M. Raffel, C. Willert, S. Wereley, and J. Kompenhans. *Particle Image Velocimetry - a practical guide*. Springer, Berlin, Heidelberg, 2007.
- C. Renotte, V. Bouffieux, and F. Wilquem. Numerical 3d analysis of oscillatory flow in the time-varying laryngeal channel. *Journal of Biomechanics*, 33(12):1637–1644, December 2000.
- R. Schwarze, W. Mattheus, J. Klostermann, and C. Brücker. Starting jet flows in a three-dimensional channel with larynx-shaped constriction. *Computers & Fluids*, 48(1):68 – 83, 2011.
- D. Sciamarella and C. d’Alessandro. On the acoustic sensitivity of a symmetrical two-mass model of the vocal folds to the variation of control parameters. *Acta Acustica united with Acustica*, 90:746–761, 2004.
- D. Sciamarella and P. L. Quéré. Solving for unsteady airflow in a glottal model with immersed moving boundaries. *European Journal of Mechanics B/Fluids*, 27:42–53, 2008.
- J. H. Seo and R. Mittal. A High-Order immersed boundary method for acoustic wave scattering and Low-Mach number Flow-Induced sound in complex geometries. *Journal of Computational Physics*, 230(4):1000–1019, 2011.
- A. H. Shapiro. *The Dynamics and Thermodynamics of Compressible Fluid Flow*. The Ronald Press Company, New York, 1954.
- D. Shinwari, R. Scherer, K. Dewitt, and A. Afjeh. Flow visualization and pressure distributions in a model of the glottis with a symmetric and oblique divergent angle of 10 degrees. *Journal of the Acoustical Society of America*, 113(1):487–497, January 2003.
- P. Šidlof. *Fluid-structure interaction in human vocal folds*. PhD thesis, Charles University in Prague, 2007.

- P. Šidlof, J. G. Švec, J. Horáček, J. Veselý, I. Klepáček, and R. Havlík. Geometry of human vocal folds and glottal channel for mathematical and biomechanical modeling of voice production. *Journal of Biomechanics*, 41(5):985–995, 2008.
- P. Šidlof, E. Lunéville, C. Chambeyron, O. Doaré, A. Chaigne, and J. Horáček. Finite element modeling of airflow during phonation. *Applied and Computational Mechanics*, 4(1):121–132, July 2010.
- P. Šidlof, O. Doaré, O. Cadot, and A. Chaigne. Measurement of flow separation in a human vocal folds model. *Experiments in Fluids*, 51(1):123–136, 2011.
- P. Šidlof, J. Horáček, and V. Řidký. Parallel CFD simulation of flow in a 3D model of vibrating human vocal folds. *Computers & Fluids*, 80:290–300, 2013.
- P. Šidlof, M. Štěpán, V. Vlček, V. Řidký, D. Šimurda, and J. Horáček. Flow past a self-oscillating airfoil with two degrees of freedom: measurements and simulations. *EPJ Web of Conferences*, 67:02108, 2014a.
- P. Šidlof, V. Vlček, M. Štěpán, J. Horáček, M. Luxa, D. Šimurda, and J. Kozánek. Wind tunnel measurements of flow-induced vibration of a NACA0015 airfoil model. In *Proceedings of the ASME 2014 PVP Conference - symposium Fluid-structure interaction*, Anaheim, CA, USA, 2014b.
- P. Šidlof, S. Zörner, and A. Hüppe. A hybrid approach to computational aeroacoustics of human voice production. *Biomechanics and Modeling in Mechanobiology*, pages 1–17, 2014c.
- B. Story and I. Titze. Voice simulation with a body-cover model of the vocal folds. *Journal of the Acoustical Society of America*, 97(2):1249–1260, February 1995.
- J. Suh and S. Frankel. Numerical simulation of turbulence transition and sound radiation for flow through a rigid glottal model. *Journal of the Acoustical Society of America*, 121(6):3728–3739, June 2007.
- J. Suh and S. Frankel. Comparing turbulence models for flow through a rigid glottal model. *Journal of the Acoustical Society of America*, 123(3):1237–1240, March 2008.
- P. Sváček. Numerical approximation of flow induced vibrations of channel walls. *Computers & Fluids*, 46(1):448 – 454, 2011.
- C. Tao and J. Jiang. Mechanical stress during phonation in a self-oscillating finite-element vocal fold model. *Journal of Biomechanics*, 40(10):2191–2198, 2007.
- C. Tao, Y. Zhang, D. Hottinger, and J. Jiang. Asymmetric airflow and vibration induced by the Coanda effect in a symmetric model of the vocal folds. *Journal of the Acoustical Society of America*, 122(4):2270–2278, October 2007.
- S. Thomson, L. Mongeau, and S. Frankel. Aerodynamic transfer of energy to the vocal folds. *Journal of the Acoustical Society of America*, 118(3 Pt 1):1689–1700, September 2005.
- I. R. Titze. *Principles of Voice Production*. Prentice Hall, 1994.
- I. R. Titze. *The Myoelastic Aerodynamic Theory of Phonation*. National Center for Voice and Speech, 1ST edition, 2006.

- M. Triep, C. Brücker, and W. Schröder. High-speed PIV measurements of the flow downstream of a dynamic mechanical model of the human vocal folds. *Experiments in Fluids*, 39:232–245, 2005.
- M. Triep and C. Brücker. Three-dimensional nature of the glottal jet. *Journal of the Acoustical Society of America*, 127(3):1537–1547, 2010.
- C. Tropea, A. L. Yarin, and J. F. F. (Eds.). *Springer Handbook of Experimental Fluid Mechanics*. Springer, 2007.
- C.-G. Tsai, J.-H. Chen, Y.-W. Shau, and T.-Y. Hsiao. Dynamic b-mode ultrasound imaging of vocal fold vibration during phonation. *Ultrasound in medicine & biology*, 35(11):1812–1818, November 2009.
- J. van de Hulst. *Light scattering by small particles*. John Wiley and Sons, New York, 1957.
- S. Verma, Y. Joshi, and K. Muralidhar. *Interferometry - Principles and Applications*, chapter 13 – Optical interferometers: Principles and Applications in Transport Phenomena, pages 353–414. Nova Publishers, 2012.
- H. Versteeg and W. Malalasekera. *An Introduction to Computational Fluid Dynamics. The Finite Volume Method*. Pearson Education Limited, second edition edition, 2007.
- A. Yang, J. Lohscheller, D. A. Berry, S. Becker, U. Eysholdt, D. Voigt, and M. Döllinger. Biomechanical modeling of the three-dimensional aspects of human vocal fold dynamics. *Journal of the Acoustical Society of America*, 127(2):1014–1031, 2010.
- Z. Zhang. Influence of flow separation location on phonation onset. *Journal of the Acoustical Society of America*, 124(3):1689–1694, Sep 2008.
- W. Zhao, C. Zhang, S. Frankel, and L. Mongeau. Computational aeroacoustics of phonation, part i: Computational methods and sound generation mechanisms. *Journal of the Acoustical Society of America*, 112(5 Pt 1):2134–2146, 2002.
- X. Zheng, Q. Xue, R. Mittal, and S. Beilamowicz. A coupled sharp-interface immersed boundary-finite-element method for flow-structure interaction with application to human phonation. *Journal of Biomechanical Engineering*, 132(11):111003, November 2010.
- X. Zheng, R. Mittal, and S. Bielamowicz. A computational study of asymmetric glottal jet deflection during phonation. *The Journal of the Acoustical Society of America*, 129(4):2133–2143, 2011a.
- X. Zheng, R. Mittal, Q. Xue, and S. Bielamowicz. Direct-numerical simulation of the glottal jet and vocal-fold dynamics in a three-dimensional laryngeal model. *The Journal of the Acoustical Society of America*, 130(1):404–415, 2011b.
- X. Zheng, S. Bielamowicz, H. Luo, and R. Mittal. A computational study of the effect of false vocal folds on glottal flow and vocal fold vibration during phonation. *Ann Biomed Eng*, 37(3): 625–642, March 2009.